



## Mise en garde

La bibliothèque du Cégep de l'Abitibi-Témiscamingue et de l'Université du Québec en Abitibi-Témiscamingue (UQAT) a obtenu l'autorisation de l'auteur de ce document afin de diffuser, dans un but non lucratif, une copie de son œuvre dans [Depositum](#), site d'archives numériques, gratuit et accessible à tous. L'auteur conserve néanmoins ses droits de propriété intellectuelle, dont son droit d'auteur, sur cette œuvre.

## Warning

The library of the Cégep de l'Abitibi-Témiscamingue and the Université du Québec en Abitibi-Témiscamingue (UQAT) obtained the permission of the author to use a copy of this document for nonprofit purposes in order to put it in the open archives [Depositum](#), which is free and accessible to all. The author retains ownership of the copyright on this document.



Université du Québec en Abitibi-Témiscamingue

DÉVELOPPEMENT D'UNE APPROCHE D'OPTIMISATION MULTI-OBJECTIFS POUR LES  
TURBOMACHINES : APPLICATION AUX COMPRESSEURS AXIAUX ET AUX  
VENTILATEURS MINIERS

Thèse présentée à l'Université du Québec en Abitibi-Témiscamingue comme exigence partielle  
du grade de Docteur en Philosophie en Ingénierie offert en extension en vertu d'un protocole  
d'entente avec l'Université du Québec à Chicoutimi

Par  
Seyyed Mojtaba Fakhkhari

Soutenue le 14 avril 2025

Jury:

Hatem Mrad, Professeur, Université du Québec en Abitibi-Témiscamingue, Directeur de Recherche

Fouad Erchiqui, Professeur, Université du Québec en Abitibi-Témiscamingue, Président du jury

Hamza Khatib, Professeur, Université Hassan II de Casablanca, Membre externe

Mohamed Bechir Ben Hamida, Professeur, Université Imam Mohammad Ibn Saud Islamic, Membre externe

Mai 2025



Université du Québec en Abitibi-Témiscamingue

DEVELOPMENT OF A MULTI-OBJECTIVE OPTIMIZATION FRAMEWORK FOR  
TURBOMACHINERY: APPLICATION TO AXIAL COMPRESSORS AND MINE VENTILATORS

Thesis presented to Université du Québec en Abitibi-Témiscamingue in partial fulfillment for the  
degree of Doctor of Philosophy (Ph.D.) in Engineering offered as an extension under an  
agreement with Université du Québec à Chicoutimi

By  
Seyyed Mojtaba Fakhkhari

Defended on April 14, 2025

Jury:

Hatem Mrad, Professor, Université du Québec en Abitibi-Témiscamingue, Research Director

Fouad Erchiqui, Professor, Université du Québec en Abitibi-Témiscamingue, President of jury

Hamza Khatib, Professor, Université Hassan II de Casablanca, External member

Mohamed Bechir Ben Hamida, Professor, Université Imam Mohammad Ibn Saud Islamic, External member

May 2025

## **DEDICATION**

To my beloved wife, whose unwavering love, patience, and support have been my greatest strength throughout this journey. To my family, for their enduring trust, encouragement, and belief in me every step of the way.

## ACKNOWLEDGEMENT

I would like to express my deepest gratitude to my research director, Professor Dr. Hatem Mrad, for his invaluable guidance, encouragement, and unwavering support throughout the course of this research. His mentorship has been a cornerstone of both my technical development and academic journey. I am equally thankful to the committee members, Professor Dr. Fouad Erchiqui, Professor Dr. Hamza Khatib, and Professor Dr. Mohamed Bechir Ben Hamida, for their time, thoughtful feedback, and constructive suggestions, which helped improve the quality and clarity of this thesis.

I am also sincerely grateful to our industrial partner, Hyperflo, for their financial support, their collaboration and practical insights, which significantly contributed to the real-world relevance of this work. My appreciation extends to my colleagues and teammates for their continuous assistance, fruitful discussions, and generous support throughout the project.

I would like to thank the Université du Québec en Abitibi-Témiscamingue (UQAT) for providing a strong research environment and the infrastructure needed to carry out this work. I am also thankful for the support of the administrative staff and funding agencies whose contributions made this research possible.

Finally, I extend my heartfelt thanks to my family for their constant encouragement, patience, and unconditional support throughout this academic journey.

## TABLE OF CONTENTS

DEDICATION .....	II
ACKNOWLEDGEMENT .....	III
TABLE OF CONTENTS .....	IV
LIST OF FIGURES .....	VIII
LIST OF TABLES .....	XI
LIST OF ACRONYMS AND ABBREVIATIONS .....	XII
LIST OF SYMBOLS AND UNITS .....	XIII
RÉSUMÉ .....	XV
ABSTRACT .....	XVI
<b>1. INTRODUCTION .....</b>	<b>17</b>
1.1    Background.....	17
1.1.1 <i>Analysis of fluid flow</i> .....	17
1.1.2 <i>Aeroelasticity (FSI) in turbomachinery</i> .....	19
1.1.3 <i>Fan performance</i> .....	20
1.1.4 <i>Design optimization</i> .....	21
1.2    Problem Definition.....	23
1.3    Objectives.....	24
1.4    Originality statement .....	25
<b>2. CONCEPTUAL AND THEORETICAL FRAMEWORK .....</b>	<b>26</b>
2.1    Governing equations .....	26
2.1.1 <i>Reynolds' Transport Theorem</i> .....	26
2.1.2    Conservation of Mass.....	27
2.1.3    Conservation of Momentum .....	27
2.1.4    Conservation of Energy .....	28
2.1.5    The Reynolds-Averaged Navier Stokes Equations .....	29
2.1.6    Turbulence models.....	31
2.1.7    Efficiency and total pressure in compressors.....	32
2.1.8    Conservation law form.....	33
2.2    Finite volume analysis.....	34
2.3    Structural mechanics.....	35
2.3.1    Stress strain relations .....	36
2.3.2    The principle of virtual work .....	39
2.4    Finite element analysis.....	39

2.5	Fluid-structure interaction.....	41
2.5.1	Conservation of loads and energy.....	41
2.5.2	Geometric conservation law .....	42
2.6	Load transfer system.....	43
2.7	Fatigue life calculation.....	45
2.7.1	Fatigue loading.....	47
2.7.2	S-N curve .....	48
2.7.3	Fatigue life treatment in Ansys .....	49
2.8	Description of fans .....	52
2.8.1	Axial-flow fan performance .....	53
2.8.2	Fan Efficiency.....	55
2.8.3	Airflow measurement.....	55
2.8.4	<i>Fan laws</i> .....	55
2.9	Methodology and summary of contributions .....	56
3.	OPTIMIZING THE OPERATION SAFETY AND PERFORMANCE OF AN AXIAL COMPRESSOR USING FLUID-STRUCTURE COUPLING AND HIGH PERFORMANCE COMPUTING .....	59
3.1	Résumé .....	59
3.2	Introduction .....	60
3.3	Experimental data .....	64
3.4	Numerical method implementation and experimental validation .....	64
3.5	Project Scheme.....	66
3.6	Computational fluid dynamics (CFD).....	68
3.6.1	Fluid domain governing equations.....	68
3.6.2	High performance computing (HPC) based on MPI parallelization .....	69
3.7	CFD analysis implementation.....	70
3.7.1	Boundary conditions.....	71
3.7.2	Mesh convergence study.....	71
3.7.3	Turbulence models theory and application .....	73
3.8	Experimental validation .....	75
3.9	Fluid-structure interaction Analysis.....	79
3.9.1	Structural deformation analysis .....	80
3.9.2	Fluid-structure coupling method implementation .....	81
3.9.3	Direct pressure implementation .....	82

3.9.4	ANSYS system coupling.....	83
3.10	Design of experiments: Parametric study.....	84
3.10.1	Multilevel Factorial Design.....	84
3.11	Response Optimization .....	86
3.12	Conclusion .....	87
4.	OPTIMIZATION OF AN AXIAL-FLOW MINE VENTILATION FAN BASED ON EFFECTS OF DESIGN PARAMETERS .....	89
4.1	Résumé .....	89
4.2	Introduction .....	90
4.3	Geometry .....	93
4.4	Numerical investigations .....	95
4.5	Computational setup and boundary conditions.....	97
4.6	Experimental validation .....	100
4.7	Fluid structure interaction analysis in stall .....	103
4.8	Sensitivity analysis and Design of experiments .....	106
4.8.1	Parametric study implementation on high performance clusters .....	107
4.8.2	Data pre-processing and sensitivity analysis .....	107
4.9	Optimization and design point prediction.....	111
4.10	Numerical validation of optimal design .....	113
4.11	Conclusion .....	114
5.	OPTIMIZATION OF UNCONSTRAINED PROBLEMS USING A DEVELOPED ALGORITHM OF SPECTRAL CONJUGATE GRADIENT METHOD CALCULATION.....	116
5.1	Résumé .....	116
5.2	Introduction .....	117
5.3	Modified SCGM.....	119
5.4	Results and discussion .....	120
5.4.1	Ackley's function .....	121
5.5	Beale test function.....	123
5.6	Conclusion .....	127
6.	AERODYNAMIC SHAPE OPTIMIZATION OF NACA AIRFOILS BASED ON A NOVEL UNCONSTRAINED CONJUGATE GRADIENT ALGORITHM .....	129
6.1	Résumé .....	129
6.2	Introduction .....	130
6.3	Airfoil shape parameterization .....	134

6.3.1	Bézier curve .....	134
6.4	Airfoil optimization technique .....	136
6.5	Flow analysis .....	136
6.6	Optimization methods .....	137
6.6.1	Conjugate gradient .....	138
6.6.2	Modified spectral conjugate gradient method .....	139
6.6.3	Aerodynamic functions and gradients .....	142
6.7	Flow analysis .....	142
6.8	Results and discussion .....	143
6.9	Conclusion .....	150
7.	ENHANCED AERODYNAMIC AND STRUCTURAL DESIGN THROUGH INTEGRATED OPTIMIZATION OF TWISTED CHINOOK-TYPE BLADES FOR AXIAL-FLOW FANS .....	153
7.1	Résumé .....	153
7.2	Introduction .....	154
7.3	Airfoil shape parameterization .....	156
7.3.1	Bézier curves .....	156
7.3.2	Geometry .....	156
7.4	Airfoil profile optimization .....	157
7.5	Flow analysis .....	158
7.6	Aerodynamic optimization .....	159
7.7	Structural analysis .....	160
7.7.1	Static analysis .....	160
7.7.2	Fatigue analysis .....	164
7.8	Structural optimization .....	165
7.9	Conclusion .....	168
	GENERAL CONCLUSION .....	170
	LIMITATIONS AND RECOMMENDATIONS .....	172
	REFERENCES .....	175

## LIST OF FIGURES

Figure 1 Injection and ejection side of the blade in circumferential view .....	18
Figure 2 Cost versus fan efficiency.....	24
Figure 3 Stress distribution in a large plate subjected to uniaxial tension.....	45
Figure 4 Crack modes: opening mode, in-plane shear and out-of-plane shear.....	46
Figure 5 Constant amplitude loading .....	48
Figure 6 Semi-Log Stress-Life (S-N curve) for Al 356-T6 from Ansys material library .....	51
Figure 7 Fan performance curve.....	54
Figure 8 Meridional view of test fan rotor showing laser anemometer and aerodynamic survey locations .....	64
Figure 9 The geometry of a full-stage compressor rotor .....	67
Figure 10 Fluid domain geometry.....	65
Figure 11 Project scheme.....	68
Figure 12 Computational mesh for fluid domain at near tip (a), and solid domain (b).....	72
Figure 13 Total pressure ratio vs mesh number.....	72
Figure 14 Total pressure ratio vs mass ratio for different turbulence models compared to experimental data.....	75
Figure 15 Efficiency vs mass ratio for different turbulence models compared to experimental data .....	76
Figure 16 Mach number at 90% span near peak efficiency, CFD results(left) and experimental data(right).....	77
Figure 17 Mach number at 70% span near stall, Numerical results (left) and Experimental Data(right) .....	77
Figure 18 Pressure distribution in flow passage in 90% of blade height near stall.....	78
Figure 19 Blade loading comparison at 50% of blade height streamwise direction (pressure and suction sides). ....	78
Figure 20 Pressure distribution on the pressure side(left) and suction side(right) of the blade...79	79
Figure 21 Pressure distribution at different locations of blade pressure and suction sides.....	79
Figure 22 Mesh convergence study for solid domain.....	82
Figure 23 Imported Pressure from CFD solution.....	83
Figure 24 Maximum total deformation of blade in direct exertion of pressure(left) and employing System Coupling(right) for fluid-solid coupling purpose.....	84
Figure 25 Individual effects of material and tip-clearance on the safety factor value.....	86
Figure 26 Individual effects of material and tip-clearance on the efficiency value.....	86

Figure 27 Cost versus fan efficiency .....	90
Figure 28 42-in Chinook type underground ventilation with modified blade .....	94
Figure 29 3D scanned blade for 42-inch fan .....	95
Figure 30 Comparison of the scanned blade with the 3D CAD file .....	95
Figure 31 Optimization progress diagram .....	96
Figure 32 Computational domain for single blade passage .....	99
Figure 33 Computational domain for the whole fan assembly .....	99
Figure 34 Details of computational mesh .....	99
Figure 35 Mesh convergence Curve .....	100
Figure 36 Campbell diagram for first three mode shapes of fan blade .....	101
Figure 37 Performance curve for the blade with angle of attack of 50 degrees .....	102
Figure 38 Velocity streamlines and vectors in stall at 80% span .....	102
Figure 39 Pressure distribution around the blade region in 80% span: Stall (left), Safe operating point (right) .....	103
Figure 40 Turbulence kinetic energy contour around the blade region in 80% span: Stall (left), Safe operating point (right) .....	103
Figure 41 (a) Pressure exported from CFD, (b) Maximum von-Mises stress, (c) Fatigue safety factor, (d) Failure caused by fatigue .....	105
Figure 42 Experimental measurements versus numerical results .....	106
Figure 43 Effects of different variables on the performance of the axial fan. a) Angle of attack, b) Speed change, c) Number of blades, d) Casing size, e) Tip clearance .....	108
Figure 44 Normal probability plot for Total Pressure (a), and Airflow Rate (b) .....	109
Figure 45 Pareto chart of standardized effects of the parameters on the Total Pressure (left) and Airflow Rate (right) .....	111
Figure 46 Desired optimal operating point .....	112
Figure 47 Pressure distribution, velocity vectors and velocity streamlines on the blade-to-blade surface in 80% span .....	114
Figure 48 Ackley test function. a) 3D view, b) 2D view .....	122
Figure 49 Ackley test function iterations paths for $x_1 = (0.1, 0.1)$ .....	123
Figure 50 Beale test Function a) 3D view, b) 2D view .....	124
Figure 51 Beale function iterations paths for $x_1 = (1, 1)$ . a) $\beta = \beta kMF$ , b) $\beta = \beta kCD$ , c) $\beta = \beta kDY$ , d) $\beta = \beta kLS$ .....	124
Figure 52 Comparison of the numerical results of Beale test function for different CG coefficients and the proposed algorithm for the initial point of (1, 0.8) .....	125

Figure 53 Bézier airfoil presentation.	135
Figure 54 Proposed Unconstrained CG optimization procedure.	137
Figure 55 Drag coefficient minimization per iteration.	145
Figure 56 a) NACA 4412 original and Optimized airfoil profiles with Bezier control points, b) NACA 2415 original and Optimized airfoil profiles with Bezier control points.	146
Figure 57 a) Lift coefficient in sequences of AOA for NACA 4412 and Optimized airfoil, b) C <sub>l</sub> /C <sub>d</sub> ratio in sequence of AOA for NACA 4412 and Optimized airfoil.	147
Figure 58 Drag coefficient minimization using Steepest Decent method.	147
Figure 59 a) Xfoil Cl/Cd prediction in 5.75° for NACA2415 b) Optimized airfoil Cl/Cd prediction.	149
Figure 60 a) Original NACA4418 profile vs optimized profile, b) Original NACA1408 profile vs optimized profile.	149
Figure 61 Chinook-type fan 3D blade, 2D profile and Bezier parameterized curves.	157
Figure 62 Original and optimized airfoil profile with control points.	159
Figure 63 a) lift to drag ratio versus angle of attack, b) lift coefficient versus angle of attack, c) drag coefficient versus angle of attack.	160
Figure 64 Stress concentration factors for shoulder fillets in flat and round bars.	162
Figure 65 Blade-root junction.	163
Figure 66 Pressure distribution on the blade resulting from CFD analysis in stall.	163
Figure 67 Maximum equivalent stress and minimum safety factor on blade-root junction.	164
Figure 68 Fatigue safety factor on the critical region.	165
Figure 69 Modified filet radius on the blade-root junction.	166
Figure 70 Maximum equivalent stress and corresponding safety factor on the optimized blade critical region.	167
Figure 71 Fatigue safety factor results for the modified blade.	167

**LIST OF TABLES**

Table 1 Characteristics: NASA Compressor Rotor 67 Specifications .....	66
Table 2 Design Points: Table of design points for k- $\epsilon$ turbulence model at different operating conditions.....	70
Table 3 Mesh study: Element number of the fluid domain, for mesh study.....	72
Table 4 Solid mesh study: mesh sensitivity study for solid.....	82
Table 5 DOE: Design of Experiments table.....	85
Table 6 Target factors: Target factors for case studies.....	87
Table 7 Optimization solution: Solutions for the response optimization for both case studies ...	87
Table 8 Specifications of axial-flow ventilator.....	96
Table 9 Factorial design variables and their levels.....	107
Table 10 Regression model summary for both total pressure and airflow rate.....	110
Table 11 Regression equations for airflow rate and total pressure.....	111
Table 12 Predictions for various optimal operating parameters and outputs .....	112
Table 13 Numerical validation of optimal solutions and errors .....	113
Table 14 Convergence speed comparison for Basic CG methods .....	125
Table 15 The performance of MF, PR, DY and LS methods according to unconstrained test functions.....	126
Table 16 Relative efficiency of CG methods .....	127
Table 17 Original NACA 4412 Bézier control points.....	144
Table 18 Optimized airfoil control points.....	145
Table 19 Lift and drag coefficients for NACA 4412 and optimized airfoil in different AOA.....	146
Table 20 Cl/Cd ratios for NACA 2415 and optimized airfoil in different AOA.....	148
Table 21 Optimization results for different types of NACA airfoils.....	149
Table 22 Optimization results comparison using different conjugate coefficients.....	150
Table 23 Stress analysis and safety factor comparison of original vs. optimized blade designs .....	169

## **LIST OF ACRONYMS AND ABBREVIATIONS**

- AOA: Angle of Attack
- CFD: Computational Fluid Dynamics
- CG: Conjugate Gradient
- CSD: Computational Solid Dynamics
- DOE: Design of Experiments
- FSI: Fluid-Structure Interaction
- HPC: High Performance Computing
- MPI: Message Passing Interface
- RANS: Reynolds-Averaged Navier-Stokes

## LIST OF SYMBOLS AND UNITS

- $a_k$ : CG step length  
 $\beta_k$ : CG coefficient  
 $B_i$ : Bézier polygon's vertices  
 $C_p$ : Specific heat at constant pressure  
 $[C]$ : Damping matrix  
 $D$ : Drag force  
 $\epsilon$ : Turbulence rate of dissipation  
 $\Gamma_k$ : Effective diffusivity of  $k$   
 $\Gamma_\omega$ : Effective diffusivity of  $\omega$   
 $\{F\}$ : Load vector  
 $G_k$ : Generation of turbulence kinetic energy due to the Mean velocity gradients  
 $G_b$ : Generation of turbulence kinetic energy due to the Buoyancy  
 $G_\omega$ : Generation of  $\omega$   
 $H$ : Hessian  
 $h$ : Static enthalpy  
 $H_{sf}$ : Interface coupling matrix  
 $\eta$ : Efficiency  
 $J_{n,i(t)}$ : Bernstein function  
 $[K]$ : Stiffness matrix  
 $k$ : Turbulent kinetic energy  
 $L$ : Lift force  
 $Ma$ : Mach number  
 $[M]$ : Structural mass matrix  
 $\mu_{eff}$ : Effective viscosity  
 $\mu_t$ : Turbulent viscosity  
 $P$ : Fluid pressure  
 $P_f$ : Pressure vector for fluid domain on the interface  
 $\Pi$ : Total pressure ratio  
 $P_s$ : Pressure vector for solid domain on the interface  
 $R$ : Specific gas constant  
 $Re$ : Reynold's number  
 $S$ : Airfoil area  
 $\sigma_k$ : Turbulent Prandtl numbers for  $k$

$\sigma_\epsilon$ : Turbulent Prandtl numbers for  $\epsilon$

$S_M$ : Sum of body forces

$\{u\}$ : Displacement vector

$U$ : Fluid velocity

$Y_k$ : Dissipation of  $k$  due to turbulence

$Y_\omega$ : Dissipation of  $\omega$  due to turbulence

## RÉSUMÉ

Cette thèse propose une exploration détaillée des techniques d'optimisation avancées et des méthodes de calcul appliquées à la turbomachine et aux composants structuraux, mettant en lumière plusieurs aspects critiques. La recherche commence par une analyse des compresseurs axiaux, utilisant une approche d'interaction fluide-structure et le calcul haute performance pour améliorer la sécurité opérationnelle et la performance. En exploitant la parallélisation MPI et la validation de maillage haute résolution, cette étude permet une amélioration de plus de 33 % de la sécurité du compresseur tout en préservant son efficacité. L'amélioration des ventilateurs de ventilation minière à flux axial est examinée ensuite. Grâce à la méthode des Plans d'Expériences (DOE) et à l'analyse de régression, des améliorations significatives de performance de 9 % sont réalisées, accompagnées de réductions du bruit, des coûts et de la consommation d'énergie. Cela souligne l'efficacité des stratégies d'optimisation pour relever les défis de la ventilation souterraine. La troisième partie introduit un nouvel algorithme de gradient conjugué spectral pour l'optimisation des problèmes non contraints, démontrant une stabilité, des taux de convergence et une efficacité supérieure par rapport aux méthodes traditionnelles. Ce nouvel algorithme représente un avancement significatif dans la résolution des défis complexes d'optimisation.

De plus, l'optimisation de la forme aérodynamique du profil d'aile est réalisée à l'aide du nouvel algorithme d'optimisation de gradient conjugué non contraint, utilisant la paramétrisation Bézier basée sur un code MATLAB couplé avec un solveur CFD. Cette approche aboutit à des améliorations notables des rapports portance/traînée, validant l'efficacité de l'algorithme proposé pour améliorer les performances aérodynamiques. Finalement, l'efficacité aérodynamique et structurelle des ventilateurs à flux axial utilisés pour la ventilation minière a été améliorée en optimisant la conception de la pale Chinook torsadée, ce qui a permis une augmentation de 14,4 % du rapport portance-trainée et une amélioration de 4,5 % des performances du ventilateur. Des modifications structurelles ont également prolongé la durée de vie en fatigue de la pale, améliorant ainsi la fiabilité à long terme en conditions de décrochage.

**Mots-clés :** Interaction fluide-structure, Cluster HPC (calcul haute performance), Plan d'expériences (DOE), Ventilation minière, Optimisation, Paramétrisation, Méthode du gradient conjugué spectral, Profils NACA, Durée de vie en fatigue.

## ABSTRACT

This thesis offers a detailed exploration of advanced optimization and computational techniques applied to turbomachinery and structural components, highlighting several critical aspects. The research begins with an analysis of axial compressors, utilizing a fluid-structure interaction approach and high-performance computing to improve operational safety and performance. By leveraging MPI parallelization and high-resolution mesh validation, this study achieves over a 33% improvement in compressor safety while preserving efficiency. The optimization of axial-flow mine ventilation fans is examined next. Through Design of Experiments (DOE) and regression analysis, significant performance enhancements of 9% are realized, alongside reductions in noise, cost, and energy consumption. This underscores the effectiveness of optimization strategies in addressing the complexities of underground ventilation.

In the third part, a novel spectral conjugate gradient algorithm for unconstrained problem optimization is introduced, demonstrating superior stability, convergence rates, and efficiency compared to traditional methods. This new algorithm represents a significant advancement in solving complex optimization challenges. Further, aerodynamic shape optimization of airfoil profile is achieved using the novel unconstrained conjugate gradient optimization algorithm, employing Bézier parameterization based on MATLAB code coupled with CFD solver. This approach results in notable improvements in lift-to-drag ratios, validating the effectiveness of the proposed algorithm in enhancing aerodynamic performance. Finally, the aerodynamic and structural efficiency of axial-flow fans used in mine ventilation are enhanced by optimizing the twisted Chinook blade design, achieving a 14.4% lift-to-drag ratio improvement and a 4.5% increase in fan performance. Structural modifications also extended the blade's fatigue life, improving long-term reliability under stall conditions.

**Keywords:** Fluid-structure interaction, HPC cluster (high-performance computing), Design of experiments, Mine ventilation, Optimization, Parameterization, Spectral conjugate gradient method, NACA airfoils, Fatigue life.

## 1. INTRODUCTION

Underground mining plays a significant role in the global mining industry, but it also poses several risks to the miners in terms of air pollution. The toxic and potentially explosive gases in the mine atmosphere, along with temperature regulation, are among the key concerns of underground mining ventilation. This is why it is essential for the mining industry to follow the regulations and innovations in ventilation.

Ventilation in underground mining not only helps to ensure the safety of miners but also involves significant energy and maintenance costs. Researchers are actively exploring ways to improve the performance of ventilation systems, predict and address potential challenges, and optimize their operation. The focus of this work is to study the performance of turbomachinery used in underground mining ventilation with the aim of developing an inverse approach for optimum design. This approach considers reliability, efficiency, and the use of low-cost components to enhance the overall performance of the ventilation system.

### 1.1 *Background*

The classification of turbomachines can be done in three ways: based on the type of working fluid, the direction of flow, and whether or not it delivers or extracts power from the fluid. One such classification based on the direction of flow is between machines working on compressible fluids such as gas turbines or high-speed fans and those working on incompressible fluids such as pumps that work with water. However, wind turbines and low-speed fans can be in both categories as they experience minimal density changes [1].

#### 1.1.1 *Analysis of fluid flow*

In the study of turbomachinery, various factors such as angle of attack, tip clearance, and rotation have been investigated. For example, a simulation was conducted on an isolated subsonic axial compressor with 54 rotor blades, inlet guide vanes, a stagger angle of 50 degrees, and a hub-to-tip ratio of 0.85 [2]. The simulation aimed to predict the occurrence frequency and amplitude of non-synchronous vibrations and suppress them. The results showed that a well-designed casing treatment could remove the trailing edge backflow and suppress flow impingement and rotating instabilities. A physical mechanism was also proposed to explain the non-synchronous vibration phenomenon based on acoustic feedback. The critical non-synchronous tip speed prediction was validated by measuring the tip speed. The study revealed three missing links between the rotational instabilities and non-synchronous vibrations, including the required pressure

unsteadiness amplification, blade pitch, and vibrational frequency and mode shift [3]. Another study experimentally investigated various tip geometry designs to control the tip leakage resulting aerodynamic loss [4]. The results showed that the effective tip leakage control scheme for a compressor cascade was the suction-side winglets, while pressure-side winglets were not effective control methods. The performance of a NASA rotor 37 compressor was studied using 3-D Reynolds-averaged Navier-Stokes equations with the  $k-\epsilon$  turbulence model [5]. The parameters studied were front and rear lengths and the height of the casing groove, and the mass flow rate of outlet. The results showed that the ejection mass flow rate did not affect the stall margin compared to the geometric parameters and that using casing grooves with both injection and ejection could increase the stall margin, peak adiabatic efficiency, and stable range extension without losing the total pressure value.

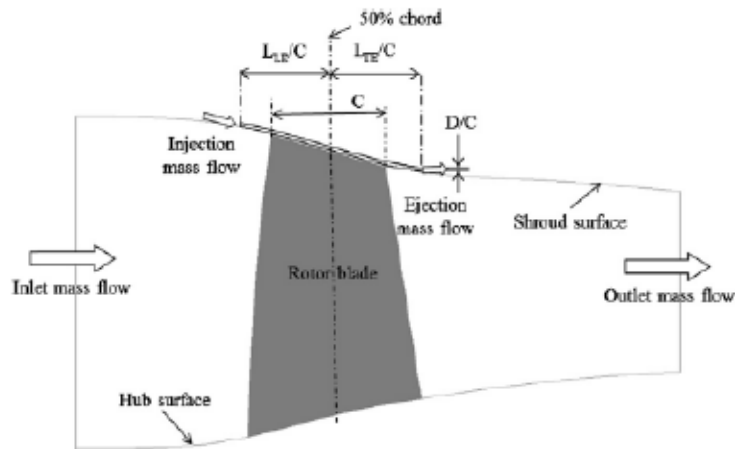


**Figure 1**  
**Injection and ejection side of the blade in circumferential view**  
Source: [5].

Asymmetry in the rotor blade tip clearance was investigated in a study, and it was found that asymmetric clearance had negligible influence on the overall compressor performance [6]. In another study, air injection at the rotor blades row tip region was utilized to improve the aerodynamic performance of a low-speed axial compressor [7]. The results showed that low air flow rate injection at the blade row tip resulted in significant beneficial effects on the whole blade height, increased pressure rise, reduced the diffusion factor, and reduced the blockage at the blade tip gap region caused by the stall phenomenon. Finally, a numerical simulation was conducted on a SR3 propeller at 35,000 feet altitude at a transonic Mach of 0.8 using the Ansys CFX package [8]. The results showed that the performance coefficients and efficiency were in good agreement with experiments, and it was found that the axial and tangential velocities, swirl

angles, and static pressure at mid-span reached their maximum values from the wake parameters of the propeller.

### *1.1.2 Aeroelasticity (FSI) in turbomachinery*

FSI simulations often involve computational fluid dynamics (CFD) and structural mechanics to model the fluid and solid domains, respectively, and to solve the equations that govern their interactions. FSI simulations can provide valuable insights into the performance and safety of systems, as well as guide the design and optimization of complex structures.

The studies in the literature review focus on the numerical analysis of fluid-structure interaction in highly loaded engine designs. The objective of these studies is to obtain reliable solutions for the nonlinear effects on the fluid-solid interface and the individual behavior of each component. To accomplish this, both structural and fluid motion governing equations must be solved simultaneously in a time-integrated manner. However, due to the computational cost, some fluid-structure couplings are implemented using a one-way coupling algorithm, where the individual solvers partially or completely converge before exchanging response information [9]. In one study, the Euler equations were solved using the modal approach for structural analysis in a partially coupled manner [10]. Two years later Doi et al. used an explicit Runge-Kutta solver for the flow and a finite element method solver for the structure to investigate the aeroelastic responses of a compressor rotor blade [11]. A numerical method is used to investigate the combined effects of (*s/c*) blade pitch to blade chord ratio and (*c/d*) the blade chord to streamwise separation between two vortices, on the aerodynamic and structural responses of the central blade. Aerodynamic and structural dynamic responses of the central blade in the cascades are found to be the function of the blade pitch to chord ratio. The results show rather insensitivity of the fluid-structure interaction to the effect of vibrating neighboring blade [12] Another study conducted a numerical parametric study for a transonic-axial compressor with treated and untreated end-walls at different tip gap heights and found that the end-wall treatments were more efficient at larger sizes of tip gap [13]. A study investigated flow-induced vibrations for wind turbine blade airfoils using a strong two-way FSI coupling in a 2-D domain with low Reynolds and incompressible flow. The results showed different results for aerodynamic load between laminar and turbulent flows, but similar responses for the airfoil [14]. Later on, Hongisk et al. developed a fully coupled FSI method for axial compressor flutter and found that the rotor flutters in stall operation with the first mode resonance [15]. In a further research work, a comparison of turbulence models for a two-dimensional subsonic flow over an airfoil with various angles of attack showed that the turbulence models in commercial CFD codes were not accurate at high angles of attack [16]. A different study investigated a full

anulus unsteady CFD for a fan-stage operating with a 120-degree stagnation pressure circumferential distortion [17]. In a later investigation on the compressor, the effect of inlet swirl and pressure distortion on the performance and stability of an axial compressor and found good agreement between the results and experimental data were numerically investigated, the validation of the numerical study was conducted employing the data published from NASA Lewis Research Center [18]. In the other hand, Wang et al. presented a one-way coupled FSI model for wind turbine composite blades at full scale, with aerodynamic forces obtained from CFD analysis and blade structural responses evaluated with FEA [19]. In a different study on wind turbines, high structure reaction to wind and turbine blade vibration were investigated using a one-way FSI coupling method and different materials and wind speeds were chosen to study the effect of blade pitch on aerodynamical and structural characteristics [20]. In a recent investigation, Ren et al. compared the deformation and vibration analysis of compressor blades based on fluid-structure coupling using three different materials and found that the maximum rotational velocity was not large enough to reach the first-order natural frequency [21]. For the reason of the investigation of different computational methods and tools, a comprehensive state-of-the-art review discussed the benefits and issues of using parallel computing tools such as MPI, OpenMp, and CUDA in CFD and identified the computational time-related issues of massive grid points for complex configurations in CFD codes. In case of MPI, its performance, ability of being used in both distributed and shared memory, ensuring the data locality and full user control, were some of its benefits, revealed by the review [22].

### 1.1.3 Fan performance

The performance of axial-flow fans has been the subject of several studies over the years. In 1987, Pericleous and Patel developed a mathematical model for the simulation of stirred biomedical reactors and found general agreement with experiments. However, they noted some deficiencies caused by turbulence in the model [23]. Pelletier et al. developed a general-purpose computational technique for turbulent free 3-D flows past propellers and found good agreement between predictions and experiments. They used the Galerkin finite element algorithm, which was found to be stable and robust [24]. In 1991 Pelletier et al. applied a numerical approach to 3-D axisymmetric flow near propellers using a mixed and penalty function finite element method. They found that the velocity and pressure fields are sensitive to the propeller's kinematic modeling and that their numerical results agreed well with experiments for uniform flow past the propeller [25]. In 1993 numerical study was conducted on a low hub-to-tip ratio axial-flow fan under distorted inlet flow conditions. They used the k- $\epsilon$  turbulence model and the SIMPLEN algorithm and found that the

flow across the fan intake has a significant impact on performance [26]. Later, Meyer investigated the effect of an axial fan on the plenum chamber aerodynamics in air-cooled heat exchangers. He found that the fan performance characteristics can vary based on the volume flow rate and blade root stagger angle and that the design guideline to coincide with maximum fan static efficiency does not ensure optimum performance [27]. Le Roux used CFD models to study an axial-flow fan and found that removing the pinch and applying a zero-shear wall resulted in better predictions, although there were over-predictions in the fan pressure rise at the design flow rate [28]. Another study was conducted in which a CFD simulation study was carried out on an axial-flow fan and presented a new design with different blade numbers, which showed better performance according to numerical results [29]. Wang et al. performed a CFD simulation and experimental validation study on a rotor-only ducted axial-flow fan with a small hub-to-tip ratio. They found that a rounded trailing edge is necessary and that the original blade with aerodynamically shaped blade sections represents the fan blade performance. They also recommended using the Spalart-Allmaras turbulence model for better accuracy and agreement with experimental measurements [30]. Soon after, Moosania et al. discussed how modifying the blade tip geometry and manipulating the trajectory of tip leakage vortex (TLV) can improve the performance of low-speed axial flow fans used in air conditioning and ventilation systems. The study found that modifying the blade tip chord shape can reduce reverse flow and TLV blockage, and increasing pressure rise can push TLVs back to the beginning of the shroud, reducing reverse flow. Cambering the blade at the tip section further reduces blockage and loss. The study concludes that these modifications can significantly improve the performance of low-speed axial flow fans [31].

#### *1.1.4 Design optimization*

Design optimization methods are used to systematically search for the best design solution given a set of constraints and objectives. These methods involve using mathematical algorithms and models to evaluate and improve the design, often requiring iterative computations. Design optimization can be used in various fields, such as engineering, architecture, and product design, to improve performance, efficiency, cost-effectiveness, and other desired characteristics of a design.

Conjugate Gradient (CG) method is still used as an alternative to solve a great variety of multivariable objective functions. Accuracy and convergence rate of this method are essential tools when treating multivariate unconstrained problems. In recent years, a number of new performant CG methods are developed by several authors [32-34]. Most of them are placed their effort on developing new CG coefficients and improving algorithms in order to ensure performances and

global convergence properties of various types of CG optimization problems. These problems are generally classified into three main groups: i) classical CG method, ii) scaled CG method, and iii) the hybrid and parameterized CG methods [35, 36]. The blade shape optimization using a quadratic rational Bezier curve (QRBC), employing a combination of genetic algorithms and response surface approximation of the artificial neural network, is represented. The optimization process aimed to reduce the secondary flow, in stator hub choking, and in the transonic region [37]. An optimization strategy based on the 3D inverse design, coupled with response surface methods and revolutionary algorithms was proposed, in which, the performance characteristics such as blade loading were used to directly control the aerodynamic flow field [38]. An optimization platform based on coupling of CFD solver with GA, ANN and inverse design methods is expressed. the most important features of this platform was first, 3D parametrization of the compressor blade and second, the stage-by-stage optimization strategy for a multistage compressor, which reduced the number of variables to ignore the computational cost [39]. Automated 3D multi-objective optimization method was proposed by combination of a self-adaptive multi-objective differential evolution algorithm (SMODE), 3D parametrization of the blade, Reynolds-averaged Navier-Stokes (RANS) solver and self-organizing map (SOM). The optimal pareto solution showed significant improvement [40]. Smooth design parameters were used to study the optimization of turbomachinery. A single objective genetic algorithm was developed to obtain the isentropic efficiency optimal value. The optimized blade shows different cross-section profiles in root, middle and the tip, which results in around one percent of increase in the efficiency of the rotor [41]. A multipoint design optimization approach, using the adjoint method is employed to increase the performance of the last stage of a compressor by modifying the aerodynamic shape and stagger angle [34]. Stator vane settings of a multi-stage compressor using a combination of artificial neural network and a genetic algorithm was investigated. Various strategies are introduced to reduce the search cost in GA. The optimization results showed that the design settings of the stator vane are good. Further, the efficiency was enhanced over 1% under part-speed conditions [42]. The blade-end treatment problem was applied as an optimization algorithm to reduce the end-wall losses and extend the stable margin. The study on the end-wall treatment was published after around 30 years. The development of end-band, end-dihedral and end-sweep designs were reviewed. The ANN surrogate model in conjunction with the GA to validate the flow mechanism. About 0.5% peak efficiency increase was gained [43]. The NSGA-II algorithm was employed to automatically define the design parameters with a user-defined pressure ratio or mass flow rate, by modifying the variable stator vane (VSV) settings. Mean-line method with a model calibration procedure was used to evaluate the performance of the compressor [44]. Optimization of Bryton cycle was studied

based on thermodynamic cycle parameters and component parameters. Stagnation isentropic efficiency (IEFF) optimization of axial flow compressor stage (AFCS) is initially studied. Five parameters were taken as design variables, such as exit and inlet angles of rotor, absolute exit angle of stator, and relative air densities at exit and inlet of stator. The results showed that the optimal stagnation isentropic efficiency increase is proportional to the increase of work coefficient and decrease of flow coefficient [45]. Artificial neural network was trained with a dataset of 2-D CFD results, which was able to predict the performance of new blades for a high-pressure turbine with good accuracy. The results showed that the optimized blade designs had significantly improved performance compared to the baseline designs [46]. The authors developed a machine learning model called Dual Convolutional Neural Network (Dual-CNN). The model was compared to two other machine learning models, Gaussian Process Regression (GPR) and Artificial Neural Network (ANN). It was found to be more accurate in predicting the efficiency and torque of the turbines. The Dual-CNN model was then used to perform a gradient-based multi-objective optimization of the turbines' efficiency and torque using the automatic differentiation method and obtained a Pareto solution. It was found that the Dual-CNN model was able to accurately predict the performance of the turbines without the need for costly computational fluid dynamics (CFD) calculations, and that the model was sensitive to the size of the training dataset [47].

## 1.2 Problem Definition

CFD analysis is computationally expensive, even for simplified models. To address this issue and reduce the wall-clock time for calculations, optimizing the setup by neglecting less critical aspects of the analysis can be effective. However, for iterative applications or design optimizations requiring higher precision, the use of super processors becomes crucial. These high-performance computing resources significantly enhance computational efficiency and accuracy, making them essential for complex and detailed CFD studies.

Conversely, understanding structural reactions to air pressure, the stall phenomenon, and fatigue failures are crucial aspects of aerodynamic studies. Fluid-structure interaction studies are particularly complex due to the coupling of structural equations with aerodynamic ones. Consequently, employing CFD calculations that focus on the aeroelastic behavior of turbomachinery in an integrated manner can enhance confidence in the design of turbomachinery.

In recent decades, compressors and turbines have been the most researched turbomachines while for the fans there is a lack of research in the literature. In terms of energy consumption, axial-flow mine ventilators have not always been the most efficient turbomachines. Considering

environmental concerns, rising energy costs, and the scarcity of energy sources in some mining areas, improving the efficiency of these ventilators is increasingly important. However, as shown in Figure 2 the initial cost of the fan can increase as its efficiency increases.

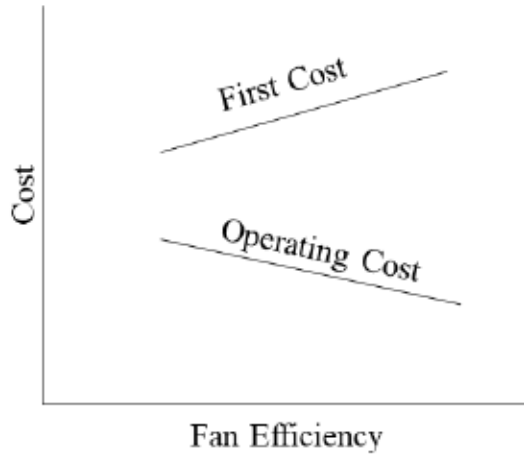


**Figure 2**  
**Cost versus fan efficiency.**  
Source: [48].

Developing a numerical approach to achieve an optimal design that balances stability, reliability, durability, and cost-efficiency is essential. Optimizing the overall performance of turbomachinery encompasses various design aspects, including aerodynamic, structural, aeroelastic, and operational conditions. To ensure a comprehensive optimization strategy, it is crucial to address and integrate as many of these categories as possible. This holistic approach facilitates the identification and refinement of multiple performance parameters, leading to more effective and efficient turbomachinery designs.

### 1.3 Objectives

The objectives of this thesis aim to develop, implement, and validate advanced optimization techniques for enhancing the performance and safety of turbomachinery components, particularly focusing on axial compressors and fans. The following specific objectives have been identified:

**Develop and validate optimization algorithms:** Create novel optimization algorithms based on unconstrained conjugate gradient methods and validate their performance against classical methods to demonstrate improved convergence rates and stability.

**Optimize aerodynamic shape of airfoils:** Implement and test new optimization algorithms to enhance the aerodynamic shape of NACA airfoils, aiming to maximize the lift-to-drag ratio while adhering to structural limitations.

**Improve compressor and fan performance:** Conduct a comprehensive study on the effects of blade deformation and tip-clearance on the performance and safety of axial compressors and mine ventilation fans, utilizing high-performance computing and fluid-structure interaction simulations.

**Experimental validation and structural optimization:** Validate numerical results through experimental data to ensure accuracy and reliability and evaluate the fatigue life and crack growth of axial fan blades under real-life loading conditions

#### 1.4 Originality statement

The originality of this thesis lies in the development and application of innovative optimization algorithms and methodologies to enhance the performance and safety of turbomachinery components. Key contributions include:

**Fluid-Structure interaction analysis:** Use of high-performance computing and fluid-structure coupling to analyze and optimize the operation safety and performance of axial compressors and fans, providing insights into the impact of blade deformation and tip-clearance.

**Experimental validation and practical applications:** Comprehensive experimental validation of numerical models and optimization results, demonstrating the practical applicability and robustness of the proposed methods.

**Novel optimization algorithms:** Introduction of new spectral conjugate gradient methods with improved convergence properties for solving unconstrained optimization problems.

**Aerodynamic shape optimization:** Application of advanced unconstrained conjugate gradient algorithms to optimize the aerodynamic shape of airfoils, achieving significant performance improvements.

**Fatigue life assessment and optimization:** Integration of static and dynamic stress analyses with fracture mechanics to assess the fatigue life of axial fan blades, contributing to the understanding of structural integrity under operational conditions.

## 2. CONCEPTUAL AND THEORETICAL FRAMEWORK

### 2.1 Governing equations

Aeroelastic problems combine aerodynamics and structural mechanics, governed by distinct principles and frames of reference: spatial (Eulerian) for fluids and material (Lagrangian) for structures. Interaction occurs through deformations, aerodynamic pressures, and viscous forces. This study focuses on key principles for transforming deformations and pressures between the two domains.

Fluid motion is described in Eulerian frame, focusing on a fixed control volume through which the fluid passes. Flow variables (e.g., density, velocity, pressure) depend on spatial coordinates and time, with unsteady flows requiring adaptations for moving boundaries. Fundamental principles like conservation of mass, momentum, and energy are applied to moving control volumes and expressed in integral form for discretization via finite volume schemes. Fluid behavior is modeled using constitutive relations, including the Newtonian fluid assumption, viscous stress-strain, Fourier's law of heat conduction, and the perfect gas law. It is important to note that the theoretical foundation for all fluid flow analyses in this thesis (Sections 3.6, 4.5 and 6.5) is based on the explanations provided in this section and the subsequent one.

#### 2.1.1 Reynolds' Transport Theorem

The Reynolds transport theorem facilitates the derivation of fluid mechanics' governing equations by relating the time-rate of change of a scalar quantity  $\chi$  within a time-dependent control volume  $V(t)$ . This control volume is bounded by a surface  $S(t)$  with an outward normal vector  $n$  and a local boundary velocity  $b$ . The theorem provides a mathematical framework for connecting changes within the volume to fluxes across its boundary.

$$\frac{d}{dt} \int_{V(t)} \chi dV = \int_{V(t)} \frac{\partial \chi}{\partial t} dV + \int_{S(t)} \chi(b \cdot n) ds \quad 2-1$$

Equation 2-1 describes the time-rate of change of a scalar quantity  $\chi$  within a varying volume  $V(t)$ , accounting for changes in the scalar's total amount due to both variations within the volume and the effect of the volume's changing size. In a Lagrangian frame, where the boundary velocity equals the fluid velocity  $u = (u_1, u_2, u_3)$ , this relationship simplifies further:

$$\frac{d}{dt} \int_{V(t)} \chi dV = \int_{V(t)} \frac{\partial \chi}{\partial t} dV + \int_{S(t)} \chi (\mathbf{u} \cdot \mathbf{n}) dS \quad 2-2$$

### 2.1.2 Conservation of Mass

In a Lagrangian frame, where the control volume  $V$  moves with the fluid and the surface  $S$  is tied to a fluid particle, the control volume's total mass remains constant, implying its time rate of change is zero. Therefore,

$$\frac{d}{dt} \int_V \rho dV = 0 \quad 2-3$$

Applying the Reynolds' transport theorem due to the equity of the velocity of the control volume  $\mathbf{u}$  and the fluid particle,

$$\int_V \frac{d\rho}{dt} dV + \int_S \rho (\mathbf{u} \cdot \mathbf{n}) dS = 0 \quad 2-4$$

In the Eulerian frame, the Reynolds transport theorem also applies to a control volume with a moving boundary at velocity  $\mathbf{b}$ . This can be expressed as:

$$\frac{d}{dt} \int_{V(t)} \rho dV = \int_{V(t)} \frac{d\rho}{dt} dV + \int_{S(t)} \rho (\mathbf{b} \cdot \mathbf{n}) dS \quad 2-5$$

In turbomachinery, the primary contribution to  $\mathbf{b}$  comes from the wheel's rotation. For a rigid grid attached to the casing or stator,  $\mathbf{b}=0$ . For a rigid grid on a rotor without elastic deformation,  $\mathbf{b}=\Omega \times \mathbf{r}$ , where  $\Omega$  is the angular velocity and  $\mathbf{r}$  is the displacement vector from the rotor axis. In aeroelastic calculations, velocities due to aeroelastic deformations are added to  $\mathbf{b}$  by equating the terms in the mass conservation equations, the resulting expression:

$$\frac{d}{dt} \int_{V(t)} \rho dV + \int_{S(t)} \rho (\mathbf{u} - \mathbf{b}) \cdot \mathbf{n} dS = 0 \quad 2-6$$

represents mass conservation for unsteady flow with moving boundaries.

### 2.1.3 Conservation of Momentum

Conservation of momentum, based on Newton's second law, states that the net force on a fluid element equals its mass times its acceleration. The forces acting on the fluid within a control

volume  $V(t)$  include surface stresses  $T$  on the boundary  $S(t)$  and body forces  $G$  throughout the volume. Using the Reynolds transport theorem, the momentum conservation equation is:

$$\frac{d}{dt} \int_{V(t)} \rho u dV + \int_{S(t)} \rho u(u - b) \cdot n dS = \int_{S(t)} T dS + \int_{V(t)} \rho G dV. \quad 2-7$$

Here,  $G$  represents body forces (e.g., gravity or electromagnetic effects) proportional to mass, and  $T$  relates to the stress tensor  $\sigma_{ij}$  as follows:

$$T = \sigma_{ij} e_i, \quad 2-8$$

where  $e_i$  is the unit vector in  $i$ -direction of the Cartesian coordinate. The surface stress tensor in a fluid is composed of the viscous stress tensor  $\tau_{ij}$  and the hydrostatic pressure  $p$ . For a Newtonian fluid, viscous stress only contributes to deformation, not to translation or rotation. Applying the Stokes hypothesis simplifies the constitutive relation, assuming that the hydrostatic pressure equals the mean of normal stresses ( $\sigma_{ij} = -3p$ ), bulk viscosity is negligible ( $\tau_{kk} = 0$ ), and the viscous stress tensor is symmetric ( $\tau_{ij} = \tau_{ji}$ ). The surface stress tensor for a Newtonian fluid is then expressed as:

$$\sigma_{ij} = -p\delta_{ij} + \tau_{ij} = -p\delta_{ij} + \mu \left[ \frac{\partial u_i}{\partial x_j} + \frac{\partial u_j}{\partial x_i} \right] - \frac{2}{3}\mu \left[ \frac{\partial u_k}{\partial x_k} \right] \delta_{ij} \quad 2-9$$

where  $\mu$  is the viscosity coefficient, and  $\delta_{ij}$  is the Kronecker delta.

#### 2.1.4 Conservation of Energy

The conservation of energy, based on the first law of thermodynamics, accounts for changes in internal energy  $e$  and kinetic energy  $\frac{1}{2}u^2$  of a fluid within a volume  $V(t)$ . Energy changes arise from two sources, work done on the fluid, which includes work by surface stresses  $T$  on the boundary  $S(t)$  and body forces  $G$  within the volume and heat flux which comprises conductive heat loss ( $-q$ ) through the surface and volumetric energy addition  $Q$  from sources like radiation or chemical reactions. Using the Reynolds transport theorem, the conservation of energy is expressed as:

$$\begin{aligned} \frac{d}{dt} \int_{V(t)} \rho(e + \frac{u^2}{2}) dV + \int_{S(t)} \rho(e + \frac{u^2}{2})(u - b) \cdot n dS &= \int_{S(t)} T \cdot (u - b) dS + \\ \int_{V(t)} \rho G \cdot u dV - \int_{S(t)} q \cdot n dS + \int_{V(t)} Q dV. \end{aligned} \quad 2-10$$

Heat conduction follows Fourier's law, where the heat flux  $q$  is proportional to the temperature gradient:

$$\mathbf{q} = -k\mathbf{\nabla}T, \quad 2-11$$

with  $k$  as the thermal conductivity and  $T$  as the fluid temperature.

To analyze compressible gas flow in equilibrium, it is essential to consider thermodynamic equilibrium conditions, which provide a constitutive relation for the fluid's physical properties. In this study, the fluid is defined as a thermally perfect gas, described by the equation:

$$p = \rho RT, \quad 2-12$$

where  $R$  is the specific gas constant. This is known as the thermal equation of state. Additionally, the gas is assumed to be calorically perfect, as represented by:

$$e = c_v T, \quad 2-13$$

where  $c_v$  is the specific heat at constant volume. This is referred to as the caloric equation of state.

### 2.1.5 The Reynolds-Averaged Navier Stokes Equations

The combination of the three conservation and the constitutive relations forms the Navier-Stokes equations, which are generally used to describe Newtonian turbulent viscous flows. However, solving these equations for high Reynolds-number flows requires very small temporal and spatial scales to capture turbulent fluctuations. For complex geometries, this would demand an immense number of mesh points, exceeding the capabilities of current computational technology. In engineering applications, the mean values of flow variables are usually of primary interest, especially for machinery performance predictions during design.

To address this, the Navier-Stokes equations can be reformulated for the mean values by averaging the flow variables over a sufficiently long period  $\tau$ , compared to the turbulent fluctuations' frequency. This results in the Reynolds-averaged Navier-Stokes equations.

Turbulent unsteady flow can often be simplified as consisting of two components: a slowly varying mean flow and a rapidly fluctuating turbulence component. The greater the difference in time scales, the more accurate this representation becomes. Each variable  $\chi$  in the Navier-Stokes equations can be expressed as the sum of the mean value  $\bar{\chi}$  over a time interval  $\tau$  and a time-dependent fluctuation  $\chi'$ :

$$\chi = \bar{\chi} + \chi' = \frac{1}{\tau} \int_t^{t+\tau} \chi dt + \chi'. \quad 2-14$$

This averaging process applies to density, pressure, the stress tensor, and heat flux:

$$\rho = \bar{\rho} + \rho', p = \bar{p} + p', \tau_{ij} = \bar{\tau}_{ij} + \tau_{ij}', q = \bar{q} + q'. \quad 2-15$$

Introducing the concept of Favre averaging [49], where a conservative variable  $\chi$  is averaged based on its mass-weighted value. This approach represents the variable as the sum of its Favre-averaged mean  $\tilde{\chi}$  and a time-dependent fluctuation  $\chi''$ ,

$$\chi = \tilde{\chi} + \chi'' = \frac{\int_t^{t+\tau} \rho \chi dt}{\tau \bar{\rho}} + \chi'' \quad 2-16$$

This averaging method simplifies the equations by applying it to velocity, specific energy, viscosity, and heat conductivity, assuming the time interval  $\tau$  is sufficiently large so that the mean values of fluctuations ( $\chi'$  and  $\chi''$ ) are zero. The flow variables are decomposed into their mean and fluctuating components as  $u = \tilde{u} + u''$ ,  $e = \tilde{e} + e''$  and  $E = e + \frac{u^2}{2} = \tilde{E} + E''$ .

For a flow domain  $\Omega$  without body forces ( $G=0$ ) or volumetric heat addition ( $Q=0$ ), substituting these decompositions into the Navier-Stokes equations and taking a time average yields the following simplified equations:

### **Mass conservation**

$$\frac{d}{dt} \int_{V(t)} \bar{\rho} dV + \int_{S(t)} \bar{\rho} (\tilde{u} - \dot{x}) \cdot \mathbf{n} dS = \mathbf{0}. \quad 2-17$$

### **Momentum conservation**

$$\frac{d}{dt} \int_{V(t)} \bar{\rho} \tilde{u} dV + \int_{S(t)} \{\bar{\rho} \tilde{u} \cdot (\tilde{u} - \dot{x}) + \bar{p} \delta_{ij}\} \mathbf{n} dS = \int_{S(t)} (\tau_{ij} - \bar{\rho} u_i'' u_j'') \mathbf{n} dS. \quad 2-18$$

### **Energy conservation**

$$\frac{d}{dt} \int_{V(t)} \bar{\rho} \bar{E} dV + \int_{S(t)} (\bar{\rho} \bar{E} + \bar{p})(\bar{u} - \bar{b}) \cdot \bar{n} dS = \int_{S(t)} \left\{ (\bar{\tau}_{ij} - \bar{\rho} u_i'' u_j'') (\bar{u} - \bar{b}) - \right. \\ \left. (\bar{q} - \bar{\rho} e'' u'') + (\bar{\tau}_{ij} - \frac{1}{2} \bar{\rho} u_i'' u_j'') u'' \right\} \cdot \bar{n} dS + .. \quad 2-19$$

Neglecting mean energy dissipation and turbulent fluctuations, the equations retain their laminar form but with additional terms for Reynolds stress ( $-\bar{\rho} u_i'' u_j''$ ) and Reynolds heat flux ( $-\bar{\rho} e'' u''$ ). These redefine viscous stresses ( $\tau_{ij, total} = \bar{\tau}_{ij} - \bar{\rho} u_i'' u_j''$ ) and heat fluxes ( $q_{j, total} = \bar{q}_j - \bar{\rho} e'' u_j''$ ).

As there are no constitutive relations to directly link Reynolds stress and heat flux to mean flow variables, turbulence closure models are necessary for further analysis.

### 2.1.6 Turbulence models

#### Standard k- $\epsilon$ turbulence model

The standard k- $\epsilon$  turbulence model is applied for the high Reynolds flow simulation in 3-D fluid domain. The standard k- $\epsilon$  model assumes the flow fully turbulent, and the effects of the molecular viscosity are negligible [50, 51]. The turbulence kinetic energy, k, and its rate of dissipation,  $\epsilon$ , are obtained from following transport equations:

$$\frac{\partial}{\partial t} (\rho k) + \frac{\partial}{\partial x_i} (\rho k u_i) = \frac{\partial}{\partial x_j} \left[ \left( \mu + \frac{\mu_t}{\sigma_k} \right) \frac{\partial k}{\partial x_j} \right] + G_k + G_b - \rho \epsilon - Y_M + S_k \quad 2-20$$

And

$$\frac{\partial}{\partial t} (\rho \epsilon) + \frac{\partial}{\partial x_i} (\rho \epsilon u_i) = \frac{\partial}{\partial x_j} \left[ \left( \mu + \frac{\mu_t}{\sigma_\epsilon} \right) \frac{\partial \epsilon}{\partial x_j} \right] + G_{1\epsilon} \frac{\epsilon}{k} (G_k + G_{3\epsilon} G_b) - G_{2\epsilon} \rho \frac{\epsilon^2}{k} + S_\epsilon \quad 2-21$$

$Y_M$  is the contribution of the fluctuating dilation in compressible turbulence to the overall dissipation rate.  $\sigma_k$  and  $\sigma_\epsilon$  are the turbulent Prandtl numbers for k and  $\epsilon$ , respectively.  $S_k$  and  $S_\epsilon$  are user defined source terms and  $C_{1\epsilon}$ ,  $C_{2\epsilon}$ , and  $C_{3\epsilon}$ , are constants.  $G_k$  and  $G_b$  represent the generation of turbulence kinetic energy due to the mean velocity gradients, and buoyancy, respectively, where  $G_k$  can be modeled using:

$$G_k = \mu_t \left( \frac{\partial U_i}{\partial x_j} + \frac{\partial U_j}{\partial x_i} \right) \frac{\partial U_i}{\partial x_j} - \frac{2}{3} \frac{\partial U_k}{\partial x_k} \left( 3\mu_t \frac{\partial U_k}{\partial x_k} + \rho k \right) \quad 2-22$$

The turbulent viscosity (eddy viscosity),  $\mu_t$ , is computed with the combination of k and  $\epsilon$ , as follows:

$$\mu_t = \rho C_\mu \frac{k^2}{\varepsilon} \quad 2-23$$

Where  $C_\mu$  is constant. The model constants  $C_{1\epsilon}$ ,  $C_{2\epsilon}$ ,  $C_\mu$ ,  $\sigma_k$  and  $\sigma_\epsilon$ , which are determined from experiments to work fairly for wide range of flows, are given as follows [16, 52]:

$$C_{1\epsilon}=1.44, C_{2\epsilon}=1.92, C_\mu=0.09, \sigma_k=1.0, \sigma_\epsilon=1.3.$$

### *Wilcox SST k- $\omega$ turbulence model*

The transport equations for the SST k- $\omega$  model can be written as follows:

$$\frac{\partial}{\partial t}(\rho k) + \frac{\partial}{\partial x_i}(\rho k u_i) = \frac{\partial}{\partial x_j}\left[(\Gamma_k) \frac{\partial k}{\partial x_j}\right] + G_k - Y_k + S_k \quad 2-24$$

$$\frac{\partial}{\partial t}(\rho \omega) + \frac{\partial}{\partial x_i}(\rho \omega u_i) = \frac{\partial}{\partial x_j}\left[(\Gamma_\omega) \frac{\partial \omega}{\partial x_j}\right] + G_\omega - Y_\omega + S_\omega + D_\omega \quad 2-25$$

Where,  $G_k$  is the production of turbulence kinetic energy.  $G_\omega$  represents the generation of  $\omega$ .  $\Gamma_k$  and  $\Gamma_\omega$  are the effective diffusivity of  $k$  and  $\omega$ .  $Y_k$  and  $Y_\omega$  are the dissipation of  $k$  and  $\omega$  due to turbulence [53].

#### 2.1.7 Efficiency and total pressure in compressors

With  $h = C_p T_s$  being the static enthalpy,  $C_p$  the specific heat at constant pressure and  $V$  the magnitude of absolute velocity.

$$P_0 = P_s \times \left(1 + \frac{\gamma - 1}{2} Ma^2\right)^{\frac{r}{r-1}} \quad 2-26$$

$$T_0 = T_s \left(1 + \frac{\gamma - 1}{2} Ma^2\right) \quad 2-27$$

with  $Ma = V/c$ ,  $c = \sqrt{\gamma RT_s}$  is the speed of sound,  $\gamma$  is the specific heat ratio and  $R$  is the specific gas constant. It follows that overall aerodynamic parameters can be defined as follows:

$$\eta = \frac{\left(\frac{P_{02}}{P_{01}}\right)^{\frac{r-1}{r}} - 1}{\frac{T_{02}}{T_{01}} - 1} \quad 2-28$$

$$\Pi = \frac{P_{02}}{P_{01}}, \quad 2-29$$

where subscripts 1 and 2 denote inlet and outlet of the rotor, respectively.  $\eta$  and  $\Pi$  represent the efficiency and total pressure ratio [54].

### 2.1.8 Conservation law form

The conservation form of the governing equations is particularly useful for numerical methods because it allows the principles of mass, momentum, and energy conservation to be expressed in a unified framework. By eliminating bars and tildes from the equations and applying appropriate nondimensionalization, the conservation laws for the averaged variables can be written in an integral form as a single generic equation:

$$\frac{d}{dt} \int_{\Omega} W dV + \int_{\partial\Omega} F \cdot dS = \frac{1}{Re} \int_{\partial\Omega} f \cdot dS, \quad 2-30$$

where  $S = (S_1, S_2, S_3)$  represents the components of the projected surface areas in the three Cartesian coordinate directions,  $W$  denotes the conserved quantity, and  $F = (F_1, F_2, F_3)$  represents the corresponding flux vectors.

$$W = \begin{pmatrix} \rho \\ \rho u_1 \\ \rho u_2 \\ \rho u_3 \\ \rho E \end{pmatrix}, F_i = \begin{pmatrix} \rho(u_i - b_i) \\ \rho u_1(u_i - b_i) + p\delta_{1i} \\ \rho u_2(u_i - b_i) + p\delta_{2i} \\ \rho u_3(u_i - b_i) + p\delta_{3i} \\ \rho H(u_i - b_i) \end{pmatrix}. \quad 2-31$$

And  $f = (f_1, f_2, f_3)$  is the vector of viscous source terms

$$f_i = \begin{pmatrix} 0 \\ \tau_{1i} \\ \tau_{2i} \\ \tau_{3i} \\ \tau_{ij}u_i + q_i \end{pmatrix}. \quad 2-32$$

The thermodynamic static pressure  $p$  is related to the total energy  $E$  by the equation:

$$p = (\gamma - 1)\rho \left( E - \frac{u^2}{2} \right), \quad 2-33$$

where  $\gamma$  represents the ratio of specific heats. Additionally, the total enthalpy  $H$  is given by:

$$H = E + \frac{p}{\rho} = \frac{c^2}{\gamma-1} + \frac{u^2}{2},$$

2-34

Total enthalpy plays a crucial role in fluid dynamics as it often remains constant for many significant fluid flows. Here,  $c_{cc}$  denotes the isentropic speed of sound, defined as:

$$c^2 = \frac{\gamma p}{\rho}.$$

2-35

## 2.2 Finite volume analysis

Analytical solutions to the Navier-Stokes equations are limited to simple flows under ideal conditions, making them impractical for real-world applications. To address complex flow scenarios, a numerical approach is employed, replacing the equations with algebraic approximations that can be solved computationally. In ANSYS CFX, this process involves discretizing the governing equations using an element-based finite volume method. The spatial domain is divided into a mesh, which forms the foundation for constructing finite volumes. These finite volumes ensure the conservation of key physical quantities, including mass, momentum, and energy, enabling accurate simulation of fluid dynamics across a wide range of engineering applications [50].

To illustrate the finite volume method, the conservation equations for mass, momentum, and a passive scalar are integrated over each control volume, and by applying Gauss' Divergence Theorem, volume integrals involving divergence and gradient operators are transformed into surface integrals. This process ensures that fluxes across the boundaries are conserved.

If the control volumes do not deform over time, the time derivatives can be taken outside the integrals, simplifying the expressions (Equations 2-6 and 2-7). However, for deforming meshes, additional terms are required to account for changes in the control volume geometry.

The next step in the numerical algorithm is to discretize the volume and surface integrals. In the discretization process, volume integrals are calculated within each element sector and then accumulated to the corresponding control volume. Surface integrals are evaluated at the integration points (ipn), which are located at the center of each surface segment within an element. These surface integrals are then distributed to the adjacent control volumes. Since the surface integrals at adjacent control volumes are equal in magnitude but opposite in direction at the integration points, the method ensures local conservation of flux.

After discretizing the volume and surface integrals, the integral equations are transformed into discrete forms as follows:

For mass conservation:

$$\mathbf{V} \left( \frac{\rho - \rho^o}{\Delta t} \right) + \sum_{ip} \dot{m}_{ip} = \mathbf{0} \quad 2-36$$

For momentum conservation:

$$\begin{aligned} & \mathbf{V} \left( \frac{\rho \mathbf{U}_i - \rho^o \mathbf{U}_i^o}{\Delta t} \right) \\ & + \sum_{ip} \dot{m}_{ip} (\mathbf{U}_i)_{ip} \\ & = \sum_{ip} (\mathbf{P} \Delta \mathbf{n}_i)_{ip} + \sum_{ip} \left( \mu_{eff} \left( \frac{\partial \mathbf{U}_i}{\partial \mathbf{x}_j} + \frac{\partial \mathbf{U}_j}{\partial \mathbf{x}_i} \right) \Delta \mathbf{n}_j \right)_{ip} + \overline{s_u} \mathbf{V} \end{aligned} \quad 2-37$$

For passive scalar transport:

$$\mathbf{V} \left( \frac{\rho \phi - \rho^o \phi^o}{\Delta t} \right) + \sum_{ip} \dot{m}_{ip} \phi_{ip} = \sum_{ip} \left( \Gamma_{eff} \frac{\partial \phi}{\partial \mathbf{x}_j} \Delta \mathbf{n}_j \right)_{ip} + \overline{s_\phi} \mathbf{V} \quad 2-38$$

Where  $m$  represents the integration point,  $\Delta t$  is the time step,  $\Delta \mathbf{n}_j$  is the outward surface vector,  $\dot{m}_{ip} = (\rho \mathbf{U}_j \Delta \mathbf{n}_j)_{ip}$  denotes the evaluation at the integration point, and the superscript  $o$  refers to the previous time step. These equations assume the use of the First-Order Backward Euler scheme for temporal discretization, though higher-order schemes, such as second-order schemes, are often used for improved transient accuracy.

### 2.3 Structural mechanics

To determine the distribution of static or dynamic displacements in a structure subjected to external forces and temperature loads, the fundamental equations of elasticity theory must be established and solved. For a general three-dimensional structure, these governing equations consist of fifteen equations for fifteen unknowns: three displacements, six strains, and six stresses. These governing equations include three motion equations, six strain-displacement relationships, and six stress-strain equations. This section provides a summary of the basic equations of elasticity and introduces the principle of virtual work, which forms the foundation of the finite element method, to facilitate numerical solutions to these equations.

In an elastic structure, the deformation under loads and temperature changes can be described using displacement vectors. The deformed shape is defined by displacement components as a function of position within the structure. Strain components (normal and shear) describe the deformation, and for small deformations, they are linear and related to displacement gradients.

Thermal stress is typically neglected in this study due to its minimal effect compared to pressure distributions. Stress is defined as force per unit area and includes normal and shear components. The relationship between stress and strain is governed by Young's modulus and Poisson's ratio, with linear stress-strain relations in isotropic materials.

Equations of motion for the stress components are derived by considering internal and external forces on a moving particle, including inertia and damping forces. These forces lead to partial differential equations governing the dynamic behavior of the structure under external forces.

### 2.3.1 Stress strain relations

In general, the stress tensor  $\underline{\underline{\sigma}}$  is proportional to the strain tensor  $\underline{\underline{\varepsilon}}$  and stiffness tensor  $\underline{\underline{C}}$

$$\underline{\underline{\sigma}} = \underline{\underline{C}} \cdot \underline{\underline{\varepsilon}} \quad 2-39$$

Given the isotropic properties of the material, we can conclude that the axial stress applied in any direction will produce the same axial strain as when applied in other directions. Likewise, for radial strains, the material will behave identically in all directions. The shear strains are related to the applied shear stresses through the shear modulus,  $G = \frac{E}{2(1+\nu)}$ . From the  $E$  and  $\nu$  ratios we can write:

$$\begin{aligned} \varepsilon_{11} &= \frac{\sigma_{11}}{E} - \frac{\nu}{E} \sigma_{22} - \frac{\nu}{E} \sigma_{33}, \\ \varepsilon_{22} &= -\frac{\nu}{E} \sigma_{11} + \frac{\sigma_{22}}{E} - \frac{\nu}{E} \sigma_{33}, \\ \varepsilon_{33} &= -\frac{\nu}{E} \sigma_{11} - \frac{\nu}{E} \sigma_{22} + \frac{\sigma_{33}}{E}. \end{aligned} \quad 2-40$$

and

$$2\varepsilon_{12} = \frac{1}{G}\sigma_{12},$$

$$2\varepsilon_{13} = \frac{1}{G}\sigma_{13},$$

2-41

$$2\varepsilon_{23} = \frac{1}{G}\sigma_{23}.$$

Since we have all six equations for the strain tensor related to stresses, we can write the strain tensor  $\underline{\underline{\varepsilon}}$  relation with stress tensor  $\underline{\underline{\sigma}}$  through the fourth-order compliance tensor  $\underline{\underline{\underline{D}}}$  as follows:

$$\underline{\underline{\varepsilon}} = \underline{\underline{\underline{D}}} \underline{\underline{\sigma}}$$

2-42

Which could be written in matrix form:

$$\begin{bmatrix} \varepsilon_{11} \\ \varepsilon_{22} \\ \varepsilon_{33} \\ \varepsilon_{12} \\ \varepsilon_{13} \\ \varepsilon_{23} \end{bmatrix} = \begin{bmatrix} \frac{1}{E} & -\frac{\nu}{E} & -\frac{\nu}{E} & 0 & 0 & 0 \\ -\frac{\nu}{E} & \frac{1}{E} & -\frac{\nu}{E} & 0 & 0 & 0 \\ -\frac{\nu}{E} & -\frac{\nu}{E} & \frac{1}{E} & 0 & 0 & 0 \\ 0 & 0 & 0 & \frac{2(1+\nu)}{E} & 0 & 0 \\ 0 & 0 & 0 & 0 & \frac{2(1+\nu)}{E} & 0 \\ 0 & 0 & 0 & 0 & 0 & \frac{2(1+\nu)}{E} \end{bmatrix} \begin{bmatrix} \sigma_{11} \\ \sigma_{22} \\ \sigma_{33} \\ \sigma_{12} \\ \sigma_{13} \\ \sigma_{23} \end{bmatrix} \quad 2-43$$

By inverting the compliance matrix  $\underline{\underline{\underline{D}}}$ , we can derive the stress tensor as  $\underline{\underline{\sigma}} = \underline{\underline{\underline{C}}} \underline{\underline{\varepsilon}}$ :

$$\begin{aligned}
 & \left[ \begin{array}{c} \sigma_{11} \\ \sigma_{22} \\ \sigma_{33} \\ \sigma_{12} \\ \sigma_{13} \\ \sigma_{23} \end{array} \right] \\
 & = \frac{E}{(1+\nu)(1-2\nu)} \underbrace{\left[ \begin{array}{cccccc} 1-\nu & \nu & \nu & 0 & 0 & 0 \\ \nu & 1-\nu & \nu & 0 & 0 & 0 \\ \nu & \nu & 1-\nu & 0 & 0 & 0 \\ 0 & 0 & 0 & \frac{1-2\nu}{2} & 0 & 0 \\ 0 & 0 & 0 & 0 & \frac{1-2\nu}{2} & 0 \\ 0 & 0 & 0 & 0 & 0 & \frac{1-2\nu}{2} \end{array} \right]}_{\text{Stiffness matrix}} \left[ \begin{array}{c} \epsilon_{11} \\ \epsilon_{22} \\ \epsilon_{33} \\ 2\epsilon_{12} \\ 2\epsilon_{13} \\ 2\epsilon_{23} \end{array} \right] \quad 2-44
 \end{aligned}$$

Thus, the stress-strain equations are:

$$\sigma_{ii} = \frac{E}{(1+\nu)(1-2\nu)} [(1-\nu)\epsilon_{ii} + \nu(\epsilon_{jj} + \nu\epsilon_{kk})], \quad \sigma_{ij} = \frac{E}{2(1+\nu)} \epsilon_{ij}, \quad 2-45$$

Under dynamic loading conditions, which are characterized by the system's natural frequencies, inertia forces  $-\rho\ddot{u}$  must be considered. Additionally, in real dynamic responses of structures, energy dissipation due to vibration is observed. This dissipation is typically modeled in vibration analysis by introducing velocity-dependent damping forces  $-\kappa\dot{u}$ , where  $\kappa$  is the viscous damping coefficient per unit volume. By resolving the inertia forces in the i-direction, three partial differential equations are derived:

$$\frac{\partial \sigma_{ij}}{\partial x_j} + \rho u_i^{\ddot{}} + \kappa u_i^{\dot{}} = G_i, \quad 2-46$$

where  $G_i$  represents the body force in the i-direction. Equation (2-46) must hold at every point within the structure. The stress components  $\sigma_{ij}$  vary across the structure, and at the boundary surface, they must balance the external forces applied to it.

### 2.3.2 The principle of virtual work

Due to the complexity of obtaining exact solutions to elasticity equations for intricate cases, approximate solutions are often achieved using energy methods. These methods are valid only under the assumption of small displacements and strains, ensuring linear behavior.

One of the most widely used energy methods assumes that forces remain constant as displacements vary from  $u$  to  $u + \delta u$ , where  $\delta u$  represents a virtual displacement. This leads to the *principle of virtual work*, which states that an elastic structure is in equilibrium under a given load distribution if the virtual work equals the virtual strain energy for any virtual displacement  $\delta u$  from a compatible deformation state  $u$ .

Inertia and damping forces, being proportional to the element's volume, also contribute to the virtual work performed by body forces. Consequently, the principle is expressed as:

$$\int_V \left( \frac{\partial \sigma_{ij}}{\partial x_j} + \rho \ddot{u}_i + \kappa \dot{u}_i \right) \delta u dV = \int_s p \delta u dS, \quad 2-47$$

where the right-hand side represents the external work done by aerodynamic pressure on the structure's boundary surface. Defining the strain and stress vectors as:

$$\varepsilon = (\varepsilon_{11}, \varepsilon_{22}, \varepsilon_{33}, \varepsilon_{12}, \varepsilon_{23}, \varepsilon_{31}), \quad \sigma = (\sigma_{11}, \sigma_{22}, \sigma_{33}, \sigma_{12}, \sigma_{23}, \sigma_{31}). \quad 2-48$$

the equation can be rewritten as:

$$\int_V \sigma \delta \varepsilon dV = \int_s p \delta u dS - \int_V \delta u [\rho \ddot{u}_i + \kappa \dot{u}_i] dV, \quad 2-49$$

here, the term on the left-hand side represents the *virtual strain energy* derived from the virtual displacement  $\delta u$ , while the terms on the right-hand side correspond to the *virtual work* done by external forces.

## 2.4 Finite element analysis

In structural finite element analysis, a body is modeled as an assembly of discrete finite elements connected at nodes along the element boundaries. The displacement within each element, measured in a local coordinate system, is interpolated from the nodal displacements [55]. For a given element  $m$ , the displacement  $u^{(m)}(x, y, z)$  at any point  $(x, y, z)$  is expressed as:

$$u^{(m)}(x, y, z) = H^{(m)}(x, y, z)q \quad 2-50$$

where  $H^{(m)}$  is the displacement interpolation matrix, and  $q$  is the vector of nodal displacements. This vector includes six components—three translational displacements and three rotational displacements. The interpolation matrix  $H^{(m)}$  depends on the element's geometry, the number of nodes, and the type of element used.

The strain at a point is derived from the displacement relation:

$$\boldsymbol{\varepsilon}^{(m)}(\mathbf{x}, \mathbf{y}, \mathbf{z}) = \mathbf{B}^{(m)}(\mathbf{x}, \mathbf{y}, \mathbf{z})\mathbf{q} \quad 2-51$$

where  $\mathbf{B}^{(m)}$  is the strain-displacement matrix obtained by differentiating  $H^{(m)}$ .

Stress is then calculated using:

$$\boldsymbol{\sigma}^{(m)} = \mathbf{C}^{(m)}\boldsymbol{\varepsilon}^{(m)} \quad 2-52$$

where  $\mathbf{C}^{(m)}$  is the elasticity matrix representing the material properties of the element.

By applying the principle of virtual work to the entire finite element assembly, the equilibrium condition becomes:

$$\begin{aligned} \sum_m \int_{V^{(m)}} \delta \boldsymbol{\varepsilon}^{(m)T} \boldsymbol{\sigma}^{(m)} dV^{(m)} \\ = \sum_m \int_{V^{(m)}} \delta \mathbf{u}^{(m)T} (-\rho^{(m)} \ddot{\mathbf{u}}^{(m)} - \kappa^{(m)} \dot{\mathbf{u}}^{(m)}) dV^{(m)} + \delta \mathbf{q}^T \mathbf{f} \end{aligned} \quad 2-53$$

where,  $\mathbf{f}$  is the vector of external forces applied to the structure, and  $\rho^{(m)}$  and  $\kappa^{(m)}$  are the mass density and damping coefficient, respectively.

Substituting the displacement, strain, and stress relations yields the equation of motion:

$$[\mathbf{M}]\{\ddot{\mathbf{q}}\} + [\mathbf{C}]\{\dot{\mathbf{q}}\} + [\mathbf{K}]\{\mathbf{q}\} = \{\mathbf{f}\} \quad 2-54$$

where:

$$[\mathbf{M}] = \sum_m \int_{V^{(m)}} \rho^{(m)} H^{(m)T} H^{(m)} dV^{(m)} \quad 2-55$$

$$[C] = \sum_m \int_{V^{(m)}} \kappa^{(m)} H^{(m)T} H^{(m)} dV^{(m)} \quad 2-56$$

$$[K] = \sum_m \int_{V^{(m)}} B^{(m)T} C^{(m)} B^{(m)} dV^{(m)} \quad 2-57$$

where  $[M]$ ,  $[C]$ ,  $[K]$  are the mass, damping and stiffness matrices.

To solve for the structural response, the equations of motion are time-integrated, starting from initial conditions on displacements  $\{q\}$  and velocities  $\{\dot{q}\}$ . This process yields the displacement history and structural response over time. In this study, all the time related parameters are neglected, and the equation of motion can be written as follows:

$$[K]\{q\} = \{f\}. \quad 2-58$$

The deformation is assumed to be continuous, and materials are linear elastic, therefore the small deformation assumption can be satisfied [11]. It is important to note that the theoretical foundation for all structural analyses in this thesis (Sections 3.9.1, 4.7 and 7.7) is based on the explanations provided in this section.

## 2.5 Fluid-structure interaction

While fluid and solid do not mix, a fluid-structure interface exists, represented as a two-dimensional surface within three-dimensional space. Interaction between the two domains occurs at this interface, where the structural system determines the displacement field, and the fluid system defines the pressure field.

For the governing equations of both structural and fluid systems to align, it is essential that the pressure and displacement fields match at the interface. Principles such as the conservation of loads and energy, which govern load transfer from the fluid to the structure, and the conservation of geometry, which ensures deformation tracking from the solid to the fluid, are fundamental to maintaining this consistency [56]. The fluid-structure interaction analyses in Sections 3.9 and 4.7 are grounded in the theories and equations presented in this section and subsequent one.

### 2.5.1 Conservation of loads and energy

To solve the structural system at the interface influenced by the pressure field, a set of concentrated forces at the interface nodes is required. The distributed pressure must first be

converted into nodal forces. These nodal forces must accurately represent the same net forces as those exerted by the pressure loads. Then,

$$\sum_m f^{(m)} = \int_{\partial\Omega} p dS, \quad 2-59$$

where  $f^{(m)}$  is the nodal force at the node  $m$ .

An infinite number of nodal force sets can satisfy this equation, but identifying the correct one is crucial. To achieve this, the principle of energy conservation is applied. By utilizing the definition of virtual work, the pressure load term in equation (2-59) is replaced with an appropriate term based on finite element method formulation. The virtual work done by the nodal forces  $f^{(m)}$  acting on a virtual nodal displacement  $\delta q^{(m)}$  is equated to the work done by the original distributed surface pressure  $p$  through the corresponding distributed virtual displacement  $\delta u$ . This relationship can be expressed as:

$$\sum_m f^{(m)} \delta q^{(m)} = \int_{\partial\Omega} p \delta u dS. \quad 2-60$$

Equations (2-59) and (2-60) collectively represent the principles of load and energy conservation.

### 2.5.2 Geometric conservation law

In computational aeroelastic applications, the domain may be bounded by moving surfaces. As these boundaries are in motion, at least a portion of the computational mesh must adapt to follow the boundary's movement. This necessitates the calculation of geometric properties such as grid positions and velocities. These calculations must adhere to the geometric conservation law [57], which stipulates that the computation of geometric parameters must ensure that the resulting numerical scheme preserves a uniform flow state, regardless of the mesh's movement.

Considering equation (2-30) for an inviscid flow, where  $\Delta t$  and  $t^n = n\Delta t$  are considered to be the chosen time step and the  $n$ th time interval, respectively. Integrating the equation (2-30) between  $t^n$  and  $t^{n+1}$  leads to:

$$\int_{t^n}^{t^{n+1}} \frac{d}{dt} \int_{\Omega} W dV dt + \int_{t^n}^{t^{n+1}} \int_{\partial\Omega} WF \cdot dS dt = 0, \quad 2-61$$

$$\int_{\Omega} W^{n+1} dV(t^{n+1}) - \int_{\Omega} W^n dV(t^n) + \int_{t^n}^{t^{n+1}} \int_{\partial\Omega} WF \cdot dS dt = 0,$$

when  $W^*$  is assumed to represent a uniform state of the flow, the proposed scheme cannot be deemed acceptable unless it preserves this state. Substituting  $W^* = W^{n+1} = W^n$  and  $F^* = F(W^*)$  into equation (2-61), we obtain the following expression:

$$W^* \left[ \int_{\Omega} dV(t^{n+1}) - \int_{\Omega} dV(t^n) \right] + \int_{t^n}^{t^{n+1}} \int_{\partial\Omega} F^* \cdot dS dt = 0, \quad 2-62$$

In this case, the diffusive components of the flux  $F^*$  vanish due to the uniform flow. Furthermore, the convective terms related to the fluid velocities are eliminated during the spatial integration over the cell boundaries. As a result, the flux integral can be expressed as:

$$\int_{\partial\Omega} F^* \cdot dS = - \int_{\partial\Omega} W^* b \cdot dS. \quad 2-63$$

By substituting this expression into the equation, we obtain:

$$W^* \left[ \int_{\Omega} dV(t^{n+1}) - \int_{\Omega} dV(t^n) \right] = \int_{t^n}^{t^{n+1}} \int_{\partial\Omega} W^* b \cdot dS dt, \quad 2-64$$

This simplifies to:

$$\int_{\Omega} dV(t^{n+1}) - \int_{\Omega} dV(t^n) = \int_{t^n}^{t^{n+1}} \int_{\partial\Omega} b \cdot dS dt, \quad 2-65$$

In its general form, this equation becomes:

$$\frac{d}{dt} \int_V dV(t) = \int_S b \cdot dS(t), \quad 2-66$$

which is recognized as the integral form of the conservation of geometry equation [58]. This equation implies that the change in the volume of each control volume over a given period must match the volume swept by the cell boundary during that period. Consequently, updating the boundary coordinates and  $b$  should not rely solely on mesh distortion [11].

## 2.6 Load transfer system

In fluid–structure interaction analyses, transferring aerodynamic loads from the fluid solver to the structural solver is a critical step. This section describes the method used to map surface pressure loads obtained from the fluid domain onto the structural domain in a way that ensures conservation of both load and energy. In this work, aerodynamic loads acting on structural surfaces are divided into two main components, pressure forces and viscous shear forces. However, since the magnitude of viscous shear forces is typically negligible compared to pressure forces, only

pressure forces are transferred to the structural model. Body forces are also neglected in this context. To ensure physical consistency, the load transfer algorithm is designed to satisfy the conservation of both virtual work (energy) and total force.

In this study, a loosely coupled approach is employed using two separate solvers for the fluid and structural domains. The resulted loads from CFD analysis are exported in terms of distributed pressure after full convergence of the fluid solver to the structural domain [9, 11]. To interpolate displacements from structural nodes to the fluid mesh points, a set of shape functions  $N(X)$  is introduced:

$$\delta\mathbf{u}(X) = [N(X)]\delta\mathbf{q} \quad 2-67$$

Substituting equation 2-67 into equation 2-60 gives:

$$\mathbf{f} \cdot \delta\mathbf{q} = \int_{\partial\Omega} p \cdot [N(X)] \delta q dS \quad 2-68$$

Assuming that the pressure  $p$  is constant over each surface face surrounding a fluid mesh point  $X_i$ , and defining a projected surface area vector  $S_i$  at that point, the above integral can be discretized as:

$$\mathbf{f} \cdot \delta\mathbf{q} = \sum_i p_i S_i \cdot [N(X_i)] \delta\mathbf{q} \quad 2-69$$

This allows the fluid pressure at each mesh point to be factored out, and the nodal force contribution from each fluid mesh point becomes:

$$\mathbf{f}_i = p_i S_i [N(X_i)] \quad 2-70$$

The total nodal force vector for a structural element  $m$ , denoted  $\mathbf{f}^m$ , is then obtained by summing all  $\mathbf{f}_i$  associated with that element:

$$\mathbf{f}^{(m)} = \sum_{i \in m} p_i S_i [N(X_i)] \quad 2-71$$

Noting that the interpolation function  $N(X_i)$  integrates to unity over each element, we arrive at:

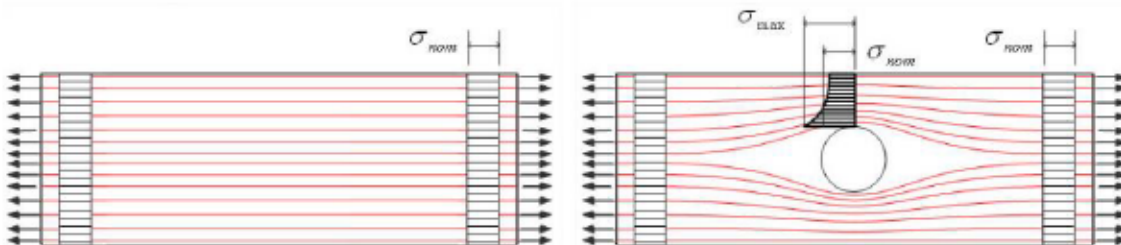
$$\sum_i p_i s_i = \int_{\partial\Omega} p dS \quad 2-72$$

Thus, both total applied load and virtual work (energy) are conserved by this algorithm, ensuring physical consistency between the fluid and structural solvers during FSI simulations [59].

## 2.7 Fatigue life calculation

The fatigue life of a structure consists of two distinct stages: crack initiation and crack propagation. Since these stages differ in nature, their quantitative representation must also be governed by different parameters.

When a plate under uniaxial tension has no local changes in its dimensions, the stress is uniformly distributed across the cross-section, known as nominal stress ( $\sigma_{nom}$ ). However, small changes like notches, holes, or fillets cause localized stress variations, leading to stress concentration. For example, a circular hole in the plate disturbs the uniform stress distribution, resulting in different stresses around the hole [60].

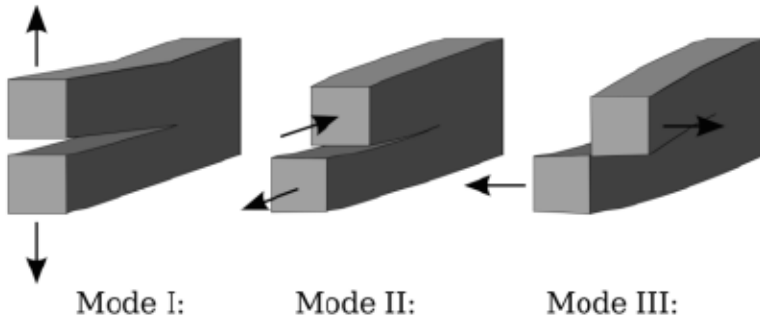


**Figure 3**  
**Stress distribution in a large plate subjected to uniaxial tension**  
Source: [60]

For a linearly elastic material, the maximum stress ( $\sigma_{max}$ ) in a specimen can reach up to three times the nominal stress. In general, the relationship between maximum stress and nominal stress is expressed as:

$$\sigma_{max} = K_t \cdot \sigma_{nom} \quad 2-73$$

where  $K_t$  is the stress concentration factor (SCF). According to Schijve [61], the SCF depends solely on the geometry of the structure. It reflects the intensity of the stress concentration and its potential impact.

**Figure 4****Crack modes: opening mode, in-plane shear and out-of-plane shear.**

Source: [62]

Stress concentration is a critical factor in predicting fatigue crack initiation. A structure with minimal stress concentration points is more resistant to fatigue. However, once a crack forms, the stress concentration factor  $K_t$  becomes irrelevant, as it tends to infinity at the crack tip.

To describe stress severity at the crack tip, the Stress Intensity Factor (SIF) is introduced. SIF reflects the applied stress magnitude near the crack and varies with geometry and loading conditions.

Crack growth occurs in different modes, with Mode I (Figure 4) being the most critical. In this mode, the crack opens perpendicular to the tensile stress direction. Other modes include Mode II with sliding crack propagation and Mode III with tearing crack propagation.

The stress intensity factor,  $K_I$ , can simply be expressed as:

$$K_I = \sigma_{\text{nom}} \sqrt{\pi a} f \quad 2-74$$

The crack length  $a$ , and function  $f$ , which depends on geometry and loading, determine the Stress Intensity Factor (SIF). The function  $f$  can be derived through finite element analysis or from existing handbooks.

It's important to distinguish between SIF and Stress Concentration Factor (SCF). SIF depends on loading type and geometry, with units of  $\text{MPa}\sqrt{m}$ . SCF is dimensionless and only reflects geometry. SIF is crucial for predicting the remaining fatigue life of cracked structures, allowing preventive measures before failure. Accurate predictions require reliable numerical models. In 1963, Paris and Erdogan established that crack growth rate per cycle can be expressed as a function of SIF [63].

This general law is known as the Paris law and can be expressed as:

$$\log \left( \frac{da}{dN} \right) = m \log(\Delta K) + \log(C) \quad 2-75$$

Taking out the logs yields:

$$\frac{da}{dN} = C(\Delta K)^m \quad 2-76$$

Where  $(\frac{da}{dN})$  is the fatigue crack growth rate,  $\Delta K = K_{max} - K_{min}$  represents the stress intensity factor range, C and M are material constants.

### 2.7.1 Fatigue loading

Structures exposed to fatigue loading undergo fluctuating stresses throughout their lifespan. Although the stress history typically varies, the simplest assumption is constant amplitude cyclic stress, as shown in Figure 5. This type of loading is common in laboratory tests since it doesn't require complex equipment. In constant amplitude loading, the structure experiences a maximum stress  $\sigma_{max}$  and a minimum stress  $\sigma_{min}$ . From this, the stress range and mean stress can be calculated as:

$$\Delta\sigma = \sigma_{max} - \sigma_{min} \quad 2-77$$

$$\sigma_{mean} = \frac{\sigma_{max} + \sigma_{min}}{2} \quad 2-78$$

Stress amplitude is ( $\sigma_a$ ) is defined as follows:

$$\sigma_a = \frac{\sigma_{max} - \sigma_{min}}{2} \quad 2-79$$

The ratio of the minimum stress to the maximum stress then defines the stress ratio as:

$$R = \frac{\sigma_{\min}}{\sigma_{\max}}$$

2-80

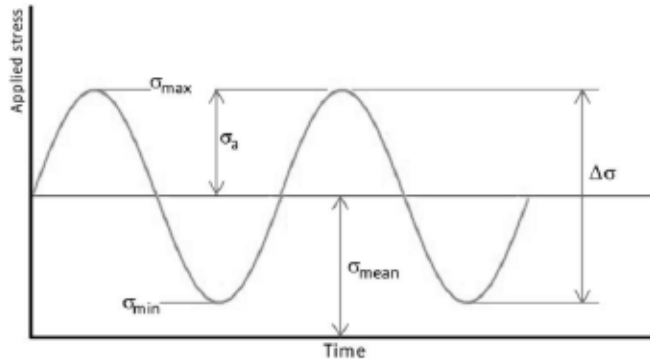


**Figure 5**  
**Constant amplitude loading**

Thus, when  $R=-1$ , the stress alternates between equal compressive and tensile values. In contrast, for  $0 \leq R \leq 1$ , the stress fluctuates between a minimum and maximum tensile load. The fatigue life of a specimen is primarily influenced by the stress range ( $\Delta\sigma$ ), where higher stress ranges lead to shorter fatigue life. However, constant amplitude loading is rarely representative of real-world conditions for structures like bridges, buildings, or turbomachinery. These structures endure random and irregular load sequences throughout their service life. This type of loading, known as variable amplitude loading, cannot be accurately described by a simple analytical model.

### 2.7.2 S-N curve

To visualize the fatigue strength of a component, an S-N diagram, also known as a Wöhler curve, is typically used. This diagram plots the logarithm of fatigue strength against the logarithm of the number of cycles at specific measurement points. Since fatigue test results often exhibit scatter, the median curve is derived, representing a 50% probability of failure. This indicates that half of the samples are expected to fail at the given stress range and corresponding number of cycles [64].

For fatigue analysis of welded structures, it is more practical to describe fatigue life using the stress range. This approach accounts for residual stresses near the yield limit, which can occur in both tension and compression. When compressive stresses are applied to a weld with residual tensile stress near the yield point, the weld may still experience a positive stress range, even under compressive loading. The stress range ( $\Delta\sigma$ ) is calculated using equation 2-77 and the load ratio  $R$  is determined by equation 2-80. Therefore, the number of cycles can be calculated as follows:

$$\log \left( \frac{N}{N_0} \right) = \log(C) - m \cdot \log(\sigma_r) \quad 2-81$$

Then one can rearrange the equation to obtain the fatigue life as:

$$N = N_0 \cdot \left( \frac{C}{\sigma_r} \right)^m \quad 2-82$$

Where  $N$  is the fatigue life,  $\sigma_r$  is the stress range,  $C$  and  $N_0$  are fatigue strength constants, and  $m$  represents a material constant. Fatigue life assessment in Section 7.7.2 is grounded in the theories and equations presented in this section and subsequent one.

### 2.7.3 Fatigue life treatment in Ansys

In ANSYS, high-cycle fatigue (HCF) is analyzed using the Stress-Life approach, which is particularly suited for cases involving a large number of load cycles, typically in the range of  $10^4$  to  $10^9$ . In HCF scenarios, the applied stresses are generally lower than the material's yield strength, meaning the material undergoes predominantly elastic deformation. ANSYS employs material-specific S-N (stress-life) curves to evaluate fatigue life, where the relationship between stress amplitude and the number of cycles to failure is defined. These curves are integrated into the software's fatigue analysis tool, allowing for accurate predictions of fatigue damage and life. By coupling these tools with detailed loading histories and advanced meshing capabilities, ANSYS provides a robust framework for evaluating the high-cycle fatigue performance of components under complex operational conditions.

As noted in previous sections, fatigue is due to repetitive loading. When the minimum and maximum stress levels are constant, this is referred to as constant amplitude loading, otherwise, the loading is known as variable amplitude or non-constant amplitude and requires special treatment.

In ANSYS, loading conditions for fatigue analysis can be categorized as proportional or non-proportional, each impacting the approach to evaluating material response. Proportional loading implies that the ratio of the principal stresses remains constant over time, and the principal stress axes do not shift. This allows for simpler calculations, as the stress response under load increases or reversals can be directly derived. On the other hand, non-proportional loading involves no fixed relationship between the stress components, leading to more complex stress states. Common scenarios of non-proportional loading include alternating between different load cases, superimposing alternating loads on static ones, or nonlinear boundary conditions.

In this study the simple case of constant amplitude, proportional loading with min and max stress values are considered. the stress variation between minimum and maximum values is crucial for fatigue analysis. The stress range ( $\Delta\sigma$ ) is the difference between the maximum and minimum stresses ( $\sigma_{max} - \sigma_{min}$ ), while the mean stress ( $\sigma_m$ ) is the average of these values ( $\sigma_{max} + \sigma_{min}/2$ ). The stress amplitude or alternating stress ( $\sigma_a$ ) is half the stress range ( $\Delta\sigma/2$ ), and the stress ratio (R) represents the relationship between minimum and maximum stress ( $\sigma_{max}/\sigma_{min}$ ). Special cases include fully reversed loading, where equal and opposite stresses are applied, resulting in  $\sigma_m = 0$  and  $R=-1$ , and zero-based loading, where stress is applied and then removed, yielding  $\sigma_m = \sigma_{max}/2$  and  $R=0$ . These parameters are fundamental in characterizing the loading conditions for fatigue analysis [65].

#### *Material properties and fatigue data*

For a fatigue analysis in ANSYS, material properties such as Young's Modulus and Poisson's Ratio are essential, as in linear static analysis. Additional properties like mass density are required for inertial loads, and thermal expansion coefficient and thermal conductivity are needed for thermal loads. If stress-based results are used, Stress Limits data is necessary, particularly for mean stress correction in fatigue analysis. The Fatigue Module requires S-N curve data to be included in the material properties under Engineering Data, specified as "Alternating Stress vs. Cycles" under "Life Data." For materials with S-N curves available for different mean stresses or stress ratios, multiple curves can also be input to enhance the analysis accuracy.

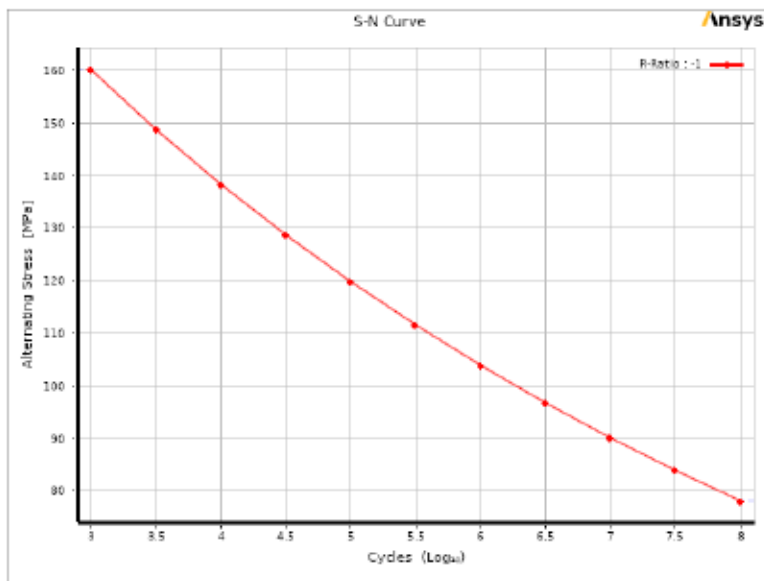


**Figure 6**  
**Semi-Log Stress-Life (S-N curve) for Al 356-T6 from Ansys material library**

The S-N curve, derived from fatigue testing under bending or axial loads, reflects a uniaxial state of stress but must be applied carefully for components experiencing multiaxial stress. Factors influencing the S-N curve include material properties (ductility, processing), geometry (surface finish, residual stresses, stress-raisers), and the loading environment (mean stress, temperature, chemical exposure). Mean stress significantly impacts fatigue life: compressive stresses lengthen life, while tensile stresses shorten it, causing the S-N curve to shift accordingly. Simulations accommodate these complexities by allowing multiple S-N curves for various mean stresses, applying mean stress correction theories when experimental data is limited, and incorporating correction factors for other influencing factors like surface finish or residual stresses.

Ansys material library contains sample fatigue data for Structural Steel and Aluminum which could be used as reference in the simulations. Figure 6 shows the Semi-Log S-N curve for Aluminum 356-T6 which is used in this study in Section 7.7.2.

#### *Mean stress effects*

In this case, multiple S-N curves are used to account for different mean stresses. For example, the material's S-N curve might change depending on whether the load is purely cyclic (zero mean stress), fully reversed (with a mean stress of zero), or has a positive or negative mean stress. This method uses experimental data to define different S-N curves for varying mean stress conditions, allowing for more accurate predictions of fatigue life for different loading conditions. The mean stress effects are neglected in this study because the required S-N curves are not available.

### *Fatigue loading type*

The type of loading can be selected as "Zero-Based," "Fully Reversed," or a specific "Ratio," with Ratio = 0 corresponding to Zero-Based loading and Ratio = -1 to Fully Reversed loading. Additionally, a scale factor can be applied to adjust all stress results. The selected loading type determines the minimum and maximum stress amplitudes. In this study, as it will be mentioned in Section 7.7.2, a fully reversed loading type is applied to estimate the fatigue life. The reference S-N curve of the Ansys material library is employed for the fatigue life estimation.

### *2.8 Description of fans*

A rotary machine which sucks the air continuously in at a certain pressure and delivers out at a higher pressure. The consumed energy is transformed to the potential energy (pressure) and kinetic energy (velocity) by the fan. The fan must be properly selected to produce the necessary pressure to overcome the resistance of the mine or the duct, in which the fan is operating [66].

Fans are named due to the type of impeller installed in the casing. In mining applications, the main fan types are as follows:

**Axial-flow** – the air flows through the impeller parallel to and in a constant distance from the axis of rotation. Direct action of the blades causes the increase of pressure.

**Centrifugal or Radial flow.** – in centrifugal fans, the air enters parallel to the axis of rotation and turns perpendicular and is discharged radially. The pressure increases due to centrifugal force.

**Mixed flow.** – in a mixed flow fan, the air enters parallel to the axis and turns through an angle in range of 30 to 60 degrees. The pressure rise is caused partially by direct blade action and partially by centrifugal action.

The main orientation of the present work is the focus on axial-flow fans, which are described in detail in the following sections.

#### *Axial Flow Fans*

Axial flow fans are the type of fans which use air as the working fluid and operates in the range of incompressible flow. the flow is assumed to be totally axial and parallel to the axis, without any radial components. The increase in the tangential velocity component causes the pressure rise.

In terms of pressure rise and capacity of the fan, axial flow fans are generally categorized into four types [67]. Propeller Fans, Tube Fans, Vane Fans, Two-Stage Fans.

### 2.8.1 Axial-flow fan performance

The performance curve of an axial flow fan, as depicted in Figure 7, has a unique shape when examining the relationship between static pressure and air volume. At the start of the curve, when there is no static pressure (also known as free delivery), the static pressure begins to increase and reaches a peak value. As the air volume decreases within the operating range, the axial velocity of the air, denoted as  $V_a$ , decreases, leading to an increase in the angle of attack and lift coefficient. This increase in the lift coefficient causes the static pressure to rise further, as air volume continues to decrease. When the lift coefficient reaches its maximum, the angle of attack becomes so large that the air flow is no longer able to follow the upper contour of the airfoil, leading to a phenomenon known as fan stall. The lift coefficient then starts to decrease and with it, the static pressure drops, following the dashed line towards zero.

However, this is not the end of the story for the fan. Something else occurs, causing the fan to pass the stalling dip and behave like an inefficient and noisy mixed-flow fan. This is typically due to turbulence and eddies in the flow as it approaches the inlet. The blades of the fan use centrifugal force to throw the air outward, leading to an increase in the static pressure within the stalling range until the fan reaches the zero-delivery point.

If the hub-tip ratio and blade angles are small, the stalling dip will be small, therefore, larger hub-tip ratios and larger blade angles, will result in a deeper stalling dip [48]. For a given diameter, long blades and small hub diameter, will give higher airflow and lower pressure than those of shorter blades and larger hub [66].

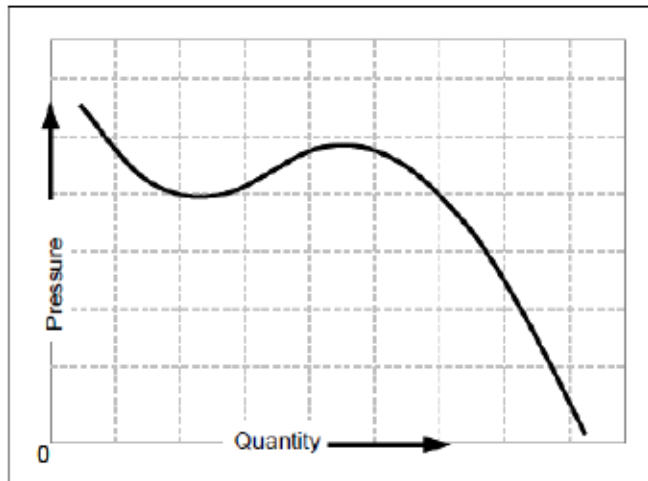


**Figure 7**  
**Fan performance curve**  
Source: [66]

To determine the fan performance, one must have the three main required data:

**Fan inlet airflow quantity**

**Fan pressure**

**Fan efficiency**

**Definition of fan parameters**

**Fan total pressure:** FTP is equal to the total pressure at the outlet ( $TP_o$ ) minus total pressure at the inlet ( $TP_i$ ).

$$FTP = TP_o - TP_i \quad 2-83$$

**Fan velocity pressure:** FVP equals to the velocity pressure at outlet ( $VP_o$ ).

$$FVP = VP_o \quad 2-84$$

**Fan Static Pressure:** FSP is equal to fan total pressure (FTP) minus the fan velocity pressure.

$$FSP = FTP - FVP \quad 2-85$$

For a pressure fan, a static pressure reading at downstream of the fan is equal to the Fan Static Pressure.

**Air Power:** AP (watts) is equal to the energy required to move a certain amount (Q) of air over a specific resistance.

$$AP = P \times Q$$

2-86

### 2.8.2 Fan Efficiency

The efficiency of the fan is critical because it addresses the cost of power required to operate the fan. Thus, a small difference in the performance of two similar fans, can lead for a significant power cost saving per year.

The fan efficiency ( $\eta$ ) can be calculated as follows:

$$\eta = \frac{Q \times P}{W} \quad 2-87$$

where the W, is the impeller power measured by a swinging frame dynamometer. For the reason of difficulty in measurement of this parameter, it is usually measured as motor input power (MIP). Therefore, by substituting the AP by  $Q \times P$ , the efficiency equation will be written as follows:

$$\eta = \frac{AP}{MIP} \quad 2-88$$

Fan efficiency can be expressed as fan total efficiency (FTE), if the total pressure (FTP) is used to calculate the air power, fan static efficiency (FSE), if static pressure (FSP) is used to obtain the airpower. The fan overall efficiency (FOE) can be expressed when any loss is included in electric driving motor, any speed change between motor and components or any other power losses.

### 2.8.3 Airflow measurement

Airflow in ducts can be measured using an anemometer or a pitot static tube, on a designed base point to point measurement. Airflow quantity can be determined by  $Q = v \cdot A$  in which  $v$  is the velocity of a point calculated by equation for velocity pressure,  $v = \sqrt{\frac{2VP}{\rho}}$ .

### 2.8.4 Fan laws

Fan performance curves are illustrated for specific operating range. Changes in particular parameters will follow the fan laws. The fan laws, referenced in Section 4.10 for optimization purposes, are thoroughly detailed in this section.

***Change in density ( $\rho$ )***

$$Q_1 = Q_2 \quad 2-89$$

$$\frac{P_1}{P_2} = \frac{\rho_1}{\rho_2} \quad 2-90$$

$$\frac{kW_1}{kW_2} = \frac{\rho_1}{\rho_2} \quad 2-91$$

$$\eta_1 = \eta_2 \quad 2-92$$

***Speed Change***

$$\frac{Q_1}{Q_2} = \frac{rpm_1}{rpm_2} \quad 2-93$$

$$\frac{P_1}{P_2} = \left( \frac{rpm_1}{rpm_2} \right)^2 \quad 2-94$$

$$\frac{kW_1}{kW_2} = \left( \frac{rpm_1}{rpm_2} \right)^3 \quad 2-95$$

$$\eta_1 = \eta_2 \quad 2-96$$

***Diameter change***

$$\frac{Q_1}{Q_2} = \left( \frac{D_1}{D_2} \right)^3 \quad 2-97$$

$$\frac{P_1}{P_2} = \left( \frac{D_1}{D_2} \right)^2 \quad 2-98$$

$$\frac{kW_1}{kW_2} = \left( \frac{D_1}{D_2} \right)^5 \quad 2-99$$

**2.9 Methodology and summary of contributions**

This thesis is organized into seven chapters, starting with introduction (Chapter 1), conceptual and theoretical framework (Chapter 2), each chapter is addressing a specific aspect of the optimization

and performance enhancement of turbomachinery components, particularly focusing on axial compressors and fans.

**Chapter 3: Optimizing the operation safety and performance of an axial compressor using Fluid-Structure Coupling and High-Performance Computing.** This chapter delves into the impact of blade radial and axial deformations on the safety and performance of axial compressors. It employs a fluid-structure interaction approach combined with high-performance computing to optimize mesh quality and computational efficiency. The chapter includes a detailed analysis of turbulence models, a multilevel factorial design of experiments, and a parametric study to identify optimal design points.

**Chapter 4: Optimization of an axial-Flow Mine ventilation fan based on effects of design parameters.** Focusing on mine ventilation fans, this chapter explores the optimization of various design parameters such as angle of attack, tip clearance, rotation speed, hub-to-tip ratio, and rotor blade count. It uses DOE and regression analysis to identify optimal configurations that enhance performance while maintaining structural integrity. The results are validated with experimental data, demonstrating the effectiveness of the optimization methods.

**Chapter 5: Optimization of unconstrained problems using a developed algorithm of spectral conjugate gradient method calculation.** This chapter introduces a novel algorithm for optimizing unconstrained problems based on the spectral conjugate gradient method. The algorithm's stability, convergence rates, and efficiency are evaluated through numerical experiments using various test functions. The findings highlight the algorithm's potential to outperform classical methods in certain cases.

**Chapter 6: Aerodynamic shape optimization of NACA airfoils based on a novel unconstrained conjugate gradient algorithm.** This chapter presents the aerodynamic shape optimization of NACA airfoils using an innovative unconstrained conjugate gradient algorithm. The Bézier parameterization method is employed to define design variables, and the XFOIL panel method-based flow solver is used for aerodynamic analysis. The optimization process achieves significant improvements in the lift-to-drag ratio, demonstrating the algorithm's robustness and efficiency.

**Chapter 7: Integrated aerodynamic and structural optimization of twisted Chinook-type blades for axial-flow fans.** In this chapter, the aerodynamic and structural optimization of axial-flow mine ventilation fans with Chinook-type blades is explored. A novel optimization

algorithm is employed to improve the fan's aerodynamic performance. Additionally, geometric modifications are made to the blades based on static and fatigue life assessments, aiming to enhance the overall structural strength and extend the blade's lifespan

### 3. OPTIMIZING THE OPERATION SAFETY AND PERFORMANCE OF AN AXIAL COMPRESSOR USING FLUID-STRUCTURE COUPLING AND HIGH PERFORMANCE COMPUTING

Cet article est rédigé par Seyyed Mojtaba Fakhari, Mariem Ben Hassen et Hatem Mrad a été publié dans la revue *Results in engineering* en 2023.

#### 3.1 Résumé

Dans cette étude, l'impact des déformations radiales et axiales des pales sur la sécurité opérationnelle et la performance d'un compresseur axial est analysé en utilisant une approche d'interaction fluide-structure partitionnée. Des clusters de calcul haute performance (HPC) et la méthode de parallélisation par Interface de Passage de Messages (MPI) sont utilisés pour optimiser l'équilibre entre la qualité du maillage et le temps de calcul. Le maillage haute résolution de l'espace de jeu est validé par une étude de convergence du maillage sur le domaine fluide. Trois modèles de turbulence ( $k-\varepsilon$ ,  $k-\omega$ , et  $k-\omega$  SST) sont comparés, et le modèle de turbulence  $k-\varepsilon$  est trouvé comme étant le meilleur en accord avec les données expérimentales. Un plan d'expériences factoriel à plusieurs niveaux est réalisé pour étudier l'influence de la variation de l'écart au bout des pales sur la sécurité et la performance du compresseur. Une étude paramétrique pour plusieurs valeurs d'écart au bout et matériaux est effectuée en utilisant ANSYS Workbench, et la déformation maximale au bout des pales est prédite à 0,7 mm. Le point de conception optimal est déterminé en fonction du poids et de l'importance des facteurs, ce qui entraîne une augmentation de plus de 33 % de la sécurité opérationnelle et une perte négligeable d'efficacité. L'étude souligne également les économies de temps de calcul obtenues, multipliées par 42, grâce à l'utilisation de super-processeurs avec un maillage de haute qualité dans les domaines solide et fluide par rapport à un ordinateur personnel. Les travaux futurs pourraient explorer l'impact d'autres facteurs tels que la géométrie des pales ou les conditions de fonctionnement sur la performance et la sécurité du compresseur de manière transitoire et fortement couplée.

**Mots-clés :** Rotor de compresseur NASA 67, Interaction fluide-structure, Cluster HPC, Parallélisation MPI, Plan d'expériences, Optimisation de réponse

## *Abstract*

In this study, the impact of blade radial and axial deformations on the operation safety and performance of an axial compressor is analyzed using a partitioned fluid-structure coupling approach. High performance computing (HPC) clusters and the Message Passage Interface (MPI) parallelization method are utilized to optimize the mesh quality and computation time balance. The chosen high-resolution tip-clearance mesh is validated through a mesh convergence study on the fluid domain. Three turbulence models ( $k-\epsilon$ ,  $k-\omega$ , and  $k-\omega$  SST) are compared and the  $k-\epsilon$  turbulence model is found to be the best option for agreement with experimental data. A multilevel factorial design of experiments (DOE) is conducted to investigate the influence of tip-clearance variation on the operation safety and performance of the compressor. A parametric study for several tip-clearance values and materials is performed using ANSYS Workbench, and the maximum deformation in the blade tip was predicted to be 0.7 mm, and the optimum design point is determined based on the weight and importance of the factors, which leads to an increase over 33% in the operation safety and a negligible loss in efficiency. The study also highlights the 42 times computational time savings obtained through the use of super-processors with high quality mesh in both solid and fluid domains in comparison with a personal computer. Future work could investigate the impact of other factors such as blade geometry, or operating conditions on the performance and safety of the compressor in a two-way strongly coupled transient manner.

**Keywords:** NASA Compressor rotor 67, Fluid-structure interaction, HPC cluster, MPI parallelization, DOE, Response optimization

### *3.2 Introduction*

The utilization of fluid-structure coupling (FSC) has become prevalent in various engineering applications, with the aim of improving material variety and design safety. The performance of aero-engine components, specifically compressor blades, has significantly improved over the years through advancements in blade geometry, material density, and strength. However, large deformations and blade vibrations can impact the efficiency and pressure ratio of the compressor. Vibration and deformation analysis of compressor blades are crucial for ensuring a safe and efficient design [10]. Solid particle erosion (SPE) also can be a major source of damage and failure cause in turbomachinery [68]. Despite the advancements in turbomachinery analysis, measuring deformations and vibrations can still be challenging. Numerical methods have therefore become a powerful tool for obtaining information about the flow field, erosion patterns, impacts, deformations, and blade vibrations. The investigation of Fluid-Structure Interaction (FSI) through

experimental and numerical research is necessary for a high-performance and stable mechanical system. Design optimization methods are used to systematically search for the best design solution given a set of constraints and objectives. These methods involve using mathematical algorithms and models to evaluate and improve the design, often requiring iterative computations. Design optimization can be used in various fields, such as engineering, architecture, and product design, to improve performance, efficiency, cost-effectiveness, and other desired characteristics of a design. Design of experiments and optimization of responses from each factor can aid in achieving this goal, with factorial designs being the most efficient for covering all possible points [10].

The studies in the literature review focus on the numerical analysis of fluid-structure interaction (FSI) in highly loaded engine designs. The objective of these studies is to obtain reliable solutions for the nonlinear effects on the fluid-solid interface and the individual behavior of each component. To accomplish this, both structural and fluid motion governing equations must be solved simultaneously in a time-integrated manner. However, due to the computational cost, some fluid-structure couplings are implemented using a one-way coupling algorithm, where the individual solvers partially or completely converge before exchanging response information [9].

In one study, the Euler equations were solved using the modal approach for structural analysis in a partially coupled manner [10]. Two years later Doi et al. used an explicit Runge-Kutta solver for the flow and a finite element method solver for the structure to investigate the aeroelastic responses of a compressor rotor blade [11]. A numerical method is used to investigate the combined effects of (s/c) blade pitch to blade chord ratio and (c/d) the blade chord to streamwise separation between two vortices, on the aerodynamic and structural responses of the central blade. Aerodynamic and structural dynamic responses of the central blade in the cascades are found to be the function of the blade pitch to chord ratio. The results show rather insensitivity of the fluid-structure interaction to the effect of vibrating neighboring blade [12]. Another study conducted a numerical parametric study for a transonic-axial compressor with treated and untreated end-walls at different tip gap heights and found that the end-wall treatments were more efficient at larger sizes of tip gap [13]. A study investigated flow-induced vibrations for wind turbine blade airfoils using a strong two-way FSI coupling in a 2-D domain with low Reynolds and incompressible flow. The results showed different results for aerodynamic load between laminar and turbulent flows, but similar responses for the airfoil [14]. Later on, Hongisk et al. developed a fully coupled FSI method for axial compressor flutter and found that the rotor flutters in stall operation with the first mode resonance [15]. In a further research work, a comparison of

turbulence models for a two-dimensional subsonic flow over an airfoil with various angles of attack showed that the turbulence models in commercial CFD codes were not accurate at high angles of attack [16]. A different study investigated a full annulus unsteady CFD for a fan-stage operating with a 120-degree stagnation pressure circumferential distortion [17]. In a later investigation on the compressor, the effect of inlet swirl and pressure distortion on the performance and stability of an axial compressor and found good agreement between the results and experimental data were numerically investigated, the validation of the numerical study was conducted employing the data published from NASA Lewis Research Center [18]. In the other hand, Wang et al. presented a one-way coupled FSI model for wind turbine composite blades at full scale, with aerodynamic forces obtained from CFD analysis and blade structural responses evaluated with FEA. Five operational conditions were selected and the maximum stresses and tip deflections in all cases were found to be within the material and structural limits, due to the design standards [19]. In a different study on wind turbines, high structure reaction to the effects of the wind in different blade pitches and turbine blade vibration were investigated using a one-way FSI coupling method. Different materials and wind speeds were chosen to study the effect of blade pitch on aerodynamical and structural characteristics. The SST  $k-\omega$  turbulence model was used for the CFD calculations. Deformations and von-Mises stress changes with respect to the velocity changes were observed for different classes of the materials [20]. In a recent investigation, Ren et al. compared the deformation and vibration analysis of compressor blades based on fluid-structure coupling using three different materials and found that the maximum rotational velocity was not large enough to reach the first-order natural frequency. The results showed that the main reason for the equivalent stress of the blade is rotation. The maximum stretched length of the blade at 100% speed could stand for 30% of the designed tip clearance [21]. In a recent study, the deformation of a T-shaped flexible beam using both experimental and numerical methods is investigated. The experimental setup involved placing the beam in a water channel with different Reynolds numbers, while a two-way fluid-structure interaction numerical method was used to simulate the deformation. The results showed that the deformation of the beam increased by 90% when the velocity was increased from 0.25 to 0.35 m/s, and decreased by 63% when the velocity was decreased from 0.25 to 0.15 m/s [52]. Optimization of Bryton cycle was studied based on thermodynamic cycle parameters and component parameters. Stagnation isentropic efficiency (IEFF) optimization of axial flow compressor stage (AFCS) is initially studied. Five parameters were taken as design variables, such as exit and inlet angles of rotor, absolute exit angle of stator, and relative air densities at exit and inlet of stator. The results showed that the optimal stagnation isentropic efficiency increase is proportional to the increase of work coefficient and decrease of

flow coefficient [45]. A comprehensive state-of-the-art review discussed the benefits and issues of using parallel computing tools such as MPI, OpenMp, and CUDA in CFD and identified the computational time-related issues of massive grid points for complex configurations in CFD codes. In case of MPI, its performance, ability of being used in both distributed and shared memory, ensuring the data locality and full user control, were some of its benefits, revealed by the review [22].

The most important novelty of this study is the use of a partitioned fluid-structure coupling approach to analyze the impact of blade radial and axial deformations on the safety and performance of an axial compressor. This method allows for a more accurate representation of the interaction between the fluid and solid domains, which is crucial for understanding the effects of blade deformation. Another novel aspect of this study is the use of a multilevel factorial design of experiments to investigate the simultaneous influence of the particular behavior of effective parameters on both operation safety and performance of the compressor, which is not considered in the literature. The parametric study performed using ANSYS Workbench also contributes to the novelty of this study, as it predicts a maximum deformation in the blade tip and determines the optimum design point based on the weight and importance of the factors, opening a new point of view. Finally, the study highlights the significant computational time savings obtained through the use of super-processors with high-quality mesh in both solid and fluid domains, implementing a manually developed python script, to enhance the system coupling process.

The research study aims to investigate the impact of blade radial and axial deformations on the safety and performance of axial compressors, which are commonly used in various industries. Blade deformation can lead to performance degradation and potentially catastrophic failures, making it crucial to understand the effects of such deformations.

To achieve this goal, the study employs a one-way fluid-structure coupling method to analyze the deformation behavior of compressor rotor blades under different operating conditions. The study examines the impacts of aerodynamic loads and rotation on the blades and uses three distinct materials, namely 17-4 PH Stainless Steel, Ti-6Al-4V, and Aluminum Alloy [69], to determine the optimal combination of performance and safety. By analyzing the effects of blade deformation, this study aims to contribute to the development of more reliable and efficient turbomachinery designs. Titanium is used in turbomachinery because of the high strength to weight ratio, corrosion, and creep resistance. The 17-4 PH stainless steel is defined because of its grate elastic behavior.

The computational fluid dynamics (CFD) approach is adopted to solve the three-dimensional Navier-Stokes equations in a steady-state, high-Reynolds flow regime. To model the turbulence in the flow, three different turbulence models are selected for a comparative analysis. These models include the standard two-equations  $k-\epsilon$  turbulence model, the  $k-\omega$  model, and the Shear Strain Transport model [16]. The surface pressure distribution is then extracted from the CFD solution and imported as a boundary condition into the structural domain, where it serves as input for the structural solver.

### 3.3 Experimental data

The Rotor 67, a transonic low aspect ratio design, is evaluated using laser anemometry to obtain detailed measurements within the blade row. The experiment is conducted at a design tip relative Mach number of 1.38, with the aim of determining the rotor's overall aerodynamic performance. Radial survey data are collected and analyzed to provide a comprehensive assessment of the rotor's behavior. The experimental results have been documented and published by Strazisar et al. from the NASA Lewis Research Center. [70]. Figure 8 and Table 1 show the aerodynamic survey locations and several design characteristics, respectively.

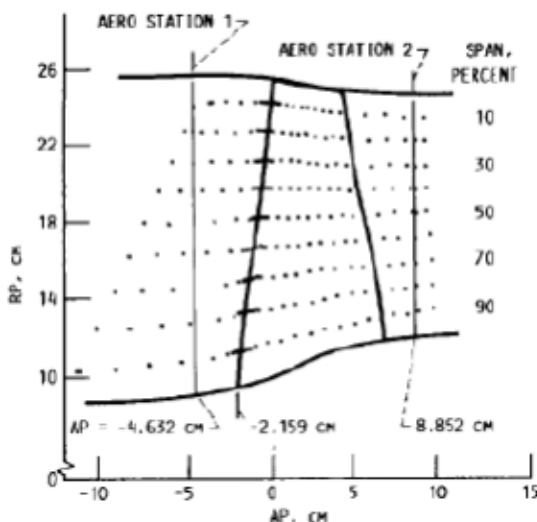


**Figure 8**  
**Meridional view of test fan rotor showing laser anemometer and aerodynamic survey locations**  
Source: [70]

### 3.4 Numerical method implementation and experimental validation

In this study, a computational fluid dynamics (CFD) simulation of NASA Compressor Rotor 67 is performed to understand the aerodynamic performance of the rotor under different operating

conditions. The simulation is conducted in the fluid domain by solving the three-dimensional Navier-Stokes equations. The mesh sensitivity study is first investigated before the aerodynamic loads were exerted on the solid surfaces as boundary conditions.

The numerical method used in the CFD simulation is validated by comparing the results with the experimental data obtained by [70]. The results show a good agreement between the numerical predictions and the experimental measurements. The solid geometry of the entire rotor is shown in Figure 9, while the fluid domain geometry is shown in Figure 10.

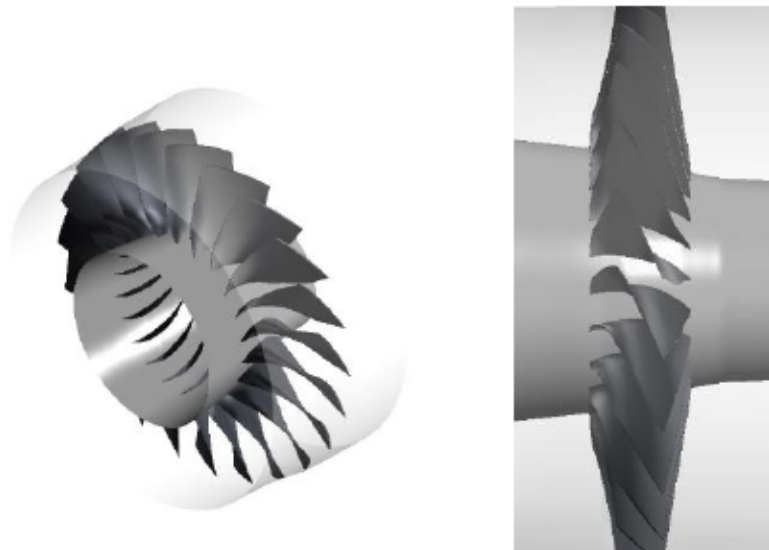


**Figure 9**  
**The geometry of a full-stage compressor rotor 67.**

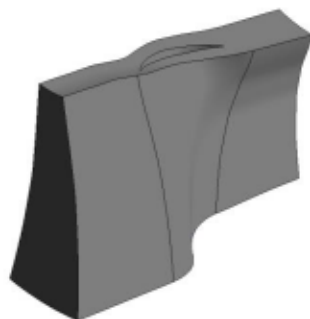


**Figure 10**  
**Fluid domain geometry.**

The fluid structure interaction analysis is then conducted using two different coupling approaches, using ANSYS System Coupling. The results of deformation and stress are discussed.

**Table 1**  
**Characteristics: NASA Compressor Rotor 67 Specifications**

Characteristics	Value
<b>Number of Blades</b>	22
<b>Rotational speed at design point (RPM)</b>	16043
<b>Tip speed (m/s)</b>	429
<b>Inlet tip relative Mach number</b>	1.38
<b>Design mass flow rate (kg/s)</b>	33.25
<b>Design pressure ratio</b>	1.63
<b>Design tip clearance (mm)</b>	1.01
<b>Average aspect ratio</b>	1.56

Source: [70].

### 3.5 Project Scheme

This paper presents a comprehensive study of the NASA Compressor Rotor 67, with the aim of determining its optimal operating conditions with respect to performance and safety factors. The study employs a combination of experimental and numerical techniques, as outlined below:

#### *Tool A: Experimental Data*

This tool involves the utilization of experimental data obtained by the NASA research center to validate the numerical approach, select the turbulence model, and determine the optimal operating conditions.

#### *Tool B: Numerical Studies*

The numerical studies of the rotor involve the use of Computational Fluid Dynamics (CFD) to analyze the fluid domain and determine the mesh independence, turbulence model preference, and aerodynamic loads. Tool B-1 focuses on the mesh convergence study, which is enhanced using high-performance computing (HPC) clusters and the MPI parallelization tool. Tool B-2 compares the results from different two-equation turbulence models to determine their precision.

#### *Tool C: Fluid-Structure Coupling*

The fluid-structure coupling approach is applied in Tool C, which employs two methods for transferring aerodynamic loads from the fluid domain to the solid domain. The first method is direct transfer, while the second method uses ANSYS System Coupling as a host.

#### *Tool D: Optimization Study*

The optimization study, presented as Tool D, involves a multilevel factorial design with two factors that are determined in a parametric study. The response optimization focuses on the safety factor and performance parameters.

The results of the study are presented in a clear and concise manner, with a schematic chart (Figure 11.) outlining the various tools used in the study.

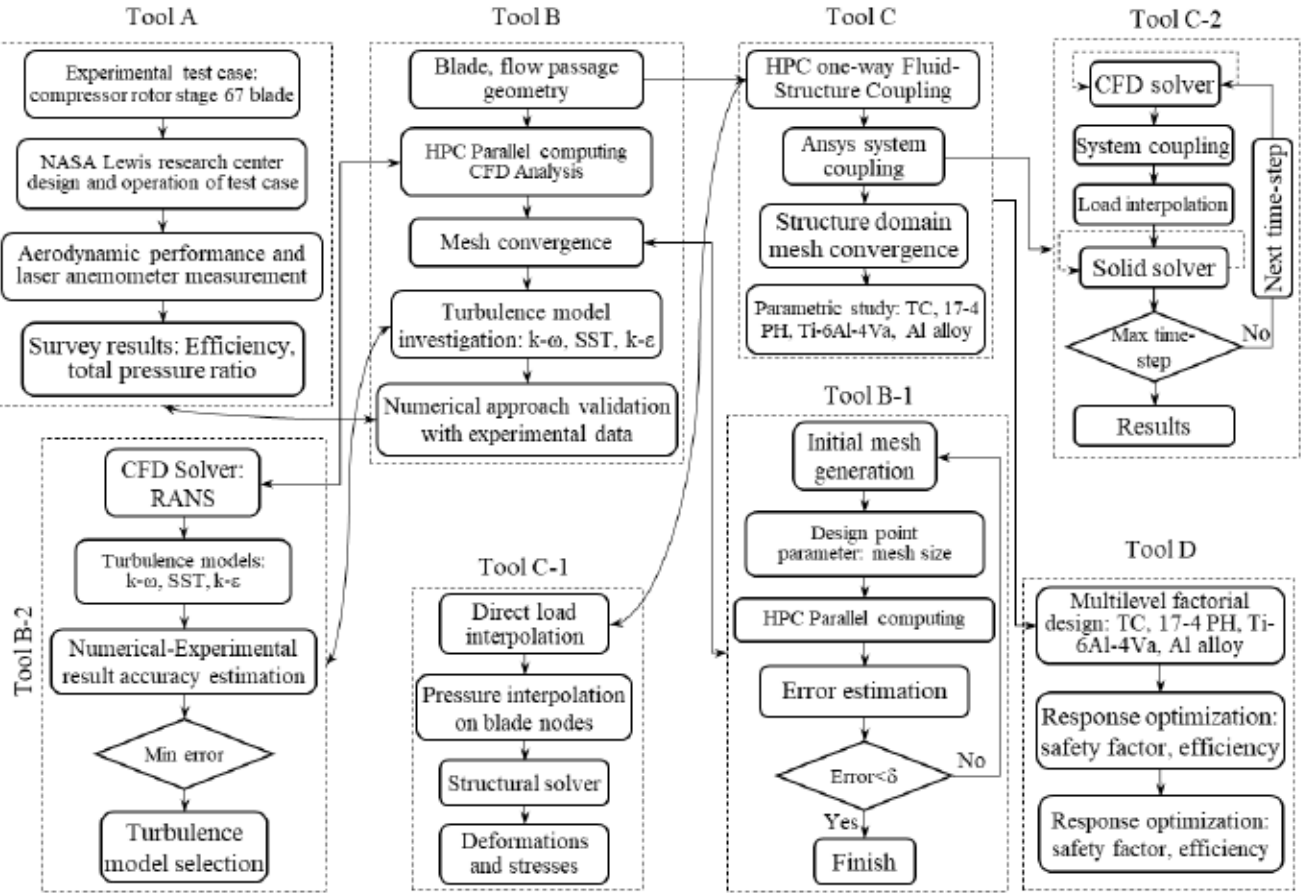


**Figure 11**  
**Project scheme.**

### 3.6 Computational fluid dynamics (CFD)

#### 3.6.1 Fluid domain governing equations

The instantaneous governing equations are solved in 3-D fluid domain [71]. The continuity equation is:

$$\frac{\partial \rho}{\partial t} + \frac{\partial}{\partial x_j} (\rho U_j) = 0. \quad 3-1$$

And the momentum equation is presented as follows:

$$\frac{\partial \rho U_i}{\partial t} + \frac{\partial}{\partial x_j} (\rho U_i U_j) = - \frac{\partial P'}{\partial x_i} + \frac{\partial}{\partial x_j} \left[ \mu_{eff} \left( \frac{\partial U_i}{\partial x_j} + \frac{\partial U_j}{\partial x_i} \right) \right] + S_M, \quad 3-2$$

where  $\mathbf{U}$  is the velocity field,  $\rho$  is the density of the fluid,  $\mathbf{S}_M$  is the sum of body forces,  $\mu_{\text{eff}}$  is the effective viscosity for the turbulence, and the  $p$  is the modified pressure. The effective viscosity can be written as

$$\mu_{\text{eff}} = \mu + \mu_t, \quad 3-3$$

$$\dot{p} = p + \frac{2}{3}\rho k + \frac{2}{3}\mu_{\text{eff}} \frac{\partial U_k}{\partial x_k}, \quad 3-4$$

A detailed explanation of the governing equations and underlying theory of fluid dynamics is provided in Section 2.1.

### 3.6.2 High performance computing (HPC) based on MPI parallelization

In this study, high performance computing technologies were employed to support the numerical simulation processes. The simulation configurations were set up on a personal computer and then submitted to a cluster scheduler via a secure shell (SSH) channel. To take advantage of parallel computation, the Intel MPI Library was utilized in the scripts. The CFD analyses were performed using 120 cores of 2 x Intel Platinum 8260 Cascade Lake CPUs, while 48 cores were utilized for the CFD-CSD coupling simulations. Using the workbench interface to control the system coupling, by default would dedicate no more than two cores for the system coupling application, therefore, a python script is prepared accompanied by the batch file to run in the UNIX operation system of the cluster to manually setup the CFD-CSD coupling to obtain better performance for the application by faster managing the data transferring between fluid and solid domains.

A comparison was made between the computational time required for a simulation on an Intel(R) Core (TM) i7-4770 CPU @ 3.40GHz with 32 GB of RAM, and that on the HPC nodes using 120 cores and 187.5 GB of RAM by applying the Distributed Parallel MPI. The results showed that the total CPU time required for the local PC was 548 minutes, whereas for the HPC nodes, it was only 13 minutes. This demonstrates that the use of HPC nodes with parallel MPI can significantly reduce the computational time compared to the use of a personal computer.

To perform a numerical study with various parameter changes, a parametric study was deemed necessary. This approach involved utilizing ANSYS Workbench Design Points, where key simulation properties were defined in tabular form and different design points were presented. The outputs were obtained after the full run was completed and combining high-performance processor units with a convenient design point increased precision while drastically reducing computational

cost and the risk of human error. Table 2 provides an illustration of the design points inputs and outputs for one case study.

**Table 2**

**Design Points: Table of design points for k- $\epsilon$  turbulence model at different operating conditions.**

Design Point Name	Mass flow ratio (%) [input]	Efficiency (%) [output]	Total pressure ratio [output]
DP0	92	81.3	1.61
DP1	93	87.9	1.63
DP2	94	90.95	1.69
DP3	95	91.12	1.68
DP4	96	91.28	1.67
DP5	97	91.04	1.64
DP6	98	89.59	1.59
DP7	99	82	1.48
DP8	100	74.7	1.301

### 3.7 CFD analysis implementation

The NASA compressor rotor 67, a low-aspect-ratio transonic axial-flow fan rotor, has been extensively studied under various operating conditions using laser anemometer surveys [70]. With the advancements in technology and the development of high-performance software with user-friendly interfaces, new algorithms and methods have been incorporated into simulation software, such as the ANSYS package [72, 73]. The numerical simulations aim to validate the pressure ratio and efficiency obtained from the experiments, by solving the steady-state compressible 3-D Navier-Stokes equations with ANSYS CFX. The convergence criteria for the residuals are set to  $10^{-6}$  to ensure an accurate solution. To ensure the mesh independency of the results, a mesh convergence study is performed, evaluating the solution's stability as the mesh size changes. Five Hexahedra meshes were used [52], [18], and the mesh numbers and their results are presented in Table 3. A detailed explanation of the CFD implementation in the Ansys CFX solver and the discretization theory are provided in Section 2.2.

### 3.7.1 Boundary conditions

The boundary conditions used in this study are based on the reported data of the NASA Research Center [70]. Total pressure is set at 1 atm, total temperature as 288 K, and uniform axial flow direction is specified for the inlet boundary. For the outlet boundary, the mass flow rate is defined as a parameter to vary in range of near stall to choke conditions. Symmetric boundary condition is also applied for the domain with respect to the axis of rotation in order to facilitate the analysis and save time and computational resources. The wall is defined as no-slip boundary condition to carry out zero fluid velocity in the wall neighborhood. Rotational velocity of 16043 rpm is applied for the rigid domain [70].

### 3.7.2 Mesh convergence study

The blade-shroud tip gap of the fluid domain experiences high flow velocity and turbulence, making the mesh independency study particularly important for the tip clearance. ANSYS turbo grid software is utilized for mesh generation. The mesh is sufficiently refined to meet the  $y^+$  requirement of the turbulence model. The study revealed that mesh number four provides a good compromise between accuracy and computational cost and was therefore chosen for the numerical calculations. The mesh independency study and the convergence results are presented in Figure 13. A total of 815700 elements are created for the domain. The numerical methods used in this study have been validated through a comparison of the results with experimental data and a mesh convergence study, providing confidence in the results obtained for various operating conditions.

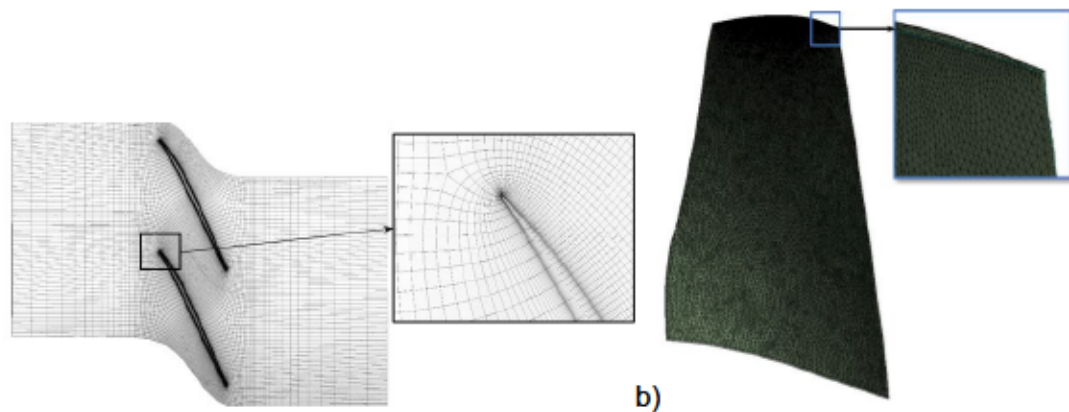


**Figure 12**  
Computational mesh for fluid domain at near tip (a), and solid domain (b)

**Table 3**

Mesh study: Element number of the fluid domain, for mesh study.

Mesh #	Total domain mesh	Tip clearance elements	Total Pressure Ratio	Efficiency	CPU clock time
1	498915	90510	1.631	90.44	00:08:26
2	544170	135765	1.648	90.84	00:09:29
3	725190	316785	1.649	90.93	00:011:56
4	815700	452550	1.648	90.84	00:12:53
5	906210	678825	1.648	90.83	00:13:50

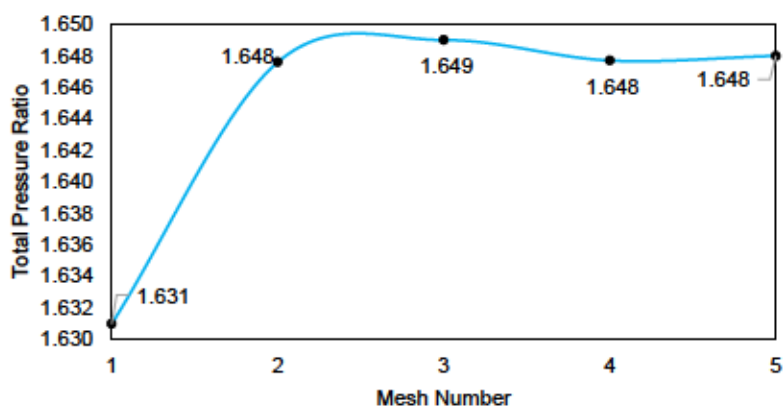


**Figure 13**  
Total pressure ratio vs mesh number

### 3.7.3 Turbulence models theory and application

This section investigates three turbulence models with the aim of improving the agreement between numerical results and experimental data. For each turbulence model, separate design point studies are conducted at different compressor mass flow ratios (as illustrated in Figure 14).

#### *Standard k- $\varepsilon$ turbulence model*

The standard k- $\varepsilon$  turbulence model is applied for the high Reynolds flow simulation in 3-D fluid domain. The standard k- $\varepsilon$  model assumes the flow fully turbulent, and the effects of the molecular viscosity are negligible [50, 51]. The turbulence kinetic energy, k, and its rate of dissipation,  $\varepsilon$ , are obtained from following transport equations:

$$\frac{\partial}{\partial t}(\rho k) + \frac{\partial}{\partial x_i}(\rho k u_i) = \frac{\partial}{\partial x_j} \left[ \left( \mu + \frac{\mu_t}{\sigma_k} \right) \frac{\partial k}{\partial x_j} \right] + G_k + G_b - \rho \varepsilon - Y_M + S_k, \quad 3-5$$

and

$$\frac{\partial}{\partial t}(\rho \varepsilon) + \frac{\partial}{\partial x_i}(\rho \varepsilon u_i) = \frac{\partial}{\partial x_j} \left[ \left( \mu + \frac{\mu_t}{\sigma_\varepsilon} \right) \frac{\partial \varepsilon}{\partial x_j} \right] + G_{1\varepsilon} \frac{\varepsilon}{k} (G_k + G_{3\varepsilon} G_b) - G_{2\varepsilon} \rho \frac{\varepsilon^2}{k} + S_\varepsilon \quad 3-6$$

$Y_M$  is the contribution of the fluctuating dilation in compressible turbulence to the overall dissipation rate.  $\sigma_k$  and  $\sigma_\varepsilon$  are the turbulent Prandtl numbers for k and  $\varepsilon$ , respectively.  $S_k$  and  $S_\varepsilon$  are user defined source terms.  $G_k$  and  $G_b$  represent the generation of turbulence kinetic energy due to the mean velocity gradients, and buoyancy, respectively, where  $G_k$  can be modeled using:

$$G_k = \mu_t \left( \frac{\partial U_i}{\partial x_j} + \frac{\partial U_j}{\partial x_i} \right) \frac{\partial U_i}{\partial x_j} - \frac{2}{3} \frac{\partial U_k}{\partial x_k} \left( 3\mu_t \frac{\partial U_k}{\partial x_k} + \rho k \right). \quad 3-7$$

The turbulent viscosity (eddy viscosity),  $\mu_t$ , is computed with the combination of k and  $\varepsilon$ , as follows:

$$\mu_t = \rho C_\mu \frac{k^2}{\varepsilon} \quad 3-8$$

where  $C_\mu$  is constant. The model constants  $C_{1\varepsilon}$ ,  $C_{2\varepsilon}$ ,  $C_\mu$ ,  $\sigma_k$  and  $\sigma_\varepsilon$ , which are determined from experiments to work fairly for wide range of flows, are given as follows:

$$C_{1\varepsilon}=1.44, C_{2\varepsilon}=1.92, C_\mu=0.09, \sigma_k=1.0, \sigma_\varepsilon=1.3$$

### Wilcox SST $k-\omega$ turbulence model

The transport equations for the SST  $k-\omega$  model can be written as follows:

$$\frac{\partial}{\partial t}(\rho k) + \frac{\partial}{\partial x_i}(\rho k u_i) = \frac{\partial}{\partial x_j}\left[\left(\Gamma_k\right)\frac{\partial k}{\partial x_j}\right] + G_k - Y_k + S_k, \quad 3-9$$

$$\frac{\partial}{\partial t}(\rho \omega) + \frac{\partial}{\partial x_i}(\rho \omega u_j) = \frac{\partial}{\partial x_j}\left[\left(\Gamma_\omega\right)\frac{\partial \omega}{\partial x_j}\right] + G_\omega - Y_\omega + S_\omega + D_\omega, \quad 3-10$$

where,  $G_k$  is the production of turbulence kinetic energy.  $G_\omega$  represents the generation of  $\omega$ .  $\Gamma_k$  and  $\Gamma_\omega$  are the effective diffusivity of  $k$  and  $\omega$ .  $Y_k$  and  $Y_m$  are the dissipation of  $k$  and  $\omega$  due to turbulence [53].

The  $k-\omega$  model is proposed to be more accurate near wall (boundary layer area) and  $k-\epsilon$  turbulent model can best describe the perturbations outside the boundary layer, however the SST  $k-\omega$  model has the blending function inheriting the aspects of the  $k-\epsilon$  and  $k-\omega$  turbulent models [74]. For each turbulence model, a separate design point study for different compressor mass ratios is conducted. Various operating points are chosen for comparison of the derived results with the experimental data. With  $h = C_p T_s$  being the static enthalpy,  $c_p$  the specific heat at constant pressure and  $V$  the magnitude of absolute velocity.

$$P_0 = P_s \times \left(1 + \frac{\gamma - 1}{2} Ma^2\right)^{\frac{1}{\gamma-1}} \quad 3-11$$

$$T_0 = T_s \left(1 + \frac{\gamma - 1}{2} Ma^2\right) \quad 3-12$$

with  $Ma = V/c$ ,  $c = \sqrt{\gamma RT_s}$  is the speed of sound,  $\gamma$  is the specific heat ratio and  $R$  is the specific gas constant. It follows that overall aerodynamic parameters can be defined as follows:

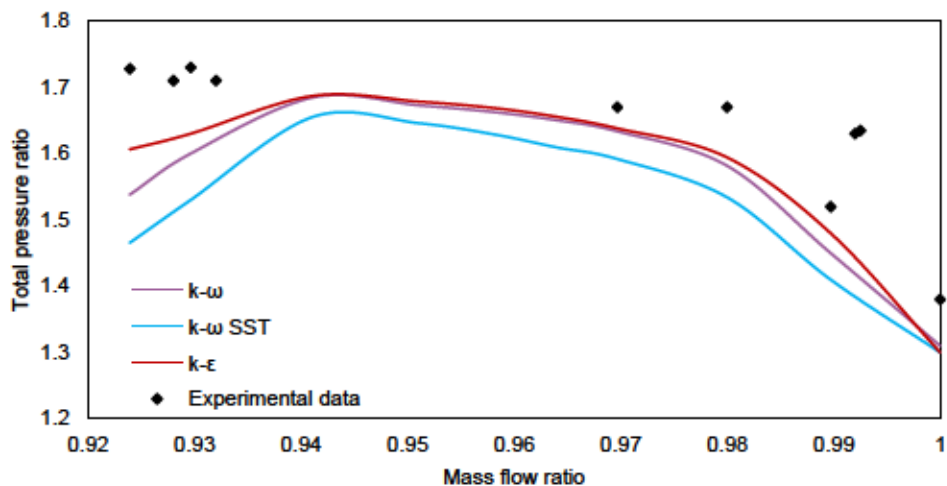
$$\eta = \frac{\left(\frac{P_{02}}{P_{01}}\right)^{\frac{1}{\gamma-1}} - 1}{\frac{T_{02}}{T_{01}} - 1} \quad 3-13$$

$$\Pi = \frac{P_{02}}{P_{01}}, \quad 3-14$$

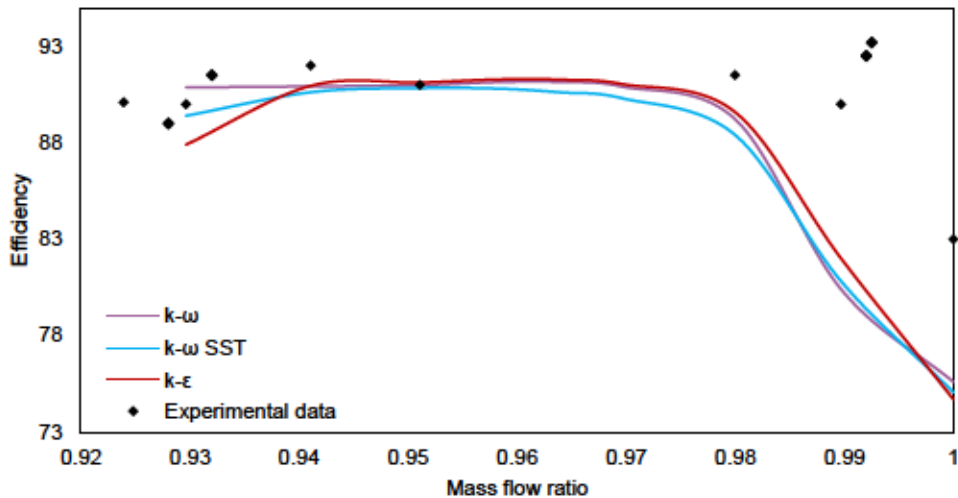
where subscripts 1 and 2 denote inlet and outlet of the rotor, respectively.  $\eta$  and  $\Pi$  represent the efficiency and total pressure ratio.[54]

### 3.8 Experimental validation

Various operating points are chosen for comparison with experimental data. Figure 14. and Figure 15 show the pressure ratio and efficiency changes respectively, as a result of the change in mass ratio. The  $k-\omega$  SST model shows the best agreement with experimental data at the design point, however, at near stall and choke, it exhibits a larger disagreement compared to the other models. The two-equation  $k-\epsilon$  model demonstrates a higher level of precision. The disagreement between numerical and experimental data is expected as the actual blade has a laminar region and turbulence models consider the flow field to be fully turbulent. Limited available operating conditions prevent the complete validation of CFD results. Factors contributing to this discrepancy include the rigid treatment of the solid domain in the CFD analysis, neglecting deformations, simplifications in the numerical implementation, and neglecting unsteady characteristics like vortex shedding and shock motion in the steady analysis.

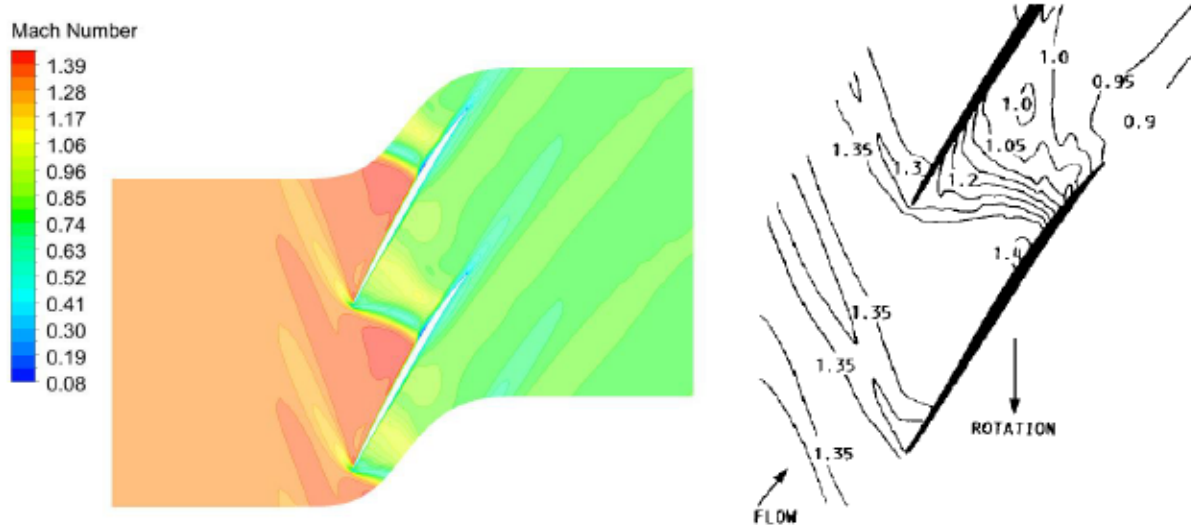


**Figure 14**  
**Total pressure ratio vs mass ratio for different turbulence models compared to experimental data**  
Source: [70].

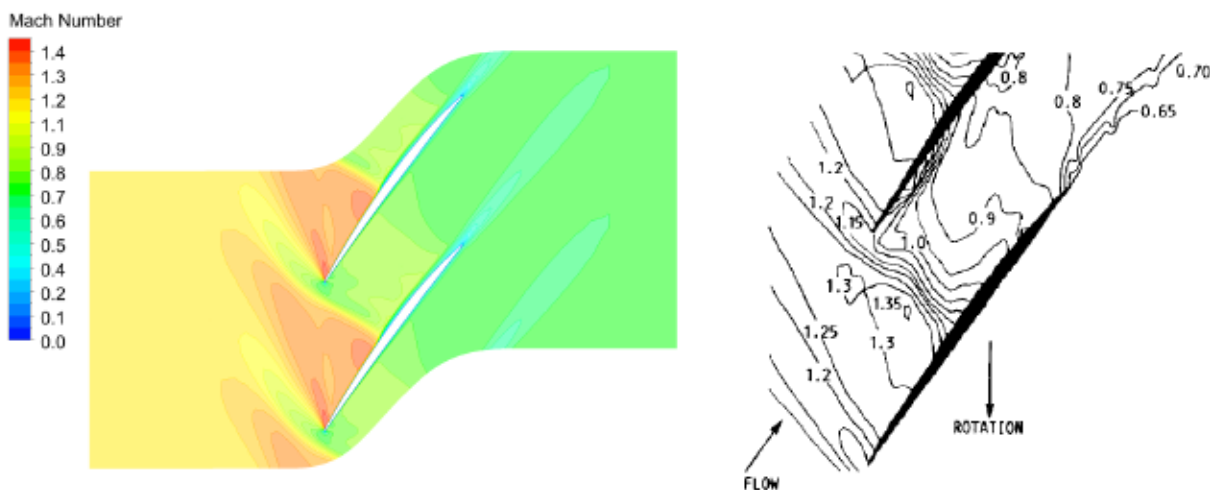
**Figure 15****Efficiency vs mass ratio for different turbulence models compared to experimental data**

Source: [70].

For further validation, the Mach number contour is compared to the experimental data. Figure 16. and Figure 17. show the Mach number distribution near peak efficiency and near stall, respectively. A shock wave is created at the leading edge, causing the passing flow along the suction side of the blade to accelerate and eventually surpass the speed of sound. The velocity decreases and static pressure increases after the formation of shock waves in the passage. On the pressure side of the blade, the static pressure increases and the flow velocity decreases. The design of a thin leading edge and a small radius of leading-edge curvature results in good aerodynamic performance near 0° angle of attack, reducing shock wave loss at high rotational velocities.

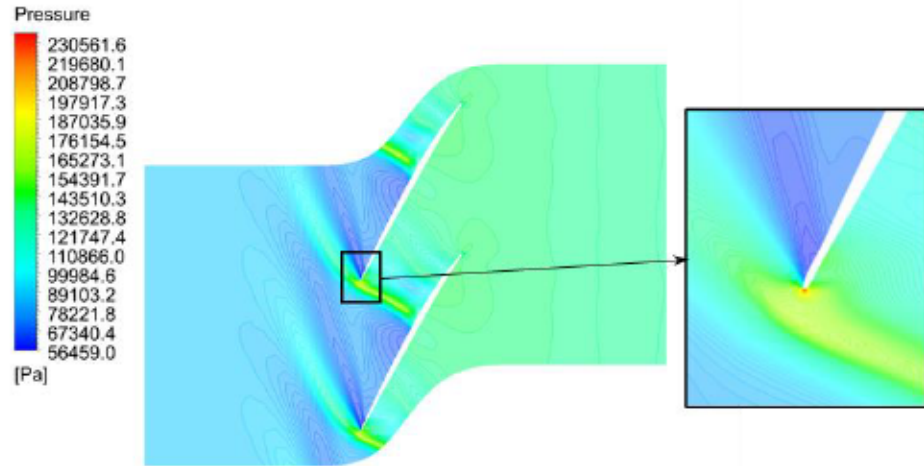


**Figure 16**  
Mach number at 90% span near peak efficiency, CFD results(left) and experimental data(right)  
Source: [70].

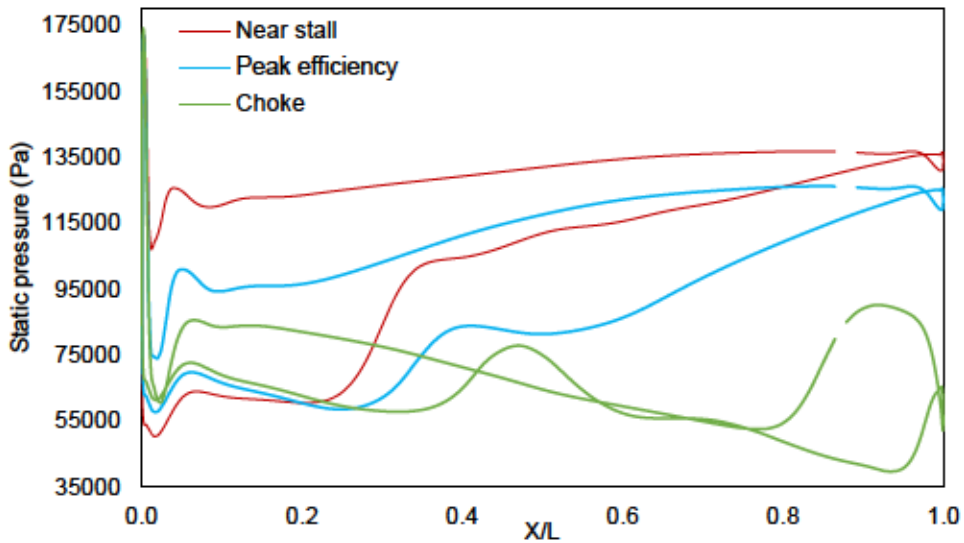


**Figure 17**  
Mach number at 70% span near stall, Numerical results (left) and Experimental Data(right)  
Source: [70].

Figure 18. shows the pressure distribution in the flow passage at 90% spanwise. The pressure at the leading edge is extremely high due to the shockwave, followed by an instant decrease in a short distance. On the suction side, the same behavior can be observed, except for the sharp increase in pressure caused by the shockwave after 50% of the chord. Figure 19 shows the blade loading at 50% span. Near stall, the difference between the rotor pressure surface and suction surface is evident, leading to an increase in blade loading and displacements.



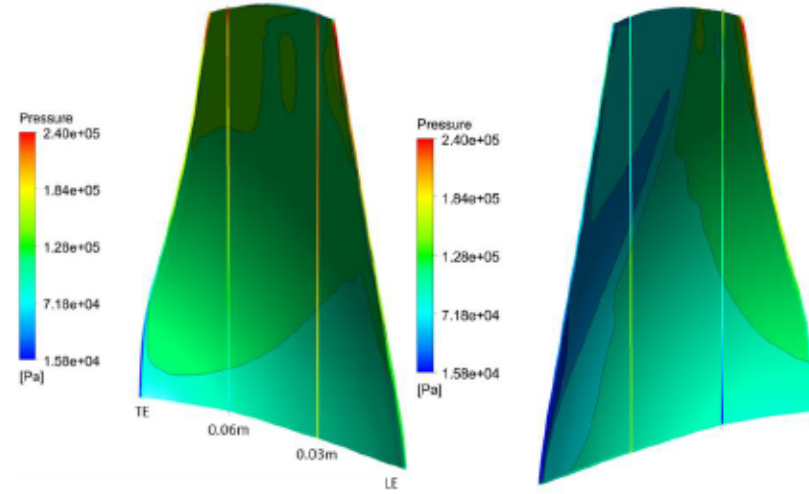
**Figure 18**  
Pressure distribution in flow passage in 90% of blade height near stall.



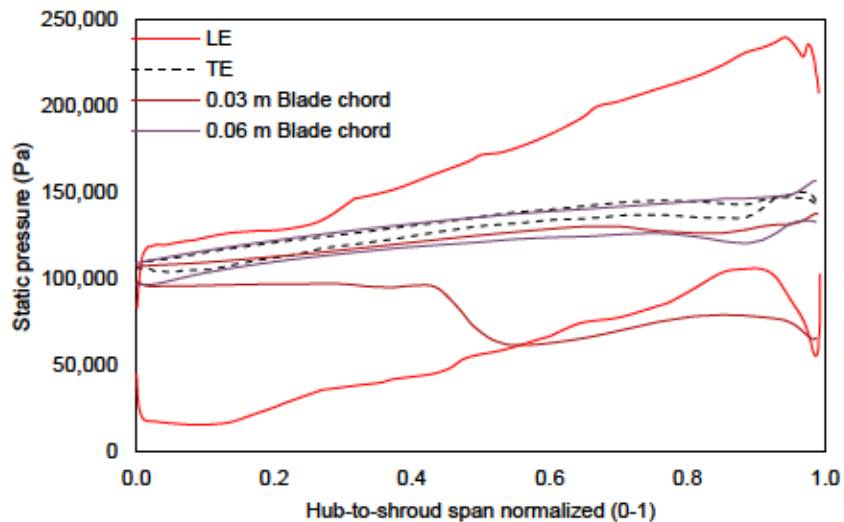
**Figure 19**  
Blade loading comparison at 50% of blade height streamwise direction (pressure and suction sides).

Figure 21. shows the pressure distribution at four different streamwise locations, starting from the leading edge, at 0.03 cm and 0.06 cm distances, and trailing edge near peak efficiency. Figure 20. shows the corresponding locations as contour lines starting from the hub surface and ending at the blade tip. The pressure magnitude increases along the leading edge from the blade root to the tip and reaches its maximum near the blade tip. On the pressure side of the blade, the overall trend of static pressure is similar, while on the suction side, there is a decrease in pressure

magnitude due to the shockwave on the second half of the blade. The trailing edge from the root to the tip experiences a slight increase in pressure. The pressure resulting from aerodynamic forces on the leading edge in the presence of centrifugal loads leads to deformation and changes in the angle of attack. The effects of the loads on the deformations on the blade are explained previous sections.



**Figure 20**  
Pressure distribution on the pressure side(left) and suction side(right) of the blade.



**Figure 21**  
Pressure distribution at different locations of blade pressure and suction sides.

### 3.9 Fluid-structure interaction Analysis

Steady-state fluid-structure interaction (FSI) is a complex phenomenon that describes the interaction between fluid and solid components. In a compressor blade, the fluid dynamics, as well as the structural response, are closely interconnected and are essential to analyze to achieve

optimal operating conditions. The purpose of FSI analysis is to simulate the behavior of the blade under various operating conditions, taking into account the aerodynamic loads and rotational speed, and considering the structural deformation [11]. The fluid dynamics of the system is analyzed by solving the Navier-Stokes equations, which describe the conservation of momentum in a fluid. The computational fluid dynamics (CFD) analysis is then used to solve the Navier-Stokes equations in a numerical manner, taking into account the boundary conditions that describe the flow properties at the inlet and outlet, as well as the boundary conditions describing the blade surface. In the FSI analysis, the fluid loads are exerted on the blade surface and are transferred to the structural domain. The structural response of the blade is modeled by using the finite element method. The fluid loads are incorporated into the structural analysis by updating the load vector  $F$  at each time step. The fluid-structure interaction analysis is then performed by iteratively solving the Navier-Stokes equations and the equation of motion, taking into account the feedback between the fluid and solid domains [50].

In conclusion, the FSI analysis of a compressor blade is essential to understand the behavior of the blade under various operating conditions and to achieve optimal performance and safety. The FSI analysis involves solving the Navier-Stokes equations for fluid dynamics and the equation of motion for the structural response, considering the interaction between the fluid and solid domains.

### 3.9.1 Structural deformation analysis

To achieve a technologically advanced modern jet engine, higher performance and safety are required. Lighter blades, higher pressure ratio and higher rotating speed are the main tools of reaching this goal in case of compressor. The deformation of a compressor blade is being investigated in this work. The motion equation describing a three-dimensional deformation of a flexible solid structure can be expressed as follows:

$$[M]\{\ddot{u}\} + [C]\{\dot{u}\} + [K]\{u\} = \{F\} \quad 3-15$$

Where  $[M]$  is the structural mass matrix,  $[C]$  is the damping matrix,  $\{u\}$  is the displacement vector,  $[K]$  is the stiffness matrix, and  $\{F\}$  is the load vector acting on the structure caused by fluid. In this study, all the time related parameters are neglected, and the equation of motion can be written as follows [75]:

$$[K]\{u\} = \{F\} \quad 3-16$$

The deformation is assumed to be continuous, and materials are linear elastic, therefore the small deformation assumption can be satisfied.

The one-way fluid structure coupling is conducted using two different coupling approaches, first, the direct approach, and second is by making use of ANSYS System Coupling. Generally, the number of computational mesh for fluid domain are more than those of structure domain, therefore a coupled matrix should be utilized to exchange the interface data. Assuming the number of nodes for the fluid and solid interface, are  $n_f$  and  $n_s$ , respectively, the pressure value on the fluid-solid interface can be written as follows:

$$\vec{P}_f = \begin{bmatrix} \vec{P}_{f1} \\ \vec{P}_{f2} \\ \vdots \\ \vec{P}_{fn} \end{bmatrix} \text{ and } \vec{P}_s = \begin{bmatrix} \vec{P}_{s1} \\ \vec{P}_{s2} \\ \vdots \\ \vec{P}_{sn} \end{bmatrix}, \quad 3-17$$

and the relation between the above vectors is:

$$\begin{bmatrix} \vec{P}_{s1} \\ \vec{P}_{s2} \\ \vdots \\ \vec{P}_{sn} \end{bmatrix} = \begin{bmatrix} H_{s1f1} & H_{s1f2} & \dots & H_{s1fn} \\ H_{s2f1} & \dots & \dots & \dots \\ \vdots & \dots & \dots & \dots \\ H_{snf1} & \dots & \dots & H_{snfn} \end{bmatrix} \begin{bmatrix} \vec{P}_{f1} \\ \vec{P}_{f2} \\ \vdots \\ \vec{P}_{fn} \end{bmatrix} \quad 3-18$$

$H_{sf}$  is the coupling matrix which transfers the pressure data from fluid  $P_f$  to the solid  $P_s$ . A detailed explanation of the structural deformation equations and underlying theory of finite element analysis are provided in Section 2.3 and Section 2.4.

### 3.9.2 Fluid-structure coupling method implementation

In this section a mesh convergence study is carried out for the sake of obtaining the precision and computational time balance. Soon after, the two methods -direct application of pressure and system coupling- for loosely coupled fluid-structure will be discussed. Tetrahedron mesh element type was used for the solid domain [52], [76]. A total of five structural mesh numbers and the 17-4 PH stainless steel as material for the solid region, are chosen to obtain the mesh-independent results. Table 4 presents the mesh refinement arrangement, the radial deformation of the blade tip, and the computational time on a 48 cores HPC cluster node. Figure 22. illustrates the convergence of the x-direction deformation of the blade tip, caused by the aerodynamic forces, centrifugal forces, and Coriolis effects. The mesh number four, corresponding to the node count

of 140919 is chosen with 78533 tetrahedron elements, as of the effective precision and computational time.

**Table 4**  
**Solid mesh study: mesh sensitivity study for solid.**

Mesh #	Mesh Number	Nodes	Radial Deformation(mm)	CPU time(m)
1	1680	3785	0.226	
2	5586	29673	0.2269	28.43
3	39348	71846	0.2269	29.66
4	78533	140919	0.2267	31.33
5	135293	239642	0.2267	34.4

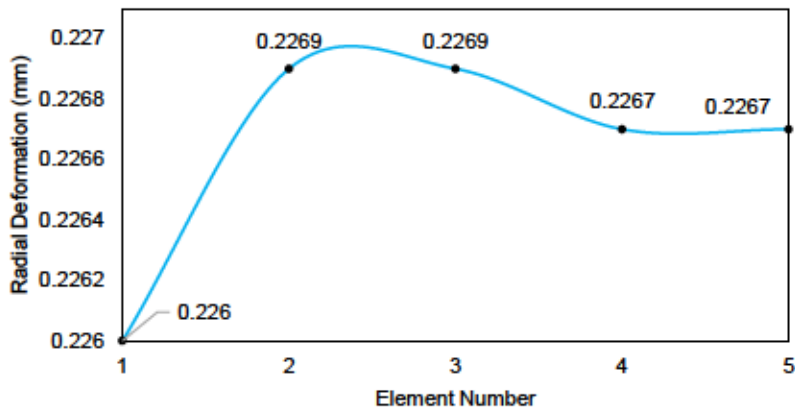


**Figure 22**  
**Mesh convergence study for solid domain.**

### 3.9.3 Direct pressure implementation

The fluid domain governing equations are solved first, and the static pressure distribution is exported and interpolated directly to the corresponding nodes on structural domain as boundary condition. Then the steady structural solution is performed for the rotating blade with previously exerted pressure on the blade's surface. Figure 23. shows the imported pressure on the blade and the source points, which obviously are denser in the blade tip. Figure 24. shows the maximum deformation value for the 17-4 PH stainless steel under design point operating condition, which is derived as 0.68 mm, and the equivalent von-Mises stress is derived as 42.02 MPa.

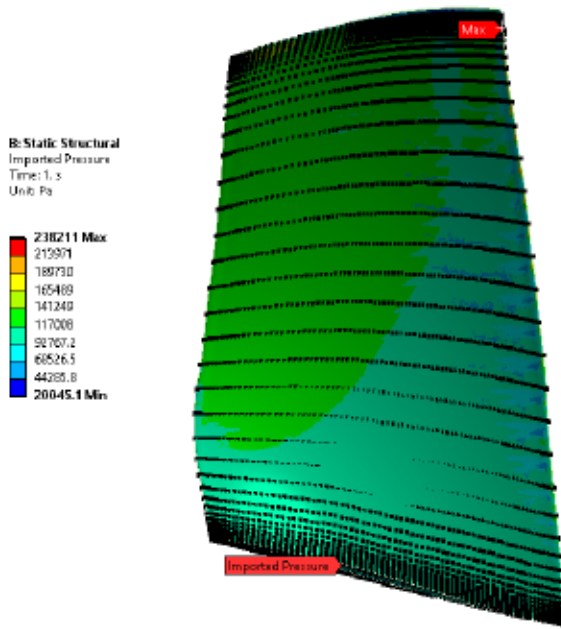


**Figure 23**  
**Imported Pressure from CFD solution.**

### 3.9.4 ANSYS system coupling

The interactions at the fluid-solid interface are studied using ANSYS System Coupling in a one-way approach. The CFD solver is executed until it reaches the pre-defined convergence criteria. Then, the system coupling takes over, interpolating the aerodynamic loads from the fluid flow solution to the structural meshes in a series of steps. This allows the structural solver to converge to the convergence criterion, after which the fluid solver is calculated for the next time step. The calculation is considered complete when the maximum number of time steps has been reached [77]. Figure 24. illustrates the total deformation magnitude for this method, which is 0.78 mm, and the equivalent von-Mises stress, determined to be 54.23 MPa. ANSYS System Coupling is preferred for the rest of the simulations in the study because it is more reliable and precise. A detailed explanation of the fluid-structure interaction equations and underlying theory of interface method are provided in Section 2.3, 2.5 and Section 2.62.4.

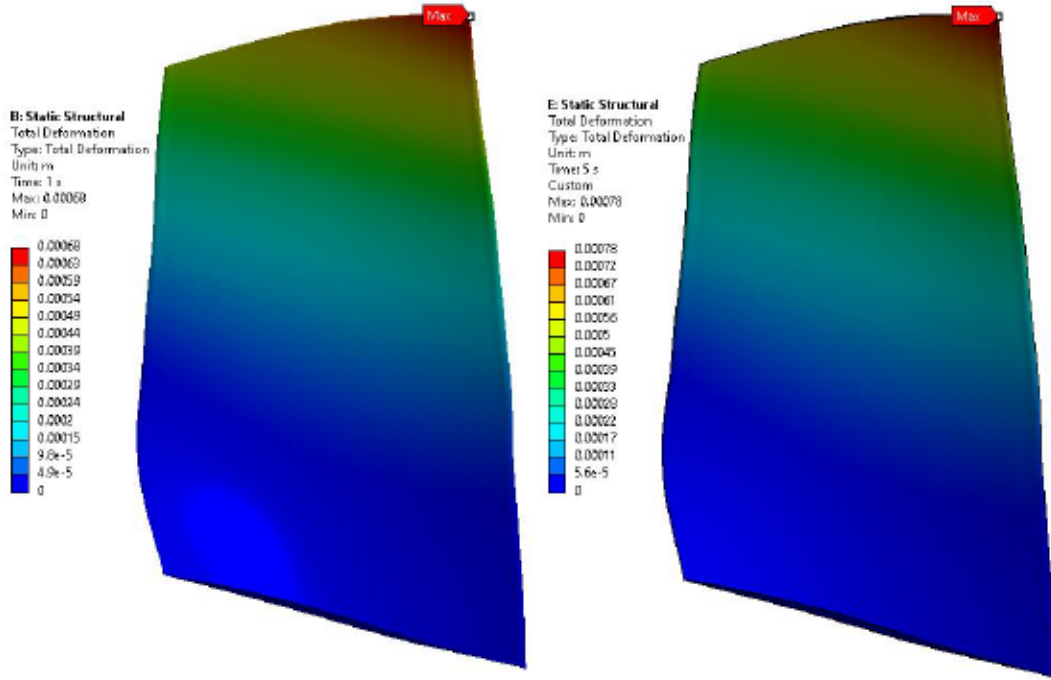


**Figure 24**  
**Maximum total deformation of blade in direct exertion of pressure(left) and employing System Coupling(right) for fluid-solid coupling purpose.**

### 3.10 Design of experiments: Parametric study

This study aims to determine the optimum design of the compressor flow passage. A design of experiments was carried out, treating the tip clearance as a quantitative factor and material as a factor, to investigate the simultaneous influence of these two factors on the design process of the compressor. A multilevel factorial method was used to satisfy the optimization requirements. The one-way fluid-structure coupling was set for a parametric study, with the radial deformation, efficiency, total pressure ratio, and von-Mises equivalent stress as the output results. Three materials - 17-4 PH stainless steel, Ti-6Al-6V, and Aluminum alloy - were used as input data, as well as five different tip clearance sizes.

#### 3.10.1 Multilevel Factorial Design

A factorial design was used to study the effects of two or more factors, as it efficiently investigates all possible combinations of the levels of the factors [78]. The study involved two factors - material (three levels) and tip clearance size (five levels) - resulting in 15 total experiments carried out in the FSC configurations. Tip clearance value is set to be discretely vary for 50-150% of the initial value by 25% increment in each level. Figure 25. And Figure 26 demonstrate the effects of the tip clearance and material on the safety factor and efficiency, respectively. The results show that a higher tip clearance results in better safety for the design but reduces efficiency. The effect of

material changes on the safety factor is expected, with steel having three times the Young's modulus of aluminum, resulting in a three times larger elastic deformation in aluminum. The CFD solver considers the walls of the fluid domain as a rigid body, so there is no change in aerodynamic forces. Response optimization is proposed to investigate the factors concurrently and determine the optimal design of the compressor rotor.

**Table 5**  
DOE: Design of Experiments table.

Run Number	Material	Tip-clearance (mm)	Radial Deformation (mm)	Safety Factor	EQ Stress (MPa)	Efficiency (%)	Total Pressure Ratio
1	17-4 PH	1.01	0.227	4.45	47.3	91	1.677
2	Al	1.51	0.58	2.60	43.5	90.39	1.64
3	Al	1.26	0.607	2.08	45.4	90.73	1.66
4	Ti-Al	1.51	0.389	3.88	43.5	90.39	1.64
5	Al	1.01	0.63	1.60	47.3	91.05	1.677
6	17-4 PH	0.757	0.236	3.21	49.2	91.3	1.69
7	Ti-Al	1.01	0.425	2.38	47.3	91.048	1.677
8	Al	0.757	0.657	1.15	49.2	91.3	1.69
9	Al	0.505	0.257	1.96	27.2	91.55	1.7
10	Ti-Al	0.757	0.44	1.72	49.2	91.3	1.69
11	17-4 PH	1.26	0.217	5.80	45.4	90.73	1.66
12	17-4 PH	1.51	0.2075	7.28	43.5	90.39	1.64
13	Ti-Al	1.26	0.407	3.09	45.4	90.73	1.66
14	Ti-Al	0.505	0.457	1.10	51.0	91.55	1.7
15	17-4 PH	0.505	0.246	2.05	51.3	91.55	1.7

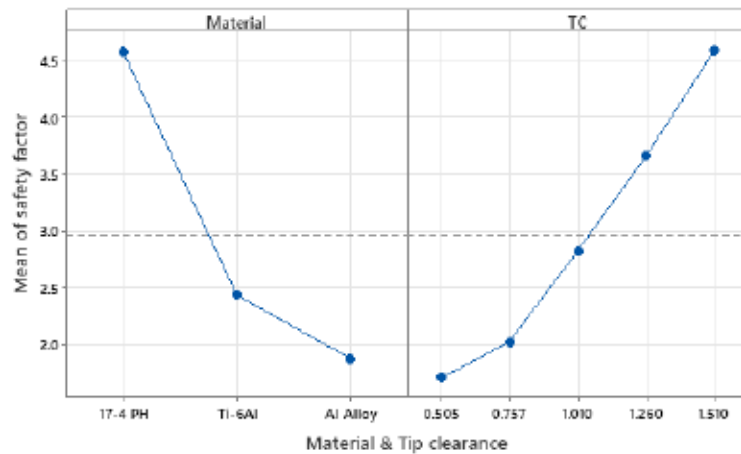


**Figure 25**  
Individual effects of material and tip-clearance on the safety factor value.

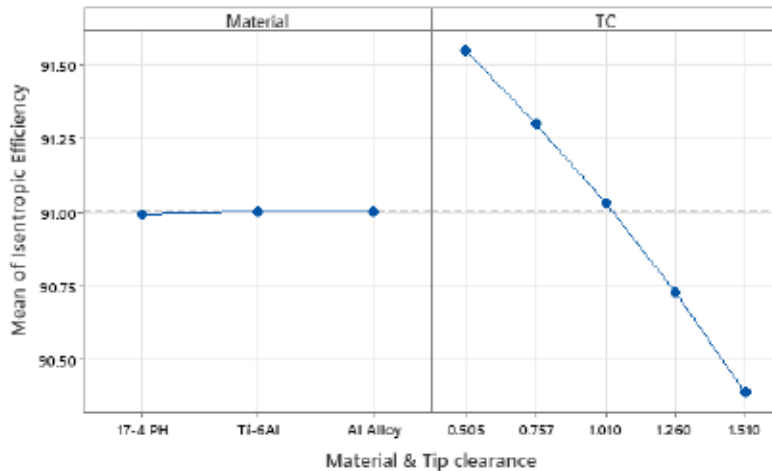


**Figure 26**  
Individual effects of material and tip-clearance on the efficiency value.

### 3.11 Response Optimization

In this study, the design of a compressor rotor is analyzed with a focus on the important parameters of efficiency and safety. Two strategies for finding the optimum design point for the compressor rotor are proposed: one approach is to give equal importance to both efficiency and safety, and the other approach is to prioritize the safety factor over the efficiency factor.

To implement these two strategies, the authors present Table 6 which outlines the target factors for the optimization process, and Table 7, which provides the solution for the desired optimal design point. The results of the analysis show that, when both efficiency and safety are given equal importance, the optimal design point obtained from the numerical simulation aligns with the

experimentally tested design point, as demonstrated in (Table 1) [70]. In the second case, where the safety factor is given twice the importance of the efficiency factor, the results show that the tip clearance is increased by 25% compared to the original design point, while the efficiency experiences a slight 0.27% reduction. As detailed in Table 7, the suggested optimal design point has a tip clearance of 1.26 mm, and the material is specified as stainless steel 17-4 PH. Overall, this study highlights the importance of considering both efficiency and safety in the design process of a compressor rotor and demonstrates the usefulness of numerical simulation in optimizing the design.

**Table 6**  
**Target factors: Target factors for case studies.**

Case Study	Response	Goal	Target	Weight	Importance
One	Efficiency	Maximum	91.55	1	1
	safety factor	Maximum	7.3	1	1
Two	Efficiency	Maximum	91.55	1	1
	safety factor	Maximum	7.3	2	2

**Table 7**  
**Optimization solution: Solutions for the response optimization for both case studies**

Case Study	Material	TC	Efficiency Fit	Safety factor Fit
One	17-4 PH	1.01	91	4.39
Two	17-4 PH	1.26	90.73	5.80

### 3.12 Conclusion

The objective of this study is to investigate the impact of blade radial and axial deformations on the safety and performance of axial compressors, and to contribute to the development of more reliable and efficient turbomachinery designs. To achieve this, the study employs a one-way fluid-structure coupling method to analyze the deformation behavior of compressor rotor blades under different operating conditions and uses three distinct materials to determine the optimal combination of performance and safety.

In conclusion, the present study utilized a loosely coupled fluid-structure interaction approach to examine the behavior of a single stage compressor rotor blade. The numerical model was first validated by comparing the results to experimental data and then, a design of experiment was carried out to investigate the effects of various factors under different operating conditions. The blade-shroud tip-clearance size was treated as a quantitative factor, and three different materials, namely Titanium, Aluminum, and Stainless-steel alloys, were compared using a parametric study in advance with parallel computation tools based on HPC clusters.

The steady-state simulation results of the CFD solver, which showed good agreement with the experimental data, were used as boundary conditions for the structural solver. The static pressure distribution was observed at various points of operation, with the general trend showing an increase in the pressure magnitude on the blade leading edge, from the root to the tip. The aerodynamic and centrifugal loads can result in a deformation on the blade leading edge near the tip, which can have detrimental effects on the safety, stability, and performance of the compressor. Moreover, increasing the tip gap size has adverse effects on the compressor performance and stability due to the generation of a low-speed region downstream of the shock-vortex interaction, which is more pronounced for larger tip clearances due to the creation of a sharper tip leakage vortex.

A multilevel-factorial experiment design was performed, with the compressor efficiency and safety factor set as the response parameters. The response optimization analysis showed that a tip clearance of 1.01 mm and a stainless-steel blade material provided the optimized operating condition that coincided with the design point given in the test case experimental report. Furthermore, the overall performance trend showed that a 25% increase in the tip clearance resulted in a performance loss of about 0.3%, which is a negligible amount and can be considered evidence that the compressor operation safety is twice as important as the efficiency. This leads to a new optimized design point and improved operation safety for the compressor.

Possible future works for this area of research include extending the investigation to multi-stage compressors to assess the effects of tip clearance size and blade materials, blade thickness, camber, and twist on the overall compressor performance and safety employing parametric study using continuous parameters with response surface method. To complement the steady-state simulations used in this study, future work could include transient simulations to analyze blade behavior under dynamic loading conditions and during start-up and shut-down procedures. Experimental studies could also be conducted to validate the numerical results and provide more accurate data for comparison and optimization. These future studies would help to provide a more comprehensive understanding of the behavior of compressor rotor blades, which could lead to improved designs and better safety and efficiency in operation.

#### 4. OPTIMIZATION OF AN AXIAL-FLOW MINE VENTILATION FAN BASED ON EFFECTS OF DESIGN PARAMETERS

*Cet article est rédigé par Seyyed Mojtaba Fakhari et Hatem Mrad a été publié dans la revue Results in engineering en 2023.*

##### 4.1 Résumé

La sécurité dans les mines souterraines dépend fortement de la ventilation, qui est énergivore et coûteuse en maintenance. Cette étude propose une méthode d'optimisation pour un ventilateur de ventilation axial Chinook, en analysant des paramètres tels que l'angle d'attaque, l'écart au bout des pales, la vitesse de rotation, le rapport moyeu-élément et le nombre de pales, en utilisant des méthodes de Plan d'Expériences (DOE) et de régression. Les solutions numériques sont confirmées par des données expérimentales. En considérant un nombre de Mach de 0,4, les conditions de flux compressibles sont analysées à l'aide d'un modèle de turbulence à deux équations. En condition de décrochage, l'efficacité du ventilateur chute à 47%. Une probabilité élevée de fatigue est observée à l'intersection entre la racine des pales en condition de décrochage. L'optimisation identifie plusieurs configurations opérationnelles qui répondent aux performances requises tout en préservant la structure du ventilateur. Un point optimal en dehors de la conception indique que la réduction du nombre de pales et la diminution de l'écart au bout des pales entraînent une amélioration moyenne de la performance de 9%, avec des avantages significatifs en termes de bruit, de coût, de poids et de consommation d'énergie. Les prévisions numériques montrent une précision avec une discordance moyenne de moins de 5%.

**Mots-clés :** Ventilation minière, Optimisation, Ventilateur axial, Interaction fluide-structure, Plan d'expériences

##### *Abstract*

Underground mining safety relies heavily on ventilation, which is energy and maintenance intensive. An optimization method for an axial-flow Chinook ventilation fan, analyzing parameters like angle of attack, tip clearance, rotation speed, hub-to-tip ratio, and rotor blade count using Design of Experiments (DOE) and regression is proposed. The numerical solutions are confirmed with experimental data. Considering a Mach number of 0.4, compressible flow conditions are analyzed using a two-equation turbulence model. During stall, fan efficiency drops to 47%. High fatigue probability is observed at the blade-root intersection in stall conditions. The optimization pinpoints several operational configurations that meet the required performance while preserving

the fan's structure. A particular off-design optimal point indicates that reducing the blade count and decreasing the tip-clearance lead to an average performance improvement of 9%, with significant benefits in noise, cost, weight, and energy consumption. The numerical forecasts demonstrate precision with an average discrepancy of less than 5%.

**Keywords:** Mine ventilation, Optimization, Axial-flow fan, Fluid-structure interaction, Design of experiments

#### 4.2 *Introduction*

Underground mining plays a significant role in the global mining industry, but it also poses several risks to the miners in terms of air pollution. The toxic and potentially explosive gases in the mine atmosphere, along with temperature regulation, are among the key concerns of underground mining ventilation. This is why it is essential for the mining industry to follow the regulations and innovations in ventilation. Ventilation in underground mining not only helps to ensure the safety of miners but also involves significant energy and maintenance costs. Researchers are actively exploring ways to improve the performance of ventilation systems, predict and address potential challenges, and optimize their operation. However, the design of the mine ventilation system, including the layout, configuration of airways, and positioning of ventilators, can impact their performance, it is necessary to study the optimal operational possibilities of the ventilators [79].

For rotary machines such as fans, fan efficiency plays a crucial role in the selection process for a particular application. A higher efficiency allows the attainment of the same air power with reduced power input [48]. However, as shown in Figure 27 the initial cost of the fan can increase as its efficiency increases.

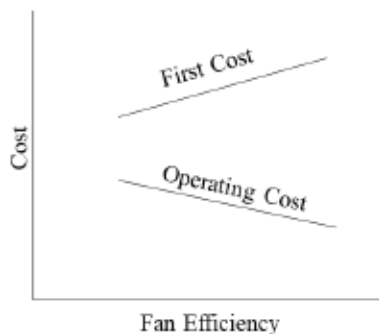


**Figure 27**  
**Cost versus fan efficiency**  
Source: [48].

The performance of axial-flow fans has been the subject of several studies over the years. In 1987, Pericleous and Patel developed a mathematical model for the simulation of stirred biomedical reactors and found general agreement with experiments. However, they noted some deficiencies caused by turbulence in the model [23]. Pelletier et al. developed a general-purpose computational technique for turbulent free 3-D flows past propellers and found good agreement between predictions and experiments. They used the Galerkin finite element algorithm, which was found to be stable and robust [24]. In 1991, Pelletier et al. employed a numerical approach, using a mixed and penalty function finite element method, to study 3D axisymmetric flow near propellers. They identified the sensitivity of velocity and pressure fields to the propeller's kinematic modeling and observed good agreement between their numerical results and experimental data for uniform flow past the propeller [25]. In 1993 numerical study was conducted on a low hub-to-tip ratio axial-flow fan under distorted inlet flow conditions. They used the k- $\epsilon$  turbulence model and the SIMPLEN algorithm and found that the flow across the fan intake has a significant impact on performance [26]. Later, Meyer investigated the effect of an axial fan on the plenum chamber aerodynamics in air-cooled heat exchangers. He found that the fan performance characteristics can vary based on the volume flow rate and blade root stagger angle and that the design guideline to coincide with maximum fan static efficiency does not ensure optimum performance [27]. Le Roux employed CFD models to investigate an axial-flow fan, revealing that eliminating the pinch and implementing a zero-shear wall led to improved predictions. However, some over-predictions in the fan pressure rise at the design flow rate were observed [28]. Another study was conducted in which a CFD simulation study was carried out on an axial-flow fan and presented a new design with different blade numbers, which showed better performance according to numerical results [29]. Moghadam et al. analyzed the tip vortex system of a ducted axial fan using large-eddy simulations. Different tip gap sizes and operating conditions are considered. Increasing the tip gap size enlarges the main tip vortex and reduces fan efficiency. Tip-gap vortices change trajectory and exhibit different behavior at design and off-design conditions. Enhanced turbulent mixing and vortex breakdown occur with larger tip clearances, leading to increased loss coefficients [80]. Wang et al. performed a CFD simulation and experimental validation study on a rotor-only ducted axial-flow fan with a small hub-to-tip ratio. They found that a rounded trailing edge is necessary and that the original blade with aerodynamically shaped blade sections represents the fan blade performance. They also recommended using the Spalart-Allmaras turbulence model for better accuracy and agreement with experimental measurements [30]. A numerical simulation was conducted on a SR3 propeller at 35,000 feet altitude at a transonic Mach of 0.8 using the Ansys CFX package [8]. Another study explores linear instabilities in hypersonic flow over a blunt object, focusing on

detached shock waves and shock regions near the body surface. The analysis assumes a reactive flow in thermal equilibrium, and the simulation converges to a steady base flow through a transient phase. Modal analysis techniques, including Proper Orthogonal Decomposition (POD), Dynamic Mode Decomposition (DMD), and High Order DMD (HODMD), are employed to identify modes in the transient. The study aims to develop reduced-order models for flow characterization and flow control strategies [81]. Sensitivity results from a novel design optimization exercise highlight the effects of parameter variation on airflow and shaft power consumption. Reduced blade number enhances fan efficiencies due to increased chord lengths and higher Reynolds numbers. A comprehensive analysis of seven varied parameters, emphasizing efficiency gains with reduced computational time using a first-principles model are involved. Additionally, a proposed methodology identifies fan losses related to irreversibility and speed maldistribution, emphasizing the importance of uniform speed distribution in axial fan design [82]. The results showed that the performance coefficients and efficiency were in good agreement with experiments, and it was found that the axial and tangential velocities, swirl angles, and static pressure at mid-span reached their maximum values from the wake parameters of the propeller. Fakhari et al. conducted a numerical study on compressor rotor 67. Ansys CFX package was used to conduct the CFD and FSI analysis using design of experiments based on high performance clusters (HPC). The numerical results were validated using the experimental data provided by NASA research center. The new optimal design showed better stability while maintaining the performance of the compressor [83]. Auxiliary ventilation systems in tunnels and mining roadways are examined, evaluating the performance of flexible ducts with diverse qualities. Employing analytical and CFD models, the research focuses on optimizing energy efficiency, sizing fans, and designing ducting systems to manage ventilation costs effectively. Notably, the study introduces innovative nomograms specifically designed for analyzing ventilation systems across a range of tunnel lengths [84]. Adibi et al. explored the impact of artificial dissipation on inviscid time-marching solvers, concluding that Euler equations are comparable to Navier-Stokes equations in capturing flow details. Applicability extends to industries like aircraft manufacturing, with suggestions for further research on fully exploiting Euler equations [85]. A new multidisciplinary optimization method is proposed for rotors, employing blade curvature constraints, significantly reduces computational burden and time costs. It enhances structural performance and aerodynamic efficiency, reducing maximum stress while maintaining or improving aerodynamic performance [86]. An optimization approach is proposed for a transonic fan stage stator which leads to improved aerodynamic performance, particularly near stall conditions. The optimized stator enhances efficiency and stall margin compared to the reference fan, with unsteady simulations providing

insights into improvements near the stall point [87]. Computational fluid dynamics simulations validated by experimental tests are used to simulate a novel design for laptop fan using k-epsilon turbulence model resulting in 20.1% increase in air flow rate and 20% increase in static pressure [88]. Static and dynamic stress analyses of axial-flow Chinook fan blades under real-life loading conditions are investigated. The study identifies crack locations, correlates predicted stress distribution with actual cracks and employs a fracture mechanics criterion for fatigue crack growth simulation using the FRANC3D code. Fatigue life evaluation is conducted using stress ratios and the Forman de Koning model. The critical region is identified to be the blade-root intersection [89].

The research introduces novel elements by applying optimization techniques to predict the performance of the Chinook axial-flow underground mine ventilator, offering a unique perspective in this domain. It systematically identifies optimal configurations, enhancing overall efficiency. The study's originality extends to the treatment of blade geometry, incorporating 3D scanned geometry to address past oversights and provide a more accurate analysis. Additionally, the research stands out in its optimization approach, considering design constraints to maximize performance within existing parameters, potentially offering cost-effective solutions. Overall, the study contributes to the field by innovatively optimizing the Chinook ventilator's performance, showcasing original methodologies, and addressing overlooked aspects from prior research.

#### 4.3 *Geometry*

This study focuses on the investigation of the underground mine Chinook type ventilation system. It specifically explores three distinct hub-to-tip ratios while maintaining a consistent 21-inch hub size for all models. To adapt to the diverse casing sizes of the ventilator, a universal blade is utilized. The creation of this blade involves cutting and machining specific sections to align with the overall assembly dimensions, as depicted in Figure 28, which illustrates a 42-inch axial ventilator with modified blades. For computational simplicity and efficiency, the root part of the blade geometry is disregarded in numerical analysis.



**Figure 28**  
**42-in Chinook type underground ventilation with modified blade**

The blades are manufactured through aluminum A356 alloy casting, resulting in inherent geometrical non-uniformities and surface irregularities. Figure 29 presents a 3D scanned image of the casted blade, highlighting the non-uniformities observed on the leading and trailing edges. Additionally, Figure 30 showcases a comparison between the 3D CAD representation and the manufactured blade. In order to ensure precise and reliable results, the 3D scanned geometry of the manufactured blade is utilized to validate the numerical study.

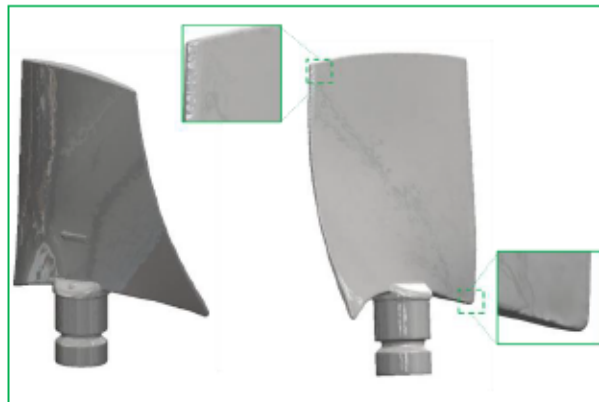


**Figure 29**  
**3D scanned blade for 42-inch fan**

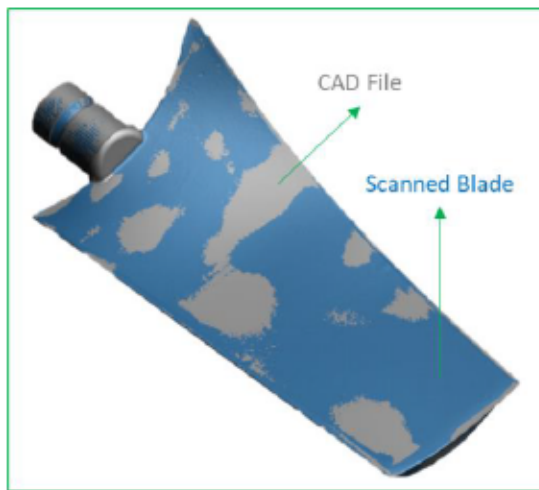


**Figure 30**  
**Comparison of the scanned blade with the 3D CAD file**

#### 4.4 Numerical investigations

Numerical methods have gained increasing popularity in recent years due to their cost-effectiveness and broader applicability compared to expensive and limited experimental works [90, 91]. Their advantages include lower costs, faster speeds, and the ability to simulate complex geometries and operational conditions, making them ideal for aerodynamic analyses. This preference for numerical simulations is shared by numerous researchers and organizations [92, 93]. Figure 31 presents a comprehensive illustration of the employed approach in this study. The figure outlines the key components and steps involved in the methodology, which is crucial for understanding the research process.

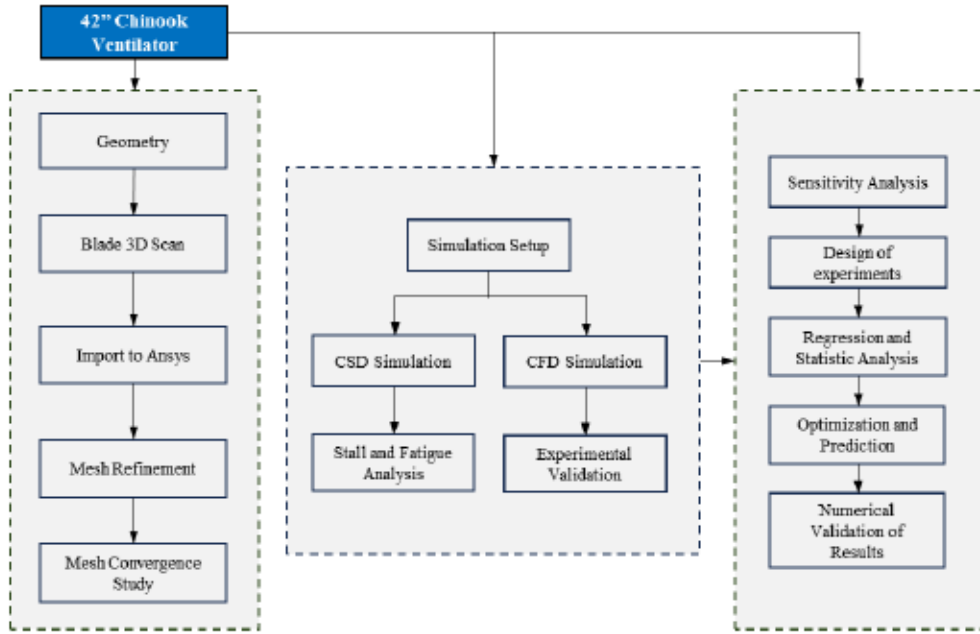


**Figure 31**  
**Optimization progress diagram**

In this study, the 3D Navier-Stokes equations are solved for the fluid domain, accompanied by the implementation of the Wilcox SST  $k-\omega$  turbulence model [51]. The shear stress  $k-\omega$  turbulence model has the advantages of both  $k-\omega$  and  $k-\epsilon$  models while treating their weaknesses in near or far regions [94, 95]. This model is used to simulate the effects of turbulent flow in the operation of a selected 100 HP, 42-inch (1/2 hub-to-tip ratio) Chinook type underground-mine ventilator. A set of 15 blades are used in the mentioned ventilator. Table 8 shows the specifications of the axial-flow ventilator. The purpose is to validate the numerical method by comparing the results with experimental measurements.

**Table 8**  
**Specifications of axial-flow ventilator**

Characteristics	Value
<b>Rotational Velocity (RPM)</b>	1800
<b>Shroud Diameter (in)</b>	42
<b>Hub-to-Tip Ratio</b>	0.5
<b>Number of Rotor Blades</b>	15

After validating the numerical methodology, an exploration of ventilator behavior under different hub-to-tip ratios is conducted. Employing a design of experiments approach, key parameters are varied for a sensitivity study. The generated data is subsequently preprocessed, and optimization methodology is implemented. The optimized design point obtained through this methodology is subsequently validated by conducting CFD simulations, as illustrated before. The comparison of the results from these simulations further confirms the reliability and effectiveness of the chosen numerical approach and the optimization methodology.

#### 4.5 Computational setup and boundary conditions

In order to evaluate the flow field and aerodynamic performance of the axial-flow fan, numerical simulations using Computational Fluid Dynamics (CFD) method is conducted [96, 97]. Reynolds-averaged Navier-Stokes (RANS) equations are solved in the flow solver. Decomposing the solution variables in the instantaneous Navier-Stokes equations into the mean (ensemble-averaged or time-averaged) and fluctuating components, will result in Reynolds averaging [83, 98].

For velocity, pressure, and other scalar quantities one can write:

$$q = \bar{q} + q' \quad 4-1$$

$\bar{q}$  and  $q'$ , are the time averaged value and the fluctuating part, respectively.

After substituting the above expressions into the instantaneous continuity and momentum equations and taking average (time or ensemble), in Cartesian frame, they can be expressed as follows:

$$\frac{\partial \rho}{\partial t} + \frac{\partial}{\partial x_i} (\rho u_i) = 0 \quad 4-2$$

$$\frac{\partial}{\partial t} (\rho u_i) + \frac{\partial}{\partial x_j} (\rho u_i u_j) = - \frac{\partial p}{\partial x_i} + \frac{\partial}{\partial x_j} \left[ \mu \left( \frac{\partial u_i}{\partial x_j} + \frac{\partial u_j}{\partial x_i} - \frac{2}{3} \delta_{ij} \frac{\partial u_l}{\partial x_l} \right) \right] + \frac{\partial}{\partial x_j} (-\overline{\rho u_i' u_j'}) \quad 4-3$$

The Reynolds stresses.  $-\overline{\rho u_i' u_j'}$ , need to be appropriately modeled to model the turbulence. Boussinesq hypothesis can relate the Reynolds stresses to the mean velocity gradients [50]:

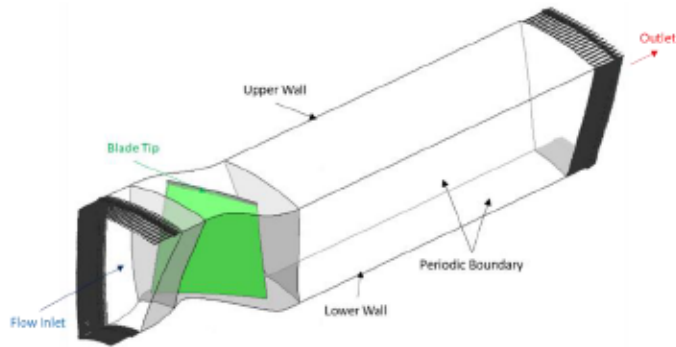
$$-\overline{\rho u_i' u_j'} = \mu_t \left( \frac{\partial u_i}{\partial x_j} + \frac{\partial u_j}{\partial x_i} \right) - \frac{2}{3} \left( \rho k + \mu_t \frac{\partial u_k}{\partial x_k} \right) \delta_{ij} \quad 4-4$$

The turbulence model is set to Wilcox SST k- $\omega$  turbulence model. The transport equations for the SST k- $\omega$  model can be written as follows:

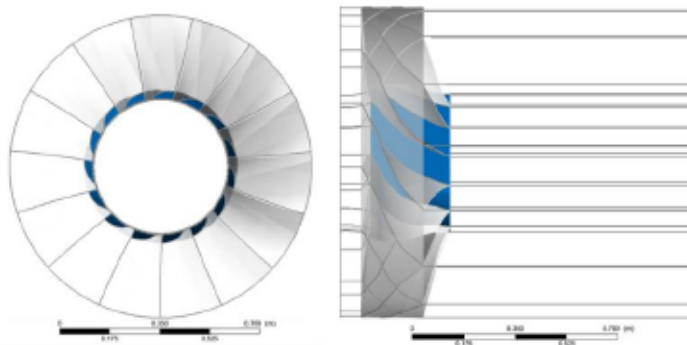
$$\frac{\partial}{\partial t}(\rho k) + \frac{\partial}{\partial x_i}(\rho k u_i) = \frac{\partial}{\partial x_j} \left[ (\Gamma_k) \frac{\partial k}{\partial x_j} \right] + G_k - Y_k + S_k \quad 4-5$$

$$\frac{\partial}{\partial t}(\rho \omega) + \frac{\partial}{\partial x_i}(\rho \omega u_j) = \frac{\partial}{\partial x_j} \left[ (\Gamma_\omega) \frac{\partial \omega}{\partial x_j} \right] + G_\omega - Y_\omega + S_\omega + D_\omega \quad 4-6$$

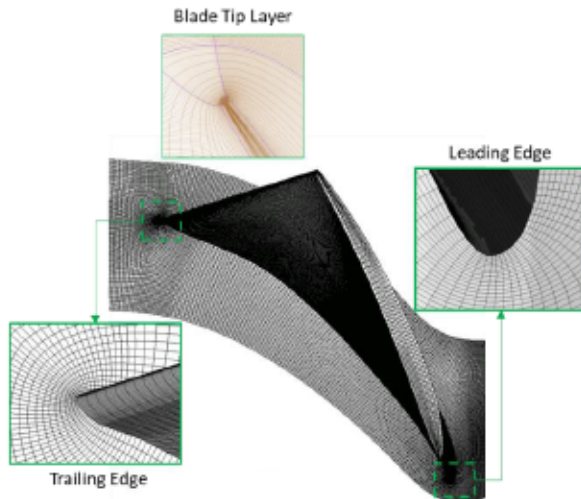
Where,  $G_k$  is the production of turbulence kinetic energy.  $G_\omega$  represents the generation of  $\omega$ .  $\Gamma_k$  and  $\Gamma_\omega$  are the effective diffusivity of  $k$  and  $\omega$ .  $Y_k$  and  $Y_\omega$  are the dissipation of  $k$  and  $\omega$  due to turbulence [53]. The air density and viscosity are set to  $1.225 \text{ kg/m}^3$  and  $1.7894 \times 10^{-5} \text{ kg/(m}\cdot\text{s)}$ , respectively. All numerical simulations are carried out using the ANSYS CFX commercial solver. The second-order upwind and central difference schemes are used to discretize the advection terms and the diffusion terms. In order to demonstrate iterative convergence for steady-state results, the residuals are set threshold of  $10^{-6}$ . Figure 32 and Figure 33 show the computational domain, which includes one single blade passage and the whole model, respectively, to model the axial-flow fan cascade using the translationally periodic condition. For the inlet boundary conditions the total temperature is set to  $298.15 \text{ K}$ , and the total pressure is set to 1 atmospheric pressure. No-slip wall condition is defined for the wall and the rotational speed is set to 1800 rpm. In order to satisfy the requirement of the experimental study, the turbulent level is 5% for the main flow. To obtain the validation performance curves, the outlet boundary is set to corresponding airflow at each simulation. A detailed explanation of the governing equations, CFD implementation and underlying theory of discretization is provided in Section 1.52.2 and Section 1.62.1.



**Figure 32**  
**Computational domain for single blade passage**



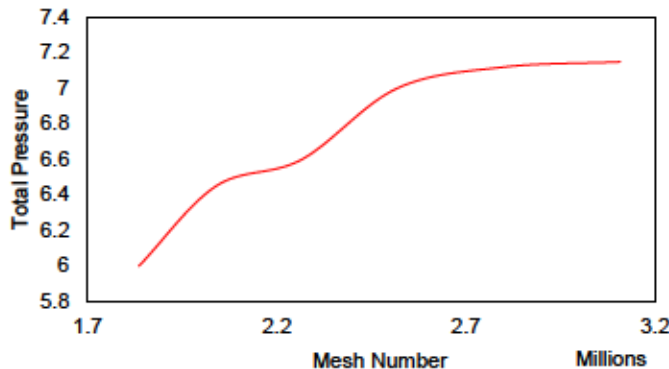
**Figure 33**  
**Computational domain for the whole fan assembly**



**Figure 34**  
**Details of computational mesh**

Ansys Turbo grid is utilized for mesh generation. The mesh is sufficiently refined to meet the  $y +$  requirement of the turbulence model and to maintain its value below 1 near the wall region (Figure 34). The mesh independency study is conducted refining the trailing edge, leading edge, and the

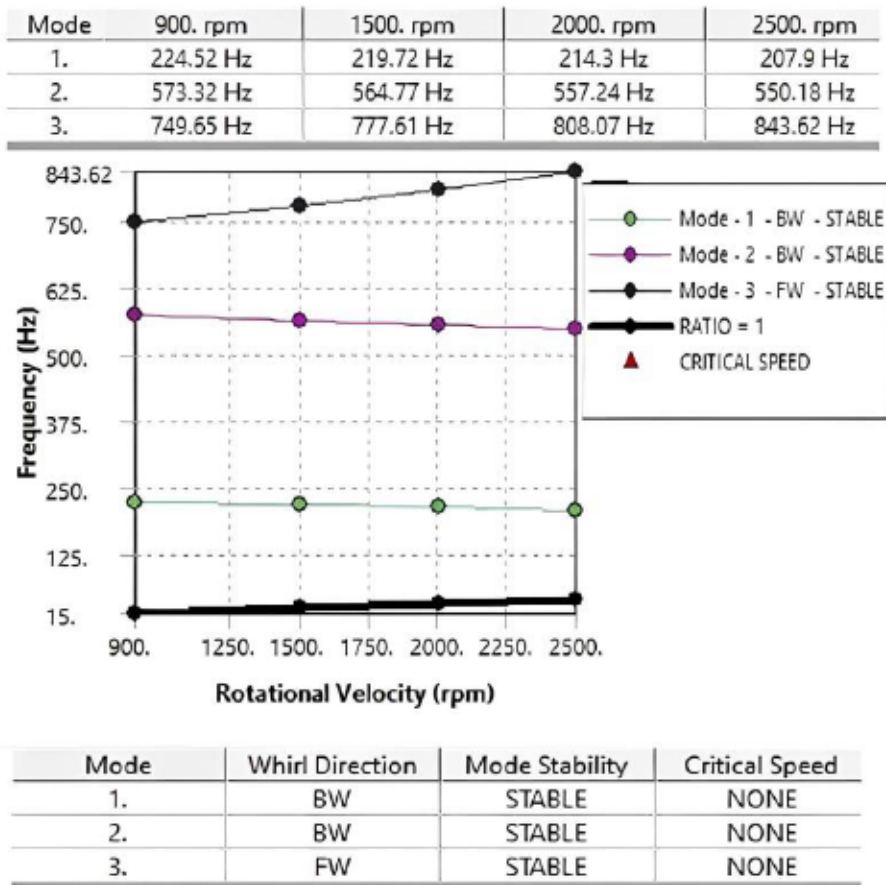
blade tip mesh. Referring to the geometrical non-uniformities and surface irregularities in the employed blade model, a high mesh quality is required on the leading and trailing edges of the blade. Figure 35 illustrates the mesh independency study, revealing that the number of 3108000 hexahedra elements [18, 52] would be sufficient to establish a mesh independent solution.



**Figure 35**  
**Mesh convergence Curve**

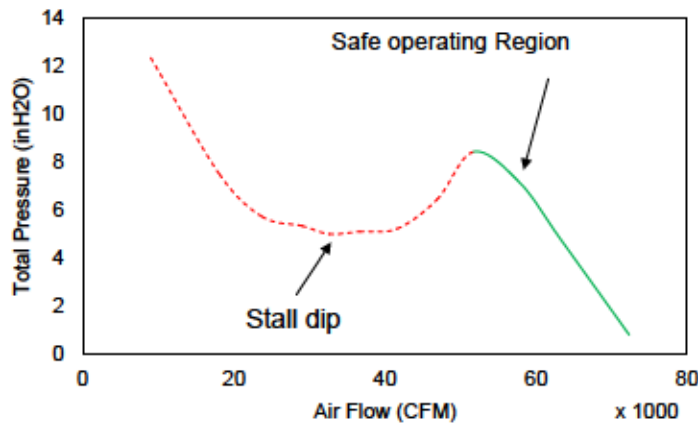
#### 4.6 Experimental validation

The modal analysis of the fan blade is conducted to assess its dynamic behavior and stability. The analysis focused on the first three modes of vibration. The results indicate that no critical speeds are observed within the tested range of rotational speeds (1800 rpm to 2500 rpm) [99]. This implies that the fan blade operates within a stable region and is not prone to resonance-related issues. The mode shapes for the identified modes are examined, revealing the spatial distribution of vibration amplitudes. Figure 36 exhibits the absence of critical speeds and the stable nature of the modes and confirms the structural integrity and operational reliability of the fan blade. These findings provide confidence in the fan blade's ability to function efficiently and mitigate the risk of excessive vibrations or mechanical failures.



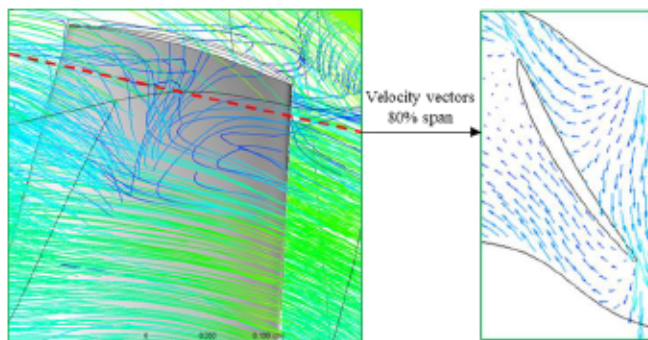
**Figure 36**  
**Campbell diagram for first three mode shapes of fan blade**

Figure 37, shows the complete performance curve for the fan employing blade set of  $55^\circ$  angle of attack ,1800 rpm rotational speed, and tip clearance value of 5 mm. The fan performance curve can be divided into safe and unsafe regions based on the occurrence of the stall. The safe region represents the operating range where the fan functions efficiently and effectively, producing the desired pressure and airflow. In this region, the airflow remains attached to the blade surface, and the fan operates without experiencing flow separation. Conversely, the unsafe region corresponds to the stall dip, where flow separation occurs, leading to decreased efficiency and compromised performance. In this region, the fan's ability to generate pressure and airflow is reduced, resulting in decreased efficiency, increased noise, and potential damage to the fan components [48].



**Figure 37**  
**Performance curve for the blade with angle of attack of 50 degrees**

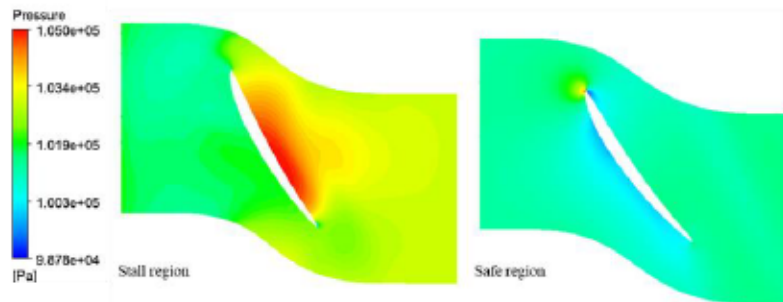
An operating point within the stall region is chosen limiting the outlet airflow at 29000 CFM which results in 5.5 inH<sub>2</sub>O total pressure. Figure 38 depicts the streamlines of velocity around the blade boundary, specifically showcasing the blade-to-blade view of velocity vectors at 80% of the span. This occurrence can be attributed to factors such as dust accumulation on the fan components or an unforeseen increase in static pressure underground. These factors lead to a blockage in the outlet boundary, causing the air to be pushed back into the system. The velocity streamlines and vector directions clearly illustrate this phenomenon, resulting in a loss of pressure and a decrease in the fan's efficiency to 47%.



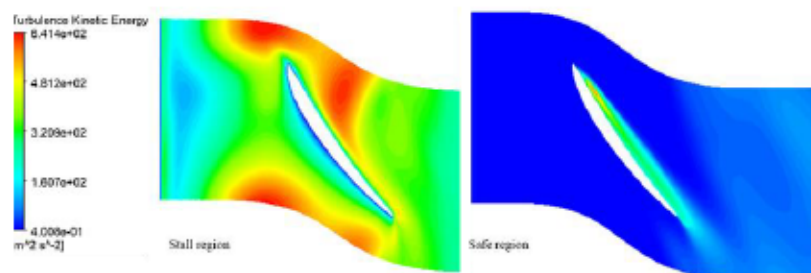
**Figure 38**  
**Velocity streamlines and vectors in stall at 80% span**

Figure 39 and Figure 40 showcase the contours of pressure distribution and turbulent kinetic energy around the blade boundary within the fluid domain, respectively. The pressure distribution reveals a significant disparity between the pressure and suction sides of the blade, with the highest intensity occurring near the blade tip. This pressure difference can give rise to detrimental consequences such as increased vibration, elevated fatigue levels, and potential structural failure at the blade-root intersection.

Additionally, the turbulent kinetic energy contour highlights regions characterized by intense turbulence occurrence. The identification and analysis of these regions are crucial for understanding and addressing the flow characteristics and associated challenges in order to optimize the performance and reliability of the fan.



**Figure 39**  
Pressure distribution around the blade region in 80% span: Stall (left), Safe operating point (right)



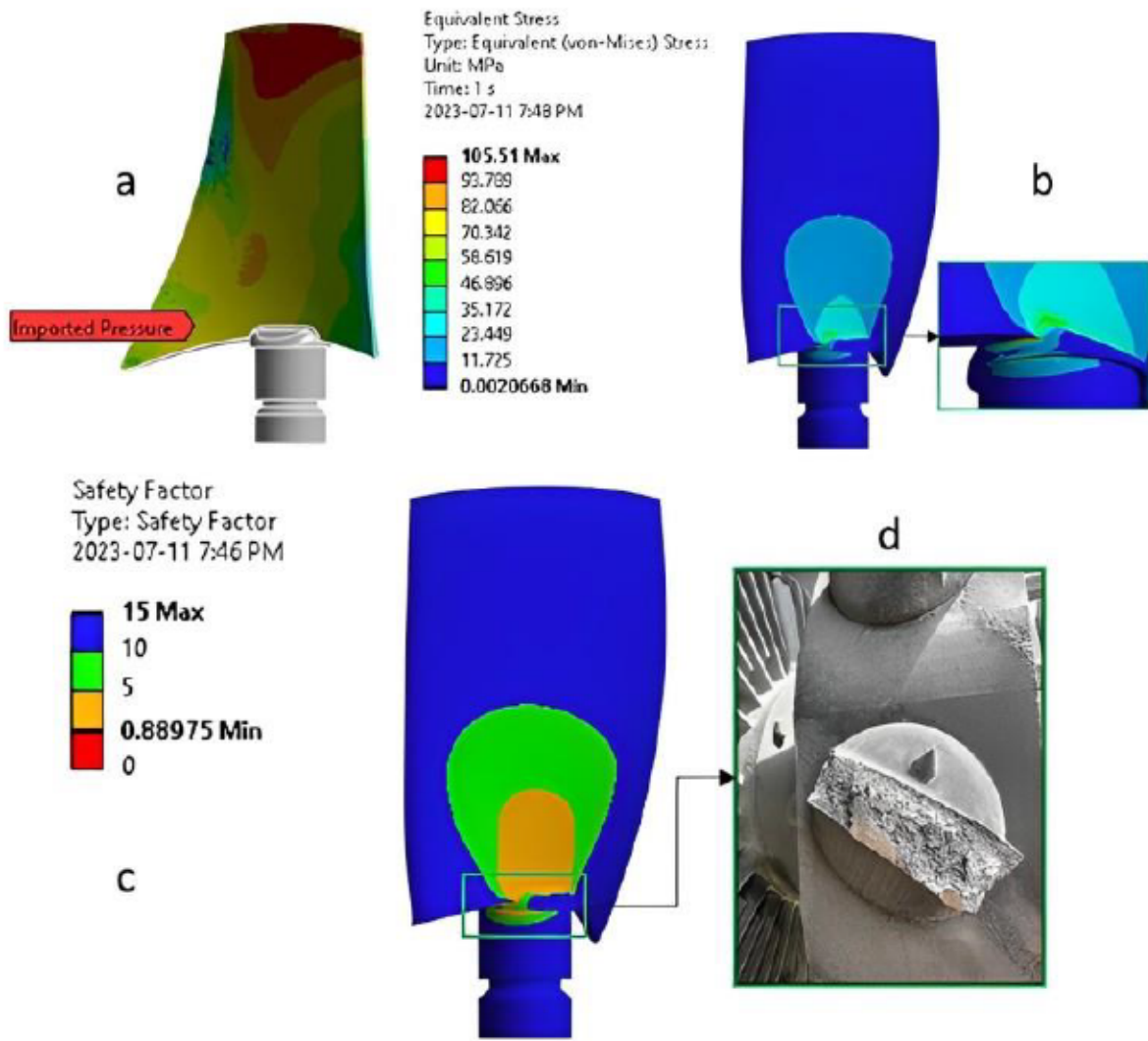
**Figure 40**  
Turbulence kinetic energy contour around the blade region in 80% span: Stall (left), Safe operating point (right)

#### 4.7 Fluid structure interaction analysis in stall

The aerodynamic loads for the stall case study are extracted and incorporated into a mechanical analysis to assess the behavior of the fan and evaluate potential failure risks. Aluminum A356 has been selected as the material for structural analysis, aligning with the material choice made by the manufacturer for producing their fan blades. Tetrahedron mesh element is used for the solid domain [52, 76]. Rotational speed is set to 1800 rpm to conduct the steady state structural analysis. Figure 41-a displays the pressure distribution on the blade surface obtained from the fluid dynamics analysis. This information provides insights into the aerodynamic forces acting on the blade. To further analyze the structural integrity, Figure 41-b showcases the maximum equivalent stress and highlights the critical region of the blade geometry. This allows for identifying areas that may be prone to high stress concentrations or potential failure. In addition to stress

analysis, the fatigue safety factor is examined in Figure 41-c. It is observed that the calculated safety factor is less than one, indicating a potential risk of fatigue failure under the applied loads.

Furthermore, Figure 41-d presents a sample of a broken blade for a 42" Chinook ventilation fan, emphasizing the occurrence of actual failures. Specifically, the blade-root intersection near the leading edge is identified as the most critical region, which experiences significant stress concentrations and vulnerability to failure [89]. A detailed explanation of the Fluid-Structure interaction implementation and the interface theory is provided in Sections 2.2, 2.5, 2.6 and Section 2.7.

**Figure 41**

(a) Pressure exported from CFD, (b) Maximum von-Mises stress, (c) Fatigue safety factor, (d) Failure caused by fatigue

To ensure both safety and operational efficiency of the fan, and to validate the numerical results, the primary emphasis was placed on investigating the safe region of the performance curve. Figure 42 presents a comparison between the experimental measured performance data and the corresponding numerical results under safe operating conditions. Airflow and the pressure in ducts are measured using an anemometer and a static pressure monometer, on a designed base point to point measurement. Airflow quantity can be determined by  $Q = v \cdot A$  in which  $v$  is the velocity of a point [48]. The findings reveal a strong agreement between the predictions and the observed in-field characteristics of the fan. On average, a discrepancy of approximately 5% is observed, which

can be attributed to various factors, including simplifications in the model. For instance, the model does not account for the blade-hub tip gap, as it becomes highly complex due to the presence of the cylindrical root, leading to intricate surfaces and edges. Additionally, uncertainties arise from the experimental measurement setup, the quality of the casted blades, assembly errors such as non-uniform casing resulting from the rolling process, non-uniformity, and misalignments of the blade angle, as well as differences in the real rotational speed. These conditions are considered as fixed values and equal in the case of symmetrical patterns, in the simulations.

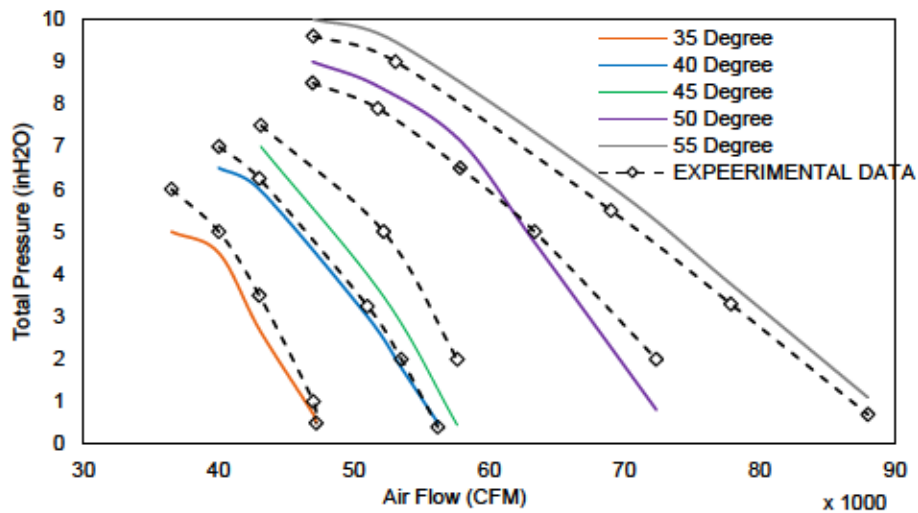


**Figure 42**  
Experimental measurements versus numerical results

#### 4.8 Sensitivity analysis and Design of experiments

A sensitivity study is conducted to determine the key parameters affecting the aerodynamic performance of an axial-flow fan. The chosen variables include blade angle of attack, number of blades, casing diameter, shroud tip-clearance, and rotational speed. In line with the fan laws, the significance of diameter and rotational speed changes are considered, which are included in a factorial design of experiment (DOE) for verification purposes. A total of 324 design points are defined by combining variations in different parameters.

**Table 9**  
**Factorial design variables and their levels.**

Parameter	Levels	Value
Angle of attack	4	40 / 45 / 50 / 55
Blade tip clearance (mm)	3	1 / 5 / 7
Rotational Speed (rpm)	3	1200 / 1800 / 2500
Number of blades	3	10 / 12 / 15
Shroud diameter (in)	3	32 / 36 / 42

#### 4.8.1 Parametric study implementation on high performance clusters

To facilitate a numerical study involving variations in parameters, a parametric approach was adopted. This involved using ANSYS Workbench design points, where essential simulation properties were defined in a tabular format, allowing for the examination of different design points. By employing high-performance processor units, precision was enhanced while significantly reducing computational costs and the potential for human error. High-performance computing (HPC) technologies were employed to support the numerical simulation processes. The simulation configurations were initially set up on a personal computer and then transferred to a cluster scheduler via a secure shell (SSH) channel. To take advantage of parallel computation, the scripts utilized the Intel MPI Library. The CFD analyses utilized a total of 240 cores from 2 x Intel Platinum 8260 Cascade Lake CPUs.

#### 4.8.2 Data pre-processing and sensitivity analysis

Figure 43, shows the influences of various parameters on the value of the total pressure of the fan. Figure 43-a, presents the effect of increase of angle of attack on the increase of the performance of the axial-flow fan, as well as the effect of increase of the rotational speed (Figure 43-b). Number of blades in a rotor stage shows ascending effect on the performance, by increasing the number of blades (Figure 43-c). Figure 43-d, shows that by increasing the casing diameter (decreasing the hub-to-tip ratio), while the airflow rate increases, it results in a loss of pressure. In the Figure 43-e, it can be seen that larger tip clearance values give less performance and the smaller tip clearance values, result in higher amount of the pressure.

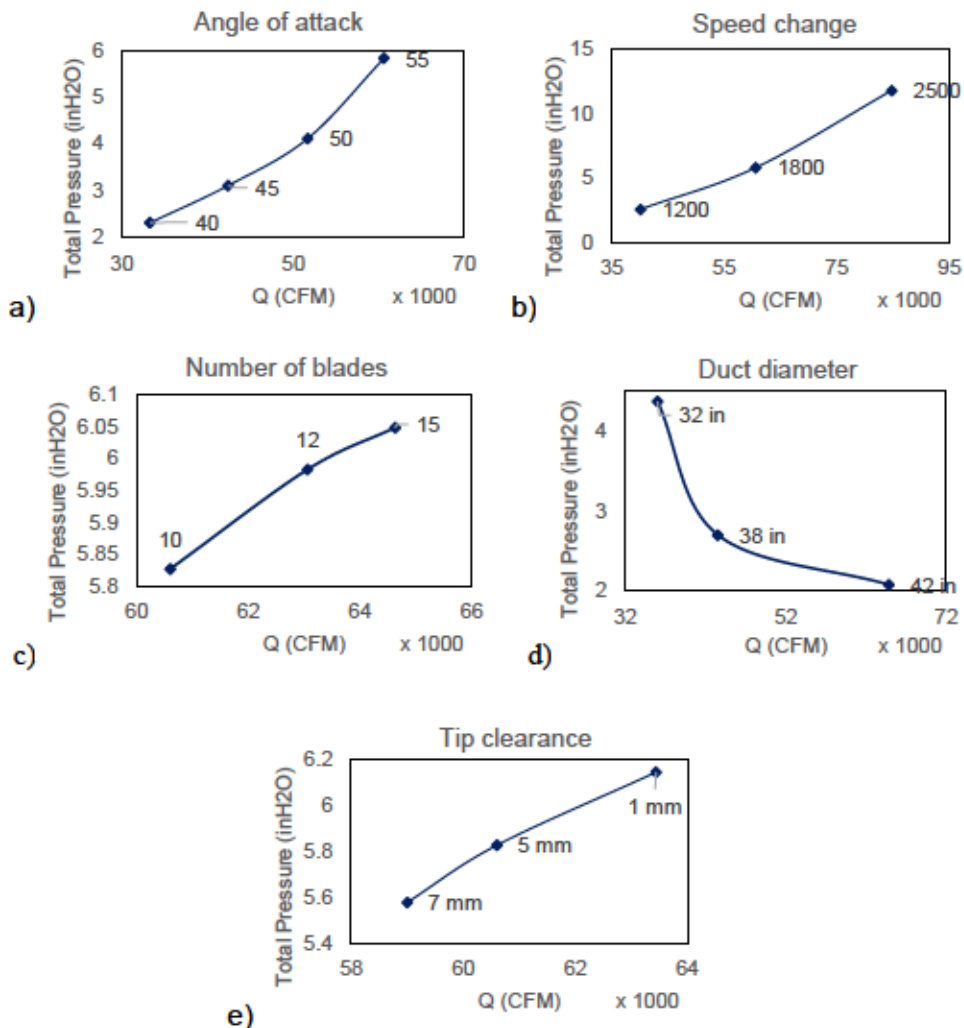


**Figure 43**  
**Effects of different variables on the performance of the axial fan.** a) Angle of attack, b) Speed change, c) Number of blades, d) Casing size, e) Tip clearance

Figure 44 displays the normal probability plots for both total pressure and airflow rate. These plots provide a visual assessment of the normality assumption of the residuals in the regression model. The model summary, presented in Table 10, provides an overview of the regression model's performance. It includes important metrics such as R-squared and predicted R-squared. The R-squared value represents the proportion of variance in the response variable that can be explained by the predictor variables. In this case, the R-squared value of 93.35% suggests that approximately 93.35% of the variability in the response variable can be explained by the predictor variables included in the model. The predicted R-squared value estimates the model's predictive performance on new, unseen data. The value of 92.17% indicates that the model can explain approximately 92.17% of the variability in the response variable when applied to new data. Overall,

by examining both the normal probability plots and the model summary, the regression results indicate a relatively good fit and predictive performance of the model.

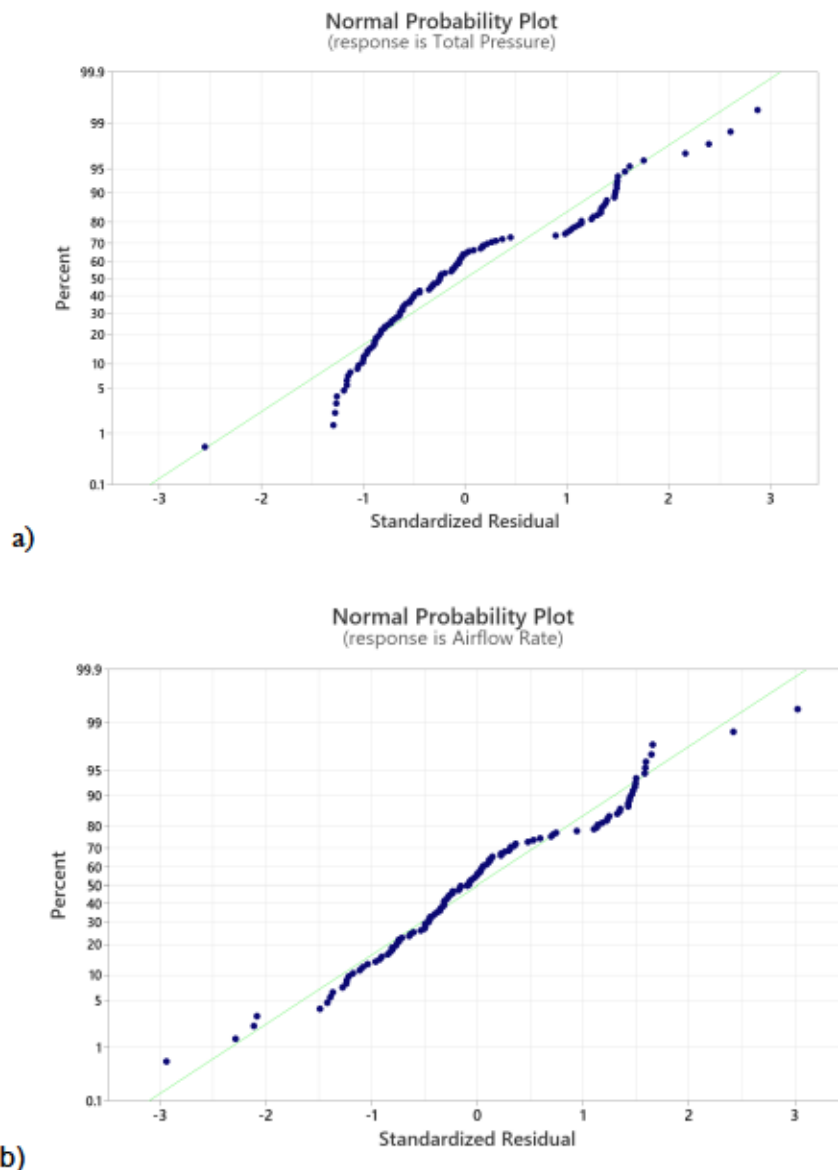


**Figure 44**  
Normal probability plot for Total Pressure (a), and Airflow Rate (b)

**Table 10**  
**Regression model summary for both total pressure and airflow rate**

	R-sq	R-sq(pred)
Airflow Rate	93.35%	92.17%
Total Pressure	86.97%	84.87%

Figure 45 presents the standardized effects of individual parameters and their combined effects on the total pressure and airflow rate of the ventilator using a linear regression model. The results of the regression analysis reveal that the rotational speed is the most influential parameter, significantly impacting the fan's performance. Adjusting the rotational speed can lead to notable improvements or changes in the overall performance of the fan. In addition, the angle of attack demonstrates significant effects on both the airflow and the amount of pressure rise within the fan system. This indicates that manipulating the angle of attack can effectively influence the fan's ability to move air efficiently and generate the desired pressure levels. Moreover, the hub-to-tip ratio plays a significant role in controlling the amount of airflow at the fan's outlet boundary. By adjusting the hub-to-tip ratio, one can effectively control the volume of air being discharged by the fan, thus affecting its overall performance.

While the number of blades and tip clearance do affect the fan's performance, their impact is comparatively less pronounced than factors such as rotational speed, angle of attack, and hub-to-tip ratio. Effectively optimizing the fan's performance necessitates a thorough examination of the combined effects and interactions among these parameters. Analyzing the relationships between rotational speed, angle of attack, hub-to-tip ratio, number of blades, and tip clearance is essential for gaining valuable insights and achieving optimal outcomes. This comprehensive approach is crucial for maximizing the fan's efficiency across diverse applications.

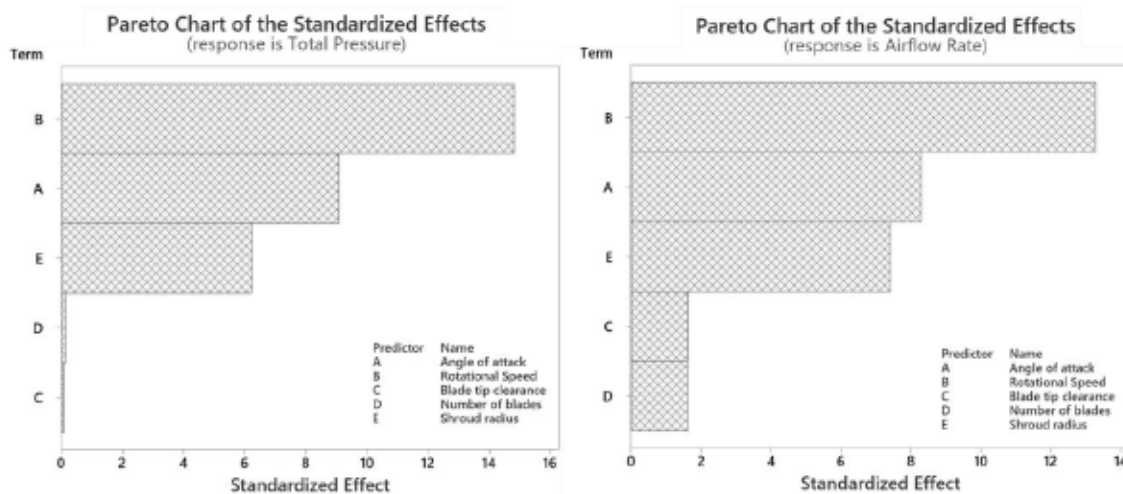


**Figure 45**  
Pareto chart of standardized effects of the parameters on the Total Pressure (left) and Airflow Rate (right)

#### 4.9 Optimization and design point prediction

The regression model serves the purpose of optimizing and predicting fan performance by quantifying the effects of sensitive parameters. Table 11 presents the linear regression equations for the airflow rate and total pressure outputs in the study.

**Table 11**  
Regression equations for airflow rate and total pressure

Airflow	=	$(-82614) + (1380 \times \text{AOA}) + (23.84 \times \omega) - (3592 \times \text{TC\_5}) - (263 \times \text{TC\_7}) + (1014 \times \text{NOB\_12}) - (2582 \times \text{NOB\_15}) + (4730 \times \text{D\_0.457}) + (27926 \times \text{D\_0.527})$
Total Pressure	=	$(-17.79) + (0.2560 \times \text{AOA}) + (0.004512 \times \omega) - (0.080 \times \text{TC\_5}) - (0.329 \times \text{TC\_7}) + (0.158 \times \text{NOB\_12}) + (0.257 \times \text{NOB\_15}) + (0.655 \times \text{D\_0.457}) + (2.169 \times \text{D\_0.527})$

These equations provide the estimated relationships between the respective parameters and the corresponding outputs, allowing for predictions and optimization of fan performance.

Considering the manufacturer's desired operating designs for the 42" ventilator, several criteria have been defined. The preferred operating region requires the ventilator to provide a minimum airflow of 55000 cfm and a total pressure of 7 inH2O. To meet these criteria, the total pressure is set as the ideal target at 7 inH2O, while the airflow is aimed to be maximized. The values of the parameters are allowed to vary within the range of existing design points. Table 12 presents different setups that have been predicted using the regression model. These setups are aimed at optimizing the airflow and total pressure rates while considering the desired operating criteria specified by the manufacturer. Figure 46 exhibits one of the predicted optimal setups with a

composite desirability value of 0.79. The predictions show that applying smooth increases or decreases in the values of the parameters while considering their combined effects, can result in the desired operating conditions for the underground-mine ventilator.

**Table 12**  
**Predictions for various optimal operating parameters and outputs**

N	Angle of attack (degree)	Blade tip clearance (mm)	Rotational Speed (rpm)	Number of blades	Casing Diameter (in)	Total Pressure (inH <sub>2</sub> O)	Airflow Rate (CFM)
1	55	7	1930	15	42	7.1	64370
2	58	7	1800	15	42	7.2	65400
3	53.3	1	1930	15	42	6.99	62300
4	55	1	1930	12	42	7	67890

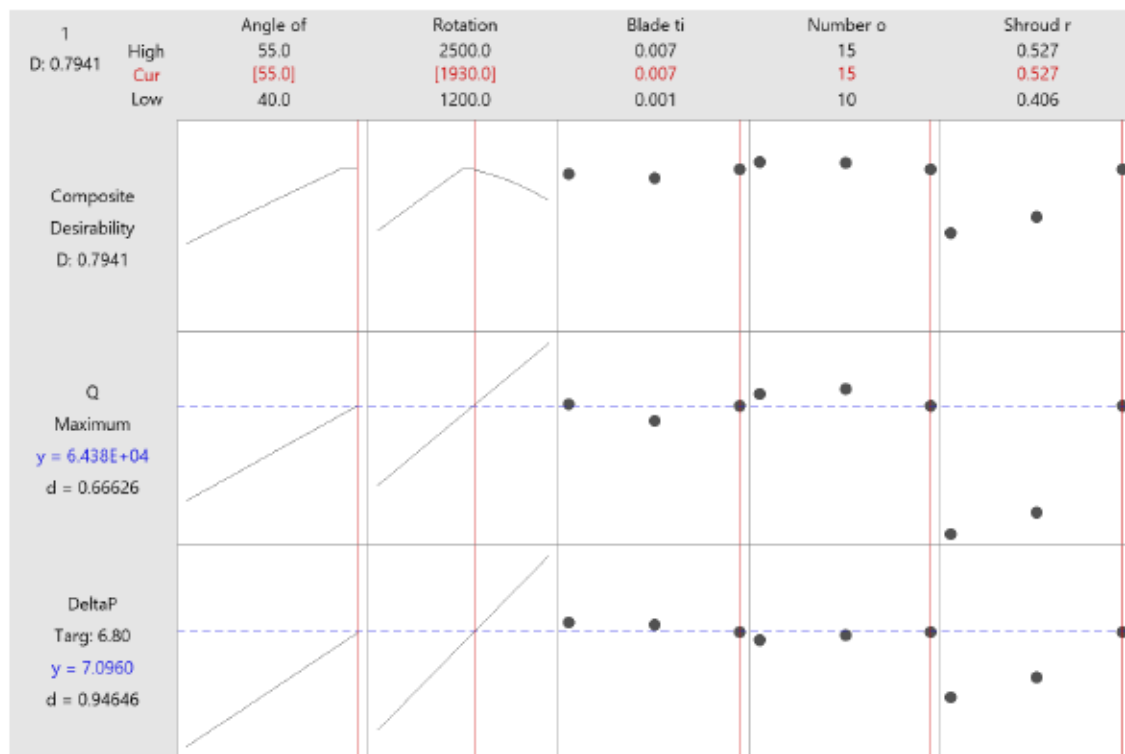


**Figure 46**  
**Desired optimal operating point**

#### 4.10 Numerical validation of optimal design

To ensure that the optimization model is precise and reliable, a set of predicted optimal points are numerically solved in this section. Based on the validated computational fluid calculations, the parameters are set from the regression model outputs. The results show a good agreement between the predictions and the simulations while respecting the power and efficiency limitations. Table 13 shows the results obtained from the numerical simulations and their errors from the actual predictions. The fan efficiency ( $\eta$ ) is calculated based on the fan laws, in which, the motor input power (MIP) is used to evaluate the efficiency of the fan [48, 100].

$$\eta = \frac{Q \times P}{MIP} \times 100$$

4-7

$Q$  and  $P$  are the air flow rate ( $\text{m}^3\text{s}^{-1}$ ), and air pressure (Pa).

Description of fans and Fan Laws are explained in detail in Section 2.8.

**Table 13**  
Numerical validation of optimal solutions and errors

N	Total Pressure (inH <sub>2</sub> O)		Airflow Rate (CFM)		Efficiency (%)	Input Power (HP)	Average Error (%)
	Predictions	Simulations	Predictions	Simulations			
1	7.1	6.62	64370	65330	68	100	4.13
2	7.2	6.9	65400	65680	71		2.30
3	6.99	6.51	62300	64700	66		5.36
4	7	7.2	67890	70450	80		3.32

The first optimal solution is chosen from Table 12 for further investigation to ensure that the fan operates within the safe region of its operating conditions. The investigation involved examining the pressure contours around the blade boundary within the domain, as well as analyzing the velocity vectors. Figure 47 displays the combination of pressure contours and velocity vectors and streamlines at 80% span. This visualization indicates that the ventilator is expected to perform within the safe operating region and will not encounter stall conditions. Importantly, the configurations predicted by the regression model adhere to the limitations imposed on power and efficiency.

The average errors for each row encompass the discrepancies between the predicted values of total pressure and airflow rate obtained from the regression model and the corresponding numerically obtained pressure and airflow values. These errors have been analyzed and found to exhibit acceptable differences when compared to the reference values. These findings provide assurance that the selected configurations derived from the regression model meet the required criteria and demonstrate satisfactory performance within the designated safe operational boundaries.

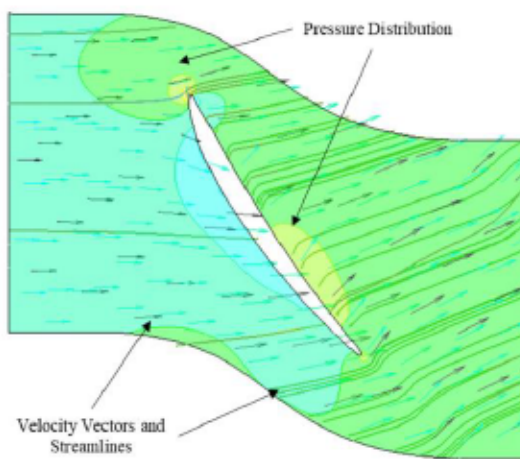


**Figure 47**  
**Pressure distribution, velocity vectors and velocity streamlines on the blade-to-blade surface in 80% span**

Additionally, the results indicate that utilizing 12 blades and 1 mm tip clearance on the fan assembly achieves the desired airflow at the outlet boundary while also meeting the target pressure. It admits the importance of the tip-clearance and its effects on the performance of the fan [7]. It is important to note that the leading edge, trailing edge, and tip clearance significantly contribute to the noise generated by a running fan. Therefore, reducing the number of blades will lead to noise reduction, as well as potential benefits in terms of cost, weight, and energy consumption for the ventilator, while maintaining comparable performance characteristics.

#### 4.11 Conclusion

Ventilation is crucial in underground mining safety, but it involves significant energy and maintenance costs. This study aims to optimize the design of Chinook type ventilation fan, considering safety, energy, maintenance, and cost factors.

The study applies Computational Fluid Dynamics (CFD) simulations to 3D scanned blade geometry, validates the methodology with experimental measurements, and uses the results to derive a performance curve for the fan, identifying safe operating regions and stall occurrences. Fluid-structure interaction and modal analyses ensure the stability of the ventilator. The efficiency of the fan drops to 47% in stall and the blade-root intersection is found to be the most critical region in context of fatigue. Post-validation, a design of experiments studies various parameters, identifying rotation speed, angle of attack, and hub-to-tip ratio as key. A regression methodology links these parameters to fan performance. Optimization suggests that reducing blade count from 15 to 12 and decreasing the tip-clearance can improve performance by 9% with significant improvement in noise, cost, weight, and energy consumption.

These findings provide valuable insights into the performance of the fan and offer opportunities for optimizing its design to enhance efficiency and cost-effectiveness. Possible future works in this area of research includes expanding the investigation to modifying the blade profile using intelligent approaches coupled with computational fluid dynamics to achieve better performance while reducing the noise produced by the fan. Another study can be conducted on structural optimization of the hub and overall fan, to reduce the increase in the stiffness-weight ratio.

## 5. OPTIMIZATION OF UNCONSTRAINED PROBLEMS USING A DEVELOPED ALGORITHM OF SPECTRAL CONJUGATE GRADIENT METHOD CALCULATION

*Cet article est rédigé par Hatem Mrad et Seyyed Mojtaba Fakhari a été publié dans la revue Mathematics and Computers in Simulation en 2024.*

### 5.1 Résumé

Cet article présente une étude numérique sur la formulation des directions conjuguées spectrales pour l'optimisation des problèmes non contraints. Un nouvel algorithme modifié est proposé, basé sur la méthode du coefficient de gradient conjugué. L'algorithme utilise les conditions de recherche linéaire inexacte de Wolfe pour déterminer la longueur de pas optimale à chaque itération et sélectionne en conséquence le coefficient de gradient conjugué approprié. L'algorithme est évalué à travers plusieurs expériences numériques utilisant différentes fonctions non contraintes. Les résultats indiquent que l'algorithme est hautement stable, quel que soit le point de départ, et présente des taux de convergence et une efficacité supérieure par rapport aux méthodes classiques dans certains cas. Globalement, cette recherche propose une approche prometteuse pour résoudre les problèmes d'optimisation non contraints.

**Mots-clés :** méthode du gradient conjugué spectral, optimisation, conditions de recherche de Wolfe

### Abstract

This paper presents a numerical investigation of the spectral conjugate directions formulation for optimizing unconstrained problems. A novel modified algorithm is proposed based on the conjugate gradient coefficient method. The algorithm employs the Wolfe inexact line search conditions to determine the optimum step length at each iteration and selects the appropriate conjugate gradient coefficient accordingly. The algorithm is evaluated through several numerical experiments using various unconstrained functions. The results indicate that the algorithm is highly stable, regardless of the starting point, and has better convergence rates and efficiency compared to classical methods in certain cases. Overall, this research provides a promising approach to solving unconstrained optimization problems.

**Keywords:** spectral conjugate gradient method, optimization, Wolfe search conditions

## 5.2 Introduction

Due to its accuracy and convergence rate, the Conjugate Gradient (CG) method remains a popular choice for solving a wide range of multivariable objective functions. In recent years, many authors have developed new, high-performance CG methods, focusing on improving CG coefficients and algorithms to ensure optimal performance and global convergence for different types of CG optimization problems [32, 101, 102]. These problems are typically grouped into three main categories: classical, scaled, hybrid, and parameterized CG. The key challenges these works address include accurately calculating step length and determining successive orthogonal conjugate directions until the optimal point is reached [35, 103]. Meeting these challenges depends heavily on the line search algorithm used and the method for evaluating CG coefficients.

Let us consider the nonlinear unconstrained optimization problem:

$$\min\{f(x): x \in R^n\}, \quad 5-1$$

where  $f(x): R^n \rightarrow R$  is a bounded, continuous, and partial differentiable function.

The classic steepest descent method based on gradient direction reaches its limits when: (i) starting point  $x_0$  is far from the optimum solution, (ii) objective function admits several local minima (iii) non differentiable function. Therefore, a better algorithm based on the conjugate gradient method must not only converge to an optimum point  $x^*$ , but also converge faster.

Finding a set of  $n$  linearly independent directions  $\{d_1, \dots, d_n\}$  allows to represent each point  $x \in IR^n$  of  $n$ -dimensional space as a linear combination:

$$x = x_0 + \sum_{i=1}^{n-1} \alpha_i d_i \quad 5-2$$

The vectors  $\{d_1, \dots, d_n\}$  are H-conjugate if they are linearly independent and:

$$d_i^T H d_j = 0, \quad \forall i \neq j \quad 5-3$$

The use of conjugated directions allows calculating iteratively a sequence  $x_k$  to the minimum  $x^*$  of  $f$ , in which:

$$x_{k+1} = x_k + \alpha_k d_k, \quad k = 1, 2, \dots \quad 5-4$$

where each direction  $d_k$  is determined by:

$$d_k = \begin{cases} -g_k & ; k = 1 \\ -g_k + \beta_k d_{k-1} & ; k \geq 2 \end{cases} \quad 5-5$$

Conjugate gradient coefficient  $\beta_k \in R$  was proposed in several previous works by Polak and Ribiere (PR) [104], Liu and Storey (LS) [105], lastly Conjugate Descent (CD) [106], and Dai and Yuan (DY) [107], respectively.

$$\beta_k^{PR} = \frac{g_k^T (g_k - g_{k-1})}{\|g_{k-1}\|^2} \quad 5-6$$

$$\beta_k^{LS} = -\frac{g_k^T (g_k - g_{k-1})}{d_{k-1}^T g_{k-1}} = -\frac{g_k^T y_{k-1}}{d_{k-1}^T g_{k-1}} \quad 5-7$$

$$\beta_k^{CD} = -\frac{\|g_k\|^2}{d_{k-1}^T g_{k-1}} \quad 5-8$$

$$\beta_k^{DY} = \frac{\|g_k\|^2}{d_{k-1}^T y_{k-1}} \quad 5-9$$

where  $y_{k-1} = (g_k - g_{k-1})$  and  $\|\cdot\|$  denote the gradient change and the Euclidean norm, respectively.

To find the minimum of the general nonlinear function  $f(x)$ , one needs to find a root of  $\nabla f(x)=0$ . The residual  $r_{k+1}$  at iterate  $x_{k+1}$  can be written as:

$$r_{k+1} = \nabla f(x) - \nabla f(x_{k+1}) \quad 5-10$$

For nonlinear function is no longer practice using a closed form expression of the step length  $\alpha_k$  as in:

$$\alpha_k = \frac{r_k^T r_k}{d_k^T H_f d_k} \quad 5-11$$

Instead, the Wolfe inexact line search conditions [108] were usually chosen in the conjugate gradient. These conditions ensure sufficient rate of decrease of function value in a given direction by considering the intersection of the acceptable step length for Armijo [109] and Wolfe conditions. Then, the step length  $\alpha_k$  must satisfy the following two inequalities:

$$f(x_k + \alpha_k d_k) \leq f(x_k) + \delta \alpha_k g_k^T d_k \quad 5-12$$

$$|g(x_k + \alpha_k d_k)^T d_k| \leq -\sigma g_k^T d_k \quad 5-13$$

Where  $0 < \delta \leq \sigma < 1$

According to these conditions, we need to solve a one-dimensional optimization problem in  $\alpha_k$  at each iteration for fixed  $x_k$  and  $d_k$ . This problem is always computationally expensive. Indeed, Wolfe inequalities provide an efficient way to determine the acceptable range of  $\alpha_k$  to ensure a sufficient decrease of the function value.

Motivated by the success of the scaled conjugate gradient method family (SCGM) [110-112] introduced by Birgin and Martinez [111], a modified method is presented in this paper. The following section describes the SCGM and the novelty of the proposed method. The validation of the cited methods is individually detailed in deep by the former authors [110-112].

This paper presents an algorithm that utilizes the conjugate gradient method for optimizing nonlinear functions. The algorithm employs a mixture of three different conjugate gradient coefficients to achieve a quicker and seamless convergence. The paper mainly focuses on an adaptive numerical approach for selecting the optimal conjugate gradient coefficient. The coefficient is determined based on the combination of two factors: (i) the Wolfe inexact line search conditions and (ii) the behavior of the optimization algorithm during runtime. The selection of the optimal coefficient is highly dependent on the specific conditions and the problem being solved at each iteration. Therefore, determining the best choice for a particular problem requires several numerical experiments using previously published conjugate gradient coefficients (LS, CD, DY, etc.).

### 5.3 Modified SCGM

In order to minimize the number of iterations and maximize the rate of decrease of the function value in a given direction, the Wolfe inexact line search direction is utilized. Conjugate gradient coefficients proposed by [104-107] ( $\beta_k^{PR}$ ,  $\beta_k^{LS}$ ,  $\beta_k^{CD}$ ,  $\beta_k^{DY}$ ) have finite convergence properties for quadratic objective functions. However, these methods will have different behaviour, especially for non-quadratic functions under the inexact line search.

In this study, we employ the  $\delta$  and  $\sigma$  parameters in the basic CG algorithm to select the most efficient gradient coefficient, which ensures fast and stable convergence. We modify the

algorithm's approach to choosing the efficient coefficient by considering the following cases:  $\beta_k^{LS}$ ,  $\beta_k^{CD}$ ,  $\beta_k^{DY}$ . A new CG coefficient  $\beta_k^{MF}$  will be calculated at each iteration according to cases mentioned above. The main objective of this study is to bring the conjugate directions  $\{d_k, d_{k+1}\}$  closer to zero at each iteration, thereby facilitating the optimization process. To achieve this objective, we propose a new formula for the conjugate gradient coefficient, which considers the following cases:

$$\beta_k^{MF} = \begin{cases} (a) & 0, & \frac{d_{k-1}^T g_k}{d_{k-1}^T g_{k-1}} \leq \sigma \\ (b) & \max \left\{ 0, \min \{ \beta_k^{LS}, \beta_k^{CD} \} \right\}, & \sigma < \frac{d_{k-1}^T g_k}{d_{k-1}^T g_{k-1}} \\ (c) & \delta \frac{\|g_k\|^2}{d_{k-1}^T g_k}, & \frac{d_{k-1}^T g_k}{d_{k-1}^T (g_k - g_{k-1})} \geq \delta \end{cases} \quad 5-14$$

The special case of  $\beta_k^{MF} = 0$  leads to the steepest descent method {Nocedal, 1999 #220}.

The modified algorithm is given as follows:

**Step 1:** Data  $x_1 \in \mathbb{R}^n$ ;  $\epsilon \geq 0$ ; set  $d_1 = -g_1$ ; if  $\|g_1\| \leq \epsilon$ ; then STOP

**Step 2:** Compute  $\alpha_k$  by the Wolfe line search conditions (5-12) and (5-13)

**Step 3:** Let  $x_{k+1} = x_k + \alpha_k d_k$ ;  $g_{k+1} = g(x_{k+1})$ ; if  $\|g_{k+1}\| \leq \epsilon$ ; then STOP

**Step 4:** Compute  $\beta_{k+1}^{MF}$  by (5-14), and generate  $d_{k+1}$  by (5-5)

**Step 5:** Set  $k=k+1$ , go to Step 2

#### 5.4 Results and discussion

In order to measure the stability and accuracy of the proposed optimization algorithm, some objective functions must have been studied. If we focus on N-dimensional quadratic functions, they converge in a maximum of N iterations using conjugate gradient method. Otherwise, the conjugate gradient method needs more investigation for the general functions (non-convex, nonlinear, multivariate, with multiple local minimums). Current numerical experiments were performed on a series of popular nonlinear unconstrained functions with at least first derivatives available.

The proposed conjugate gradient algorithm results are compared to PR, DY, CD and LS methods under Wolfe line search conditions. The implementation of the algorithm is done with the following parameters:  $\delta=0.01$ ,  $\sigma=0.6$ ;  $\|g\| = \epsilon \leq 10^{-6}$  (stopping criteria);  $N=5000$  (maximum iteration number). Codes are written in MATLAB R2022a edition, with double precision and run on a PC with Windows 10 operating system, Intel core 3.60 GHz i7-4790 CPU processor and 32.0 GB of RAM.

As shown in figure 49, and figure 51, the convergence was obtained for most of the programmed cases. However, the behaviour of the proposed algorithm for some cases is found to be different.

As expected, the chosen value of initial step length,  $\alpha_1$ , is very important to ensure convergence. As shown in figure 49b, increasing  $\alpha_1$  from 1.4 to 1.6 causes strong convergence instability. When  $\alpha_1=1.6$  the algorithm leads to an arbitrary path to finally converge to a local minimum. This behavior occurs because, at the boundary between two local minimums, Wolfe line search conditions ignore saddle points. Step length and programming parameters can be set to a specific value once a desired local minimum has been identified to avoid multiple jumps between local minimums. This approach effectively stabilizes the optimization process.

According to the numerical results, it can be seen that the step length and iteration number are very similar at the beginning of the iterations. Numerical results of two selected test functions with respect to the CD, DY and LS methods are reported in Table 14, to show the effectiveness of the proposed algorithm.

#### 5.4.1 Ackley's function

This function is characterized by a nearly flat outer region, and a large hole at the center. For several optimization algorithms, this function poses a main risk of being trapped in one of its many local minima, as shown in Figure 48.

$$f(x) = -20 \exp \left[ -\frac{1}{5} \sqrt{\frac{1}{n} \sum_{i=1}^n x_i^2} \right] - \exp \left[ -\frac{1}{n} \sum_{i=1}^n \cos(2\pi x_i) \right] + 20 + e \quad 5-15$$

Where  $n$  is the dimension (1, 2, ...); and  $x = (x_1, \dots, x_n)^T$ . This function has a global minimum  $f^* = 0$  at  $x^* = (0, \dots, 0)$ .

In its two-dimensional form ( $n=2$ ), Ackley's function can be written as:

$$f(x)_{n=2} = -20 \exp\left[-0.2\sqrt{0.5(x^2 + y^2)}\right] - \exp[-0.5 \cos(2\pi x) + \cos(2\pi y)] + 20 + e \quad 5-16$$

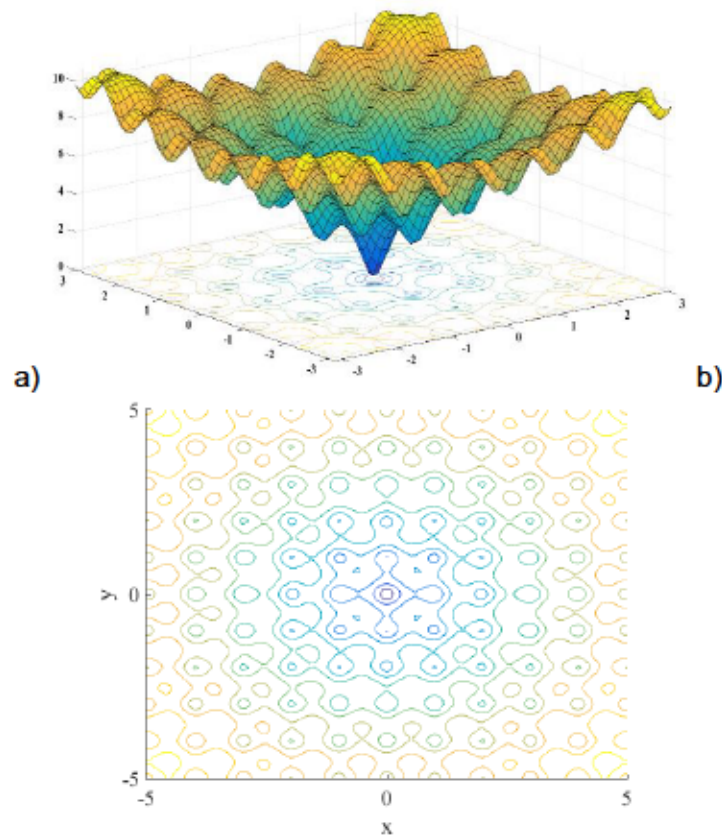


**Figure 48**  
Ackley test function. a) 3D view, b) 2D view.

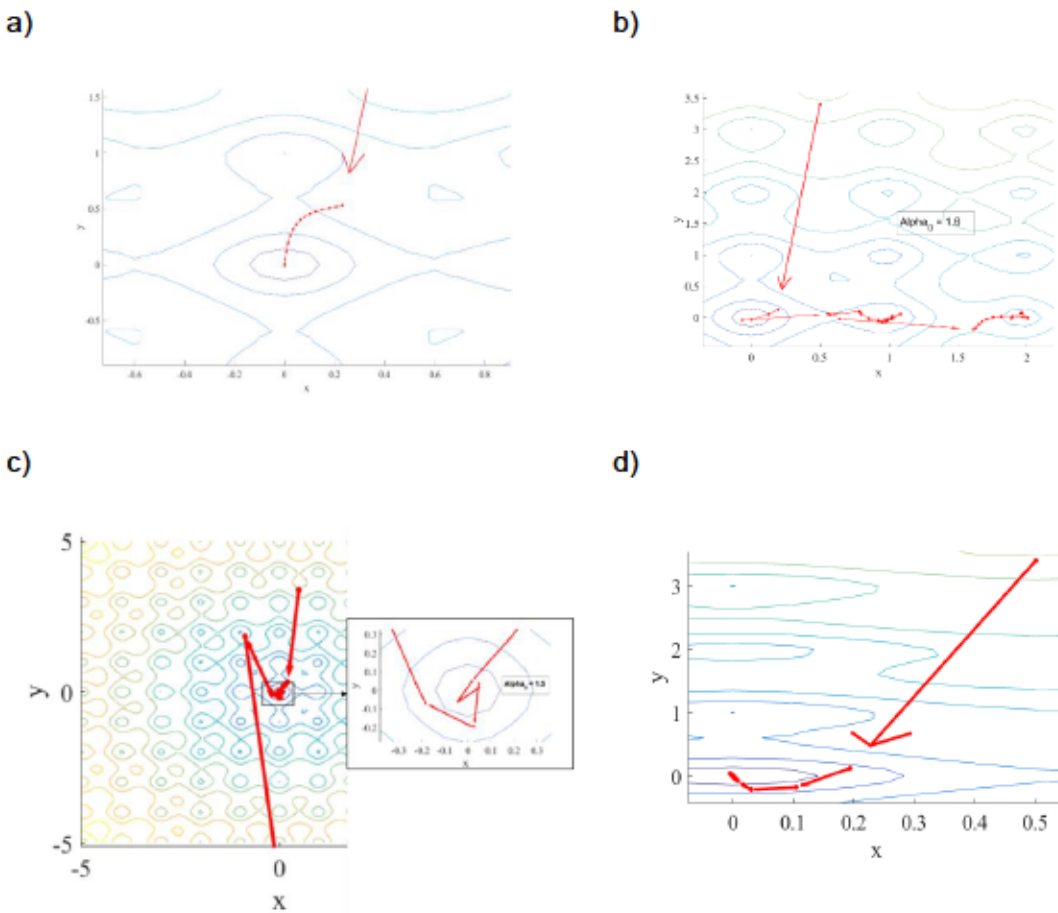


**Figure 49**  
**Ackley test function iterations paths for  $x_1 = (0.1, 0.1)$ .**  
**a)  $\beta = \beta_k^{MF}$ , b)  $\beta = \beta_k^{CD}$ , c)  $\beta = \beta_k^{DV}$ , d)  $\beta = \beta_k^{LS}$**

### 5.5 Beale test function

The Beale function is multimodal, with sharp peaks at the corners of the input domain (Figure 50), which is defined from the general Beale function as follows:

$$f(x) = [1.5 - x_1(1 - x_2)]^2 + [2.25 - x_1(1 - x_2^2)]^2 + [2.625 - x_1(1 - x_2^3)]^2, \quad x_1 = (1,1)^T \quad 5-17$$

This function is also used as a test function to evaluate the performance of optimization algorithms.

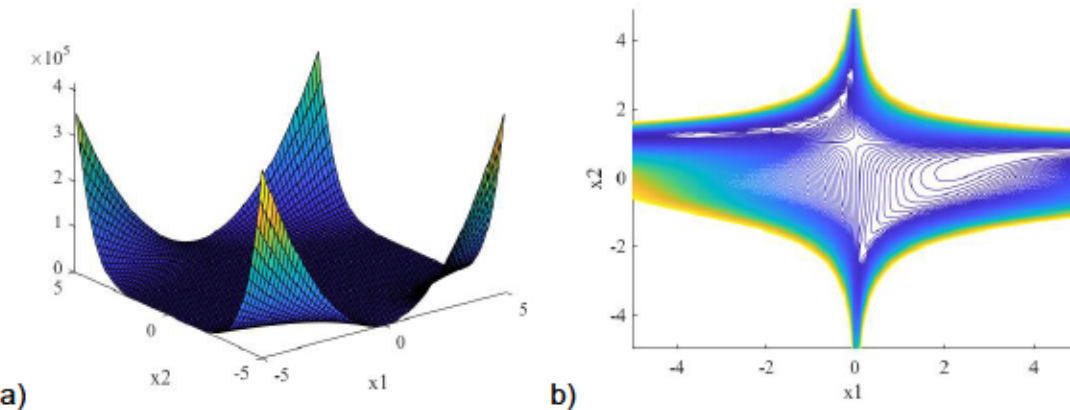


**Figure 50**  
Beale test Function a) 3D view, b) 2D view

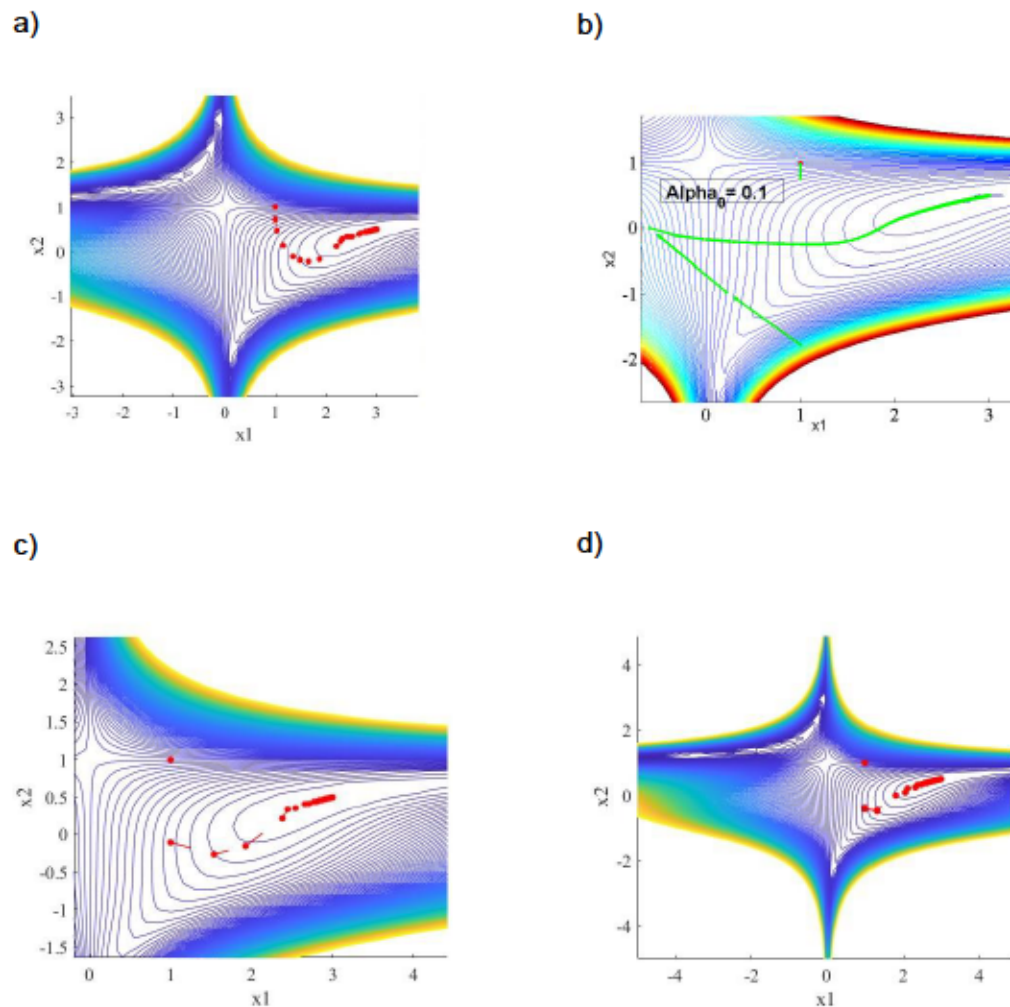


**Figure 51**  
Beale function iterations paths for  $x_1 = (1, 1)$ . a)  $\beta = \beta_k^{MF}$ , b)  $\beta = \beta_k^{CD}$ , c)  $\beta = \beta_k^{DV}$ , d)  $\beta = \beta_k^{LS}$

For further investigation, the initial point is chosen as (1, 0.8) for applying all CG coefficients. Results show that the proposed approach follows a better trend and converges faster than the others in lower ranges of  $\sigma$ . Figure 52 show the comparison of the numerical results of Beale test function for different CG coefficients and the proposed algorithm for the initial point of (1, 0.8).

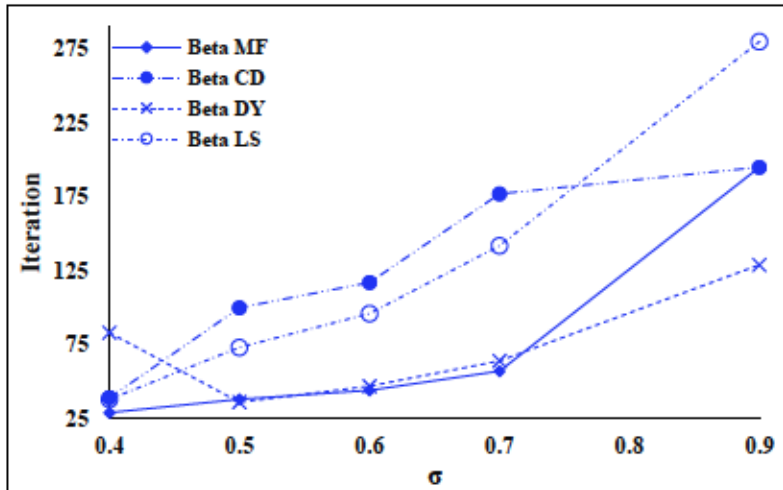


**Figure 52**  
Comparison of the numerical results of Beale test function for different CG coefficients and the proposed algorithm for the initial point of (1, 0.8).

**Table 14**  
Convergence speed comparison for Basic CG methods

Test function	CG coefficient	$N_{\text{iter}}$
Ackley	$\beta = \beta_k^{MF}$	26
	$\beta = \beta_k^{CD}$	226
	$\beta = \beta_k^{DY}$	42
	$\beta = \beta_k^{LS}$	35
Beale	$\beta = \beta_k^{MF}$	32
	$\beta = \beta_k^{CD}$	87
	$\beta = \beta_k^{DY}$	36
	$\beta = \beta_k^{LS}$	92

We observed that the Conjugate Descent (CD) conjugate coefficient is less stable when compared to the other cases. Therefore, we use the Polak and Ribiere (PR) coefficient to compare the performance of different coefficients. Table 15 presents the numerical results of the proposed CG coefficient  $\beta_k^{MF}$  and Liu and Storey (LS), Polak and Ribiere (PR), and Dai and Yuan (DY) conjugate coefficients. Numerical comparisons are listed in the form of  $N_{\text{iter}}$ ,  $F_{\text{eval}}$ , where  $N_{\text{iter}}$  and  $F_{\text{eval}}$  are the number of iterations, and function evaluations, respectively. Our proposed algorithm outperforms the other coefficients in various convergence cases [113, 114]. Specifically, the MF

method exhibits smooth convergence in most cases, surpassing the performance of PR, DY, and LS conjugate gradient coefficients.

**Table 15**

**The performance of MF, PR, DY and LS methods according to unconstrained test functions.**

Test Function	MF		LS		DY		PR	
	N <sub>iter</sub>	F <sub>eval</sub>						
<b>Booth</b>	61	1.69E-13	61	1.57E-13	61	1.57E-13	61	1.57E-13
<b>Beale</b>	32	9.04E-13	36	9.00E-13	92	7.02E-12	-	Inf
<b>CrossInTray</b>	23	-2.06261	23	-2.06261	23	-2.06261	23	-2.06261
<b>DropWave</b>	23	-1	23	-0.93625	22	-0.93625	22	-0.93625
<b>Easom</b>	20	-1	20	-1	20	-1	20	-1
<b>Griewank</b>	26	6.69E-13	27	7.54E-13	27	7.54E-13	27	7.54E-13
<b>Himmel blau</b>	27	1.25E-14	41	9.30E-15	41	9.30E-15	41	9.30E-15
<b>Holder Table</b>	31	-19.20	27	-19.2085	27	-19.2085	27	-19.2085
<b>LeviN13</b>	127	1.67E-13	-	Inf	-	-	-	Inf
<b>McCormick</b>	30	-1.91	33	-1.91322	33	-1.91322	33	-1.91322
<b>Rastrigin</b>	24	0	27	0	12	0	12	0
<b>SchafferN1</b>	15	1.09E-10	15	1.08E-10	15	1.08E-10	15	1.08E-10
<b>SchafferN3</b>	26	9.27E-14	26	8.85E-14	26	8.85E-14	26	8.85E-14
<b>Sphere</b>	28	1.92E-13	28	2.17E-13	28	2.17E-13	28	2.17E-13
<b>Three Hump Camel</b>	47	2.66E-13	51	2.99E-01	51	2.55E-13	36	1.65E-13
<b>Matyas</b>	71	8.49E-12	52	5.77E-12	52	5.77E-12	49	1.19E-11
<b>Trid</b>	31	-2	37	-2	37	-2	37	-2
<b>Branin</b>	47	0.3980	48	0.397887	48	0.397887	48	0.397887
<b>Schwefel</b>	31	-418.983	31	-418.983	31	-418.983	31	-418.983
<b>Six hump camel</b>	30	-1.03163	33	-1.03163	31	-1.03163	33	-1.03163
<b>Rosenbrock</b>	82	7.65E-07	296	9.9773e-07	73	9.4668e-07	-	Inf

When comparing the basic conjugate gradient coefficient methods, it is evident that the proposed coefficient ( $\beta_k^{MF}$ ) exhibits the best average performance among the other methods. Therefore, we will use the MF method as the base to evaluate efficiency. Specifically, we will collect the number of iterations required to achieve convergence for each problem using the four methods. Then, we will define the ratio of the total iterations for the PR, LS, and DY methods with respect to the number of iterations of the MF method as follows:

$$R_i = \frac{N_{Tot}(i)}{N_{Tot}(MF)} \quad 5-18$$

Where  $R_i$  denote the relative efficiency of a selected CG method (DY/LS/PR), while  $N_{Tot(i)}$  and  $N_{Tot(MF)}$ , represent the total number of iterations required for the selected method and the MF method to converge, respectively.

**Table 16**  
**Relative efficiency of CG methods**

MF	LS	DY	PR
1.00	1.37	1.06	1.13

Table 16 shows the relative efficiency of the four mentioned CG methods. A value of  $R_{(MF)} = 1$  serves as the base of comparison, indicating the performance of the MF method. However, the CD method is excluded from this comparison due to its instability. The DY method exhibits faster convergence than the LS and PR methods among the remaining basic CG methods. However, it may suffer from divergence for certain difficult functions. On the other hand, the MF method performs well even in such challenging cases, showcasing its robustness and efficiency.

### 5.6 Conclusion

This paper proposes an efficient algorithm to optimize nonlinear functions using the conjugate gradient method. A combination of three conjugate gradient coefficients is used to ensure faster and smooth convergence. The following conclusions can be drawn regarding the numerical implementation and particular convergence cases:

- Step length is calculated at each iteration using Wolfe inexact line search.
- Results show that the choice of  $\delta$  and  $\sigma$  coefficients was significant. Furthermore, optimum accuracy and iteration number depend strongly on the value of these coefficients.
- The proposed conjugate gradient coefficient method ( $\beta_{MF}$ ) demonstrates better average performance compared to other basic methods, and the MF method is used as the base to evaluate efficiency. The relative efficiency ( $R_i$ ) of selected CG methods (DY/LS/PR) is determined by calculating the ratio of total iterations required for convergence with respect to the MF method.
- The DY method has faster convergence than the LS and PR methods, but it may experience divergence for difficult functions. In contrast, the MF method exhibits robustness and efficiency even in challenging cases.

- The MF method is much more efficient and stable than basic classic methods, which rely on a single conjugate gradient coefficient.
- Numerical demonstrations show the global convergence of the proposed algorithm under specific conditions.

Overall, the proposed algorithm with  $\beta_{MF}$  conjugate gradient coefficient shows superior performance and robustness compared to other basic methods, which can be attributed to the use of three conjugate gradient coefficients and the optimization of the  $\delta$  and  $\sigma$  values.

## 6. AERODYNAMIC SHAPE OPTIMIZATION OF NACA AIRFOILS BASED ON A NOVEL UNCONSTRAINED CONJUGATE GRADIENT ALGORITHM

*Cet article est rédigé par Seyyed Mojtaba Fakhari et Hatem Mrad a été publié dans la revue Journal of Engineering Research en 2023.*

### 6.1 Résumé

Les profils aérodynamiques sont essentiels pour maximiser l'efficacité des turbomachines. La configuration idéale du profil est conçue pour générer une portance significative tout en minimisant la traînée, tout en respectant des contraintes structurelles spécifiques. Cette étude propose un algorithme innovant basé sur des techniques de gradient conjugué non contraint pour optimiser la forme aérodynamique des profils. Les profils NACA4412 et NACA2415 sont examinés en détail. La méthode de paramétrisation Bézier est utilisée pour définir les variables de conception. L'optimisation est réalisée à l'aide d'un code MATLAB et du solveur de flux basé sur la méthode des panneaux XFOIL pour atteindre les résultats aérodynamiques souhaités. Le processus d'optimisation a amélioré les performances aérodynamiques en augmentant le rapport portance/traînée et en réduisant l'angle d'attaque pour obtenir le rapport portance/traînée maximum. Une augmentation de 13,7 % des performances pour le profil NACA 4412 et de 32 % pour le profil NACA 2415 a été réalisée. Les comparaisons avec les méthodes traditionnelles ont démontré l'efficacité et la robustesse de l'algorithme proposé.

**Mots-clés :** méthode du gradient conjugué non contraint, optimisation, profils NACA, paramétrisation Bézier

### *Abstract*

Airfoils are key factors in maximizing the efficiency of turbomachinery. The ideal configuration of the airfoil is engineered to produce significant lift while minimizing drag, all while adhering to specific structural limitations. In this investigation, an innovative algorithm based on unconstrained conjugate gradient techniques to optimize the aerodynamic shape of airfoils is proposed. NACA4412 and NACA2415 airfoils are chosen to be investigated in detail. Bézier parameterisation method is employed to define the design variables. Optimization is conducted utilizing a MATLAB code and the XFOIL panel method-based flow solver to attain the desired aerodynamic outcomes. The optimization process enhanced aerodynamic performance by increasing the lift-to-drag ratio and decreasing the angle of attack for maximum lift-to-drag ratio.

An increase of 13.7% in performance for the NACA 4412 airfoil and 32% for the NACA 2415 airfoil was achieved. Comparisons with traditional methods demonstrated the efficiency and robustness of the proposed algorithm.

**Keywords:** unconstrained conjugate gradient method, optimization, NACA airfoils, Bézier parameterisation

## 6.2 Introduction

Aircraft aerodynamics heavily relies on airfoil design for reducing drag and enhancing efficiency. Traditionally, wind tunnels have been crucial for this process. Achieving high lift-to-drag ( $C_l/C_d$ ) ratios is vital in applications such as wind turbine blades, where various constraints must be considered. Optimization involves minimizing or maximizing quantities while meeting specified constraints. This field has evolved since the seventeenth century, with significant advancements driven by mathematical theory and algorithm design. Increasingly powerful computing has led to widespread optimization applications across disciplines such as economic studies and managements [115, 116]. Classification of problems based on properties helps define scope. However this optimization must be studied in case of Fluid Structure Interaction analysis to investigate the structural [89] and aeroelastic behavior of the airfoil [83, 117].

<b>Nomenclature</b>			
$J_{n,i}(t)$	Bernstein function	$L$	lift force
$B_t$	Bézier polygon's vertices	$D$	drag force
$H$	Hessian	$S$	airfoil area
$\alpha_k$	CG step length	$Re$	Reynold's number
$\beta_k$	CG coefficient	$Ma$	Mach number

Although initial efforts relied on a basic steepest descent approach [118, 119], the intricate non-linearity present in both aerodynamic objective and constraint functions has spurred the preference for second-order optimization techniques. This inclination stems from the necessity to account for curvature inherent in the design space. Notably, methods such as conjugate gradient and quasi-Newton algorithms have garnered favor due to their ability to incorporate considerations of design space curvature without requiring direct evaluation of the Hessian matrix. In a recent study, the conjugate gradient method is employed for aerodynamic optimization of a benchmark problem [120]. Kishida et al. proposed a developed method based on the concept of Newton's method [121, 122]. Optimization problems in image processing, such as image reconstruction,

denoising, and segmentation, often employ unconstrained conjugate gradient methods to minimize energy or cost functions associated with these tasks [123, 124], on the other hand, in finance, conjugate gradient methods are used in portfolio optimization, option pricing, and risk management to find optimal investment strategies and manage financial risks effectively [125]. Optimization problems in engineering design, such as structural optimization, control system design, and parameter estimation, frequently utilize unconstrained conjugate gradient methods to optimize design parameters and improve system performance [126].

Hager et al. proposed a new Conjugate Gradient method incorporating a novel line search technique, referred to as L-BFGS. They conducted extensive numerical comparisons between the proposed method and traditional Conjugate Gradient (CG) methods using unconstrained optimization problems and approximate Wolfe conditions. The results demonstrated the efficiency and robustness of the new method. However, traditional CG methods continue to exhibit superior efficiency in certain scenarios. [127]. Liu J.K et al. introduced a novel approach called the spectral conjugate gradient method for addressing unconstrained optimization problems. In this method, the conjugate parameter and the spectral parameter adhere to a specific relationship. Importantly, the search direction ensures sufficient descent without needing to restart the process per iteration. Unlike some other methods, this feature remains consistent regardless of any line searches. The authors also establish the global convergence of their method under standard Wolfe line searches, provided that a certain condition regarding the conjugate gradient coefficient is met. [128]. Later Mrad H. and Fakhari S.M. proposed a novel conjugate gradient method introducing a novel gradient coefficient to solve the unconstrained optimization problems employing the Wolfe inexact line search conditions to determine the optimum step length at each iteration and choose the appropriate conjugate gradient coefficient accordingly. The results indicate that the algorithm is highly stable, regardless of the starting point, and has better convergence rates and efficiency compared to classical methods in certain cases [129]. The drag minimization is a common objective function as a single-point optimization; therefore, it can lead to non-robust solutions [130, 131]. Other studies are carried out about multi objective applications of optimization approaches [132] which can cause a high CFD evaluation cost depending on the number of design variables.

Sederberg et al. introduced a free-form deformation method for solid geometric models, compatible with any solid modeling system like CSG or B-rep. It can deform various surface primitives, both globally and locally, while preserving volume. Local deformations can maintain desired derivative continuity. The method uses trivariate Bernstein polynomials for intuitive design effects [133]. The PARSEC parameterization method, introduced by Sobieczky, is tailored for

airfoil shapes, allowing for the expression of a diverse range of shapes without reliance on a baseline shape. This feature enhances its effectiveness in airfoil optimization tasks [134]. Sripathakul et al. conducted a comparison of five different techniques for airfoil shape parameterization, including Ferguson's curves, Hicks-Henne bump functions, B-Splines, PARSEC, and Class/Shape function transformation. The evaluation criteria included Parsimony, Intuitiveness, Orthogonality, Completeness, and Flawlessness characteristics to assess the effectiveness of these parameterization techniques [135]. In another study Bézier-PARSEC parameterization method is employed along with neural networks for better results. Mukesh et al. introduced the PARSEC geometry representation method to describe general airfoil shapes using twelve parameters and utilized a Genetic Algorithm to optimize aerodynamic characteristics. They developed a MATLAB program integrating PARSEC, Panel Technique, and Genetic Algorithm, tested it on a NACA 2411 airfoil, and validated the optimized airfoil using wind tunnel data, showing an improved lift coefficient compared to the original [136]. Della Vecchia et al. employed PARSEC shape parameterisation method in conjunction with genetic algorithm for airfoil optimization [137]. Salunke et al. investigated the combination of Bézier curves and PARSEC methods [138]. Rajnarayan et al. investigated the efficiency of B-Spline methods and showed that the parameterisation using different approximation methods are higher order Bézier curves [139]. Lu et al. proposed a novel parameterization method called the IGP method. They showed comparative aerodynamic performance results between the fitted airfoils and original airfoil shapes [140]. Bézier curve shape parameterisation method and radial basis function interpolation is used by Yang et al. for aerodynamic optimization employing genetic algorithm [141]. Hansen proposed an optimization method in which the class-shape-transformation technique is utilised for airfoil parameterisation and the derivative-free Covariance Matrix Adaptation Evolution Strategy is used in combination with an adaptive penalty function to find the optimal point. The XFOIL flow solver is employed to perform the analysis [142]. Later another study is carried out using the B-Spline shape parameterization method. Hybrid evolutionary-adaptive directional local search method is used employing XFOIL and a two-dimensional RANS solver for airfoil multi-objective optimization purpose [143]. Ümütlu et al. investigated an airfoil optimization using Bézier curves and genetic algorithms. The research shows an enhancement in lift coefficient value which is validated using XFOIL and Ansys fluent [144]. On the other hand, surrogate methods demonstrate impressive efficiency, precision, and robustness in high-dimensional spaces compared to CFD solutions or direct calculations [145]. Examples of these applications include the multi-fidelity deep neural network (MFDNN) model [145], Convolutional Neural Network (CNN) [146] and Multivariate Adaptive Regression Splines (MARS) based methods. The Multivariate Adaptive Regression

Splines method is a non-parametric regression technique that models complex, non-linear relationships by fitting piecewise linear splines to data. It automatically selects and combines the most relevant input variables to create an accurate predictive model [147]. Access to extensive datasets from experimental or simulation results enables the use of advanced Spline-based surrogate methods. Innovations such as Conic Multivariate Adaptive Regression Splines (CMARS), SMARS, SCMARS and GPLM offer enhanced time efficiency in data mining. These methods employ a penalized residual sum of squares and mapping techniques to improve performance and efficiency, achieving superior accuracy, complexity, stability, and robustness compared to existing methods [148-150]. Additionally, the RCMARS technique further contributes to robustness in these applications [151]. Integrating MARS with Global Response Surface (GRS) and Move-Limit Strategy (MLS) represents a novel engineering approach, advancing structural design optimization [152].

While surrogate models offer computational efficiency, they require extensive datasets for training and validation, which can be resource-intensive to generate. Conversely, in optimization cases with a manageable number of iterations, using computational methods like XFOIL can provide accurate and reliable performance evaluations without the extensive data requirements of surrogate models. This approach simplifies the setup process and maintains acceptable computational times, making it a practical choice for direct and precise optimization. The main objective of this study is to apply the unconstrained conjugate-gradient optimization method combined with Wolf inexact line search conditions, employing a new approach to compute the conjugate gradient coefficient  $\beta^{MF}$ , which is introduced in a recent publication by the authors [129]. This novel coefficient significantly improves the convergence properties of the optimization algorithm, making it more efficient and robust compared to traditional methods. By introducing this advanced coefficient, we achieve a higher degree of precision and flexibility in defining airfoil geometry. Bézier parameterization technique is utilized, ensuring a smooth and aerodynamically optimal airfoil profile. This innovation not only enhances the efficiency and accuracy of airfoil design but also provides a substantial theoretical advancement in optimization methods, offering new perspectives on achieving optimal solutions in aerodynamic design problems.

In this study, MATLAB R2023a is employed for conducting both parameterization and optimization procedures, leveraging its computational capabilities to handle complex calculations efficiently. Additionally, the XFOIL 6.99 solver is used for flow analysis, providing accurate aerodynamic performance predictions. This combination of state-of-the-art tools and methodologies not only streamlines the optimization process but also ensures the reliability of the results.

In this study, the Bézier airfoil parameterization method is employed to define the design variables. The selected parameterization technique utilises six control points. Among these points, two are anchored at the airfoil's origin and tip, while the remaining control points are adjusted to define the optimized airfoil profile.

### *6.3 Airfoil shape parameterization*

Airfoil shape parameterization is a pivotal aspect of aerodynamic design, involving the representation of an airfoil's geometry in a mathematical form. It enables efficient manipulation and optimization of the airfoil's shape to enhance its performance characteristics. Various techniques, such as FFD [133], Spline-Based Methods [153], PARSEC [154] and Bézier methods [153, 155], are commonly employed for parameterizing airfoil shapes, providing a versatile framework for aerodynamic optimization studies. Free-Form Deformation (FFD) is highly flexible and allows extensive deformation of the airfoil shape, but this can lead to a high-dimensional design space, complicating optimization. FFD offers global shape control, yet it lacks the precise local control of Bézier curves, making fine-tuning challenging [133]. Polynomial-based methods like PARSEC provide a compact representation with polynomial coefficients, capable of capturing a wide range of shapes but struggling with complex geometries. These methods offer global shape control, but adjustments to one coefficient can have widespread effects, reducing local control compared to Bézier parameterization. Splines, including B-splines and NURBS, offer high flexibility and can model very complex shapes with smooth transitions, but managing a large number of control points can become complex and computationally intensive. Compact Airfoil Parameterization (CAP) methods reduce the number of parameters needed, maintaining flexibility but potentially sacrificing detail in highly intricate shapes [153]. CAP provides a balance between global and local control but may not offer the same intuitive local control as Bézier curves. In conclusion, Bézier airfoil parameterization stands out for its combination of smoothness, local control, simplicity, and computational efficiency, making it particularly well-suited for precise and efficient aerodynamic optimization tasks.

#### *6.3.1 Bézier curve*

In this study, the airfoil shape is defined using Bézier curves. The point cloud for the airfoil shape is chosen to calculate the Bézier curves to perform the aerodynamic performance analysis. A parametric Bézier curve can be defined as follows [153]:

$$P(t) = \sum_{i=0}^n B_i J_{n,i}(t), \quad 0 \leq t \leq 1, \quad 6-1$$

$$J_{n,i}(t) = \binom{n}{i} t^i (1-t)^{n-i}, \quad 6-2$$

$$\binom{n}{i} = \frac{n!}{i! (n-i)!}, \quad 6-3$$

where  $B_i$  is the Bézier polygon's vertices,  $J_{n,i}(t)$  is the Bernstein function and  $n$  is the degree of Bernstein basis function.

$$\sum_{i=0}^n J_{n,i}(t) = 1. \quad 6-4$$

As shown in Figure 53, the Bézier parameterization is basically combination of two curves corresponding the upper and lower surface of the airfoil.

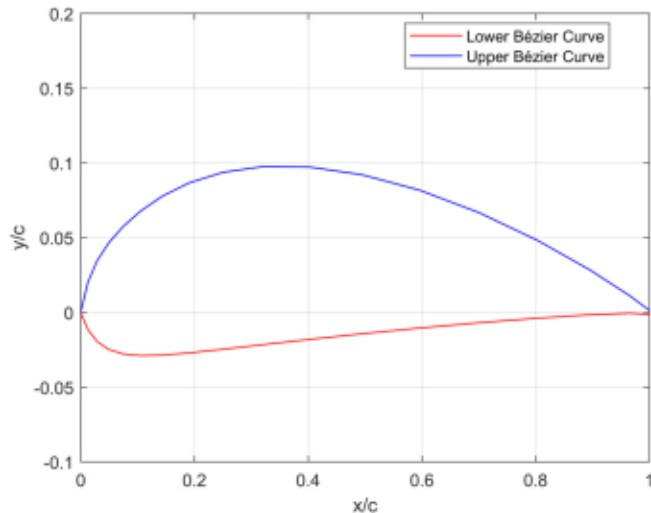


**Figure 53**  
**Bézier airfoil presentation.**

To ensure the uniformity and continuity of the curves in the junction points, one must consider the first and second derivatives of the Bézier curves.

$$P'(t) = \sum_{i=0}^n B_i J'_{n,i}(t), \quad 6-5$$

$$P''(t) = \sum_{i=0}^n B_i J''_{n,i}(t), \quad 6-6$$

where derivatives of the basis function could be expressed as follows:

$$J'_{n,i}(t) = \frac{(i - nt)}{t(1-t)} J_{n,i}(t). \quad 6-7$$

$$J''_{n,i}(t) = \frac{(i - nt)^2 - (nt)^2 - i(1 - 2t)}{t^2(1-t)^2} J_{n,i}(t). \quad 6-8$$

#### 6.4 Airfoil optimization technique

The main goal of this study is to implement a developed unconstrained spectral conjugate-gradient optimization algorithm [129] for the sake of airfoil aerodynamic shape optimization. To be able to employ the gradient-based optimization algorithm, the direct optimization method is chosen. For this purpose, an original airfoil shape is chosen to initialize the algorithm. The airfoil shape is parameterized using the Bézier curves employing a set of control points, the XFOIL solver is used to calculate the drag coefficient. The objective function in this study is chosen to be the minimization of the drag coefficient  $C_d$ . Once the initialization is done, the optimizer will search for new control points and XFOIL will be called via MATLAB code, and the loop will continue until either the minimization criteria or the maximum iteration is reached. Figure 54 illustrates the outlines and steps of the optimization approach.

#### 6.5 Flow analysis

XFOIL open-source solver code written in Fortran is employed to perform the flow analysis around the airfoil. XFOIL (V6.99) is an interactive program created by Drela and Youngren at the Massachusetts Institute of Technology [156]. A panel method solver combined with an integral boundary layer formulation. XFOIL operates primarily in the subsonic flow regime and is capable of predicting the lift, drag, and moment coefficients for isolated airfoils. The low computational cost and precision level of XFOIL analysis results are promising, which makes it a great option in this study. For a given airfoil profile, XFOIL will calculate the resulting lift and drag coefficients in different angles of attack and Reynolds numbers. In the case of the NACA 4412 airfoil, when considering a fixed  $C_l = 1$  value, the  $C_l/C_d$  ratio is slightly overestimated. Specifically, the  $C_l/C_d$  value for the actual airfoil is reported as 107.5 at  $6^\circ$ , while XFOIL predicts it to be 108.4, resulting

in a difference of less than 1%. The solver is called from MATLAB code to calculate the drag coefficient  $C_d$  to use it as the minimization objective function [157].

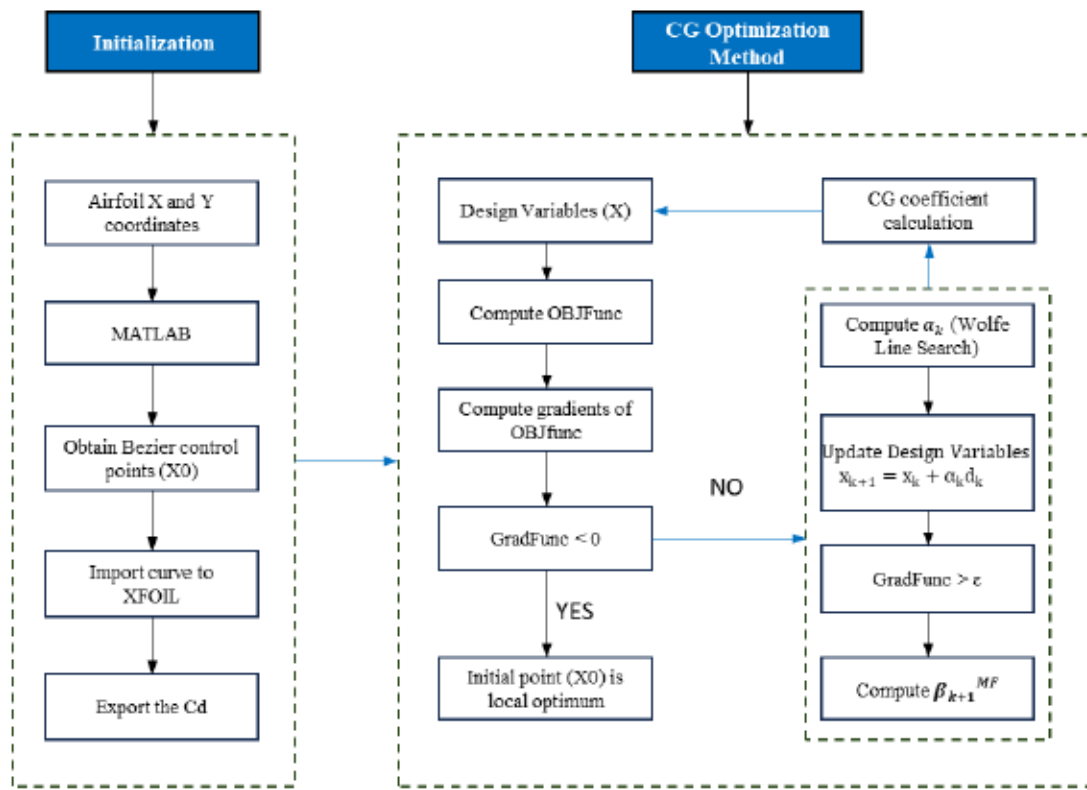


**Figure 54**  
Proposed Unconstrained CG optimization procedure.

### 6.6 Optimization methods

While the standard conjugate gradient method is efficient, it may lack the rapid and robust convergence exhibited by the spectral variant, especially when dealing with intricate geometries and highly nonlinear objective functions [158], on the other hand, despite its simplicity, gradient descent often suffers from slow convergence and sensitivity to step size selection, making it less suitable for high-dimensional and nonlinear optimization tasks compared to spectral conjugate gradient methods [159]. Offering rapid convergence via second-order derivative information, Newton's method can be computationally demanding due to the necessity of computing and inverting the Hessian matrix. In contrast, the spectral conjugate gradient method strikes a balance by approximating the Hessian without the need for its full computation. Although efficient and robust, quasi-Newton methods typically demand more memory and computational resources for maintaining and updating the Hessian approximation. The spectral conjugate gradient method presents a more memory-efficient alternative [160].

The spectral conjugate gradient method emerges as a comprehensive optimization approach for airfoil design, offering rapid convergence, computational efficiency, robustness, and scalability. These attributes position it as a superior choice for aerodynamic optimization compared to standard conjugate gradient, gradient descent, Newton's method, and quasi-Newton methods.

### 6.6.1 Conjugate gradient

General expression of unconstrained minimization of  $F(x)$  objective as a function of a design vector  $x$  can be illustrated as:

$$\min_{x \in R^N} F(x) \quad 6-9$$

where  $x$  is the vector of design variables and  $x^*$  is the optimal solution. For all  $x \neq x^*$ , if  $F(x^*) < F(x)$ , then  $x^*$  is an optimizer. Assuming that the first and second derivatives of the  $F(x)$  exist, the unconstrained local minimizer  $x^*$  exists if:

$$g(x^*) = 0, \quad 6-10$$

$$d^T H(x^*) d > 0, \quad \forall d \in R^N \quad 6-11$$

Here  $g = \nabla_x F$ ,  $H$  is the Hessian, and  $d$  is a vector in the same space as  $x$ . the strict second order condition guarantees the positive Hessian to exclude the saddle points.

General gradient-based algorithms start from initial point  $x_0$  and iterate to solve the unconstrained non-linear problem.

$$x_{k+1} = x_k + \alpha_k d_k, \quad k = 1, 2, \dots \quad 6-12$$

where each direction  $d_k$  is determined by:

$$d_k = \begin{cases} -g_k, & \text{if } k = 1, \\ -g_k + \beta_k d_{k-1}, & \text{if } k \geq 2. \end{cases} \quad 6-13$$

The conjugate gradient method commonly adopts the Wolfe inexact line search conditions [161] to calculate the  $\alpha_k$ , which prioritize the adequate reduction of function value along a specified direction. These conditions ensure a suitable rate of decrease by intersecting the acceptable step length criteria defined by the Armijo [162] and Wolfe conditions. Consequently, the step length  $\alpha_k$  must adhere to the following set of inequalities:

$$f(x_k + \alpha_k d_k) \leq f(x_k) + \delta \alpha_k g_k^T d_k \quad 6-14$$

$$|g(x_k + \alpha_k d_k)^T d_k| \leq -\sigma g_k^T d_k. \quad 6-15$$

With  $0 < \delta \leq \sigma < 1$ , the task involves resolving a one-dimensional optimization problem for  $\alpha_k$  at each iteration, with  $x_k$  and  $d_k$  held constant. This process is inherently computationally intensive. However, leveraging the Wolfe inequalities offers an effective means to identify the acceptable range of  $\alpha_k$ , guaranteeing a significant reduction in function value.

Calculation of conjugate gradient coefficient  $\beta_k$  was proposed by Polak-Ribiere (PR) [163], Liu and Storey (LS) [164], Conjugate Descent (CD) [165], and Dai and Yuan (DY) [107], respectively.

$$\beta_k^{PR} = \frac{g_k^T (g_k - g_{k-1})}{\|g_{k-1}\|^2}. \quad 6-16$$

$$\beta_k^{LS} = -\frac{g_k^T (g_k - g_{k-1})}{d_{k-1}^T g_{k-1}} = -\frac{g_k^T y_{k-1}}{d_{k-1}^T g_{k-1}}. \quad 6-17$$

$$\beta_k^{CD} = -\frac{\|g_k\|^2}{d_{k-1}^T g_{k-1}}. \quad 6-18$$

$$\beta_k^{DY} = \frac{\|g_k\|^2}{d_{k-1}^T y_{k-1}}. \quad 6-19$$

Here  $y_{k-1} = (g_k - g_{k-1})$  and  $\|\cdot\|$  denote the gradient change and the Euclidean norm, respectively.

### 6.6.2 Modified spectral conjugate gradient method

The modified spectral conjugate gradient method (SCGM) proposes a new calculation method for  $\beta_k$ . The main purpose of the  $\beta^{MF}$  [129] is to bring the conjugate direction closer to zero in order to facilitate the optimization process. The  $\beta^{MF}$  calculation process is summarized as follows:

$$\beta_k^{MF} = \begin{cases} a: 0, & \text{if } \frac{d_{k-1}^T g_k}{d_{k-1}^T g_{k-1}} \leq \sigma, \\ b: \max \left\{ 0, \min \left\{ \beta_k^{LS}, \beta_k^{CD} \right\} \right\}, & \text{if } \sigma < \frac{d_{k-1}^T g_k}{d_{k-1}^T g_{k-1}}, \\ c: \delta \frac{\|g_k\|^2}{d_{k-1}^T g_k}, & \text{if } \frac{d_{k-1}^T g_k}{d_{k-1}^T (g_k - g_{k-1})} \geq \delta. \end{cases} \quad 6-20$$

The special case of  $\beta_k^{MF} = 0$  leads to the steepest descent method [158].

Thus, the modified algorithm for the proposed conjugate gradient optimization method can be expressed as:

**1. Initialize:**

- Set  $x_1 \in R^N$ ;  $\epsilon \geq 0$ .
- Compute  $d_1 = -g_1$ .
- If  $\|g_1\| \leq \epsilon$ , STOP.

**2. Compute Step Size ( $\alpha_k$ ):**

- Wolf line search conditions

$$f(x_k + \alpha_k d_k) \leq f(x_k) + \delta \alpha_k g_k^T d_k,$$

$$|g(x_k + \alpha_k d_k)^T d_k| \leq -\sigma g_k^T d_k.$$

**3. Update Design Variable Vector and Evaluate Gradient:**

- Update design variables:  $x_{k+1} = x_k + \alpha_k d_k$ .
- Compute the gradient:  $g_{k+1} = g(x_{k+1})$ .
- If  $\|g_{k+1}\| \leq \epsilon$ , STOP.

**4. Compute Conjugate Gradient Coefficient ( $\beta_{k+1}^{MF}$ ):**

- Calculate  $\beta_{k+1}^{MF}$  using (6-20).

- Generate  $d_{k+1}$  using (6-13).

**5. Update Iteration Count:**

- Set  $k=k+1$ .
- Proceed to Step 2.

**6. Repeat:**

- Continue iterations until convergence criteria are met.

Conjugate Gradient methods such as CD, PR, DY, LS, and FR are known for their strong convergence properties; however, they can occasionally experience performance issues due to jamming. Therefore, combining these methods can leverage the strengths of each, potentially enhancing overall performance and robustness [166, 167]. The proposed hybrid method combines various techniques that have been studied for global convergence by previous researchers. The convergence study is established based on the following assumptions, and the corresponding lemmas and theorems are proved [168-171].

**Assumption A:** the objective function  $f(x)$  is continuously differentiable and has a lower bound on the level set  $L_1 = \{x \in R^n / f(x) \leq f(x_1)\}$ , where  $x_1$  is the starting point.

**Assumption B:** the gradient  $g(x)$  of  $f(x)$  is Lipschitz continuous in a neighbourhood  $U$  of  $L_1$ , that is, there exists a constant  $L > 0$ , such that  $\|g(x) - g(y)\| \leq L\|x - y\|$ ,  $\forall x, y \in U$ .

**Lemma 1:** Let  $\{x_k\}$  and  $\{d_k\}$  be generated by (6-12) and (6-13), where  $\beta_k$  is computed by (6-20),  $\alpha_k$  satisfies Wolfe line search conditions, if  $g_k \neq 0$  for all  $k \geq 1$ , then  $g_k^T d_k < 0$ .

**Lemma 2:** Suppose assumptions A and B hold. If the conjugate gradient method satisfies  $g_k^T d_k < 0$ , for all  $k \geq 1$  and  $\alpha_k$  satisfies the Wolfe line search, then the following Zoutendijk condition holds [153]:

$$\sum_{k=1}^{+\infty} \frac{(g_k^T d_k)^2}{\|d_k\|^2} < +\infty. \quad 6-21$$

**Theorem:** suppose that assumptions (A) and (B) hold. Consider Algorithm and  $\alpha_k$  satisfies the Wolfe line search if  $g_k \neq 0$  holds for any  $k$ , then the method is globally converged if:

$$\liminf_{k \rightarrow \infty} \|g_k\| = 0. \quad (22)$$

### 6.6.3 Aerodynamic functions and gradients

Standard single point drag minimization is used for aerodynamic investigations. General form of the drag minimization problem can be illustrated as follows:

$$\min_{x \in R^N} C_d \quad 6-22$$

The non-linear aerodynamic constraint  $C_L = C_L^0$ . Central difference method is used to calculate the sensitivities, implementing the difference of two perturbed states:

$$\frac{dF}{dx_i} \approx \frac{F(x + r\varepsilon) - F(x - r\varepsilon)}{2r}, \quad 6-23$$

where  $r$  is the step size and  $\varepsilon$  is the unit vector aligned with the  $i^{\text{th}}$  dimension.

### 6.7 Flow analysis

In this study, a dimensionless study is performed. The lift  $C_l$  and drag  $C_d$  coefficients are used to evaluate the airfoil aerodynamic performance in a defined Reynold's number  $Re$ :

$$C_l = \frac{2L}{\rho v^2 S'} \quad 6-24$$

$$C_d = \frac{2D}{\rho v^2 S'}. \quad 6-25$$

Here  $L$ ,  $D$ , and  $S$  are the lift force, drag force and airfoil area, respectively [144]. Reynolds Averaged Navier Stokes (RANS) equations are employed to solve for lift and drag coefficients [172]:

*Conservation of mass:*

$$\nabla \cdot u = 0. \quad 6-26$$

*Conservation of momentum:*

$$\rho \frac{D\mathbf{u}}{Dt} = -\nabla P + \mu \nabla^2 \mathbf{u} + \rho \mathbf{F}, \quad 6-27$$

where  $\mathbf{u}$ ,  $-\nabla P + \mu \nabla^2 \mathbf{u}$ , and  $\rho \mathbf{F}$ , represent the velocity vector, internal and external forces, respectively.

Increasing angle of attack (AOA) results in an increase in both lift and induced drag, up to a point. In a certain angle of attack, the airflow across the upper surface of the airfoil becomes detached resulting in a loss of lift known as Stall. A detailed explanation of the fluid flow governing equations is provided in Section 2.1.

### 6.8 Results and discussion

In this study, the NACA 4412 airfoil is selected as the primary focus for applying the optimization algorithm. However, several other airfoils are examined as initial points for validation purposes such as NACA2415, NACA0010, NACA4418 and NACA1408. The key shape specifications for the NACA 4412 airfoil include a maximum thickness of 12% at 30% chord and a maximum camber of 4% at 40% chord.

The airfoil coordinates are extracted from the database and imported to a MATLAB code to calculate the Bézier control points. A set of six control points are chosen for both upper and lower curves of the airfoil geometry. For original NACA 4412, the control points are given in Table 17.

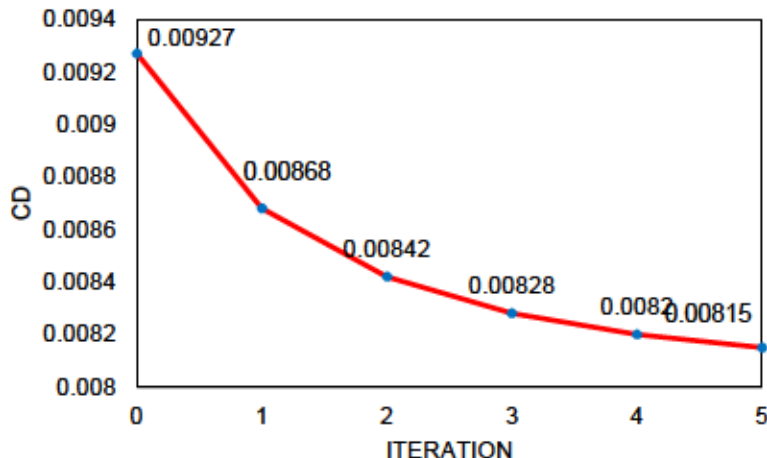
The lift coefficient serves as an aerodynamic constraint  $C_l = 1$ , guiding the algorithm in searching for design variables that minimize the drag coefficient, thereby maximizing the  $C_l/C_d$  ratio. The Reynolds number is consistently maintained at  $5 \times 10^5$  across all cases. The optimization process commences from the initial control point and iterates until reaching convergence criteria or the maximum iteration limit.

**Table 17**  
Original NACA 4412 Bézier control points.

	(x, y) Upper Curve	(x, y) Lower Curve
<b>1</b>	(1, 0.001300),	(1, -0.001300)
<b>2</b>	(0.965594, 0.013843),	(0.965594, 0.004929)
<b>3</b>	(0.158481, 0.233907),	(0.158481, -0.022575)
<b>4</b>	(0.147439, 0.025456),	(0.147439, -0.031099)
<b>5</b>	(0.034116, 0.082329),	(0.034116, -0.045739)
<b>6</b>	(0, 0),	(0, 0)

$\delta$  is the parameter associated with the Armijo condition, which ensures a sufficient decrease in the objective function value along the search direction. It defines the minimum acceptable decrease in the objective function value relative to the decrease predicted by the linear approximation of the function.  $\sigma$  is the parameter associated with the curvature condition, which ensures that the gradient of the objective function does not become too negative. It defines the maximum allowable angle between the search direction and the negative gradient direction. Together, these parameters help guide the optimization algorithm to ensure that it converges to a suitable solution while balancing the trade-off between sufficient decrease in the objective function value and the avoidance of excessive curvature in the optimization path. Adjustment of the  $\delta$  and  $\sigma$  parameters varies the Wolfe search conditions, enabling fine-tuning of the algorithm, with additional adjustments made to the initial step size. The evolution of the minimization of objective function is drag coefficient is shown in

Figure 55. Alternatively, when the optimizer reaches the stage of determining  $X_{k+1}$  from Eq. (6-12) and Eq. (6-13), using equations (6-20), it selects the optimal conjugate gradient coefficient  $\beta_k^{MF}$  to facilitate swifter and more accurate convergence.

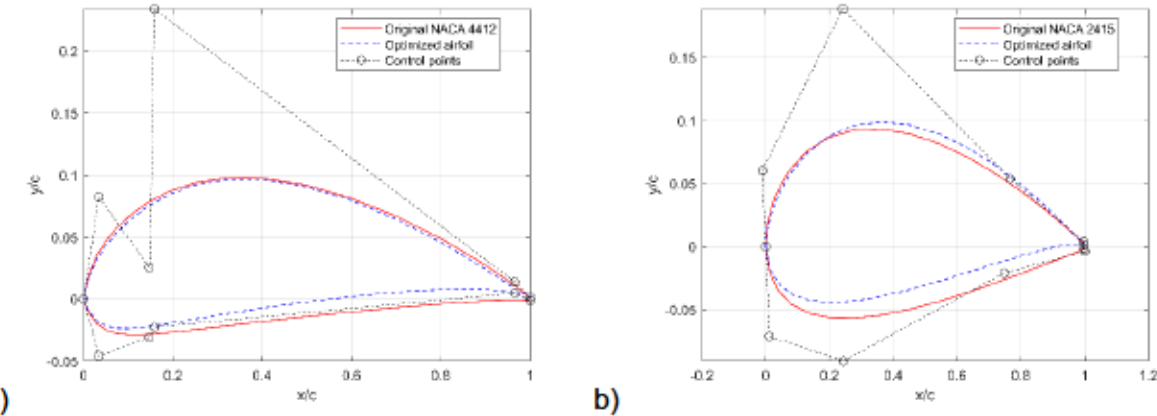


**Figure 55**  
Drag coefficient minimization per iteration.

Table 18 shows the Bézier control points for the optimized airfoil. Figure 56 shows the airfoil profiles for the NACA 4412 and the optimized airfoil. The solid red lines depict the original NACA 4412 profile, while the dashed blue lines illustrate the optimized airfoil profile. A noticeable reduction in the maximum thickness of the airfoil profile and a shift in camber are apparent in the optimized version. These alterations are intended to enhance the  $C_l/C_d$  ratio.

**Table 18**  
Optimized airfoil control points.

	(x, y) Upper Curve	(x, y) Lower Curve
<b>1</b>	(1, 0.001300),	(1, -0.001300)
<b>2</b>	(0.965594, 0.001361),	(0.965594, 0.029674)
<b>3</b>	(0.158481, 0.247523),	(0.158481, -0.013369)
<b>4</b>	(0.147439, 0.016394),	(0.147439, -0.025458)
<b>5</b>	(0.034116, 0.076107),	(0.034116, -0.041085)
<b>6</b>	(0, 0),	(0, 0)

**Figure 56**

a) NACA 4412 original and Optimized airfoil profiles with Bezier control points, b) NACA 2415 original and Optimized airfoil profiles with Bezier control points.

As outlined in the preceding section, with the lift coefficient  $C_l$  set to 1, the objective of the algorithm is to minimize the drag coefficient  $C_d$ . Initially, the drag coefficient corresponding to  $C_l = 1$  is computed as  $C_d = 0.00927$  using XFOIL, resulting in a ratio of  $C_l/C_d = 107.87$ . Post-optimization, the minimized drag coefficient is found to be  $C_d = 0.00815$ , resulting in an improved ratio of  $C_l/C_d = 122.7$ , reflecting a 13.7% enhancement. These optimization outcomes are summarized in Table 19 for the angle of attack (AOA) sequences. The last column of the table shows the differences between the original airfoil and optimized airfoil flow analysis.

**Table 19**

Lift and drag coefficients for NACA 4412 and optimized airfoil in different AOA.

AOA	$C_l$ original	$C_d$ original	$C_l$ optimized	$C_d$ optimized	$C_l / C_d$ original	$C_l / C_d$ optimized	Difference %
-5°	-0.0731	0.01107	0.0350	0.00960	-6.60	3.65	155
-3°	0.1456	0.00916	0.2572	0.00875	15.89	29.38	85
-1°	0.3646	0.00821	0.4833	0.00800	44.39	60.4	36
1°	0.5897	0.00712	0.6869	0.00691	82.8	99.39	20
3°	0.7992	0.00827	0.8873	0.00735	96.68	119.78	24
5°	1.0099	0.00957	1.0938	0.00936	105.53	116.91	11

Figure 57 illustrates variations in the lift coefficient and  $C_l/C_d$  ratio across a range of AOA values spanning from -10° to 20°. The results indicate an enhanced aerodynamic performance of the airfoil overall. Notably, a decrease in the lift coefficient is observed near stall as the AOA

approaches  $15^\circ$ . This decline may be attributed to single-point optimization, as the proposed method operates without constraints and lacks topological constraints.

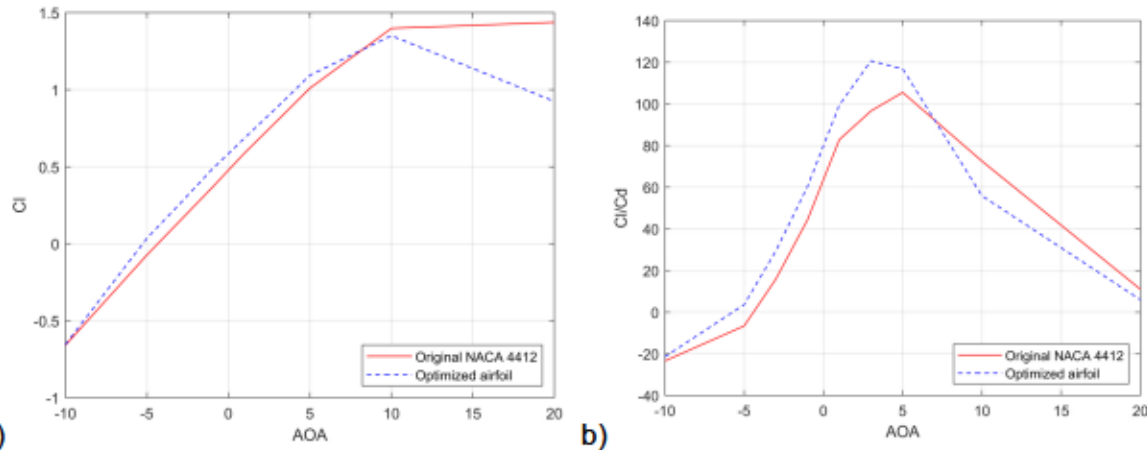


**Figure 57**  
a) Lift coefficient in sequences of AOA for NACA 4412 and Optimized airfoil, b)  $C_l/C_d$  ratio in sequence of AOA for NACA 4412 and Optimized airfoil.

In a similar optimization scenario, instead of computing  $\beta_k^{MF}$ , the Steepest Descent method is employed with  $\beta_k = 0$ , while  $\beta_k^{LS}$  and  $\beta_k^{CD}$  are defined in separate algorithmic approaches. The results (Figure 58) demonstrate no more than 8.4% improvement in the minimum within 12 iterations.

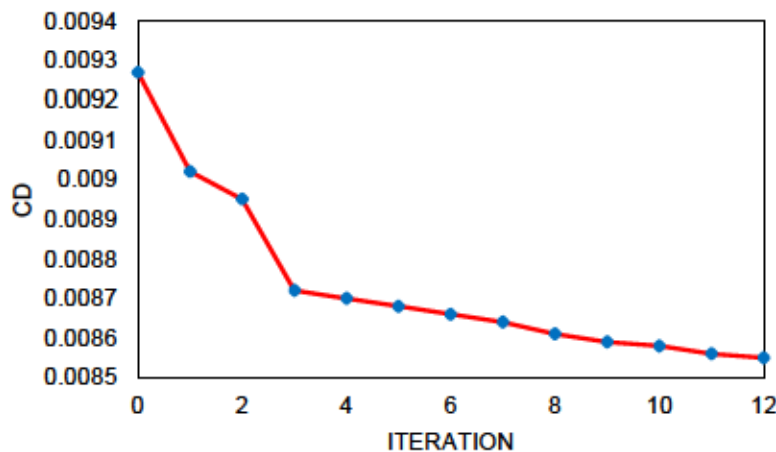


**Figure 58**  
Drag coefficient minimization using Steepest Descent method.

Further analyses are conducted on the NACA2415 airfoil under the same application conditions. The maximum  $C_l/C_d$  for this airfoil is reported in AOA of  $5.75^\circ$  as 87.1, while XFOIL predicts the  $C_l/C_d$  ratio 88.21 which is slightly over predicted Figure 59-a. the optimization sequence is then

applied and the results show that in AOA of  $5.75^\circ$  the  $C_l/C_d$  is increased about 22% Figure 59-b. However, after the optimization is applied, the peak  $C_l/C_d$  ratio takes place in  $5.15^\circ$  of angle of attack, which represents an increase of 32% of its performance. Table 20 shows the optimization results for the NACA2415 airfoil profile.

**Table 20**  
Cl/Cd ratios for NACA 2415 and optimized airfoil in different AOA.

AOA	$C_l/C_d$ original NACA2415	$C_l/C_d$ optimized airfoil	Difference %
-5°	-28.47	0.99	103
-3°	-9.54	31.75	433
-1°	16.45	67.41	310
0°	30.85	83.45	170
1°	44.42	96	116
3°	66.8	109.1	63
5°	86.37	114.52	32
7°	87.34	96.18	10
10°	72.35	49.79	-31

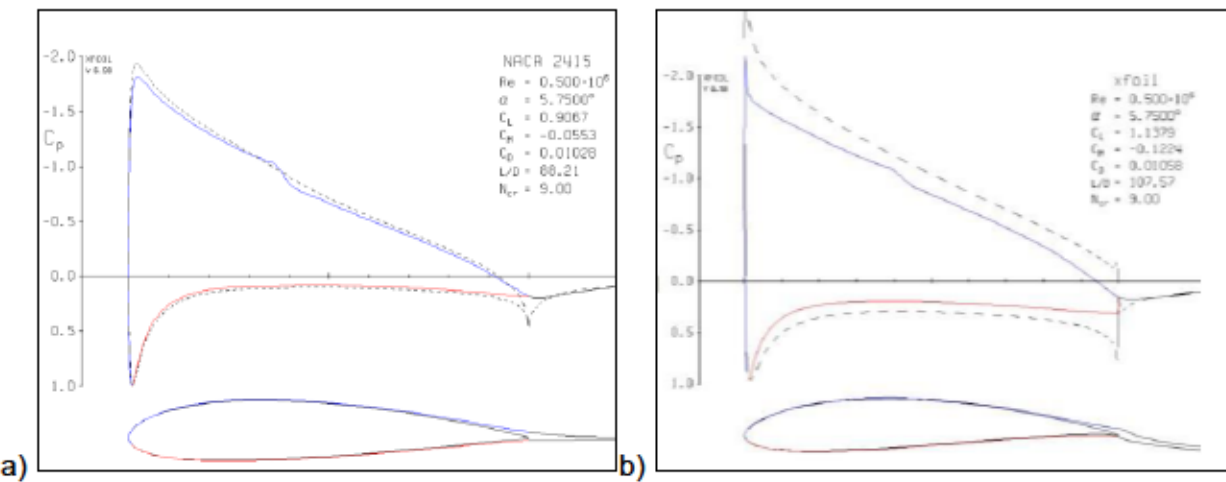


**Figure 59**  
a) Xfoil CI/Cd prediction in  $5.75^\circ$  for NACA2415 b) Optimized airfoil CI/Cd prediction.

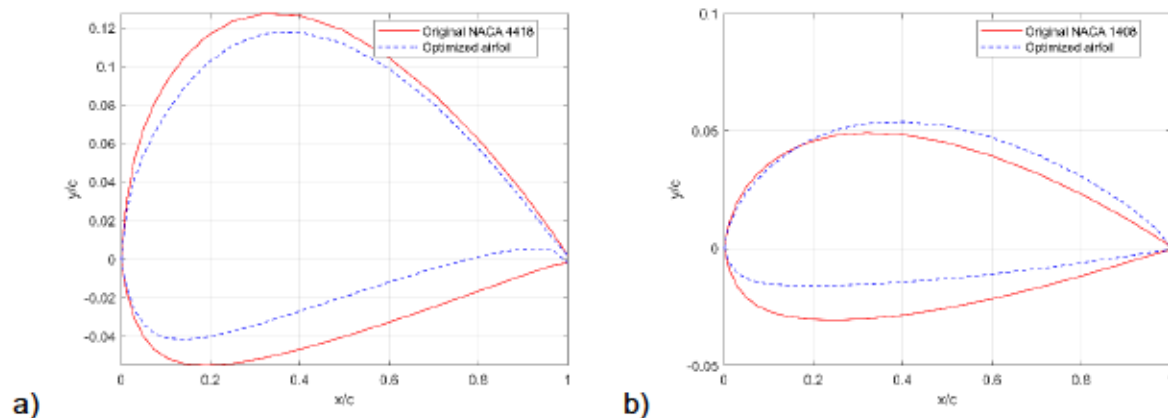


**Figure 60**  
a) Original NACA4418 profile vs optimized profile, b) Original NACA1408 profile vs optimized profile.

**Table 21**  
Optimization results for different types of NACA airfoils.

Airfoil	Original $C_L/C_d$	Optimized $C_L/C_d$	Iterations	Difference %	Original AOA	Optimized AOA
NACA4412	107.87	122.7	5	14	6	4
NACA2415	87.1	115.42	5	32	5.75	5.15
NACA0010	55.2	68.24	6	24	4.25	4.15
NACA4418	93.3	119.59	10	28	6.5	5.02
NACA1408	66.6	97.90	9	47	3.25	2.75

Optimization was applied to various NACA airfoils, leading to notable improvements in their aerodynamic performance. Each optimized airfoil exhibited a higher  $C_l/C_d$  and a reduced angle of attack for maximum efficiency. This demonstrates the method's effectiveness in enhancing performance characteristics and robustness across different airfoil designs (Figure 60), making it a versatile tool for aerodynamic optimization. Aircraft frequently operate at or near lower AOAs, and better performance in this range improves handling and stability, which are crucial for safety and comfort. Additionally, a 32% increase in the  $C_l/C_d$  ratio represents a substantial improvement in aerodynamic efficiency, allowing the airfoil to generate more lift for a given amount of drag (Table 21). This leads to reduced fuel consumption and extended range for aircraft, enhancing overall performance by enabling them to fly further and faster with less energy.

To investigate the efficiency of the proposed unconstrained conjugate gradient method with the novel  $\beta_k^{MF}$  coefficient, an analysis was conducted using different coefficients, as shown in Table 22. The analysis focused on the NACA 1408 airfoil.

**Table 22**  
**Optimization results comparison using different conjugate coefficients.**

	<b>Steepest Decent</b>	$\beta_k^{LS}$	$\beta_k^{DY}$	$\beta_k^{PR}$	$\beta_k^{MF}$
<b>Optimized <math>C_l/C_d</math></b>	91.31	88.13	94.44	96.02	97.9
<b>Difference %</b>	37.1	32.33	41.8	44.17	47
<b>Iterations</b>	11	18	14	8	9

The results indicate that the Beta MF coefficient achieves the highest optimized  $C_l/C_d$  ratio of 97.9, with a 47% improvement, and requires 9 iterations, highlighting its superior efficiency compared to other coefficients.

### 6.9 Conclusion

The main goal of this research is to investigate an aerodynamic shape optimization process, to utilize the unconstrained conjugate-gradient optimization method in conjunction with Wolf inexact line search conditions, implementing a novel approach for computing the conjugate gradient coefficient  $\beta_k^{MF}$ .

NACA 4412 and NACA 2415 airfoils are used as starting points for the optimizer. Bézier curves serve as the parameterization method for airfoil shapes, facilitated by a MATLAB code developed to import airfoil points and export Bézier control points. Subsequently, the XFOIL flow solver is

invoked to compute the drag coefficient  $C_d$ , the objective function targeted for minimization. Employing an unconstrained conjugate gradient method, the optimization algorithm maintains the lift coefficient  $C_l$  fixed while minimizing  $C_d$ . Wolfe line search conditions are utilized to determine the step length, with the conjugate gradient coefficient guided by a proposed algorithm to select the optimal performance. The optimization process significantly improves the performance of NACA 4412 and NACA 2415 airfoils. Single-point optimization yields enhancements of 13.7% and 32%, respectively. XFOIL simulations on the optimized airfoil at varying angles of attack demonstrate a maximum 155% and 432% improvement in  $C_l/C_d$  for NACA 4412 and NACA 2415 airfoils, respectively, at varying angles of attack. Compared to traditional methods, the new optimization algorithm utilizing the novel conjugate coefficient achieves these improvements more efficiently. This methodology is applicable to a wider range of airfoil shapes, providing an efficient starting point for optimization. To validate its robustness, the method was tested on various airfoils, confirming its reliability and effectiveness.

In all case studies, the optimization process results in a reduction of the angle of attack at which the maximum lift-to-drag ratio is achieved, while simultaneously achieving a significant increase in the  $C_l/C_d$  ratio itself. This means that after optimization, the airfoil reaches its peak aerodynamic efficiency at a lower AOA. The increase in the  $C_l/C_d$  ratio indicates that the airfoil is now capable of generating more lift for a given amount of drag. This enhancement implies a more efficient aerodynamic performance, as the aircraft can achieve better lift characteristics without the need to increase the AOA, thereby reducing the overall drag. The decrease in the optimal AOA for maximum  $C_l/C_d$  ratio also suggests that the optimized airfoil is better suited for conditions where lower AOAs are prevalent, such as in cruising flight, leading to improved fuel efficiency and reduced structural stress on the airframe.

The Bézier airfoil parameterization method, while flexible, is limited to six control points. This constraint may not capture highly complex airfoil geometries accurately, potentially leading to suboptimal designs for highly specialized applications. On the other hand, while the method is tailored for airfoil optimization, its generalization to other aerodynamic shapes may require significant adjustments to the parameterization and optimization processes.

To further improve the efficiency of the optimization algorithm, the integration of adjoint methods could significantly reduce differentiation time. Additionally, exploring a multi-objective optimization approach could yield more precise optimization results. Moreover, optimizing the 3D shape of the airfoil and conducting experimental validation in the future are necessary steps. Future works

could also employ surrogate methods, to create accurate and computationally efficient models that predict the airfoil performance. This would allow for rapid evaluations of design alternatives, thereby avoiding extensive calculations and improving optimization speed. Utilizing experimental or CFD results datasets to train these surrogate models could enhance their accuracy and robustness, ensuring reliable predictions. Furthermore, incorporating machine learning techniques to dynamically refine the surrogate models during the optimization process could lead to even better performance.

## 7. ENHANCED AERODYNAMIC AND STRUCTURAL DESIGN THROUGH INTEGRATED OPTIMIZATION OF TWISTED CHINOOK-TYPE BLADES FOR AXIAL-FLOW FANS

*Cet article est rédigé par Seyyed Mojtaba Fakhari et Hatem Mrad est sous la révision.*

### 7.1 Résumé

La ventilation efficace des mines est cruciale pour garantir des conditions de travail sûres, minimiser la consommation d'énergie et améliorer la performance opérationnelle globale. Cette étude se concentre sur l'amélioration de l'efficacité aérodynamique et structurelle des ventilateurs axiaux utilisés dans la ventilation des mines en optimisant la conception des pales de type Chinook torsadées. Un nouveau profil d'aile est proposé pour la pale Chinook, développé à l'aide d'un nouvel algorithme d'optimisation qui atteint une augmentation de 14,4 % du rapport portance-trainée. Cette amélioration aérodynamique conduit à une augmentation globale des performances du ventilateur. De plus, des modifications structurelles au niveau de l'emplanture de la pale ont été mises en œuvre pour prolonger la durée de vie en fatigue, notamment en conditions de décrochage, améliorant ainsi la fiabilité à long terme du ventilateur. Les résultats de l'optimisation structurelle indiquent une augmentation d'environ 40 % du facteur de sécurité en fatigue de la pale. Ces optimisations aérodynamiques et structurelles combinées représentent une avancée significative dans la conception de ventilateurs de ventilation haute performance pour les applications minières.

**Mots-clés :** Ventilation minière, Optimisation de profil d'aile, Durée de vie en fatigue, Optimisation structurelle, Condition de décrochage

### *Abstract*

Efficient mine ventilation is critical for ensuring safe working conditions, minimizing energy consumption, and enhancing overall operational performance. This study focuses on improving the aerodynamic and structural efficiency of axial-flow fans used in mine ventilation by optimizing the twisted Chinook-type blade design. A new airfoil profile is proposed for the Chinook blade, developed using a novel optimization algorithm that achieves a 14.4% increase in lift-to-drag ratio. This aerodynamic improvement leads to an overall increase in fan performance. Additionally, structural modifications at the blade root were implemented to enhance fatigue life, particularly under stall conditions, thus improving the long-term reliability of the fan. The structural optimization results indicate an increase of approximately 40% in fatigue safety factor of the fan blade. These

combined aerodynamic and structural optimizations demonstrate a significant step forward in the design of high-performance ventilation fans for mining applications.

**Keywords:** Mine ventilation, Airfoil optimization, Fatigue life, Structural optimization, Stall condition

## 7.2 *Introduction*

Rotating blades are critical components in turbomachinery and have been the focus of extensive research over the past several decades. Various blade designs, each with unique characteristics, are employed depending on the specific operational requirements and performance goals of the machinery. Researchers have explored diverse blade configurations to optimize aerodynamic efficiency, structural integrity, and durability, ensuring that they meet the stringent demands of applications in industries such as energy, aerospace, and ventilation [173]. Axial flow fans, on the other hand, play a vital role in a range of critical applications, including mine ventilation, construction, and biomedical environments. Their ability to efficiently move large volumes of air makes them indispensable in scenarios requiring reliable airflow management, where performance, safety, and precision are of paramount importance [172].

Researchers employ a variety of optimization approaches to enhance fan performance. In a recent study, Chen et al. applied the Taguchi quality loss function for multi-response optimization of bionic fan characteristics, using parameters such as blade number, boss ratio, and blade stagger angle. This method resulted in significant improvements in mass flow rate and A-weighted sound pressure level (SPL), demonstrating the effectiveness of these adjustments in optimizing fan efficiency and acoustic performance [174].

An optimized airfoil series was used by Wu, to design blades for an axial fan, with the chord length and installation angle optimized through orthogonal optimization. Among three blade designs (straight, C-type, and forward-swept), the forward-swept blade showed the highest efficiency under design conditions, while both forward-swept and C-type blades performed better than straight blades under off-design conditions [175]. Fakhari et al. proposed design of experiments for the sake of optimization of the compressor rotor 67 employing computational fluid dynamics and fluid-structure interaction based on published experimental data [83]. Later on, they proposed a design optimization approach for an axial-flow mine ventilation fan considering the parameters such as blade number, angle of attack, tip gap, rotational velocity and the hub-tip ratio. They demonstrated more efficient operation conditions by combination of the optimized parameters. The stall condition was studied and the structural analysis showed the possibility of fatigue failure

in the blade-root intersection [172]. Amankawa et al. presented a multi-objective optimization strategy for turbomachinery blade design using sparse active subspaces, specifically applied to a turbofan stage. The approach combines sparse polynomial chaos expansion with active subspace techniques to build a surrogate model, which is then optimized using a multi-objective genetic algorithm [176]. Among the efficient optimization techniques, conjugate gradient-based methods like spectral and hybrid CG methods have been recently developed by researchers [111, 113]. In recent research, Mrad et al. introduced a novel unconstrained conjugate gradient optimization algorithm that integrates Wolf line search conditions, utilizing a new method for calculating the conjugate gradient coefficient. This approach demonstrates rapid convergence and robust performance [129]. Additionally, they applied the algorithm to optimize the NACA airfoil profile, successfully enhancing the lift-to-drag ratio by minimizing the drag coefficient. The results indicate a significant improvement in the aerodynamic performance of the airfoils. [177]. Conversely, structural failures in components can lead to failures in the entire rotating system, prompting researchers to investigate the underlying causes of these failures. In a study conducted by Liu et al., stress concentration was identified as a primary factor in crack initiation [178]. This study performed failure analysis and design optimization of a shrouded blade in a transonic fan. In a similar research work, authors studied the crack initiation at the critical region of the blade and revealed that the stress concentration affects the fatigue life cycle of the rotating blade in stall condition [89].

This study presents the industrial application of a novel optimization algorithm, focusing on enhancing the overall performance and safety of axial-flow fans. By addressing the critical issue of stall, the algorithm not only aims to improve operational efficiency but also contributes to the longevity and reliability of the fan system. This dual focus on performance enhancement and safety makes the approach particularly relevant in the context of increasing demands for efficient and safe ventilation solutions in various applications.

In addition to the optimization algorithm, a comprehensive analysis of the blade geometry has been conducted. This detailed examination identifies key structural features that influence the safety factor and fatigue life cycle of the fan blade. The study proposes practical modifications to the blade design that effectively increase its safety factor while also extending its fatigue life. This approach not only mitigates the risk of structural failures but also ensures that the optimized fan can operate reliably under varying conditions, making it a significant contribution to the field of turbomachinery and ventilation technology.

### 7.3 Airfoil shape parameterization

#### 7.3.1 Bézier curves

Airfoil shape parameterization plays a key role in aerodynamic design, providing a mathematical way to represent the airfoil's geometry for easier adjustment and optimization to improve performance. In this research, Bézier curves are utilized to define the airfoil's shape. A point cloud is selected to compute the Bézier curves, facilitating aerodynamic performance analysis [153]:

$$P(t) = \sum_{i=0}^n B_i J_{n,i}(t) \quad 0 \leq t \leq 1; \quad 7-1$$

$$J_{n,i}(t) = \binom{n}{i} t^i (1-t)^{n-i}; \quad 7-2$$

$$\binom{n}{i} = \frac{n!}{i! (n-i)!} \quad 7-3$$

where  $B_i$  is the Bézier polygon's vertices,  $J_{n,i}(t)$  is the Bernstein function and  $n$  is the degree of Bernstein basis function.

$$\sum_{i=0}^n J_{n,i}(t) = 1. \quad 7-4$$

#### 7.3.2 Geometry

To apply the parameterization, the airfoil coordinates are required. In this study, the actual 3D geometry of the Chinook blade was used to obtain the blade's cross-sectional data. SolidWorks 2024 was utilized to extract 35 points in two dimensions, with the X and Y coordinates normalized to a range of 0 to 1 for standardization and consistency in the analysis (Figure 53).

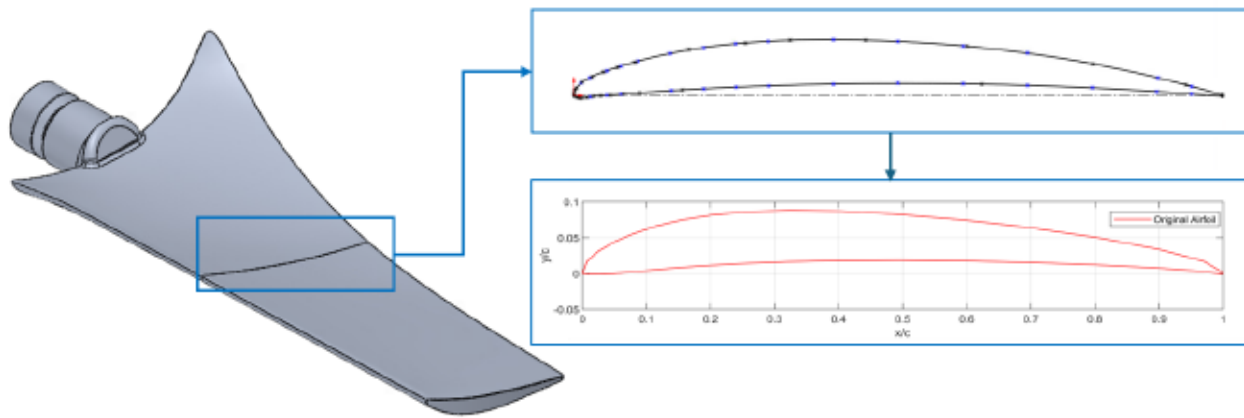


**Figure 61**  
Chinook-type fan 3D blade, 2D profile and Bezier parameterized curves.

#### 7.4 Airfoil profile optimization

In their previous study, the authors developed an unconstrained spectral conjugate-gradient optimization algorithm [129, 177]. While there are numerous algorithms available for aerodynamic optimization of airfoils—such as the genetic algorithm, particle swarm optimization [179], and surrogate-based optimization methods [145, 146]—the primary goal of this research is to apply the developed optimization method to industrial applications. By focusing on real-world scenarios, we aim to enhance the practical applicability of optimization techniques in improving airfoil performance in various engineering contexts.

The airfoil's shape was parameterized using Bézier curves, with control points optimized to minimize the drag coefficient. The XFOIL (V6.99) solver, integrated into MATLAB, calculated aerodynamic performance, particularly the lift and drag coefficients. The optimization algorithm iteratively updated the airfoil shape until the desired criteria were met [177].

Flow analysis was performed using XFOIL, a low-cost, high-precision tool for calculating aerodynamic properties such as lift and drag at various angles of attack and Reynolds numbers. This solver was crucial in determining the performance of airfoils like the NACA 4412, where the predicted lift-to-drag ratio closely matched real-world values [156].

The optimization method leveraged a conjugate-gradient approach, minimizing an objective function  $F(x)$ , where  $x$  represents the design variables. Iterations were guided by gradient-based updates, with step sizes computed through Wolfe line search conditions, ensuring efficient convergence. Several methods for calculating the conjugate gradient coefficient  $\beta_k$  were

employed, including the Polak-Ribiere, Liu-Storey, and Conjugate Descent formulations [161, 163], ultimately leading to the development of the modified spectral conjugate gradient method (SCGM). This method introduced a new calculation for  $\beta_k$  to enhance convergence towards optimal solutions [129].

### 7.5 Flow analysis

Aerodynamic sensitivity analysis was conducted using the central difference method, and the aerodynamic performance was evaluated in terms of the lift and drag coefficients under specified Reynolds numbers. The flow was modeled using Reynolds Averaged Navier-Stokes (RANS) equations, providing accurate assessments of mass and momentum conservation. Stall effects were also analyzed, focusing on the impact of increasing angles of attack on aerodynamic behavior.

$$C_l = \frac{2L}{\rho v^2 S} \quad 7-5$$

$$C_d = \frac{2D}{\rho v^2 S} \quad 7-6$$

where L and D, are the lift and drag force and S is the airfoil area, respectively [144]. Reynolds Averaged Navier Stokes (RANS) equations calculate the lift and drag [172]:

*Conservation of mass:*

$$\nabla \cdot \underline{u} = 0 \quad 7-7$$

*Conservation of momentum:*

$$\rho \frac{D\underline{u}}{Dt} = -\nabla P + \mu \nabla^2 \underline{u} + \rho \underline{F} \quad 7-8$$

Where  $\underline{u}$ ,  $(-\nabla P + \mu \nabla^2 \underline{u})$ , and  $\rho \underline{F}$ , represent the velocity vector, internal and external forces, respectively. A detailed explanation of the governing equations for fluid flow is provided in Section 2.1.

As the angle of attack (AOA) increases, both lift and induced drag rise until a certain limit. Beyond this point, the airflow over the airfoil's upper surface separates, leading to a reduction in lift, a phenomenon referred to as stall.

## 7.6 Aerodynamic optimization

The airfoil aerodynamic optimization process focuses on minimizing the drag coefficient while maintaining a fixed lift coefficient. Using the algorithm outlined by the authors in previous research [129, 177], the point cloud representing the airfoil geometry is inputted to generate the upper and lower surfaces through Bézier parameterization, along with the control points. The airfoil is then analyzed using XFOIL to compute the drag coefficient, which is subsequently fed back into the MATLAB code to iteratively refine the design until convergence criteria are met.

For this specific airfoil profile, the optimization algorithm achieved convergence in 11 iterations. The resulting optimized airfoil demonstrates a significant improvement, showing a 14.4% increase in aerodynamic performance. Figure 62 shows the original airfoil profile, the optimized airfoil and the control points in a scaled and real grid.

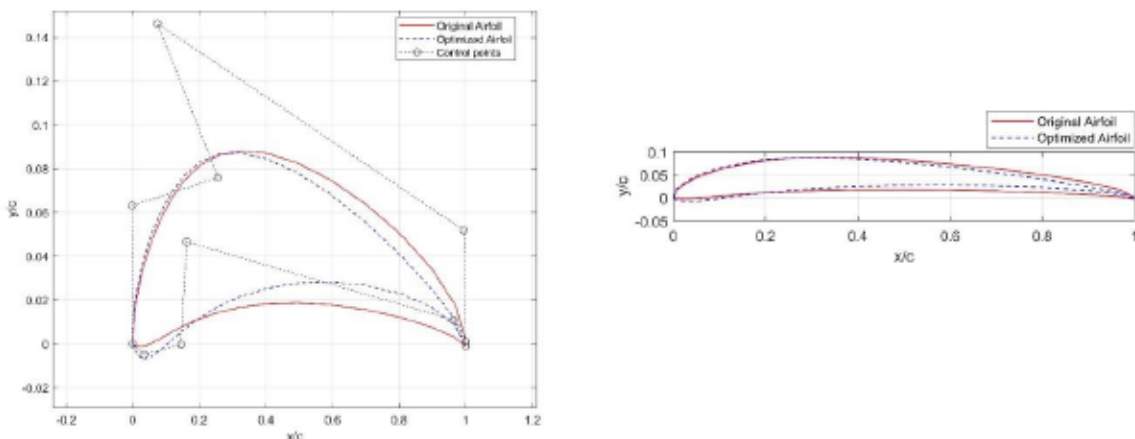


**Figure 62**  
Original and optimized airfoil profile with control points.

Further analysis was conducted across a range of angles of attack to better understand the impact of the optimization process. Figure 63-a compares the lift-to-drag ratio for both the original and optimized airfoil profiles over various angles of attack. The results clearly indicate that the optimized airfoil outperforms the original design, achieving a maximum lift-to-drag ratio of approximately 116 at an angle of attack of 4.5 degrees. This demonstrates that the optimized airfoil is capable of achieving superior aerodynamic efficiency at lower angles of attack, while the original airfoil reaches a maximum lift-to-drag ratio of only 101.5 at 6 degrees, just before encountering stall conditions.

This shift towards improved performance at lower angles of attack is a key advantage, as it suggests better stability and efficiency during operation. Figure 63-b and Figure 63-c further confirm that this enhancement in lift-to-drag ratio is primarily due to an increase in lift coefficient coupled with a reduction in drag coefficient. The optimized profile manages to lower the drag forces acting on the airfoil while simultaneously increasing its lifting capacity, effectively improving overall aerodynamic performance across a wider operational range.

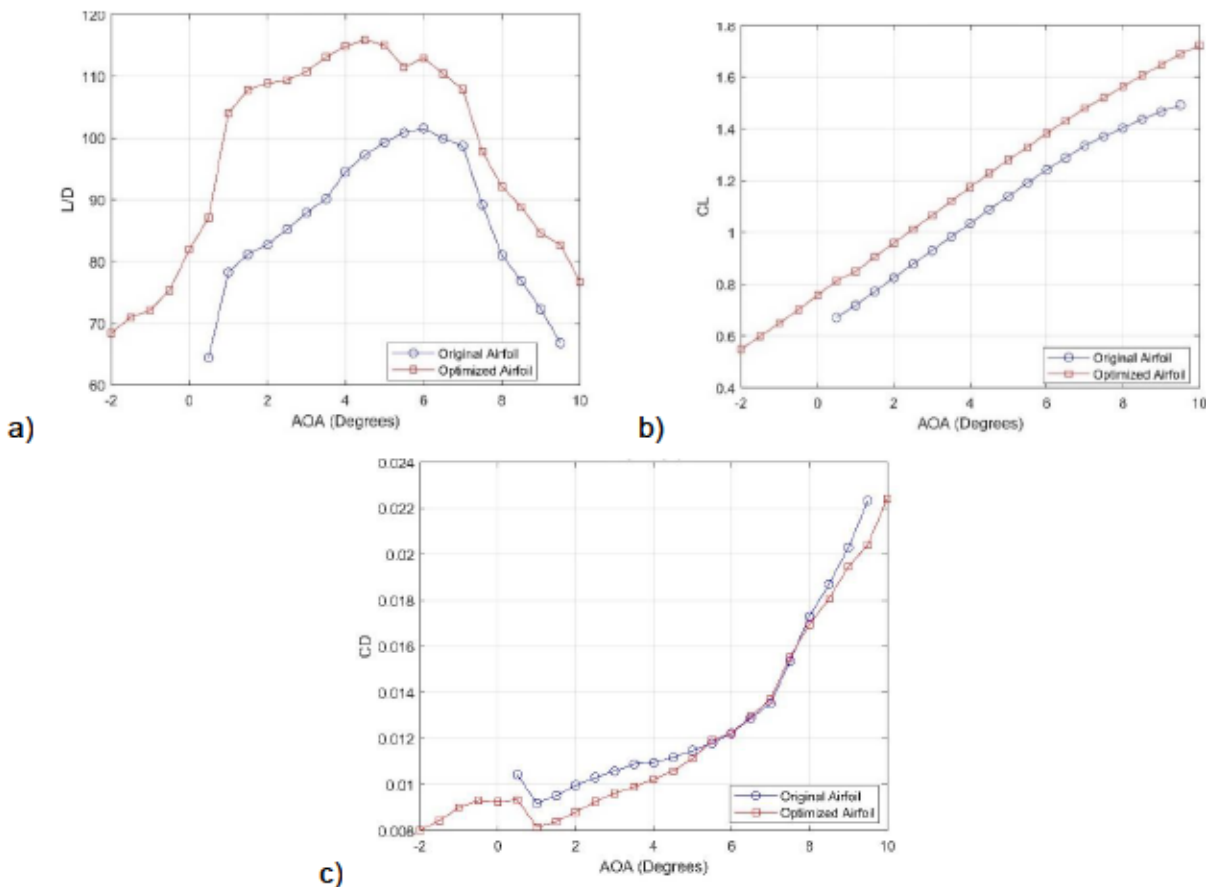


**Figure 63**  
**a) lift to drag ratio versus angle of attack, b) lift coefficient versus angle of attack, c) drag coefficient versus angle of attack.**

These findings emphasize the effectiveness of the optimization approach, as the modification not only enhances aerodynamic efficiency but also extends the operational window before stall conditions are encountered, contributing to a more robust and reliable airfoil design.

## 7.7 Structural analysis

### 7.7.1 Static analysis

The Chinook blade geometry is utilized across various sizes of ventilators. To ensure the calculations are applicable to other models, the smallest hub-to-tip ratio is selected as the worst-

case scenario. This corresponds to a 54" (1.37 m) ventilator with a 21" (0.533 m) hub. The blade, weighing 4 kg, is made from cast aluminum A356-T6 and undergoes heat treatment. The aluminum alloy, used in the blade design, has a yield strength of 170 MPa and an ultimate tensile strength of 240 MPa. The system operates at a speed of 1800 rpm (188.5 rad/s).

To calculate the forces acting on the blade, the equivalent centrifugal force can be determined using the following equation [180]:

$$F_c = m\omega^2 r, \quad 7-9$$

where  $F_c$  is the equivalent centrifugal force,  $m$  is the mass of the blade,  $r$  is the radius to the blade's center of gravity, and  $\omega$  is the angular velocity of the rotating blade.

Considering the blade-root intersection as the critical region, it is essential to account for the stress concentration factor [181], which plays a significant role in accurately assessing the localized stress at this junction (Figure 65). The calculated equivalent centrifugal force is 49.5 kN, which acts on the blade-root junction, generating both normal and shear stresses at this critical point. To evaluate the combined effect of these stresses, the von-Mises equivalent stress is used, yielding a nominal stress of 43.2 MPa. Considering the geometry of the blade-root junction, a stress concentration factor of  $K=3$  is applied [182], amplifying the stress to a maximum of 129.6 MPa.

$$K = \frac{\sigma_{max}}{\sigma_{nom}}, \quad 7-10$$

Figure 64 illustrates the stress concentration curves for flat and round bars. In practical applications, particularly regarding the geometry of a twisted blade, it is essential to consider the interplay of various factors. In this specific case, the small  $r/d$  ratio allows for an average approximation of the stress concentration factor, which shows good agreement with numerical

simulations. This consistency emphasizes the importance of understanding geometrical influences on stress distribution in structural designs.

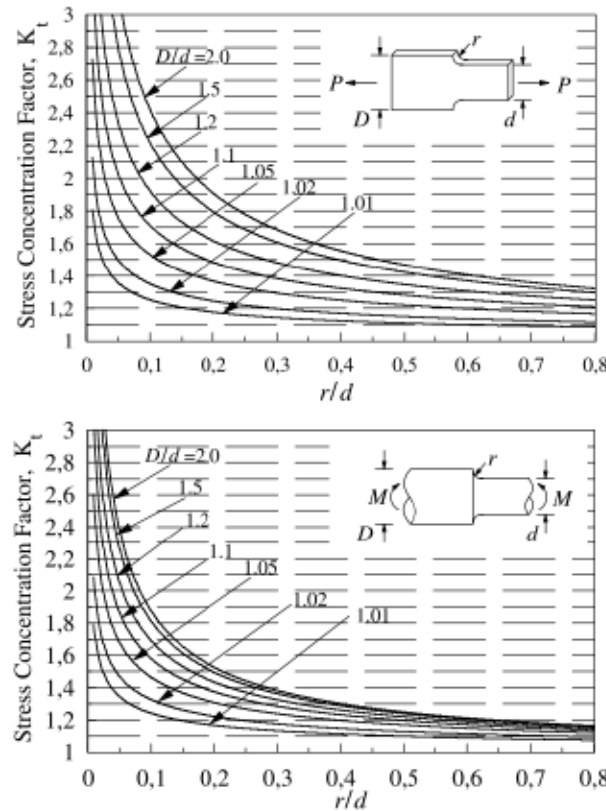


**Figure 64**  
**Stress concentration factors for shoulder fillets in flat and round bars**  
Source: [183, 184].

This amplified stress represents the peak stress experienced at the blade-root intersection due to the localized concentration of forces. Based on the maximum stress and the material's yield strength, the static safety factor is calculated to be 1.31. This factor indicates that the blade can withstand the applied loads with a margin of safety.

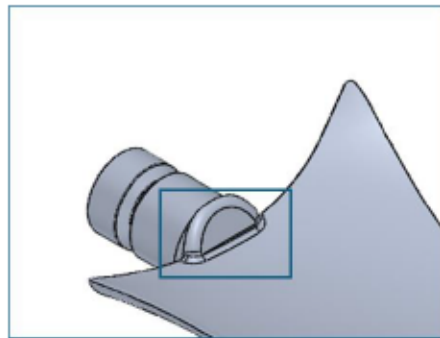


**Figure 65**  
**Blade-root junction.**

Further analysis is performed using the finite element method (FEM) with the ANSYS Mechanical solver to validate the initial findings through fluid-structure interaction (FSI) coupling [9, 10] (Figure 67). First, a CFD analysis under stall conditions is carried out [172], as shown in Figure 66. The pressure distribution obtained from the CFD results is then imported into the ANSYS Mechanical interface for the FSI analysis. A detailed explanation of the structural deformation and motion equations, application of finite element method and the fluid structure interaction theory is provided in Sections 2.1, 2.3, 2.4, and 2.5.

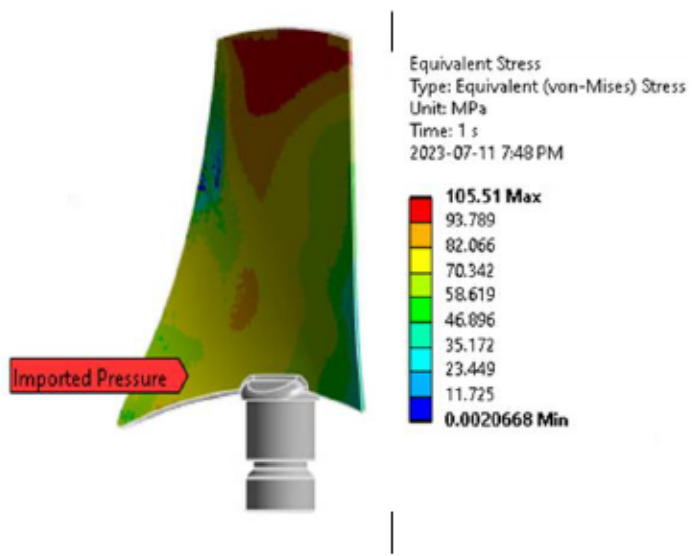


**Figure 66**  
**Pressure distribution on the blade resulting from CFD analysis in stall**  
Source: [172].

The FEM results demonstrated a difference of approximately 1% when compared to the analytical calculations, confirming the accuracy of the theoretical approach. Additionally, the simulation revealed a maximum vertical displacement of 0.35 mm at the blade tip, which remains well within

safe limits given the minimum tip-to-shroud clearance of 3 mm. This displacement is not deemed critical and poses no risk of contact, ensuring the system's operational integrity (Figure 67).

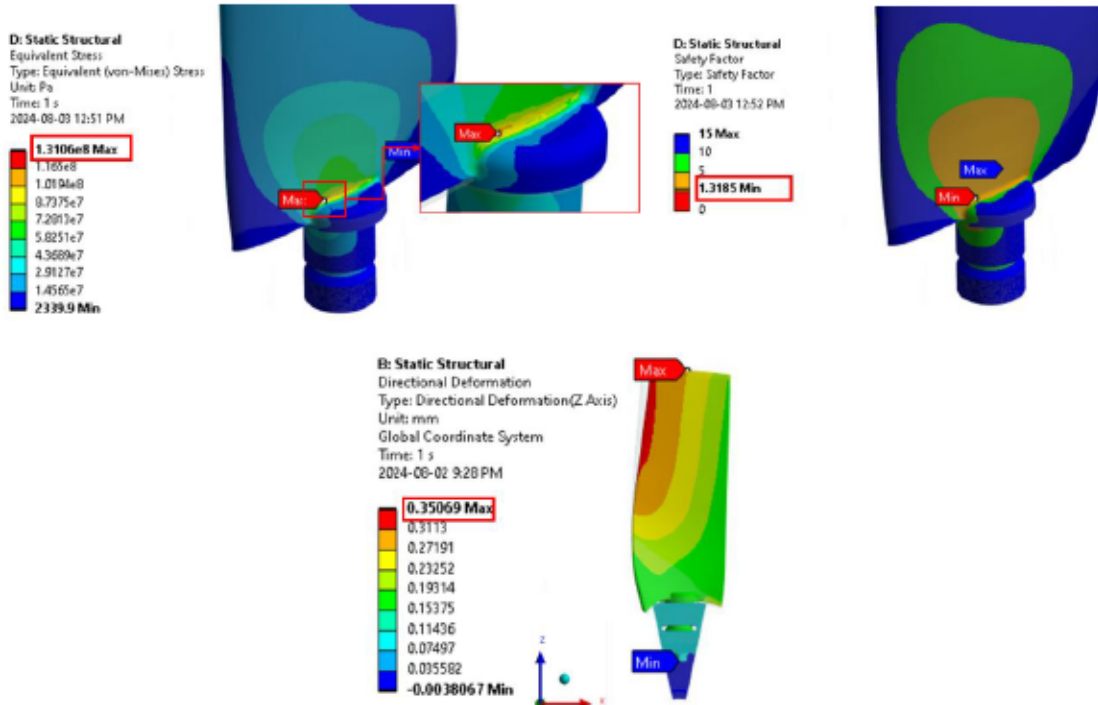


**Figure 67**  
**Maximum equivalent stress and minimum safety factor on blade-root junction.**

### 7.7.2 Fatigue analysis

Fatigue failure is a common phenomenon in rotating systems [185, 186], particularly under unstable conditions, where pressure variations can significantly affect performance. When static pressure rises, airflow can decrease drastically, causing a weak or intense stall, depending on the severity of the pressure change. To estimate the aerodynamic forces acting on a blade during normal operation, electrical power consumption is used to calculate the torque, from which the applied force is derived:

$$P = \frac{T\omega}{\eta}, \quad 7-11$$

Where P is the power, T is the torque,  $\omega$  is the rotational velocity and  $\eta$  is the electric motor efficiency.

In this case a 350 (HP) motor is considered rotating at 1800 rpm. The result force is found to be 260 N on the surface of each blade. In this analysis, a 350 horsepower (HP) motor operating at 1800 RPM is considered. The resulting aerodynamic force acting on the surface of each blade is calculated to be 260 N. This force represents the steady-state load under normal operating conditions. This approach provides a reliable estimate of the forces under typical operating conditions. To simulate the more demanding stall scenario, the calculated forces are amplified about 50% cyclically to mimic the fluctuating aerodynamic loads that occur during instabilities. This amplification represents the added stresses blades endure when airflow separation occurs, leading to potential fatigue failures over time. By considering these dynamic loads, the analysis captures the worst-case operational stresses, aiding in the design and optimization of the blade for enhanced durability.

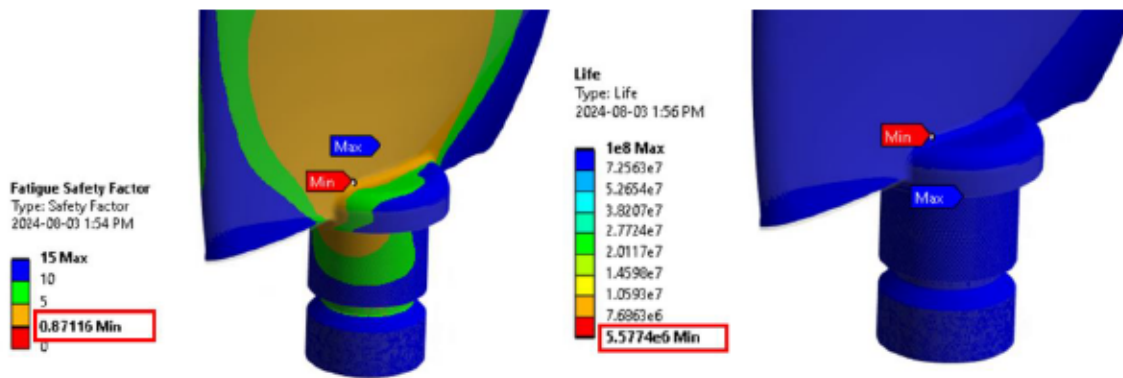


**Figure 68**  
**Fatigue safety factor on the critical region.**

The analysis reveals a fatigue safety factor of 0.87, under fully reversed loading condition indicating that the blade can endure up to 5.6 million life cycles under continuous unstable conditions. However, when subjected to cyclic forces with each rotation, the estimated operational limit is only about 52 hours. This suggests that fatigue failure is likely to occur at the blade-root junction within this timeframe. Therefore, the design needs to be reassessed to enhance fatigue resistance and extend the blade's operational life. Detailed explanation of fatigue life calculation methods and related equations are provided in Section 2.7.

### 7.8 Structural optimization

The previous analysis identified the blade-root junction as the most critical region in the blade geometry due to its high stress concentration, providing key insights for the optimization process. In the current blade design, the fillet radius-to-diameter ratio is approximately 0.05, resulting in a significant stress concentration factor. This high concentration intensifies the localized stress,

especially during cyclic loading, increasing the risk of fatigue failure. By modifying the fillet radius to be five times larger than the original design (Figure 69), the stress concentration factor can theoretically be reduced by approximately 50%. This reduction in stress concentration will lead to a proportional decrease in the maximum equivalent stress, thus improving the overall safety factor of the blade. Figure 70 demonstrates a significant reduction in the maximum equivalent stress, which has decreased to 68.7 MPa. This reduction is a direct result of increasing the fillet radius at the blade-root junction. Consequently, the static safety factor has been notably improved, rising to 2.5. This enhancement indicates a considerable improvement in the structural integrity of the blade, particularly in critical stress regions, ensuring greater durability and safety during operation. The modification effectively reduces stress concentrations, leading to a more resilient design under operational loads. This design modification not only extends the fatigue life but also increases the blade's resilience to both normal and stall-induced operating conditions.

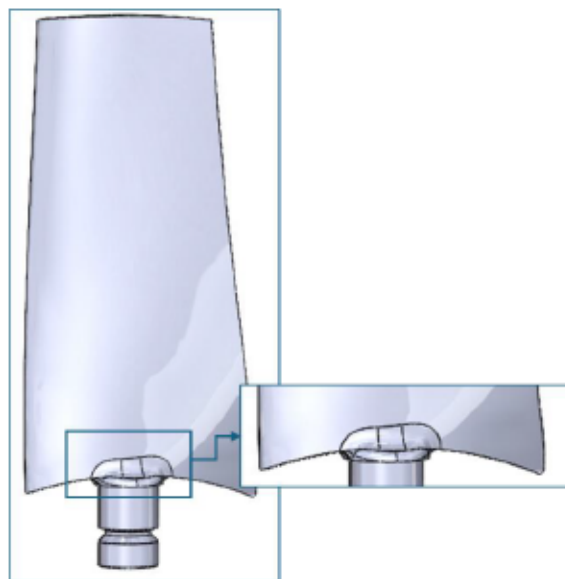


**Figure 69**  
**Modified fillet radius on the blade-root junction.**

This approach not only aligns with standard engineering practices, where increasing the fillet radius in high-stress regions is a well-established method for mitigating fatigue failure but also offers a practical solution.

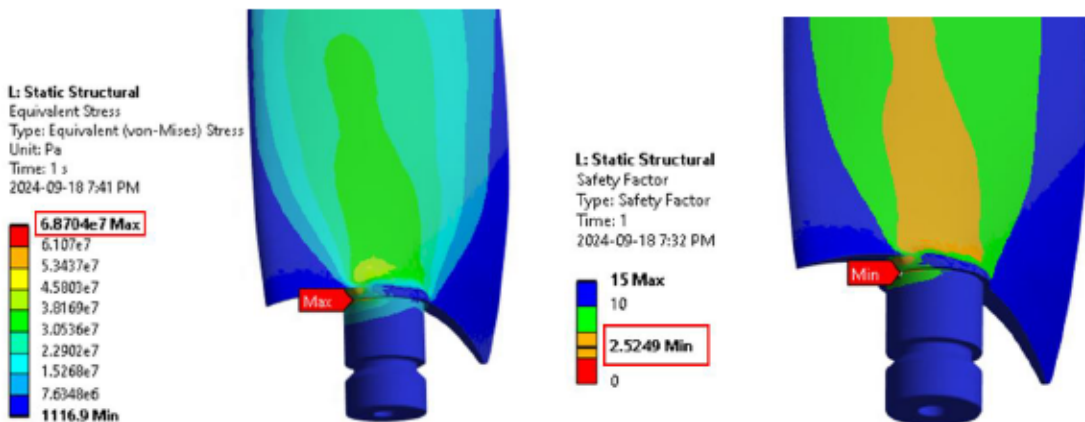


**Figure 70**  
**Maximum equivalent stress and corresponding safety factor on the optimized blade critical region.**

Moreover, the proposed modification introduces additional material to the blade geometry, improving its load distribution. Importantly, this adjustment can be made using the existing mold without requiring a complete redesign or replacement, making it an efficient and cost-effective improvement. This allows for better performance and durability without significant manufacturing disruptions or increased production costs, making it a highly viable optimization strategy.

The fatigue analysis of the modified blade under unstable conditions, using the same operational parameters as the original design, demonstrates a significant improvement in the fatigue safety factor. With the applied modifications—primarily the increase in fillet radius—the fatigue safety factor rises to 1.2, indicating a substantial enhancement in the blade's durability (Figure 71).

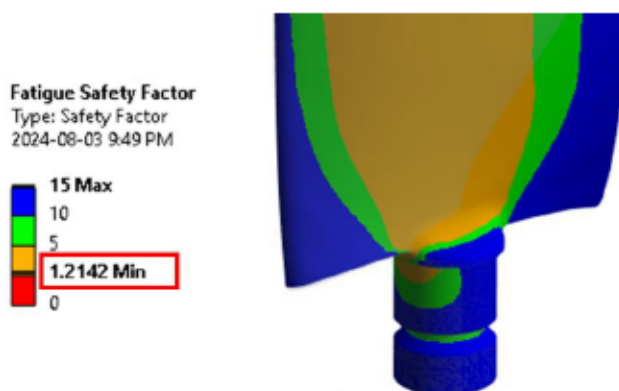


**Figure 71**  
**Fatigue safety factor results for the modified blade.**

This increase suggests that the modified blade can now withstand higher cyclic loads and stress variations without succumbing to fatigue failure, even in the demanding environment of stall

conditions. The higher fatigue safety factor ensures that the fan can operate safely for longer periods, reducing the risk of unexpected failure and improving the overall reliability of the system. These results affirm that the design optimization effectively addresses the critical fatigue concerns present in the original blade geometry, leading to safer and more robust fan operation.

### 7.9 Conclusion

This study focused on the aerodynamic and structural optimization of an airfoil profile and its application to a Chinook blade in ventilators. By refining the blade geometry through iterative optimization and increasing the fillet radius in critical regions, both aerodynamic efficiency and structural integrity were significantly enhanced. The optimized airfoil showed a 14.4% increase in performance, and the modified blade exhibited improved safety factors, reducing the risk of fatigue failure.

The optimization process for the airfoil profile was highly effective, achieving convergence in 11 iterations and resulting in a 14.4% improvement in aerodynamic performance. The optimized airfoil demonstrated a maximum lift-to-drag ratio of 116 at a 4.5-degree angle of attack, significantly outperforming the original airfoil, which had a maximum ratio of 101.5 at 6 degrees before stalling.

Structurally, the blade's most critical region was identified as the blade-root junction, where high-stress concentrations were found. The equivalent centrifugal force acting on the blade was calculated at 49.5 kN, resulting in a von-Mises stress of 43.2 MPa, which was amplified to 129.6 MPa due to a stress concentration factor of 3. The fatigue analysis using revealed a safety factor of 0.87 for the original blade, predicting failure after 5.6 million life cycles or approximately 52 hours of continuous operation under unstable conditions. To address this, an optimization strategy focused on increasing the fillet radius at the blade-root junction. This modification reduced the stress concentration, reducing the maximum equivalent stress to 68.7 MPa and improving the static safety factor to 2.5. The fatigue safety factor also improved, rising to 1.2 after the modifications, indicating enhanced durability and resistance to cyclic loads, even during demanding stall conditions. Table 23 summarizes the equivalent von Mises stress, static safety factor, and fatigue safety factor under stall conditions.

**Table 23**  
**Stress analysis and safety factor comparison of original vs. optimized blade designs**

Parameter	Original blade	Optimized blade
<b>von-Mises stress (MPa)</b>	131	69
<b>Static safety factor</b>	1.32	2.52
<b>Fatigue safety factor</b>	0.87	1.21

Future contributions could focus on optimizing additional components that rotate with the blade, such as the hub and attachment structures. By refining these elements, it may be possible to further enhance the overall performance of the ventilators while simultaneously reducing production and operational costs.

## GENERAL CONCLUSION

This thesis presents a unified approach to optimizing various aspects of turbomachinery and structural components through advanced computational techniques and experimental validation. The research encompasses a broad range of applications, including axial compressors, mine ventilation fans, and aerodynamic shape optimization, reflecting a comprehensive examination of performance, safety, and efficiency improvements.

The investigation into axial compressors highlighted the crucial role of fluid-structure interaction and high-performance computing (HPC) in understanding and optimizing blade deformations. The study demonstrated that a well-calibrated FSI approach, validated through extensive parametric analysis, can significantly enhance operational safety while maintaining performance. The results underscored the importance of material selection and geometric considerations in achieving optimal compressor design.

The analysis of mine ventilation fans revealed significant insights into the balance between operational performance and structural integrity. By employing CFD simulations and Design of Experiments (DOE), the research identified key design parameters that influence efficiency and safety. The optimized configurations not only improved performance by 9% but also offered reductions in noise, cost, and energy consumption, highlighting the potential for practical applications in mining operations.

In the domain of optimization algorithms, the development of a novel spectral conjugate gradient method demonstrated superior convergence and efficiency in solving unconstrained optimization problems. This advancement provides a robust tool for tackling complex optimization challenges, with implications for a wide range of engineering applications.

The aerodynamic shape optimization of NACA airfoils using an unconstrained conjugate gradient algorithm and Bézier parameterization resulted in significant performance improvements. The research showcased how advanced optimization techniques could enhance aerodynamic efficiency, reduce drag, and achieve better lift-to-drag ratios, with potential benefits for aircraft and turbomachinery designs.

Finally, the study highlights the importance of optimizing both aerodynamic and structural aspects of axial-flow fans used in mine ventilation to improve safety, performance, and energy efficiency. By applying a novel optimization algorithm to the twisted Chinook blade design, a significant 14.4%

improvement in the lift-to-drag ratio and a 4.5% increase in overall fan performance were achieved. Furthermore, structural modifications at the blade root enhanced fatigue life, particularly under stall conditions, leading to greater long-term reliability. These advancements represent a critical step toward developing high-performance ventilation systems for mining applications.

## LIMITATIONS AND RECOMMENDATIONS

This research introduced a multi-objective optimization framework tailored for turbomachinery components, with a focus on axial compressors and underground mine ventilation fans. While the proposed methodology achieved promising results in aerodynamic and structural performance improvement, certain modeling assumptions and limitations open up avenues for future enhancement. These are detailed below:

### ***Fluid-Structure Interaction Modeling***

#### *Limitation:*

The current FSI simulations were performed using a one-way coupling approach, in which the aerodynamic pressure loads computed from the CFD solver were transferred to the structural domain using interpolation techniques. While this approach is efficient and widely used in literature for preliminary design stages, it neglects the feedback effect of structural deformation on the fluid domain.

#### *Recommendation:*

Future work should consider implementing two-way or strong coupling strategies (e.g., Euler-Lagrange methods or partitioned solvers), where deformation of the structure can influence the flow field in real time. This would yield more realistic predictions, particularly in scenarios involving high aerodynamic loads or flutter-prone blades.

### ***Mesh Adaptivity and Interface Resolution***

#### *Limitation:*

The mesh used in CFD, and structural domains was fixed, with high refinement near critical regions, but did not include dynamic or adaptive meshing at the fluid-structure interface.

#### *Recommendation:*

Incorporating adaptive meshing techniques, especially near the fluid-solid interface, would enhance solution accuracy in regions of high gradient or geometric complexity. Future studies should explore mesh sensitivity analyses in greater depth and implement dynamic remeshing strategies to maintain computational efficiency while improving resolution.

### ***Startup and Transient Fan Operation***

#### ***Limitation:***

The analysis assumed steady-state or quasi-steady aerodynamic conditions for performance evaluation. Transient phenomena, such as fan startup and shutdown phases, were not modeled in detail.

#### ***Recommendation:***

Transient simulation of fan startup is essential for evaluating mechanical stresses, resonance risks, and torque variations that affect fatigue life and structural integrity. Future studies should integrate time-dependent boundary conditions and consider fluid transients to more accurately replicate operational behavior under real-life duty cycles.

### ***Structural and Geometrical Optimization***

#### ***Limitation:***

While aerodynamic and basic structural evaluations were conducted, full structural optimization (e.g., stiffness-to-mass ratio, hub/duct integration) was not addressed in depth.

#### ***Recommendation:***

A more integrated structural optimization approach could be applied to critical components such as hubs, ducts, and junctions. This would reduce material usage, enhance reliability, and shorten manufacturing lead times, especially when coupled with topology optimization or design-for-manufacturing strategies.

### ***Surrogate Modeling and Machine Learning***

#### ***Limitation:***

Although a novel optimization algorithm was developed, adjoint-based sensitivity analysis and surrogate modeling were not employed to reduce computational cost.

#### ***Recommendation:***

Integrating adjoint methods and machine learning-enhanced surrogate models can significantly accelerate optimization while preserving accuracy. Adaptive surrogate models that evolve during the optimization process, supported by data-driven strategies, offer great potential for scaling the methodology to more complex geometries and real-time applications.

### ***Influence of Temperature in Underground Applications***

#### ***Limitation:***

CFD simulations assumed constant ambient conditions and did not include temperature variations, which can be significant in underground mines.

#### ***Recommendation:***

Future CFD models should account for thermodynamic effects such as temperature-induced changes in air density, viscosity, and pressure gradients. This is especially relevant for deep mining environments, where elevated temperatures impact both fan performance and structural loading.

### ***Prototyping and Experimental Validation***

#### ***Limitation:***

The results and models developed in this work were validated against developed numerical or analytical benchmarks, but not through physical testing.

#### ***Recommendation:***

To further enhance the credibility of the proposed framework, experimental validation of optimized airfoil geometries and fan components should be pursued. This will support the development of more robust and industrially deployable designs.

## REFERENCES

- [1] G. Ingram, *Basic Concepts in Turbomachinery*. Bookboon.
- [2] H. D. Vo, "Role of Tip Clearance Flow in the Generation of Non-Synchronous Vibrations," in *44th AIAA Aerospace Sciences Meeting and Exhibit*, 2006.
- [3] J. Thomassin, H. D. Vo, and N. W. Mureithi, "Blade Tip Clearance Flow and Compressor Nonsynchronous Vibrations: The Jet Core Feedback Theory as the Coupling Mechanism," *Journal of Turbomachinery*, vol. 131, no. 1, 2008, doi: 10.1115/1.2812979.
- [4] J. Zhong, S. Han, H. Lu, and X. Kan, "Effect of tip geometry and tip clearance on aerodynamic performance of a linear compressor cascade," *Chinese Journal of Aeronautics*, vol. 26, no. 3, pp. 583-593, 2013/06/01/ 2013, doi: <https://doi.org/10.1016/j.cja.2013.04.020>.
- [5] C.-T. Dinh, M.-W. Heo, and K.-Y. Kim, "Aerodynamic performance of transonic axial compressor with a casing groove combined with blade tip injection and ejection," *Aerospace Science and Technology*, vol. 46, pp. 176-187, 2015/10/01/ 2015, doi: <https://doi.org/10.1016/j.ast.2015.07.006>.
- [6] S.S. Kumar et al., "Aerodynamic characterization of a transonic axial flow compressor stage – with asymmetric tip clearance effects," *Aerospace Science and Technology*, vol. 82-83, pp. 272-283, 2018/11/01/ 2018, doi: <https://doi.org/10.1016/j.ast.2018.09.001>.
- [7] R. Taghavi-Zenouz and M. H. Ababaf Behbahani, "Improvement of aerodynamic performance of a low speed axial compressor rotor blade row through air injection," *Aerospace Science and Technology*, vol. 72, pp. 409-417, 2018/01/01/ 2018, doi: <https://doi.org/10.1016/j.ast.2017.11.028>.
- [8] R. Santhi and P. Vasanthakumar, "Computational fluid dynamics for turbomachinery technologies with a focus on high-speed rotor blades," *Materials Today: Proceedings*, vol. 68, pp. 2310-2317, 2022/01/01/ 2022, doi: <https://doi.org/10.1016/j.matpr.2022.08.555>.
- [9] R. Kamakoti and W. Shyy, "Fluid–structure interaction for aeroelastic applications," *Progress in Aerospace Sciences*, vol. 40, no. 8, pp. 535-558, 2004/11/01/ 2004, doi: <https://doi.org/10.1016/j.paerosci.2005.01.001>.
- [10] V. Gnesin, R. Rzqdkowski, and L. Kolodyazhnaya, "A Coupled Fluid-Structure Analysis for 3D Flutter in Turbomachines," presented at the Volume 4: Manufacturing Materials and Metallurgy; Ceramics; Structures and Dynamics; Controls, Diagnostics and Instrumentation; Education, 2000.
- [11] H. Doi and J. J. Alonso, "Fluid/Structure Coupled Aeroelastic Computations for Transonic Flows in Turbomachinery," presented at the Volume 4: Turbo Expo 2002, Parts A and B, 2002.
- [12] R. C. K. Leung, Y. L. Lau, and R. M. C. Si, "Analysis of Fluid-Structure Interaction of an Elastic Blade in Cascade," presented at the 5th International Symposium on Fluid Structure Interaction, Aeroelasticity, and Flow Induced Vibration and Noise, 2002.
- [13] B. H. Beheshti, J. A. Teixeira , P. C. Ivey, K. Ghorbanian, and B. Farhanieh, "Parametric Study of Tip Clearance—Casing Treatment on Performance and Stability of a Transonic Axial Compressor," *Journal of Turbomachinery*, vol. 126, no. 4, pp. 527-535, 2004, doi: 10.1115/1.1791643.

- [14] O. Guerri, A. Hamdouni, and A. Sakout, "Fluid Structure Interaction of Wind Turbine Airfoils," *Wind engineering* vol. 32, 2008.
- [15] I. Hongsik, C. Xiangying, and Z. Gecheng, "Detached eddy simulation of transonic rotor stall flutter using a fully coupled fluid-structure interaction," in *ASME Turbo Expo 2011*, Vancouver, Canada, 2011.
- [16] C. E. Douvi, "Evaluation of the turbulence models for the simulation of the flow over a National Advisory Committee for Aeronautics (NACA) 0012 airfoil," *Journal of Mechanical Engineering Research*, vol. 4, no. 3, 2012, doi: 10.5897/jmer11.074.
- [17] V. J. Fidalgo, C. A. Hall, and Y. Colin, "A Study of Fan-Distortion Interaction Within the NASA Rotor 67 Transonic Stage," *Journal of Turbomachinery*, vol. 134, no. 5, 2012, doi: 10.1115/1.4003850.
- [18] A. Naseri, M. Boroomand, and S. Sammak, "Numerical investigation of effect of inlet swirl and total-pressure distortion on performance and stability of an axial transonic compressor," *Journal of Thermal Science*, vol. 25, no. 6, pp. 501-510, 2016, doi: 10.1007/s11630-016-0891-6.
- [19] L. Wang, R. Quant, and A. Kolios, "Fluid structure interaction modelling of horizontal-axis wind turbine blades based on CFD and FEA," *Journal of Wind Engineering and Industrial Aerodynamics*, vol. 158, pp. 11-25, 2016, doi: 10.1016/j.jweia.2016.09.006.
- [20] R. Roul and A. Kumar, "Fluid-Structure Interaction of Wind Turbine Blade Using Four Different Materials: Numerical Investigation," *Symmetry*, vol. 12, no. 9, 2020, doi: 10.3390/sym12091467.
- [21] H. Sun, A. Ren, Y. Wang, M. Zhang, and T. Sun, "Deformation and vibration analysis of compressor rotor blades based on fluid-structure coupling," *Engineering Failure Analysis*, vol. 122, 2021, doi: 10.1016/j.engfailanal.2021.105216.
- [22] A. Afzal, Z. Ansari, A. R. Faizabadi, and M. K. Ramis, "Parallelization Strategies for Computational Fluid Dynamics Software: State of the Art Review," *Archives of Computational Methods in Engineering*, vol. 24, no. 2, pp. 337-363, 2016, doi: 10.1007/s11831-016-9165-4.
- [23] K. A. Pericleous and M. K. Patel, "The Modelling of Tangential and Axial Agitators in Chemical Reactors," *PCH. Physicochemical hydrodynamics*, vol. 8, 1987.
- [24] D. H. Pelletier and J. A. Schetz, "Finite element Navier-Stokes calculation of three-dimensional turbulent flow near a propeller," *AIAA Journal*, vol. 24, no. 9, pp. 1409-1416, 1986, doi: 10.2514/3.9457.
- [25] D. Pelletier, A. Garon, and R. Camarero, "Finite element method for computing turbulent propeller flow," *AIAA Journal*, vol. 29, no. 1, pp. 68-75, 1991, doi: 10.2514/3.10546.
- [26] G. D. Thiat and T. W. von Backström, "Numerical simulation of the flow field near an axial flow fan operating under distorted inflow conditions," *Journal of Wind Engineering and Industrial Aerodynamics*, vol. 45, no. 2, pp. 189-214, 1993/05/01/ 1993, doi: [https://doi.org/10.1016/0167-6105\(93\)90270-X](https://doi.org/10.1016/0167-6105(93)90270-X).
- [27] C. J. Meyer, "A numerical investigation of the plenum chamber aerodynamic behaviour of mechanical draught air-cooled heat exchangers," Ph.D., Mechanical Engineering), University of Stellenbosch, 2000.

- [28] F. N. Le Roux, 'The CFD simulation of an axial flow fan,' *Mechanical Engineering*, University of Stellenbosch, 2010.
- [29] H. Kumawat, "Modeling and Simulation of Axial Fan Using CFD," *International Journal of Aerospace and Mechanical Engineering*, vol. 95, 2014, doi: <https://publications.waset.org/pdf/10000214>.
- [30] J. Wang and N. P. Kruyt, "Computational Fluid Dynamics Simulations of Aerodynamic Performance of Low-Pressure Axial Fans With Small Hub-to-Tip Diameter Ratio," *Journal of Fluids Engineering*, vol. 142, no. 9, 2020, doi: 10.1115/1.4047120.
- [31] M. Moosania, C. Zhou, and S. Hu, "Effect of tip geometry on the performance of low-speed axial flow fan," *International Journal of Refrigeration*, vol. 134, pp. 16-23, 2022, doi: 10.1016/j.ijrefrig.2021.07.041.
- [32] Z. Wei, G. Li, and L. Qi, "New nonlinear conjugate gradient formulas for large-scale unconstrained optimization problems," *Applied Mathematics and Computation*, vol. 179, no. 2, pp. 407-430, 2006/08/15/ 2006, doi: <https://doi.org/10.1016/j.amc.2005.11.150>.
- [33] G. Yuan, S. Lu, and W. Z, "A Line Search Algorithm for Unconstrained Optimization," *Journal of Software Engineering and Applications*, vol. 3, pp. 503-509, 2010, doi: <http://dx.doi.org/10.4236/isea.2010.35057>.
- [34] J. Yang, J. Luo, J. Xiong, and F. Liu, "Aerodynamic design optimization of the last stage of a multi-stage compressor by using an adjoint method," in *Turbo Expo: Power for Land, Sea, and Air*, 2016, vol. 49712: American Society of Mechanical Engineers, p. V02CT39A033.
- [35] M. Rivaie, M. Mamat, and A. Abashar, "A new class of nonlinear conjugate gradient coefficients with exact and inexact line searches," *Applied Mathematics and Computation*, vol. 268, pp. 1152-1163, 2015, doi: 10.1016/j.amc.2015.07.019.
- [36] N. H. M. Yussoff, M. Mamat, M. Rivaie, and I. Mohd, "A new conjugate gradient method for unconstrained optimization with sufficient descent," 2014.
- [37] M. Arabnia and W. Ghaly, "A strategy for multi-point shape optimization of turbine stages in three-dimensional flow," in *Turbo Expo: Power for Land, Sea, and Air*, 2009, vol. 48883, pp. 489-502.
- [38] D. Bonaiuti and M. Zangeneh, "On the coupling of inverse design and optimization techniques for the multiobjective, multipoint design of turbomachinery blades," *Journal of Turbomachinery*, Article vol. 131, no. 2, 2009, Art no. 021014, doi: 10.1115/1.2950065.
- [39] L. He and P. Shan, 'Three-dimensional aerodynamic optimization for axial-flow compressors based on the inverse design and the aerodynamic parameters,' *Journal of Turbomachinery*, Article vol. 134, no. 3, 2012, Art no. 031004, doi: 10.1115/1.4003252.
- [40] Z. Guo, L. Song, Z. Zhou, J. Li, and Z. Feng, "Multi-Objective Aerodynamic Optimization Design and Data Mining of a High Pressure Ratio Centrifugal Impeller," *Journal of Engineering for Gas Turbines and Power*, Article vol. 137, no. 9, 2015, Art no. 092602, doi: 10.1115/1.4029882.
- [41] S. M. H. Mahmood, M. G. Turner, and K. Siddappaji, "Flow characteristics of an optimized axial compressor rotor using smooth design parameters," in *Turbo Expo: Power for Land, Sea, and Air*, 2016, vol. 49712: American Society of Mechanical Engineers, p. V02CT45A018.

- [42] B. Li, C.-w. Gu, X.-t. Li, and T.-q. Liu, "Numerical optimization for stator vane settings of multi-stage compressors based on neural networks and genetic algorithms," *Aerospace Science and Technology*, vol. 52, pp. 81-94, 2016/05/01/ 2016, doi: <https://doi.org/10.1016/j.ast.2016.02.024>.
- [43] Z. Li and Y. Liu, "Blade-end treatment for axial compressors based on optimization method," *Energy*, vol. 126, pp. 217-230, 2017/05/01/ 2017, doi: <https://doi.org/10.1016/j.energy.2017.03.021>.
- [44] J. Yang, M. Zhang, C. Peng, M. Ferlauto, and Y. Liu, "Stator re-stagger optimization in multistage axial compressor," *Propulsion and Power Research*, vol. 10, no. 2, pp. 107-117, 2021/06/01/ 2021, doi: <https://doi.org/10.1016/j.ippr.2021.03.002>.
- [45] L. Chen and G. Lorenzini, "Efficiency optimized axial flow compressor stage with a given shape of flow-path," *Case Studies in Thermal Engineering*, vol. 36, p. 102156, 2022/08/01/ 2022, doi: <https://doi.org/10.1016/j.csite.2022.102156>.
- [46] C. Zhang and M. Janeway, "Optimization of Turbine Blade Aerodynamic Designs Using CFD and Neural Network Models," *International Journal of Turbomachinery, Propulsion and Power*, vol. 7, no. 3, 2022, doi: 10.3390/ijtpp7030020.
- [47] Y. Wang, T. Liu, D. Zhang, and Y. Xie, "Dual-convolutional neural network based aerodynamic prediction and multi-objective optimization of a compact turbine rotor," *Aerospace Science and Technology*, vol. 116, 2021, doi: 10.1016/j.ast.2021.106869.
- [48] F. Bleier, *Fan Handbook, selection, application and design*. McGraw Hill, 1998.
- [49] M. W. Rubesin and W. C. Rose, "The Turbulent Mean-Flow, Reynolds-Stress, and Heat Flux Equations in Mass-Averaged Dependent Variables," NASA-TM-X-62248, 1973.
- [50] ANSYS Fluent Theory Guide. 2013.
- [51] B. E. Launder and D. B. Spalding, "The numerical computation of turbulent flows," *Computer Methods in Applied Mechanics and Engineering*, vol. 3, no. 2, pp. 269-289, 1974/03/01/ 1974, doi: [https://doi.org/10.1016/0045-7825\(74\)90029-2](https://doi.org/10.1016/0045-7825(74)90029-2).
- [52] M. Tabatabaei Malazi, E. T. Eren, J. Luo, S. Mi, and G. Temir, "Three-Dimensional Fluid-Structure Interaction Case Study on Elastic Beam," *Journal of Marine Science and Engineering*, vol. 8, no. 9, p. 714, 2020. [Online]. Available: <https://www.mdpi.com/2077-1312/8/9/714>.
- [53] D. C. Wilcox, "Formulation of the k-w Turbulence Model Revisited," *AIAA Journal*, vol. 46, no. 11, pp. 2823-2838, 2008, doi: 10.2514/1.36541.
- [54] "Principles of Turbomachine Analysis," in *Principles of Turbomachinery*, 2011, pp. 105-134.
- [55] E. Ramm, "Finite element procedures in engineering analysis, K-J. Bathe, Prentice-Hall, 1982. No. of pages: 735," *International Journal for Numerical and Analytical Methods in Geomechanics*, vol. 7, no. 4, pp. 500-500, 1983, doi: <https://doi.org/10.1002/nag.1610070412>.
- [56] M. Lesoinne and C. Farhat, "Geometric conservation laws for flow problems with moving boundaries and deformable meshes, and their impact on aeroelastic computations," *Computer Methods in Applied Mechanics and Engineering*, vol. 134, no. 1, pp. 71-90, 1996/07/15/ 1996, doi: [https://doi.org/10.1016/0045-7825\(96\)01028-6](https://doi.org/10.1016/0045-7825(96)01028-6).

- [57] P. Thomas and C. Lombard, "Geometric conservation law and its application to flow computations on moving grids," *AIAA journal*, vol. 17, no. 10, pp. 1030-1037, 1979.
- [58] C. Farhat, M. Lesoinne, and N. Maman, "Mixed explicit/implicit time integration of coupled aeroelastic problems: Three-field formulation, geometric conservation and distributed solution," *International Journal for Numerical Methods in Fluids*, vol. 21, no. 10, pp. 807-835, 1995.
- [59] T. Tzong, H. H. Chen, K. C. Cheng, T. Wu, and T. Cebeci, "A general interface method for aeroelastic analysis of aircraft," NASA Ames Research Center, 1996.
- [60] M. Heshmati, "Fatigue Life Assessment of Bridge Details Using Finite Element Method," Master's, Civil and Environmental Engineering, CHALMERS UNIVERSITY OF TECHNOLOGY, 2012.
- [61] J. Schijve, "Stress Concentration at Notches," in *Fatigue of Structures and Materials*, J. Schijve Ed. Dordrecht: Springer Netherlands, 2009, pp. 59-88.
- [62] I. Barmicho, "Fatigue Life Assessment of Cut Edges in High Strength Steel," Aeronautical and Vehicle Engineering, Royal Institute of Technology, Stockholm, 2015.
- [63] P. C. Paris and F. Erdogan, "A Critical Analysis of Crack Propagation Laws," *Journal of Basic Engineering*, vol. 85, pp. 528-533, 1963.
- [64] L. Zhang et al., "Methods for fatigue-life estimation: A review of the current status and future trends," *Nanotechnology and Precision Engineering*, vol. 6, no. 2, 2023, doi: 10.1063/10.0017255.
- [65] ANSYS Fatigue Module Training, I. ANSYS, 2015.
- [66] G. Agricola, *Basic Mine Ventilation*. AMC Consultants Pty Ltd, 2005.
- [67] T. Köktürk, "Design and Performance Analysis of a Reversible Axial Flow Fan," M.Sc. Thesis, The Graduate School of Natural and Applied Sciences Middle East Technical University, 2005.
- [68] J. Alqallaf and J. A. Teixeira, "Numerical study of effects of solid particle erosion on compressor and engine performance," *Results in Engineering*, vol. 15, 2022, doi: 10.1016/j.rineng.2022.100462.
- [69] O. Takehiro, "Materials for Aircraft Engines," in "ASEN 5063 Aircraft Propulsion Final Report," Colorado University, 2015.
- [70] A. J. Strazisar and J. R. Wood, "Laser Anemometer Measurements in a Transonic Axial-Flow Fan Rotor", NASA Technical Paper 2879, 1989.
- [71] M. Musto and G. Rotondo, "CFD analysis of a realistic reduced-scale modeling equipped with axial jet fan," *Fire Safety Journal*, vol. 74, pp. 11-24, 2015, doi: 10.1016/j.firesaf.2015.03.006.
- [72] H. Laouira, F. Mebarek-Oudina, A. K. Hussein, L. Kolsi, A. Merah, and O. Younis, "Heat transfer inside a horizontal channel with an open trapezoidal enclosure subjected to a heat source of different lengths," *Heat Transfer-Asian Research*, vol. 49, no. 1, pp. 406-423, 2020, doi: 10.1002/htj.21618.

- [73] F. Mebarek-Oudina et al., "Mixed Convection inside a Duct with an Open Trapezoidal Cavity Equipped with Two Discrete Heat Sources and Moving Walls," *Mathematics*, vol. 10, no. 6, 2022, doi: 10.3390/math10060929.
- [74] G. Gunawan, D. I. Permana, and P. Soetikno, "Design and numerical simulation of radial inflow turbine of the regenerative Brayton cycle using supercritical carbon dioxide," *Results in Engineering*, vol. 17, 2023, doi: 10.1016/j.rineng.2023.100931.
- [75] Y. Zhao and X. Su, *Computational Fluid-Structure Interaction*. Elsevier, 2019.
- [76] i. H. Abu-Hamdeh, K. Daqrouq, F. Mebarek-Oudina, and H. Ahmad, "Simulation and Analysis with Wavelet Transform Technique and the Vibration Characteristics for Early Revealing of Cracks in Structures," *Mathematical Problems in Engineering*, vol. 2021, pp. 1-16, 2021, doi: 10.1155/2021/6626232.
- [77] F.-K. Benra, H. J. Dohmen, J. Pei, S. Schuster, and B. Wan, "A Comparison of One-Way and Two-Way Coupling Methods for Numerical Analysis of Fluid-Structure Interactions," *Journal of Applied Mathematics*, vol. 2011, p. 853560, 2011/11/03 2011, doi: 10.1155/2011/853560.
- [78] Design and analysis of experiments, 8th edition (Environmental Progress & Sustainable Energy, no. 1). 2013, pp. 8-10.
- [79] L. B. N. Laboratory, *Improving Fan System Performance*. 1989.
- [80] S. M. A. Moghadam, M. Meinke, and W. Schröder, "Analysis of tip-leakage flow in an axial fan at varying tip-gap sizes and operating conditions," *Computers & Fluids*, vol. 183, pp. 107-129, 2019/04/15/ 2019, doi: <https://doi.org/10.1016/j.compfluid.2019.01.014>.
- [81] J. M. Pérez and C. Jimenez, "Characteristics of linear modal instabilities in hypersonic flows with detached shock waves," *Results in Engineering*, vol. 10, 2021, doi: 10.1016/j.rineng.2021.100219.
- [82] G. L. Podgaietsky, M. L. C. de Oliveira, and C. J. L. Hermes, "Model-based efficiency mapping and parametric analysis of low-pressure axial fans," *International Journal of Refrigeration*, vol. 144, pp. 136-144, 2022, doi: 10.1016/j.ijrefrig.2022.08.018.
- [83] S. M. Fakhari, M. Ben Hassen, and H. Mrad, "Optimizing the operation safety and performance of an axial compressor using fluid-structure coupling and high-performance computing," *Results in Engineering*, vol. 18, 2023, doi: 10.1016/j.rineng.2023.101061.
- [84] J. Menéndez et al., "Auxiliary ventilation systems in mining and tunnelling: Air leakage prediction and system design to optimize the energy efficiency and operation costs," *Tunnelling and Underground Space Technology*, vol. 140, 2023, doi: 10.1016/j.tust.2023.105298.
- [85] T. Adibi, S. E. Razavi, S. F. Ahmed, H. Hassanpour, S. C. Saha, and S. M. Muyeen, "Predicting airfoil stalling dynamics using upwind numerical solutions to non-viscous equations," *Results in Engineering*, vol. 20, 2023, doi: 10.1016/j.rineng.2023.101472.
- [86] Z. Song, X. Zheng, B. Wang, K. Zhou, and R. Amankwa Adjei, "Aerodynamic and structural multidisciplinary optimization design method of fan rotors based on blade curvature constraints," *Aerospace Science and Technology*, vol. 136, 2023, doi: 10.1016/j.ast.2023.108187.

- [87] K. S. Park, A. Zamiri, M. Choi, B. J. Lee, and J. T. Chung, "Numerical optimization of a stator blade to enhance aerodynamic performance in a transonic fan stage," *European Journal of Mechanics - B/Fluids*, vol. 103, pp. 163-181, 2024, doi: 10.1016/j.euromechflu.2023.10.003.
- [88] M. Amer, "A novel bionic impeller for laptop cooling fan system," *Results in Engineering*, vol. 20, 2023, doi: 10.1016/j.rineng.2023.101558.
- [89] M. B. Hassen, S. M. Fakhari, and H. Mrad, "Assessment of Crack Growth and Fatigue Life of an Axial Fan Blade Based on a Co-Simulation Approach," *Advances in Materials Science*, vol. 23, no. 3, pp. 61-79, 2023, doi: doi:10.2478/adms-2023-0017.
- [90] K. Khani Aminjan et al., "Numerical and experimental investigation to design a novel morphing airfoil for performance optimization," *Propulsion and Power Research*, vol. 12, no. 1, pp. 83-103, 2023/03/01/ 2023, doi: <https://doi.org/10.1016/j.ippr.2023.02.004>.
- [91] K. K. Aminjan, "Aerodynamic Analysis of NACA 65-2012 airfoils at different attack angles with computational fluid dynamics (CFD) method," *International Journal of Mechanical Handling and Automation*, vol. 4, no. 2, pp. 9-16, 2018.
- [92] J. Winslow, H. Otsuka, B. Govindarajan, and I. Chopra, "Basic Understanding of Airfoil Characteristics at Low Reynolds Numbers (104-105)," *Journal of Aircraft*, vol. 55, no. 3, pp. 1050-1061, 2018, doi: 10.2514/1.C034415.
- [93] K. Gharali and D. A. Johnson, "Numerical modeling of an S809 airfoil under dynamic stall, erosion and high reduced frequencies," *Applied Energy*, vol. 93, pp. 45-52, 2012/05/01/ 2012, doi: <https://doi.org/10.1016/j.apenergy.2011.04.037>.
- [94] P. I. Muiruri, O. S. Motsamai, and R. Ndeda, "A comparative study of RANS-based turbulence models for an upscale wind turbine blade," *SN Applied Sciences*, vol. 1, no. 3, p. 237, 2019/02/18 2019, doi: 10.1007/s42452-019-0254-5.
- [95] M. Shekaridahaj, F. K. Mirza, and B. Farhaneh, "Numerical investigation of aerodynamic performance of an axial fan blade equipped with vortex generators," *AIP Advances*, vol. 13, no. 4, 2023, doi: 10.1063/5.0143486.
- [96] A. Subramanian et al., "Effect of airfoil and solidity on performance of small scale vertical axis wind turbine using three dimensional CFD model," *Energy*, vol. 133, pp. 179-190, 2017/08/15/ 2017, doi: <https://doi.org/10.1016/j.energy.2017.05.118>.
- [97] B. Huang, P. Wang, L. Wang, T. Cao, D. Wu, and P. Wu, "A combined method of CFD simulation and modified Beddoes-Leishman model to predict the dynamic stall characterizations of S809 airfoil," *Renewable Energy*, vol. 179, pp. 1636-1649, 2021/12/01/ 2021, doi: <https://doi.org/10.1016/j.renene.2021.07.131>.
- [98] K. J. Oh and S. H. Kang, "A numerical investigation of the dual performance characteristics of a small propeller fan using viscous flow calculations," *Computers & Fluids*, vol. 28, no. 6, pp. 815-823, 1999/07/01/ 1999, doi: [https://doi.org/10.1016/S0045-7930\(98\)00035-8](https://doi.org/10.1016/S0045-7930(98)00035-8).
- [99] A. Shahsavari and M. Nili-Ahmabadi, "A novel approach for the design of axial flow fan by increasing by-pass ratio in a constant-diameter turbofan," *Propulsion and Power Research*, vol. 9, no. 2, pp. 142-158, 2020/06/01/ 2020, doi: <https://doi.org/10.1016/j.ippr.2020.04.005>.

- [100] S.-C. Lin and M.-L. Tsai, "An integrated performance analysis for a backward-inclined centrifugal fan," *Computers & Fluids*, vol. 56, pp. 24-38, 2012/03/15/ 2012, doi: <https://doi.org/10.1016/j.compfluid.2011.11.009>.
- [101] G. Yuan, S. Lu, and Z. Wei, "A line search algorithm for unconstrained optimization," *J. Softw. Eng. Appl.*, vol. 3, no. 5, pp. 503-509, 2010.
- [102] G. Yuan, X. Lu, and Z. Wei, "A conjugate gradient method with descent direction for unconstrained optimization," *Journal of Computational and Applied Mathematics*, vol. 233, no. 2, pp. 519-530, 2009, doi: 10.1016/j.cam.2009.08.001.
- [103] N. Andrei, "Open problems in nonlinear conjugate gradient algorithms for unconstrained optimization," *Bulletin of the Malaysian Mathematical Sciences Society*, vol. 34, no. 2, pp. 319-330, 2011.
- [104] E. Polak and G. Ribiére, "Note sur la convergence de directions conjuguées," *Rev. Fr. Inf. Rech. Oper.*, vol. 16, pp. 35-43, 1969.
- [105] Y. Liu and C. Storey, "Efficient generalized conjugate gradient algorithms, part 1: Theory," *Journal of Optimization Theory and Applications*, vol. 69, no. 1, pp. 129-137, 1991, doi: 10.1007/BF00940464.
- [106] R. Fletcher, *Practical Methods of Optimization*, 1987.
- [107] Y. H. Dai and Y. Yuan, "A Nonlinear Conjugate Gradient Method with a Strong Global Convergence Property," *SIAM Journal on Optimization*, vol. 10, no. 1, pp. 177-182, 1999, doi: 10.1137/s1052623497318992.
- [108] P. Wolfe, "CONVERGENCE CONDITIONS FOR ASCENT METHODS," *SIAM Review*, vol. 11, no. 2, pp. 226-235, 1969, doi: 10.1137/1011036.
- [109] L. Armijo, "Minimization of functions having lipschitz continuous first partial derivatives," *Pacific Journal of Mathematics*, vol. 16, no. 1, pp. 1-3, 1966, doi: 10.2140/pjm.1966.16.1.
- [110] N. Andrei, "A scaled BFGS preconditioned conjugate gradient algorithm for unconstrained optimization," *Applied Mathematics Letters*, vol. 20, no. 6, pp. 645-650, 2007, doi: 10.1016/j.aml.2006.06.015.
- [111] E. G. Birgin and J. M. Martínez, "A Spectral Conjugate Gradient Method for Unconstrained Optimization," *Applied Mathematics and Optimization*, vol. 43, no. 2, pp. 117-128, 2001, doi: 10.1007/s00245-001-0003-0.
- [112] J. K. Liu, Y. M. Feng, and L. M. Zou, "A spectral conjugate gradient method for solving large-scale unconstrained optimization," *Computers and Mathematics with Applications*, vol. 77, no. 3, pp. 731-739, 2019, doi: 10.1016/j.camwa.2018.10.002.
- [113] A. B. Abubakar, P. Kumam, M. Malik, and A. H. Ibrahim, "A hybrid conjugate gradient based approach for solving unconstrained optimization and motion control problems," *Mathematics and Computers in Simulation*, vol. 201, pp. 640-657, 2022, doi: 10.1016/j.matcom.2021.05.038.
- [114] M. Farid, "Accelerated diagonal gradient-type method for large-scale unconstrained optimization," *Mathematics and Computers in Simulation*, vol. 120, pp. 24-30, 2015, doi: 10.1016/j.matcom.2014.12.009.

- [115] G. Kara, A. Özmen, and G.-W. Weber, "Stability advances in robust portfolio optimization under parallelepiped uncertainty," *Central European Journal of Operations Research*, vol. 27, no. 1, pp. 241-261, 2017, doi: 10.1007/s10100-017-0508-5.
- [116] M. Graczyk-Kucharska et al., "Modeling for Human Resources Management by Data Mining, Analytics and Artificial Intelligence in the Logistics Departments," in *Smart and Sustainable Supply Chain and Logistics – Trends, Challenges, Methods and Best Practices: Volume 1*, P. Golinska-Dawson, K.-M. Tsai, and M. Kosacka-Olejnik Eds. Cham: Springer International Publishing, 2020, pp. 291-303.
- [117] A. Amiri, N. Saeedi, S. M. Fakhari, and R. Shabani, "Size-dependent Vibration and Instability of Magneto-electro-elastic Nano-scale Pipes Containing an Internal Flow with Slip Boundary Condition," *International Journal of Engineering*, vol. 29, no. 7, 2016, doi: 10.5829/idosi.ije.2016.29.07a.15.
- [118] P. Castonguay and S. Nadarajah, "Effect of Shape Parameterization on Aerodynamic Shape Optimization," in 45th AIAA Aerospace Sciences Meeting and Exhibit.
- [119] A. Jameson, L. Martinelli, and N. A. Pierce, "Optimum Aerodynamic Design Using the Navier-Stokes Equations," *Theoretical and Computational Fluid Dynamics*, vol. 10, no. 1-4, pp. 213-237, 1998, doi: 10.1007/s001620050060.
- [120] A. D. J. Payot, T. C. S. Rendall, and C. B. Allen, "Restricted snakes volume of solid (RSVS): A parameterisation method for topology optimisation of external aerodynamics," *Computers & Fluids*, vol. 182, pp. 60-84, 2019/03/30/ 2019, doi: <https://doi.org/10.1016/j.compfluid.2019.02.008>.
- [121] M. Kishida and T. Kurahashi, "Proposal of a modified optimality criteria method for topology optimization analysis in 3-dimensional dynamic oscillation problems," *International Journal for Numerical Methods in Engineering*, vol. 123, no. 3, pp. 866-896, 2022, doi: <https://doi.org/10.1002/nme.6880>.
- [122] A. F. P. Ribeiro, A. M. Awruch, and H. M. Gomes, "An airfoil optimization technique for wind turbines," *Applied Mathematical Modelling*, vol. 36, no. 10, pp. 4898-4907, 2012/10/01/ 2012, doi: <https://doi.org/10.1016/j.apm.2011.12.026>.
- [123] T. F. Chan and L. A. Vese, "Active contours without edges," *IEEE Transactions on Image Processing*, vol. 10, no. 2, pp. 266-277, 2001, doi: 10.1109/83.902291.
- [124] J. Cao and J. Wu, "A conjugate gradient algorithm and its applications in image restoration," *Applied Numerical Mathematics*, vol. 152, pp. 243-252, 2020/06/01/ 2020, doi: <https://doi.org/10.1016/j.apnum.2019.12.002>.
- [125] D. G. Luenberger, & Ye, Y., *Linear and nonlinear programming*. Springer Science & Business Media, 2008.
- [126] S. S. Rao, *Engineering Optimization Theory and Practice*. John Wiley & Sons, Inc., 2009.
- [127] W. W. Hager and H. Zhang, "A New Conjugate Gradient Method with Guaranteed Descent and an Efficient Line Search," *SIAM Journal on Optimization*, vol. 16, no. 1, pp. 170-192, 2005, doi: 10.1137/030601880.
- [128] J. K. Liu, Y. M. Feng, and L. M. Zou, "A spectral conjugate gradient method for solving large-scale unconstrained optimization," *Computers & Mathematics with Applications*, vol. 77, no. 3, pp. 731-739, 2019, doi: 10.1016/j.camwa.2018.10.002.

- [129] H. Mrad and S. M. Fakhari, "Optimization of unconstrained problems using a developed algorithm of spectral conjugate gradient method calculation," *Mathematics and Computers in Simulation*, vol. 215, pp. 282-290, 2024/01/01/ 2024, doi: <https://doi.org/10.1016/j.matcom.2023.07.026>.
- [130] C. S. Morawetz, "On the non-existence of continuous transonic flows past profiles III," *Communications on Pure and Applied Mathematics*, vol. 11, no. 1, pp. 129-144, 1958, doi: <https://doi.org/10.1002/cpa.3160110107>.
- [131] S. T. LeDoux et al., "Study Based on the AIAA Aerodynamic Design Optimization Discussion Group Test Cases," *AIAA Journal*, vol. 53, no. 7, pp. 1910-1935, 2015, doi: 10.2514/1.J053535.
- [132] H. P. Buckley, B. Y. Zhou, and D. W. Zingg, "Airfoil Optimization Using Practical Aerodynamic Design Requirements," *Journal of Aircraft*, vol. 47, no. 5, pp. 1707-1719, 2010, doi: 10.2514/1.C000256.
- [133] T. W. Sederberg, & Parry, S. R., "Free-form deformation of solid geometric models," *SIGGRAPH Computer Graphics*, 1986.
- [134] H. Sobieczky, "Parametric airfoils and wings," in *Recent development of aerodynamic design methodologies: inverse design and optimization*: Springer, 1999, pp. 71-87.
- [135] V. Sripathadkul, M. Padulo, and M. Guenov, "A Comparison of Airfoil Shape Parameterization Techniques for Early Design Optimization," in *13th AIAA/ISSMO Multidisciplinary Analysis Optimization Conference*.
- [136] R. Mukesh, K. Lingadurai, and U. Selvakumar, "Airfoil shape optimization using non-traditional optimization technique and its validation," *Journal of King Saud University - Engineering Sciences*, vol. 26, no. 2, pp. 191-197, 2014, doi: 10.1016/j.jksues.2013.04.003.
- [137] P. Della Vecchia, E. Daniele, and E. D'Amato, "An airfoil shape optimization technique coupling PARSEC parameterization and evolutionary algorithm," *Aerospace Science and Technology*, vol. 32, no. 1, pp. 103-110, 2014/01/01/ 2014, doi: <https://doi.org/10.1016/j.ast.2013.11.006>.
- [138] N. P. Salunke, Juned Ahamad R. A., and S.A. Channiwala., "Airfoil Parameterization Techniques: A Review," *American Journal of Mechanical Engineering*, vol. 2, 2014, doi: <https://doi.org/10.12691/ajme-2-4-1>.
- [139] D. Rajnarayan, A. Ning, and J. A. Mehr, "Universal Airfoil Parametrization Using B-Splines," presented at the 2018 Applied Aerodynamics Conference, 2018.
- [140] X. Lu, J. Huang, L. Song, and J. Li, "An improved geometric parameter airfoil parameterization method," *Aerospace Science and Technology*, vol. 78, pp. 241-247, 2018/07/01/ 2018, doi: <https://doi.org/10.1016/j.ast.2018.04.025>.
- [141] F. Yang, Z. Yue, L. Li, and W. Yang, "Aerodynamic optimization method based on Bezier curve and radial basis function," *Proceedings of the Institution of Mechanical Engineers, Part G: Journal of Aerospace Engineering*, vol. 232, no. 3, pp. 459-471, 2018, doi: 10.1177/0954410016679433.
- [142] T. H. Hansen, "Airfoil optimization for wind turbine application," *Wind Energy*, vol. 21, no. 7, pp. 502-514, 2018, doi: <https://doi.org/10.1002/we.2174>.

- [143] H. Lim and H. Kim, "Multi-objective airfoil shape optimization using an adaptive hybrid evolutionary algorithm," *Aerospace Science and Technology*, vol. 87, pp. 141-153, 2019/04/01/ 2019, doi: <https://doi.org/10.1016/j.ast.2019.02.016>.
- [144] H. C. A. Ümütlu and Z. Kiral, "Airfoil Shape Optimization Using BÉzier Curve and Genetic Algorithm," *Aviation*, vol. 26, no. 1, pp. 32-40, 2022, doi: 10.3846/aviation.2022.16471.
- [145] X. Zhang, F. Xie, T. Ji, Z. Zhu, and Y. Zheng, "Multi-fidelity deep neural network surrogate model for aerodynamic shape optimization," *Computer Methods in Applied Mechanics and Engineering*, vol. 373, 2021, doi: 10.1016/j.cma.2020.113485.
- [146] V. Esfahanian, M. J. Izadi, H. Bashi, M. Ansari, A. Tavakoli, and M. Kordi, "Aerodynamic shape optimization of gas turbines: a deep learning surrogate model approach," *Structural and Multidisciplinary Optimization*, vol. 67, no. 1, 2023, doi: 10.1007/s00158-023-03703-9.
- [147] S. Crino and D. E. Brown, "Global optimization with multivariate adaptive regression splines," *IEEE Trans Syst Man Cybern B Cybern*, vol. 37, no. 2, pp. 333-40, Apr 2007, doi: 10.1109/tsmc.2006.883430.
- [148] G.-W. Weber, İ. Batmaz, G. Köksal, P. Taylan, and F. Yerlikaya-Özkurt, "CMARS: a new contribution to nonparametric regression with multivariate adaptive regression splines supported by continuous optimization," *Inverse Problems in Science and Engineering*, vol. 20, no. 3, pp. 371-400, 2011, doi: 10.1080/17415977.2011.624770.
- [149] G.-W. Weber, Z. Çavuşoğlu, and A. Özmen, "Predicting default probabilities in emerging markets by new conic generalized partial linear models and their optimization," *Optimization*, vol. 61, no. 4, pp. 443-457, 2012, doi: 10.1080/02331934.2011.654343.
- [150] E. K. Koc, C. Iyigun, İ. n. Batmaz, and G.-W. Weber, "Efficient adaptive regression spline algorithms based on mapping approach with a case study on finance," *Journal of Global Optimization : An International Journal Dealing with Theoretical and Computational Aspects of Seeking Global Optima and Their Applications in Science, Management and Engineering*, vol. 60, no. 1, pp. 103-120, 2014, doi: 10.1007/s10898-014-0211-1.
- [151] A. Özmen, G. W. Weber, İ. Batmaz, and E. Kropat, "RCMARS: Robustification of CMARS with different scenarios under polyhedral uncertainty set," *Communications in Nonlinear Science and Numerical Simulation*, vol. 16, no. 12, pp. 4780-4787, 2011, doi: 10.1016/j.cnsns.2011.04.001.
- [152] H.-p. Mao, Y.-z. Wu, and L.-p. Chen, "Multivariate adaptive regression splines based simulation optimization using move-limit strategy," *Journal of Shanghai University (English Edition)*, vol. 15, no. 6, pp. 542-547, 2011/12/01 2011, doi: 10.1007/s11741-011-0783-2.
- [153] D. F. Rogers and J. A. Adams, *Mathematical Elements for Computer Graphics*. McGraw-Hill, 1976.
- [154] B. Kulfan and J. Bussolletti, "'Fundamental' parameteric geometry representations for aircraft component shapes," in *11th AIAA/ISSMO multidisciplinary analysis and optimization conference*, 2006, p. 6948.
- [155] G. Farin, *Curves and Surfaces for CAGD: A Practical Guide*. MORGAN KAUFMAN N, 2002.
- [156] D. M. and Y. H. "XFOIL 6.99 User Primer." (accessed).

- [157] D. Anitha, G. K. Shamili, P. Ravi Kumar, and R. Sabari Vihar, "Air foil Shape Optimization Using Cfd And Parametrization Methods," *Materials Today: Proceedings*, vol. 5, no. 2, Part 1, pp. 5364-5373, 2018/01/01 / 2018, doi: <https://doi.org/10.1016/j.matpr.2017.12.122>.
- [158] N. Jorge and W. Stephen J, *Numerical Optimization* (Springer Series in Operations Research and Financial Engineering). Springer New York, NY, 2006.
- [159] L. Bottou, & Bousquet, O., "The tradeoffs of large scale learning. In Advances in neural information processing systems," 2008.
- [160] R. H. Byrd, P. Lu, J. Nocedal, and C. Zhu, "A Limited Memory Algorithm for Bound Constrained Optimization," *SIAM Journal on Scientific Computing*, vol. 16, no. 5, pp. 1190-1208, 1995, doi: 10.1137/0916069.
- [161] P. Wolfe, "Convergence Conditions for Ascent Methods. II: Some Corrections," *SIAM Review*, vol. 13, no. 2, pp. 185-188, 1971, doi: 10.1137/1013035.
- [162] L. Armijo, "Minimization of functions having Lipschitz continuous first partial derivatives," *Pacific Journal of Mathematics*, vol. 16, no. 1, pp. 1-3, 3, 1966.
- [163] E. Polak and G. Ribiere, "Note sur la convergence de méthodes de directions conjuguées," *R.I.R.O.*, vol. 3, no. 16, pp. 35-43, 1969. [Online]. Available: <https://doi.org/10.1051/m2an/196903R100351>.
- [164] S. Sanmatías and E. Vercher, "A Generalized Conjugate Gradient Algorithm," *J. Optim. Theory Appl.*, vol. 98, no. 2, pp. 489–502, 1998.
- [165] R. Fletcher, "Conjugate Direction Methods," in *Practical Methods of Optimization*, 2000, pp. 80-94.
- [166] W. W. Hager and H. Zhang, "A SURVEY OF NONLINEAR CONJUGATE GRADIENT," 2005.
- [167] Y. Narushima and H. Yabe, "A survey of sufficient descent conjugate gradient methods for unconstrained optimization," *SUT Journal of Mathematics*, vol. 50, no. 2, pp. 167-203, 37, 2014. [Online]. Available: <https://doi.org/10.55937/sut/1424782608>.
- [168] Y. F. Hu and C. Storey, "Global convergence result for conjugate gradient methods," *Journal of Optimization Theory and Applications*, vol. 71, no. 2, pp. 399-405, 1991/11/01 1991, doi: 10.1007/BF00939927.
- [169] Y. Dai, J. Han, G. Liu, D. Sun, H. Yin, and Y.-X. Yuan, "Convergence Properties of Nonlinear Conjugate Gradient Methods," *SIAM Journal on Optimization*, vol. 10, no. 2, pp. 345-358, 2000, doi: 10.1137/s1052623494268443.
- [170] J. C. Gilbert and J. Nocedal, "Global Convergence Properties of Conjugate Gradient Methods for Optimization," *SIAM Journal on Optimization*, vol. 2, no. 1, pp. 21-42, 1992, doi: 10.1137/0802003.
- [171] A. Y. Al-Bayati and W. H. Sharif, "Computational Treatments of an Improved Conjugate Gradient Method for Unconstrained Minimization," *International Journal of Mathematical Archive*, 2012.
- [172] S. M. Fakhari and H. Mrad, "Optimization of an axial-flow mine ventilation fan based on effects of design parameters," *Results in Engineering*, vol. 21, p. 101662, 2024/03/01 / 2024, doi: <https://doi.org/10.1016/j.rineng.2023.101662>.

- [173] C. Fan, R. Amankwa Adjei, Y. Wu, and A. Wang, "Parametric study on the aerodynamic performance of a ducted-fan rotor using free-form method," *Aerospace Science and Technology*, vol. 101, doi: 10.1016/j.ast.2020.105842.
- [174] S. Chen, D. Wang, and S. Sun, "Bionic Fan Optimization Based on Taguchi Method," *Engineering Applications of Computational Fluid Mechanics*, vol. 5, no. 3, pp. 302-314, 2011, doi: 10.1080/19942060.2011.11015373.
- [175] Wu and Huang, "Optimization design of axial fan blade," *Journal of the Chinese Institute of Engineers*, vol. 42, no. 6, pp. 473-478, 2019, doi: 10.1080/02533839.2019.1611478.
- [176] A. Richard Amankwa and F. Chengwei, "Multi-objective design optimization of a transonic axial fan stage using sparse active subspaces," *Engineering Applications of Computational Fluid Mechanics*, vol. 18, no. 1, doi: 10.1080/19942060.2024.2325488.
- [177] S. M. Fakhari and H. Mrad, "Aerodynamic shape optimization of NACA airfoils based on a novel unconstrained conjugate gradient algorithm," *Journal of Engineering Research*, 2024/07/30/ 2024, doi: <https://doi.org/10.1016/j.jer.2024.07.020>.
- [178] Y.-X. Liu, P.-H. Cong, Y.-W. Wu, J.-L. Li, and X.-P. Wang, "Failure analysis and design optimization of shrouded fan blade," *Engineering Failure Analysis*, vol. 122, doi: 10.1016/j.engfailanal.2020.105208.
- [179] M. Khurana, H. Winarto, and A. Sinha, "Application of Swarm Approach and Artificial Neural Networks for Airfoil Shape Optimization," in *12th AIAA/ISSMO Multidisciplinary Analysis and Optimization Conference*.
- [180] J. L. Meriam and L. G. Kraige, *Engineering Mechanics: Dynamics*, 7th Edition: Dynamics. Wiley, 2012.
- [181] R. C. Hibbeler, *Mechanics of Materials*. Pearson Prentice Hall, 2011.
- [182] S. Timoshenko and J. N. Goodier, *Theory of Elasticity*. McGraw-Hill, 1969.
- [183] F. O. Sonmez, "Optimal shape design of shoulder fillets for flat and round bars under various loadings," *Proceedings of the Institution of Mechanical Engineers, Part C: Journal of Mechanical Engineering Science*, vol. 223, no. 8, pp. 1741-1754, 2009, doi: 10.1243/09544062jmes1457.
- [184] R. G. Budynas, J. K. Nisbett, and J. E. Shigley, *Shigley's mechanical engineering design*, 9th ed. (McGraw-Hill series in mechanical engineering). New York: McGraw-Hill (in English), 2011.
- [185] S. Beden, S. Abdullah, and A. Ariffin, "Review of fatigue crack propagation models for metallic components," *European Journal of Scientific Research*, vol. 28, no. 3, pp. 364-397, 2009.
- [186] R. Forman, "Study of fatigue crack initiation from flaws using fracture mechanics theory," *Engineering Fracture Mechanics*, vol. 4, no. 2, pp. 333-345, 1972.